GaN based polar and nonpolar heterostructures grown on ZnO for optoelectronic applications

Yuanyang Xia

UNIVERSITE DE NICE-SOPHIA ANTIPOLIS - UFR Sciences
Ecole Doctorale de Sciences Fondamentales et Appliquées

T H E S E

pour obtenir le titre de
Docteur en Sciences
de l'UNIVERSITE de Nice-Sophia Antipolis

Discipline : Physique

présentée et soutenue par
Yuanyang XIA

Hétérostructures Polaires et Non Polaires à base de Nitrure de Gallium épitaxiées sur ZnO pour Applications Optoélectroniques

Thèse dirigée par Jean MASSIES
et co-dirigée par Julien BRAULT
soutenue le 01. 10. 2013

Jury

X. Wallart	Directeur de Recherche, CNRS	Rapporteur
G. Feuillet	Ingénieur, CEA	Rapporteur
M. De Micheli	Directeur de Recherche, CNRS	Examinateur
O. Brandt	Senior Researcher, Paul Drude Institute, Berlin	Examinateur
J. Brault	Chargé de Recherche CNRS	Co-directeur de thèse

Contents

List of abbreviations

AFM	Atomic Force Microscopy
BE	Band Edge
BL	Blue Luminescence
BSF	Basal Stacking Faults
CB	Conduction Band
DAP	Donor Acceptor Pair
DBE	Donor Bound Exciton
DG	Disoriented Grain
D^0X	Neutral Donor Bound Exciton
EBL	Electron Blocking Layer
EBS	Electronic Band Structure
EDX	Energy Dispersive X-ray Analysis
E_g	Band Gap Energy
EL	Electroluminescence
FWHM	Full Width at Half Maximum
LD	Laser Diode
LED	Light Emitting Diode
LM	Lattice Mismatch
LO	Longitudinal Optical Phonon
LP	Lattice Parameter
MBE	Molecular Beam Epitaxy
MOCVD	Metal Organic Chemical Vapour Deposition
MQW	Multi Quantum Well
NBE	Near Band Edge
NID	Non-intentional Doping
PD	Partial Dislocation
PL	Photoluminescence
PSF	Prismatic Stacking Faults
QW	Quantum Well
R_y	Excitonic Rydberg Energy
rms	Root Mean Square
SEM	Scanning Electron Microscopy
TD	Threading Dislocation
TDD	Threading Dislocation Density
TEC	Thermal Expansion Coefficient
TEM	Transmission electron Microscopy
VB	Valence Band
WG	Waveguide
XRD	X-Ray Diffraction
YL	Yellow Luminescence

Résumé

Le chapitre I présente les connaissances fondamentales concernant le projet de recherche de cette thèse. Ce chapitre se compose de quatre parties: la structure cristalline, la structure de bande électronique, les hétérostructures nitrures d'éléments III et l'épitaxie du nitrure de gallium (GaN) sur substrat d'oxyde de zinc (ZnO). La partie concernant la structure cristalline présente les structures du saphir, de ZnO et de GaN, incluant le groupe de symétrie, les propriétés thermiques et mécaniques, ainsi que les défauts fréquemment observés. La deuxième partie se concentre sur la structure de bande électronique du cristal wurtzite. La structure de la bande de GaN, qui a une bande interdite directe, est présentée. La modification de la structure de bande d'un matériau contraint, en particulier dans le cas de contraintes anisotropes, est discutée. Les niveaux profonds dans la bande interdite sont également brièvement présentés. La partie hétérostructure présente les structures et les applications des dispositifs optoélectroniques basés sur des hétérostructures à base de nitrures. La largeur de bande interdite et les problèmes de désaccords de paramètre de maille des différents alliages de nitrures d'éléments III sont discutés. Les avantages et les progrès récents des hétérostructures à base de nitrures épitaxiées le long des orientations non polaires sont introduits. Dans la dernière partie, les propriétés générales et les derniers développements des substrats ZnO sont introduits. Les avantages et inconvénients de la croissance de GaN sur des substrats ZnO sont discutés, et l'état de l'art dans ce domaine est présenté.

Dans le chapitre II, les techniques expérimentales utilisées pour la croissance et les caractérisations des échantillons sont introduites. Tous les échantillons ont été épitaxiés en utilisant des réacteurs d'épitaxie par jets moléculaires (EJM) de la société RIBER. En particulier, les hétérostructures à base de GaN ont été épitaxiées dans une chambre Riber 32P. Les caractéristiques générales du réacteur EJM (en particulier le chauffage des échantillons, le vide et les systèmes de surveillance in situ) sont introduites. Le principe de la croissance épitaxiale est brièvement présenté, et les différentes méthodes de croissance sont discutées. Les morphologies de surface ont été étudiées par microscopie à force atomique (Digital instruments Nanoscope IV fonctionnant en mode non contact) et par microscopie électronique à balayage (JEOL JSM 3000F). Ce dernier a également été utilisé pour effectuer des mesures d'échantillons en coupe transverse. La qualité cristalline des couches de GaN a été évaluée en

utilisant la diffraction de rayons X (DRX). La raie Kα1 du cuivre (Cu), avec une longueur d'onde de 1,5406 Å, est utilisée comme source de rayons X. Différents modes de balayage et de configurations de diffraction sont introduits. Les méthodes pour déterminer les paramètres de maille de la couche épitaxiale en utilisant la DRX sont développées. La photoluminescence (PL) a été utilisée pour étudier la structure de bande électronique des hétérostructures. La configuration du banc de PL utilisé dans notre laboratoire est présentée, et un spectre de GaN est pris comme exemple pour l'illustration de cette étude.

Le chapitre III traite des hétérostructures non polaires (Al, Ga)N épitaxiées sur des couches tremplins de (Zn, Mg)O. Dans cette étude, une série de couches de GaN plan a (11-20) est épitaxiée sur des couches tremplins de (Zn, Mg)O déposées sur des substrats de saphir plan r (1-102). Un procédé de croissance en deux étapes a été développé, et les conditions de croissance des couches de GaN ont été optimisées. L'influence de la concentration en Mg dans les couches tremplins de (Zn, Mg)O sur la croissance des couches de GaN est discutée. Les couches tremplins de (Zn, Mg)O dont la concentration en Mg est comprise entre 25% et 40% se trouvent être les plus appropriées pour la croissance de GaN. Les couches de GaN plan a présentent des propriétés structurales et optiques anisotropes. Les fissures présentes à la surface sont observées le long de la direction c-<0001>. La largeur à mi-hauteur (LMH) de la raie de diffraction de GaN (11-20) mesurée par DRX a une valeur minimale lorsque le faisceau incident est le long de la direction <0001>. L'émission de bord de bande de GaN domine le spectre de photoluminescence (PL) et l'émission est polarisée parallèlement à la direction <0001>. Les forces d'oscillateur entre la bande de conduction et les sous-bandes de valence ont été étudiées théoriquement et la recombinaison excitonique X_2 a été identifiée comme étant à l'origine de la polarisation de l'émission de photoluminescence du GaN. Une série d'échantillons de multi-puits quantiques (MPQs) $Al_{0.2}Ga_{0.8}N$/GaN plan a, avec des épaisseurs de puits quantiques variant de 0,5 à 7 nm, a été fabriquée sur des couches tremplins de GaN plan a. Les énergies de transition des MPQs ont été étudiées par PL, et l'absence d'effet Stark confiné quantique dans les hétérostructures non polaires est mise en évidence.

Le chapitre IV traite de la croissance et de la caractérisation d'hétérostructures (In, Ga)N sur des substrats de ZnO massifs plan c. Dans la première partie, la préparation de la surface des substrats ZnO est introduite. Un procédé de recuit a été développé pour préparer les substrats ZnO pour la croissance épitaxiale, et une surface « épi-ready » de ZnO avec des marches atomiques a été obtenue après recuit.

La deuxième partie se concentre sur la croissance de couches de GaN, en particulier sur le contrôle de la polarité sur les faces O et Zn des substrats ZnO. Des couches de GaN avec une polarité Ga ou N ont été épitaxiées sur la face O de ZnO. Le mécanisme de détermination de la polarité a été analysé et une couche interfaciale de gallate de zinc ($ZnGa_2O_4$) a été identifiée comme étant le centre d'inversion de polarité. La formation de cette couche interfaciale cubique peut être contrôlée à l'aide de la température de croissance de la couche de nucléation et du rapport III/V. Une couche de polarité N est obtenue lors de la croissance directe de GaN sur la face O de ZnO (sans formation d'une couche interfaciale), et une couche de polarité Ga est obtenue en présence d'une couche interfaciale de $ZnGa_2O_4$. D'autre part, les couches de GaN de polarité Ga sont systématiquement obtenues sur la face Zn des substrats ZnO.

Dans la troisième partie, les propriétés structurales et optiques des couches de GaN sont étudiées. Il est montré que les couches de GaN d'épaisseur ~ 600 nm sont contraintes en tension sur ZnO. L'émission d'excitons liés à des donneurs ainsi que l'émission d'excitons libres ont été observées dans les spectres de PL à basse température (10 K), et l'évolution en température de ces émissions est discutée.

Enfin, une approche efficace pour la fabrication monolithique de dispositifs émetteurs de lumière (DELs) à base de nitrures d'éléments III sur ZnO par EJM a été démontrée, et les propriétés optiques et électriques ont été étudiées et discutées. Un procédé de croissance pour la fabrication de DELs émettant dans le bleu avec une zone active constituée de multi-puits quantiques (MPQs) (In, Ga)N/GaN sur substrats ZnO plan c-(0001) a été développé. Les caractéristiques optiques et électriques des structures DELs sont présentées. Ces caractéristiques constituent un pas de plus vers la fabrication de dispositifs optoélectroniques à base de nitrures sur substrats ZnO et fournissent une solution alternative pour la réalisation et le développement d'une technologie de films minces (auto-supportés) à base de GaN.

Le chapitre V présente une étude de la croissance de couches de GaN sur substrats ZnO plan a, ainsi que la réalistion d'hétérostructures (In, Ga)N sur ZnO (plan a). Dans la première étape, le procédé de recuit de la surface de substrats ZnO plan a est étudié, et une fenêtre de température située entre 700 et 800°C (sous O_2) est proposée comme conditions de préparation optimales. Deux méthodes, basées sur l'utilisation soit du précurseur ammoniac (NH_3), soit d'une source plasma pour fournir des atomes d'azote, ont été proposées pour la croissance des couches de nucléation de GaN. Les propriétés optiques de MPQs (In, Ga)N/GaN sont étudiées et comparées. Des couches de GaN plan a, avec ces deux procédés

de nucléation ont été épitaxiées avec succès sur des substrats ZnO plan a et leurs propriétés structurales et optiques sont comparées. Les couches de GaN avec une couche de nucléation épitaxiée à l'aide d'une source plasma d'azote montrent une plus grande perfection cristalline et une émission de photoluminescence (PL) avec une intensité 30 fois supérieure à celle obtenue dans le cas du procédé avec ammoniac.

Dans la dernière partie, des MPQs (In, Ga)N/GaN polaires (plan c) et non polaires (plan a) ont été fabriqués sur des couches tremplins de GaN/ZnO. L'émission de PL des MPQs est observée sur les deux plans de croissance. L'efficacité de l'incorporation de l'In des couches (In, Ga)N plan a se trouve être inférieure à celle des couches (In, Ga)N plan c (avec des conditions de croissance identiques). Lorsque la température augmente, l'intensité de l'émission de PL des MPQs non polaires diminue plus rapidement que dans le cas des MPQs polaires, et les processus possibles de recombinaisons thermiquement activées ont été analysés. Enfin, l'émission des MPQs non polaires est polarisée suivant la direction <1-100> en raison de la rupture de symétrie dans le plan de croissance, en accord avec l'étude théorique des éléments de la matrice de transition entre la bande de conduction et la bande de valence sur la base de la théorie k • p.

En conclusion, des perspectives à ce travail sont proposées, avec notamment la nécessité de développer et d'optimiser un procédé de croissance utilisant une source plasma d'azote (N). En effet,, cette approche s'inscrit dans la continuité des résultats présentés dans le chapitre V liés à l'utilisation d'une couche de nucléation de GaN par EJM à source plasma N, qui a conduit à une amélioration significative des propriétés structurales et optiques de GaN. Le procédé de croissance de couches (In, Ga)N doit être optimisé pour améliorer l'efficacité d'incorporation de l'In sur plan a. La croissance sur substrats ZnO plan m, orientation sur laquelle il a été montré une efficacité d'incorporation de l'In plus élevée que sur plan a, devrait être étudiée. Ces développements devraient conduire à la fabrication de DELs nitrures non polaires sur substrats ZnO.

Introduction

In the early 60s, the demonstration of high efficiency electroluminescence from semiconductor devices paved the way to the fabrication of light emitting diodes (LEDs),[1] which is the building block for general solid state lighting. Nowadays, nitride semiconductors are the materials of choice for a wide range of applications, in particular in UV-visible optoelectronics.[2] Since the beginning of the 1990s, the development of nitride based devices has been accelerated owing to the improvement of the gallium nitride (GaN) crystal quality. Thanks to the continuous enhancement of the LED performances, the solid state lighting technology is now leading a revolution of the lighting technology. This new generation of lighting technology, represented by LEDs, is characterized by higher efficiency, lower energy consumption, longer lifetime and smaller volume, *etc.*, compared to the traditional incandescent and fluorescent lamps.

GaN is at the basis of the solid state light emitting technology. The hexagonal phase of GaN is a large band gap semiconductor (~ 3.4 eV), with a high chemical stability. By adjusting the III-group elementary compositions in the (In,Ga)N and (Al,Ga)N alloys, optoelectronic devices operating in the UV-visible range can be fabricated.

Currently, most of the devices are fabricated along the [0001] direction of the wurtzite crystal, along which strong polarization fields exist.[3] The total polarization consists of spontaneous and piezoelectric polarizations, and it varies with the composition and strain state of the nitride compounds. The discontinuity of the polarization at the interface of heterostructures may lead to the accumulation of charges, which may separate the electron and hole wave functions and reduce the radiative recombination efficiency. This is the well known quantum Confined stark effect (QCSE).[4,5] To avoid the QCSE, growing GaN on semipolar or nonpolar planes is proposed.[6] Along these directions, very weak or even no internal electric field exists.[7]

GaN substrates have become available in the recent years, which make the homoepitaxy of GaN possible. However, GaN substrates are still expensive and limited to small size, especially along the nonpolar orientations (~ 1000 euro / cm^2),[8] which limit the large scale production of LEDs on GaN substrates. Due to the lack of native substrates, researchers have been searching alternative substrates for the growth of GaN during the last two decades. Sapphire, silicon carbide and silicon are currently the most commonly used substrates for GaN, among which sapphire dominates ~ 80% of the market. However, the large lattice mismatch between the epitaxial layer and the substrate leads to the presence of

high densities of structural defects in the nitride heterostructure, which may reduce the radiative recombination efficiency of light emitting devices.

Zinc oxide (ZnO) substrates offer several advantages for the growth of GaN. They have the same crystal structure (wurtzite), close lattice parameters and thermal expansion coefficients with GaN, which provide the possibility to grow high quality GaN crystals on ZnO. In addition, the strong chemical selectivity between GaN and ZnO allows removing the ZnO substrates by a chemical etching process, which enables the thin film engineering of GaN by a simple method. However, several problems, such as impurity incorporations and interfacial reactions, still exist.

In this study, the growth of GaN, as well as the fabrication of quantum well (QW) heterostructures and light emitting devices, are carried out on (Zn,Mg)O / sapphire templates and bulk ZnO substrates, on both *a*- (11-20) and *c*- (0001) planes. The structural and optical properties of heterostructures are studied, and the performance of the first monolithic light emitting diode on ZnO substrate is characterized.

Chapter I gives the fundamental knowledge concerning the crystal structures and the electronic band structures of nitrides. The strain modification of the crystal and the electronic structures are discussed. Commonly observed defects in nitrides are introduced. The properties and applications of nitride heterostructures, grown on both polar and nonpolar planes are presented and discussed. In the last part, the properties of ZnO substrates are briefly introduced.

Chapter II introduces the main growth and characterization tools used in this work. Molecular beam epitaxy (MBE) is the growth technique used in this study, and the system configuration and working principles are presented. The main tools used for the characterization of the surface morphology, structural, optical and electronic properties, such as atomic force microscopy (AFM), scanning electron microscopy (SEM), x-ray diffraction (XRD), and photoluminescence (PL) are introduced.

Chapter III discusses the growth and properties of a-plane (Al,Ga)N heterostructures grown on (Zn,Mg)O / r-sapphire templates. The influence of Mg content in the templates on the GaN epi-layer properties is studied. The structural and optical properties of the *a*-plane GaN layers are characterized. A series of nonpolar $Al_{0.2}Ga_{0.8}N$ / GaN multi quantum wells (MQWs) is fabricated on a-plane GaN surfaces, and their optical properties are discussed.

Chapter IV focuses on the growth of GaN and the fabrication of (In,Ga)N / GaN multi-quantum well (MQW) based LEDs on *c*-plane bulk ZnO substrates. We show that GaN layers with both Ga- and N- polarities can be grown on O face *c*-ZnO and the polarity

determination mechanisms are analyzed. The structural and optical properties of GaN / ZnO structures are presented. Finally, the monolithic integration of (In,Ga)N / GaN MQW based LEDs fabricated on ZnO substrates are demonstrated and characterized.

Chapter V presents a brief study about the growth of GaN layers on bulk *a*-plane ZnO substrates. Two methods, using ammonia and N plasma as nitrogen sources, are adapted for the growth of the GaN nucleation layers. The optical and structural properties are characterized and compared. In addition, *a*- and *c*-plane (In,Ga)N / GaN MQWs are grown on ZnO substrates. The indium incorporation efficiencies in the (In,Ga)N layers and the MQW optical properties are compared and discussed.

Finally, general conclusions are made and perspectives of this study are presented.

Introduction

Au début des années 60, la démonstration de dispositifs semi-conducteurs électroluminescents de « haute efficacité » a ouvert la voie à la fabrication de diodes électroluminescentes (DELs).[1] Le développement de ces composants a progressivement conduit à remplacer les sources classiques de lumière par des DELs. Aujourd'hui, les semi-conducteurs nitrures sont les matériaux de choix pour un large éventail d'applications, et notamment pour les DELs fonctionnant dans l'ultra-violet (UV) et le visible.[2] Depuis le début des années 1990, le développement de dispositifs à base de nitrure s'est accéléré en raison de l'amélioration de la qualité structurale des matériaux à base de nitrure de gallium (GaN). Grâce à l'amélioration continue des performances des DELs nitrures, en particulier dans le bleu autour de 450 nm, la technologie de l'éclairage est actuellement en pleine révolution. En effet, l'impact environnemental, lié à la consommation d'énergie, est le critère qui suscite aujourd'hui le remplacement des sources traditionnelles d'éclairage par le développement d'une nouvelle technologie : l'éclairage par sources à l'état solide dont le composant de base est la DEL. Cette nouvelle génération d'éclairage à base de DELs nitrures se caractérise par des sources lumineuses de plus grande efficacité, une consommation d'énergie plus faible, une durée de vie accrue, des dimensions réduites, une meilleure robustesse aux chocs, etc…, par rapport aux lampes incandescentes et fluorescentes traditionnelles.

Le GaN, dont la phase thermodynamiquement stable est la phase hexagonale « wurtzite », est un semi-conducteur à grande largeur de bande interdite (~ 3,4 eV à température ambiante), avec une grande stabilité chimique. En ajustant les compositions des élements de la colonne III du tableau périodique (In, Ga, Al) pour constituer différents alliages, on peut fabriquer des dispositifs optoélectroniques émettant de la gamme UV au visible.

Actuellement, la plupart des composants sont fabriqués le long de la direction [0001] du cristal wurtzite, le long de laquelle des propriétés de polarisation macroscopique apparaissent.[3] En particulier, les propriétés optiques d'une hétérostructure sont modifiées par la présence d'un champ électrique interne qui provient d'une différence de polarisation macroscopique entre les différents matériaux constituant l'hétérostructure. La polarisation

totale se compose de polarisations dites « spontanées » et « piézo-électriques ». Elle varie en fonction de la composition et de l'état de contrainte de l'hétérostructure. Ainsi, la discontinuité de la polarisation à l'interface d'une hétérostructure de type puits quantique (PQ) peut conduire à l'accumulation de charges qui peuvent séparer les fonctions d'onde des électrons et des trous et réduire l'efficacité de recombinaison radiative. C'est l'effet Stark confiné quantique (ESCQ).[4,5] Pour réduire voire supprimer l'ESCQ dans les PQs, la croissance de GaN sur des plans dits « semi-polaires » ou « non polaires » a récemment été envisagée.[6] Le long de ces directions, de très faibles, voire aucun champ électrique interne n'est observé.[7]

Les substrats de GaN sont devenus commercialement disponibles au cours des dernières années, ce qui rend l'homoépitaxie de GaN possible. Cependant, les substrats de GaN sont encore chers et limités à de petites tailles, en particulier le long des axes non polaires (~ 1000 euros/cm^2),[8] ce qui limite la production à grande échelle de DELs sur substrats de GaN. En raison du manque de substrats natifs, les chercheurs ont travaillé sur des substrats alternatifs pour la croissance de GaN au cours des deux dernières décennies. Le saphir, le carbure de silicium, et le silicium sont actuellement les substrats les plus couramment utilisés, parmi lesquels domine le saphir pour près de 80% de part de marché. Toutefois, le grand désaccord de maille entre la couche épitaxiale et le substrat conduit à la présence de fortes densités de défauts structuraux dans les hétérostructures, ce qui réduit le taux de recombinaisons radiatives des dispositifs émetteurs de lumière.

Les substrats d'oxyde de zinc (ZnO) offrent plusieurs avantages pour la croissance du GaN. Ils ont la même structure cristalline (wurtzite), des paramètres de maille et des coefficients de dilatation thermique proches du GaN, ce qui permet d'envisager la possibilité de produire des cristaux de GaN de « haute qualité » sur ZnO. En outre, la forte sélectivité chimique entre GaN et ZnO offre la possibilité de retirer le substrat de ZnO par un procédé simple de gravure chimique, permettant d'obtenir des films minces de GaN. Cependant, quelques difficultés, telles que l'incorporation d'impuretés et les réactions interfaciales entre GaN et ZnO, restent encore à résoudre.

Dans cette étude, la croissance de GaN, ainsi que la fabrication d'hétérostructures à puits quantiques et de DELs, sur tremplins (Zn, Mg)O/saphir et substrats massifs de ZnO, sont présentées. Les propriétés structurales et optiques des hétérostructures, sur les plans a-

(11-20) et c-(0001), ainsi que les performances de premières diodes électroluminescentes monolithiques à base de GaN sur substrats ZnO sont étudiées.

Le chapitre I détaille les propriétés fondamentales concernant les structures cristallines et les structures de bandes électroniques des matériaux nitrures. La modification de la contrainte du cristal et les structures électroniques associées sont discutées. Les défauts les plus communs dans les nitrures sont présentés. Les propriétés et les applications des hétérostructures à base de nitrure d'éléments III, épitaxiées sur les deux plans polaire, (0001), et non polaire, (11-20), sont présentées et discutées. Dans la dernière partie, les propriétés des substrats ZnO sont brièvement présentées.

Le chapitre II présente la technique de croissance et les outils de caractérisation utilisés dans ce travail. L'épitaxie par jets moléculaires (EJM) est la technique de croissance utilisée dans cette étude. La configuration du système d'épitaxie et ses principes sont présentés. Les principales techniques utilisés pour la caractérisation de la morphologie de surface, des propriétés structurales, optiques et électroniques, telles que la microscopie à force atomique (AFM), la microscopie électronique à balayage (MEB), la diffraction des rayons X (XRD) et la photoluminescence (PL) sont introduites.

Le chapitre III traite de la croissance et des propriétés des hétérostructures à base d'(Al, Ga)N sur plan z fabriquées sur des couches tremplins (Zn, Mg)O plan a épitaxiés sur substrats saphir plan r-(1-102). L'influence de la concentration en Mg dans les tremplins (Zn, Mg)O sur les propriétés des couches de GaN est étudiée. En particulier, les propriétés structurales et optiques des couches de GaN plan a sont caractérisées. Ensuite, une série d'échantillons constitués de multi-puits quantiques $Al_{0.2}Ga_{0.8}N$/GaN non polaires, d'épaisseur de GaN variant entre 0,5 et 7 nm, est fabriquée sur des surfaces de GaN plan a. Leurs propriétés optiques sont présentées et discutées.

Le chapitre IV porte sur la croissance de GaN et la fabrication de DELs à base de multi-puits quantiques (MPQs) (In, Ga)N/GaN épitaxiées sur substrats massifs de ZnO plan c. Nous montrons que des couches de GaN de polarités Ga ou N peuvent croître sur la face oxygène du ZnO plan c. Les mécanismes de détermination de la polarité des couches épitaxiales sont analysés. Les propriétés structurales et optiques des structures GaN/ZnO sont présentées. Enfin, l'intégration monolithique de DELs nitrures à base de MPQs

(In, Ga)N/GaN fabriquées sur des substrats ZnO plan c est démontrée et les performances sont présentées.

Le chapitre V présente une brève étude sur la croissance des couches de GaN épitaxiées sur substrats massifs ZnO plan a. Deux sources d'azote, soit l'ammoniac gaz comme précurseur d'azote, soit un plasma d'azote, ont été utilisées pour la croissance des couches de nucléation de GaN. Les propriétés optiques et structurales des couches de GaN sont alors caractérisées et comparées. Par ailleurs, des MPQs de (In, Ga)N/GaN sont épitaxiés sur des substrats ZnO plan a et c. Les efficacités d'incorporation de l'indium dans les couches (In, Ga)N et les propriétés optiques des MPQs sont comparées et discutées.

Enfin, les conclusions générales et les perspectives de ce travail constituent la dernière partie de ce mémoire.

References

[1] J. Black, H. Lockwood, and S. Mayburg, J. Appl. Phys. **34**, 178 (1963).

[2] F. A. Ponce and D. P. Bour, Nature **386**, 351 (1997).

[3] F. Bernardini, V. Fiorentini, and D. Vanderbilt, Phy.Rev. B **56**, R10024 (1997).

[4] T. Takeuchi, S. Sota, M. Katsuragawa, M. Komori, H. Takeuchi, H. Amano, and I. Akasaki, Jpn. J. Appl. Phys. **36**, L382 (1997).

[5] M. Leroux, N. Grandjean, M. Laugt, J. Massies, B. Gil, P. Lefebvre, and P. Bigenwald, Phys. Rev. B **58**, R13371 (1998).

[6] P. Waltereit, O. Brandt, A. Trampert, H. T. Grahn, J. Menniger, M. Ramsteiner, M. Reiche, and K. H. Ploog, Nature **406**, 865 (2000).

[7] A. E. Romanov, J. Appl. Phys. **100** (023522) (2006).

[8] http://ammono.com/products.

Chapter I. Fundamentals

In this chapter, the fundamental knowledge concerning my thesis research project is introduced. This chapter consists of four parts: the first part introduces the crystal structures of sapphire, Zinc Oxide (ZnO) and Gallium Nitride (GaN), including the symmetry group, thermal and mechanical properties, as well as the commonly observed defects; the second part focuses on the electronic band structure of the wurtzite crystal, the strain modification of the band structure and the deep levels in the band gap; the third part presents the advantages and the recent progresses of nitride based heterostructures grown along the nonpolar orientations; the last part gives a brief introduction to the growth of GaN on ZnO substrates.

I.1. Crystal structures

I.1.1. Introduction to sapphire, ZnO and GaN

I.1.1.a. Sapphire

Sapphire (Al_2O_3), also called 'blue stone', is a type of crystal used widely in industrial and for decoration purposes. Nowadays, it is the substrate of choice for the fabrication of nitride-based light emitting diodes (LEDs), which dominates 80% of the market. As a substrate, it has several advantages: it is chemically stable, inexpensive (compared to SiC and GaN substrates), and available in large sizes (8-inch substrates have been demonstrated[1]. However, it is limited by a poor thermal conductivity and is difficult to be etched off from the epitaxial layers, which are fundamental requirements for the high-power LED technology under development.

Sapphire is a corundum type of crystal, which belongs to the ditrigonal scalenohedral class of the trigonal symmetry $D^6_{3d} - R\bar{3}C$. The structure of this spatial symmetry group may be considered as a slightly distorted closest hexagonal packing of oxygen ions, as shown in Figure I.1.

At room temperature, the lattice parameters (LPs), or hexagonal lattice constants are $a = b = 4.759$ *Å* and $c=12.992$ *Å*.[2] It needs to be noticed that the ratio $c / a \sim 2.73$, far exceeds that of an ideal hexagonal packing ($\sqrt{8/3} \approx 1.633$). The four most commonly used planes in

the epitaxial growth are the *c*-plane (0001), *a*-plane (11-20), *m*-plane (1-100) and *r*-plane (1-102).

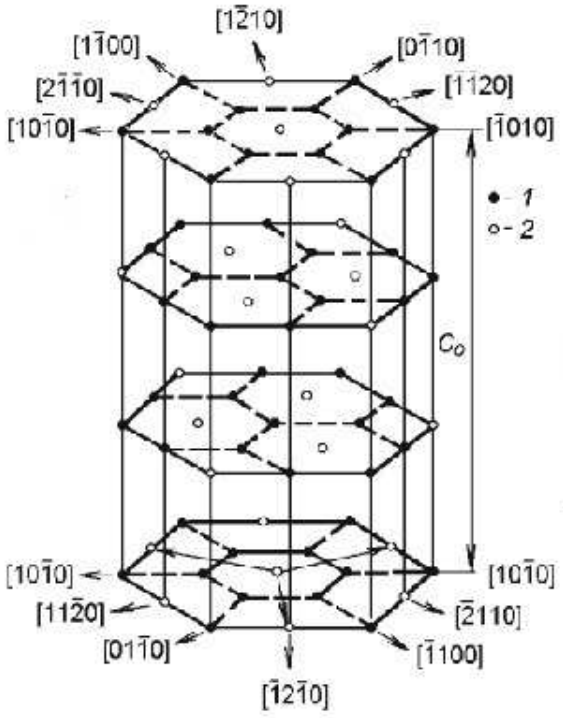

Figure I.1. Structure of the hexagonal elementary cells: the full circles represent octahedral hollows formed by the closely packed O^{2-} ions and the open circles represent aluminium ions (adapted from ref. 3).

The thermal expansion coefficients (TECs), which describe how the lattice parameters change with temperature, are defined as $\alpha_a = \Delta a / a$ and $\alpha_c = \Delta c / c$, along *a*- and *c*- axes, respectively. The TECs of sapphire vary significantly with temperature and crystal axis. At room temperature, the TECs are $\alpha_a = 5.22 \times 10^{-6} / K$ and $\alpha_c = 5.92 \times 10^{-6} / K$.[4]

Sapphire is one of the best dielectric at room temperature, and its resistance is 5×10^{18} Ω cm along the perpendicular to *c* [0001] direction and 2×10^{18} Ω cm along *c* direction. This value diminishes when increasing the temperature, like the other oxides.

I.1.1.b. ZnO and GaN

Zinc oxide (ZnO) is a II-VI inorganic compound semiconductor, which can be found naturally in mines or produced synthetically. ZnO is a relatively soft material with smaller elastic constants than III-V compounds. ZnO has a high heat conductivity (Table I. 1), which makes it easier to be heated as a substrate than sapphire. Usually, ZnO has *n*-type

characteristics even in absence of intentional doping, and it has a better conductivity than non-intentionally doped (NID) Gallium Nitride (GaN).

GaN is a III-V compound semiconductor, which is hard and mechanically stable. Like ZnO, it has high heat capacity and thermal conductivity (Table I. 1).[5]

	Bandgap (eV)	Thermal conductivity (W cm^{-1} K^{-1}) (300K)	Heat capacity (J mol^{-1} K^{-1}) (300 K)	Thermal expansion coefficient (K^{-1}) (300K)
GaN	3.510[6] (0 K)	1.5-2.1[7]	36 [8]	$\alpha_a = 3.1\times10^{-6}$ [9] $\alpha_c = 2.8\times10^{-6}$
ZnO	3.437[10] (4.2 K)	1.0[11]	41[12]	$\alpha_a = 4.75\times10^{-6}$ [13] $\alpha_c = 2.9\times10^{-6}$
Al_2O_3	8.7	0.35	80[14]	$\alpha_a = 5.6\times10^{-6}$ $\alpha_c = 5.0\times10^{-6}$

Table I.1. Comparison of bandgap energy, thermal conductivity and linear expansion coefficients between GaN, ZnO and sapphire.

GaN and ZnO have many similar electrical and structural properties. They are wide band gap semiconductors (Table I. 1). They have three types of crystal structures: wurtzite, zinc blende and rocksalt. Here we mainly discuss the wurtzite phase, which is the thermodynamically stable phase under ambient condition.

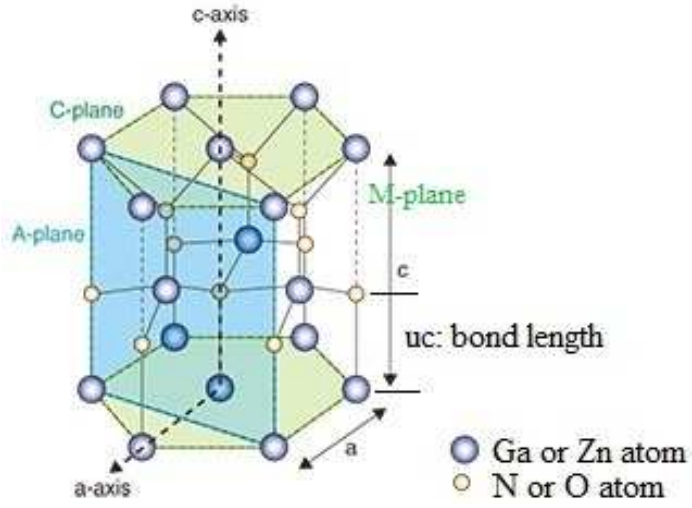

Figure I.2. Unit cell of a wurtzite structure.

Figure I. 2 shows the unit cell of a wurtzite structure. The wurtzite structure belongs to the $P6_3mc$ space group, and it has a hexagonal unit cell. In GaN, the $+c$ direction is defined pointing from Ga to N in a nearest 'Ga-N' bond. Some commonly used planes in wurtzite crystal are noted in Figure I. 2. The basal plane of the hexagonal structure, which is perpendicular to the *c*-axis, is called ''*c*-plane'', also noted as ''polar plane''. The prismatic plane, which is perpendicular to the *m* [1-100] direction, is named ''*m*-plane''. And finally, the plane which is perpendicular to the *a*-axis [11-20] is named ''*a*-plane''. Both *a*- and *m*-planes represent the two nonpolar planes of the wurtzite crystal.

In a wurtzite crystal, the two LPs *a* and *c* obey to the relation $c/a = \sqrt{8/3} = 1.633$, and the ratio between the V-III (VI-II) bond length along the [0001] direction and the LP *c* is *u=3/*8. The parameter *uc* then corresponds to the bond length. In the real case of ZnO and GaN, as the crystals are distorted, the c / a ratio is smaller than the ideal wurtzite structure, and the *u* value is slightly larger. LPs can be influenced by many factors, including chemical composition, free charge density, defects, external stress and temperature. Table I. 2 shows the LPs and corresponding ratios of GaN and ZnO, under zero strain and ambient condition.

	a (*Å*)	c (*Å*)	c/a	Ref.	u	Ref.
GaN	3.189	5.185	1.626	[6]	0.376	[15]
ZnO	3.250	5.204	1.601	[16]	0.382	[16]

Table I.2. Lattice parameters and corresponding ratios of GaN and ZnO.

Iwanaga *et al.* have given the second order polynomials of GaN and ZnO LPs varying with temperature (Eq. I. 1 and Eq. 1. 2), by fitting the experimental data[17]. The LPs at different temperatures were obtained by performing x-ray diffraction measurements on GaN and ZnO powders.

$$\begin{aligned} a_{ZnO}(T) &= 3.2468 + 0.623\times10^{-5}T + 12.94\times10^{-9}T^2, \\ c_{ZnO}(T) &= 5.2042 + 0.522\times10^{-5}T + 12.13\times10^{-9}T^2. \end{aligned} \quad \textbf{(I. 1)}$$

$$\begin{aligned} a_{GaN}(T) &= 3.1840 + 0.739\times10^{-5}T + 5.92\times10^{-9}T^2, \\ c_{GaN}(T) &= 5.1812 + 1.455\times10^{-5}T + 4.62\times10^{-9}T^2. \end{aligned} \quad \textbf{(I. 2)}$$

The simulated evolution of GaN and ZnO lattice parameters with temperature are shown in Figure I. 3.

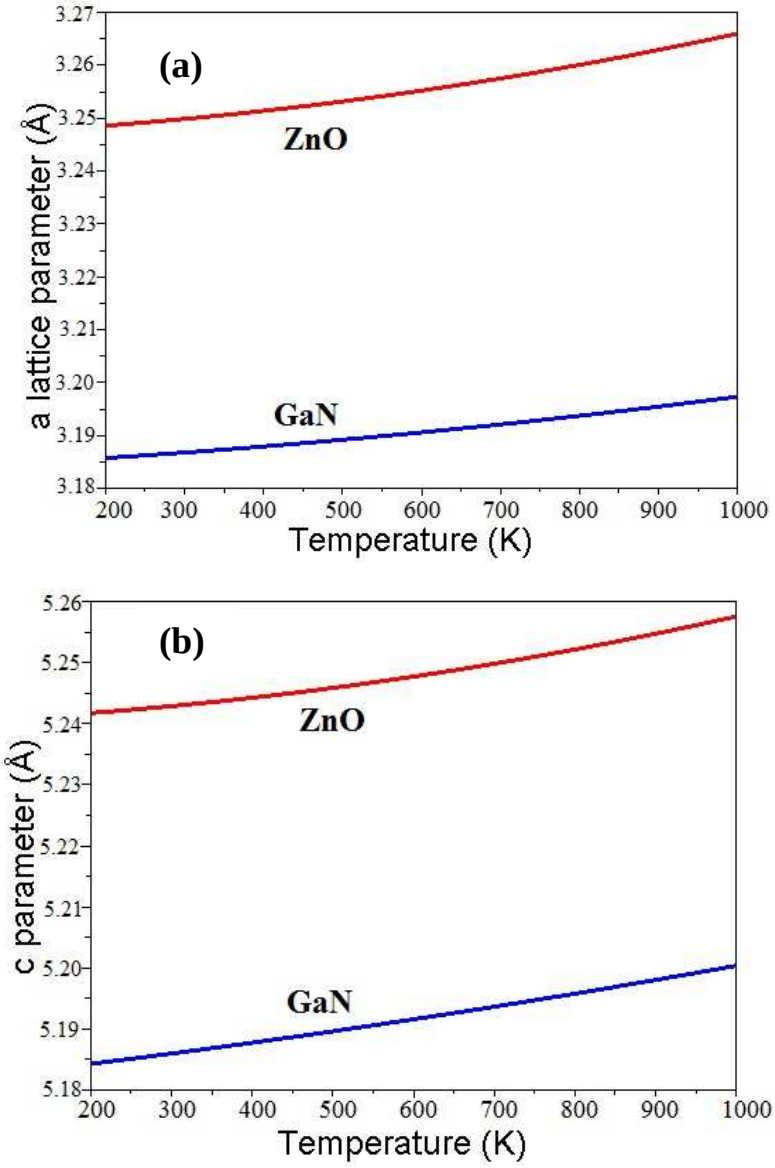

Figure I.3. Evolution of lattice parameters (a) a and (b) c of GaN and ZnO, as a function of temperature.

The thermal expansion coefficients (TECs) of GaN, ZnO and sapphire are listed in table I. 1. It should be noticed that, in a wurtzite structure, TECs are different in the basal plane and along the *c* axis, and they also vary with temperature. When the temperature is above 100 K, TECs increase significantly with temperature.

I.1.2. Epitaxial relationships

I.1.2.a. ZnO and GaN grown on sapphire (0001)

Sapphire is the most commonly used substrate for GaN and ZnO, and the *c*-plane (0001) is the most commonly used growth plane. LPs of sapphire, ZnO and GaN in the basal c-plane are $a_{sapphire} = 4.759$Å, $a_{ZnO} = 3.25$ Å and $a_{GaN} = 3.189$ Å, respectively. In this case, the lattice mismatch between ZnO and sapphire is $\frac{a_{ZnO} - a_{sap}}{a_{sap}} = -31.7\%$, and that between GaN and sapphire is $\frac{a_{GaN} - a_{sap}}{a_{sap}} = -33\%$. It has been demonstrated experimentally that the epitaxial relationship between ZnO and c-plane sapphire is: $(0001)_{ZnO} \parallel (0001)_{Sapphire}$ and $(10\bar{1}0)_{ZnO} \parallel (11\bar{2}0)_{sapphire}$.[18] Figure I. 4 (a) shows the scheme of the atomic arrangement in the basal plane when growing ZnO on *c*-plane sapphire. It shows that the *c* plane of ZnO rotates by 30° in the basal plane of sapphire. In this case, the in plane periodicity in the substrate and the epitaxial film are $d_s = a_{sap}/\sqrt{3} = 2.75$ Å and $d_f = a_{ZnO} = 3.25$ Å, respectively. Under this arrangement, the lattice mismatch between ZnO and sapphire is 18.3%.

It has been shown by Narayan *et al.* that the strain in epitaxial films can be accommodated in the form of domain matching epitaxy (DME) when the film has a large lattice mismatch with the substrate (> 7 – 8 %).[19] In the concept of DME, the film plane d_f with the substrate lattice plane d_s is considered to have a similar crystal symmetry. The initial misfit strain $\varepsilon = \frac{d_f - d_s}{d_s}$ can be very large, but this strain can be relaxed by matching *m* film planes with *n* substrate planes following:[19]

$$(m + \alpha) d_f = (n + \alpha) d_s, \qquad \textbf{(I. 3)}$$

where α is the frequency factor: if $\alpha = 0$, it means that there is a perfect lattice plane match between *m* film planes and *n* substrate planes; if $\alpha = 0.5$, *m / n* and *(m+1) / (n+1)* domains appear with an equal frequency. Between ZnO and sapphire, there is almost a perfect matching with *5.5* x d_f and *6.5* x d_s, while $\alpha = 0.5$. It means that even if there is a planar mismatch of $\varepsilon \sim 18.3\%$, the film and substrate still have domain matching by coupling five film planes with six substrate planes or six film planes with seven substrate planes.

Figure I. 4 (b) shows the transmission electron microscopy (TEM) image of the ZnO / sapphire interface, which follows the arrangement of DME.

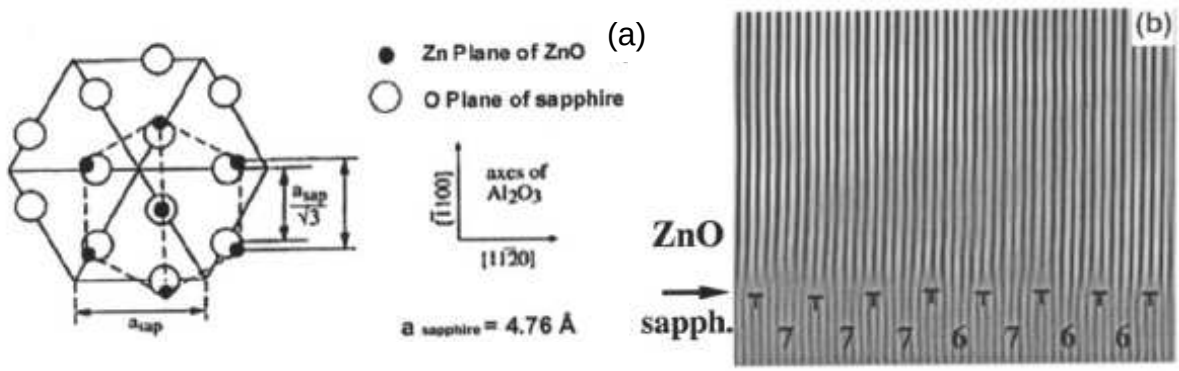

Figure I.4. (a) Scheme of atomic arrangement in the basal plane of ZnO and sapphire and (b) TEM image of the ZnO / sapphire interface in the case of domain matching epitaxy (adapted from ref. 19).

In the case of GaN, similar plane matching happens by rotating the *c*-plane of GaN by 30° in the basal plane of sapphire, the planar mismatch is ε ~ 16% and the epitaxial relation is: $(0001)_{GaN} \parallel (0001)_{Sapphire}$ and $(\bar{2}110)_{GaN} \parallel (10\bar{1}0)_{sapphire}$.[20]

I.1.2.b. a-plane ZnO (GaN) on r-plane sapphire

It has been shown experimentally that *a*-plane $(11\bar{2}0)$ ZnO layers can be grown on *r*-plane $(10\bar{1}2)$ sapphire substrates.[21,22] Figure I. 5 shows the high resolution images of the ZnO / sapphire interface, along the <1-100> and <0001> directions of ZnO. The in plane epitaxial relationships are found to be: $(0001)_{ZnO} \parallel (\bar{1}101)_{sap}$ and $(\bar{1}100)_{ZnO} \parallel (\bar{1}\,\bar{1}20)_{sap}$.

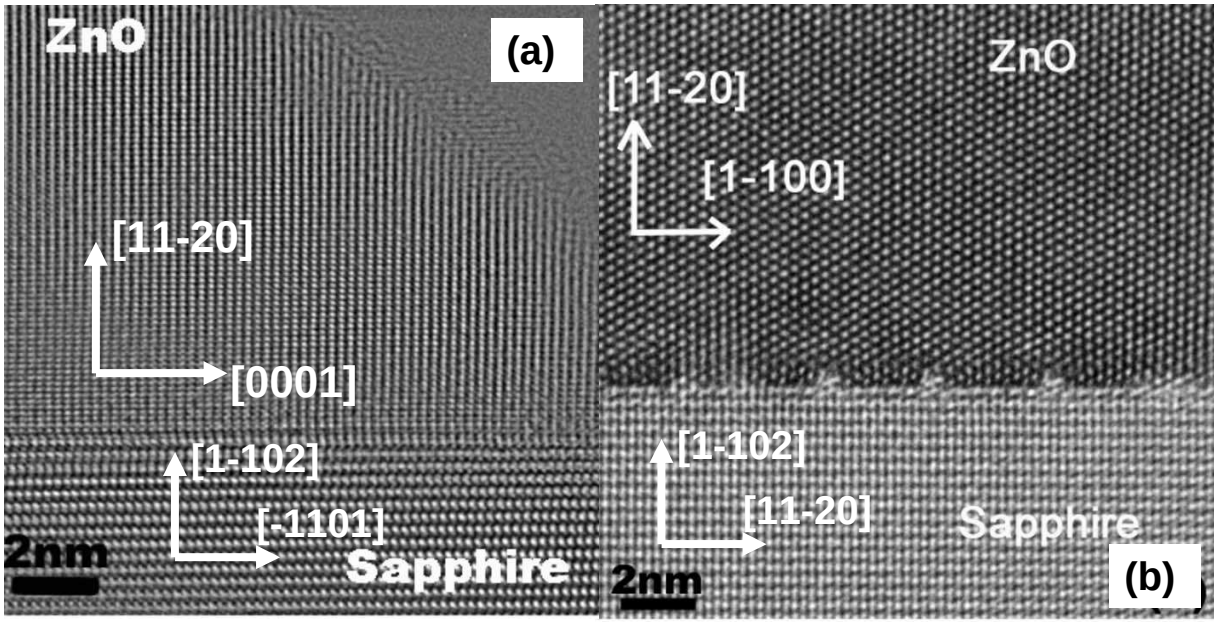

Figure I.5. TEM images of the interface between a ZnO film and a *r*-plane sapphire substrate, along the (a) <1-100>$_{ZnO}$ and (b) <0001>$_{ZnO}$ directions (adapted from ref. 23).

Different from the polar case, the *a*-plane ZnO layer has a misfit anisotropy with the substrate.[22,24] As illustrated in Figure I. 6, the lattice spacing of ZnO is $c_{ZnO} = 5.206$ *Å* along the [0001] direction of ZnO and that of the sapphire substrate is $c'_{sap} = \sqrt{3a_{sap}^2 + c_{sap}^2} = 15.384$ *Å*. Such a large lattice mismatch can be accommodated by matching three ZnO (0001) planes with one sapphire $(\bar{1}101)$ plane, with 1.26% misfit left. Along the [-1100] direction of ZnO, the lattice periodicities of ZnO and that of sapphire are $\sqrt{3}a_{ZnO} = 5.629$ *Å* and a_{sap}=*4.756 Å*, respectively, and there is a compressive lattice misfit of 18.3%. This misfit is accommodated in the form of DME, as introduced in the case of *c*-plane growth[24].

When the III-nitrides are grown on *r*-plane sapphire, similar crystal matching arrangements with ZnO / sapphire have been identified.[25] As shown in Figure I. 6, the epitaxial relationships between *a*-plane GaN and *r*-plane sapphire are: $(0001)_{GaN} \parallel (\bar{1}101)_{sap}$ and $(\bar{1}100)_{GaN} \parallel (\bar{1}\,\bar{1}20)_{sap}$, and the lattice misfits are accommodated in a similar form with that of ZnO and sapphire. The lattice misfit is ~ 1.13% along GaN <0001> direction and 16.1% along <1-100> direction.

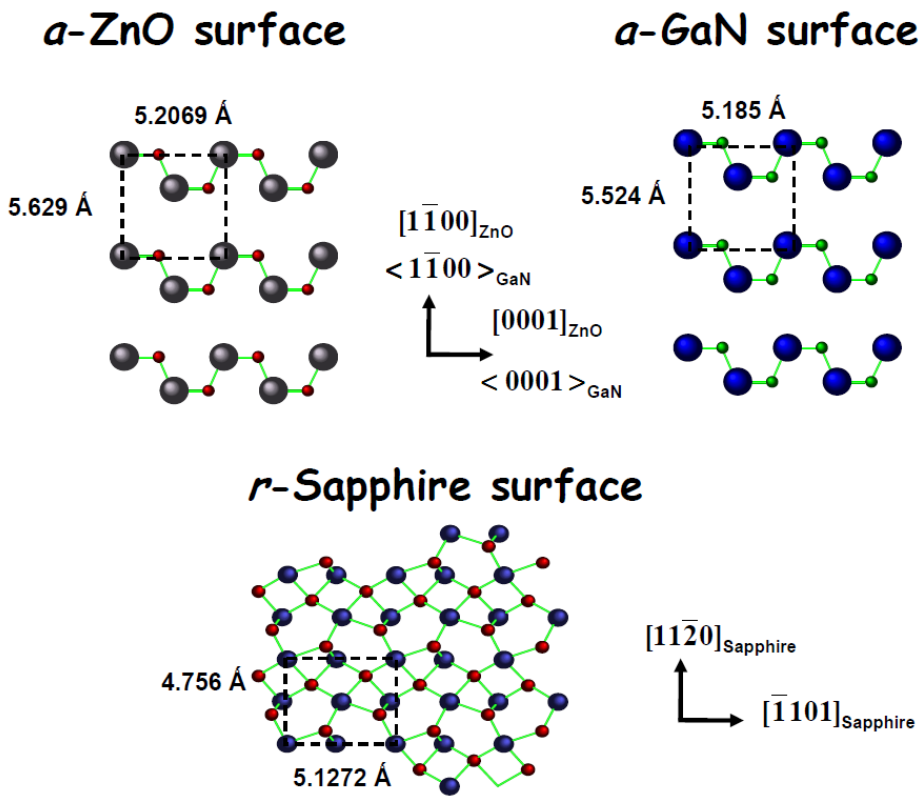

Figure I.6. Scheme of the atomic arrangements and lattice constants of *a*-plane ZnO, *a*-plane GaN and *r*-plane sapphire.

I.1.2.c. GaN grown on ZnO

GaN has very small lattice mismatches with ZnO (-1.87% and -0.42% along [11-20] and [0001] directions, respectively). When growing GaN on ZnO, GaN follows exactly the stacking orientation of ZnO, either along polar or nonpolar directions.[18,26] The epitaxial relationships are: $(0001)_{GaN} \parallel (0001)_{ZnO}$, $(11\bar{2}0)_{GaN} \parallel (11\bar{2}0)_{ZnO}$ and $(10\bar{1}0)_{GaN} \parallel (10\bar{1}0)_{ZnO}$.

I.1.3. Strain and stress

The strain of a crystal describes the degree of deformation, which arises from an external stress. The strain has an influence in both crystal fundamental properties and device related characteristics, including lattice parameters, electronic band structure, as well as polarization. Strains along *a* and *c* axes can be calculated using the following expressions:

$$\varepsilon_a = \frac{a - a_0}{a_0},$$

$$\varepsilon_c = \frac{c - c_0}{c_0}. \qquad \textbf{(I. 4)}$$

where a_0 and c_0 are the relaxed lattice parameters, and *a* and *c* are the strained lattice parameters. In the GaN epitaxial layer, the strain is usually generated from the lattice mismatch between the substrate and the epi-layer. For instance, when growing on *c* plane, a GaN film exhibits a compressive in-plane strain on sapphire, and a tensile strain on ZnO. When growing on nonpolar planes, the situation is more complicated as there are in-plane anisotropies for the lattice parameters and the thermal expansion coefficients along *a* (or *m*) and *c* directions, so in-plane strains are usually anisotropic.[26] As illustrated in Figure I. 6, the lattice mismatches between GaN and ZnO are -1.9% and -0.4% along [1-100] and [0001] directions, respectively, while those between GaN and sapphire are 13.9% and 1.13% along [1-100] and [0001] directions, respectively.

There are two types of strains: normal strain and shear strain. Normal strains are noted as ε_{xx}, ε_{yy}, and ε_{zz}, representing strains along the three orthogonal directions [11-20], [1-100] and [0001], respectively. Shear strains are noted as ε_{xy}, ε_{yz}, and ε_{xz}, and they describe the change of angles between the three principle directions, owing to the stress along non-principle axes. In the case of heteroepitaxy, only normal strains are present when growing on polar and nonpolar orientations. Shear strains occur when growing on semipolar planes.[27]

The relation between the strain and the stress obeys to the Hook's law:

$$\sigma_{ij} = C_{ijkl}\varepsilon_{kl} \qquad \textbf{(I. 5)}$$

In the wurtzite system, both stress and strain vectors have six elements, and the stiffness matrix elements $C_{mn}(m,n \subset [1,6])$ have only five independent constants: C_{11}, C_{12}, C_{13}, C_{33} and C_{44}. The strain-stress relations can be expressed as:

$$\begin{pmatrix} \sigma_{xx} \\ \sigma_{yy} \\ \sigma_{zz} \\ \sigma_{yz} \\ \sigma_{xz} \\ \sigma_{xy} \end{pmatrix} = \begin{pmatrix} C_{11} & C_{12} & C_{13} & 0 & 0 & 0 \\ C_{12} & C_{11} & C_{13} & 0 & 0 & 0 \\ C_{13} & C_{13} & C_{33} & 0 & 0 & 0 \\ 0 & 0 & 0 & C_{44} & 0 & 0 \\ 0 & 0 & 0 & 0 & C_{44} & 0 \\ 0 & 0 & 0 & 0 & 0 & (C_{11}-C_{12})/2 \end{pmatrix} \begin{pmatrix} \varepsilon_{xx} \\ \varepsilon_{yy} \\ \varepsilon_{zz} \\ \varepsilon_{yz} \\ \varepsilon_{xz} \\ \varepsilon_{xy} \end{pmatrix} \qquad \textbf{(I. 6)}$$

The elastic stiffness coefficients of GaN and ZnO have been measured experimentally as shown in Table I. 3:

	Structure	C_{11}	C_{12}	C_{13}	C_{33}	C_{44}
GaN[28]	wurtzite	390	145	106	398	105
InN[28]	wurtzite	223	115	92	224	48
AlN[28]	wurtzite	396	137	108	373	116
ZnO[29]	wurtzite	209.7	121.1	105.1	210.9	42.5

Table I.3. Elastic stiffness coefficients of nitride binaries and ZnO (GPa).

When growing GaN on the (0001) plane, there is no shear strain, and the in-plane strain is isotropic ($\varepsilon_{xx} = \varepsilon_{yy} = \varepsilon_{//}$). The crystal space group does not change. The stress along the growth direction vanishes because of the free surface, we have:

$$\sigma_{zz} = 2C_{13}\varepsilon_{//} + C_{33}\varepsilon_{zz} = 0 \qquad \textbf{(I. 7)}$$

Then the relation between the transversal strain $\varepsilon_{//}$ and axial strain ε_{zz} can be expressed as:

$$\varepsilon_{//} = -v\varepsilon_{zz}, \qquad \textbf{(I. 8)}$$

where $v = C_{33} \big/ 2C_{13}$ is Poisson's ratio.

When growing GaN on the (11-20) plane, the epitaxial layer is strained on the *yz* plane (cf. Fig. I. 13), and the strain is anisotropic due to the different lattice mismatches along the *y*-[1-100] and the *z*-[0001] directions. In this case, the crystal symmetry is changed from wurtzite C_v^6 to C_v^2. The stress along the growth direction satisfies:

$$\sigma_{xx} = C_{11}\varepsilon_{xx} + C_{12}\varepsilon_{yy} + C_{13}\varepsilon_{zz} = 0 \qquad \textbf{(I. 9)}$$

The strain along the growth direction can be deduced from:

$$\varepsilon_{xx} = -\frac{C_{12}}{C_{11}}\varepsilon_{yy} - \frac{C_{13}}{C_{11}}\varepsilon_{zz} \qquad \textbf{(I. 10)}$$

I.1.4. Defects

I.1.4.a. point defects

Point defects mainly have two sources: native defects and impurities. There are several types of native point defects in GaN, like Ga (V_{Ga}) and N (V_N) vacancies, self-interstitials (Ga_i and N_i), and antisites (Ga_N and N_{Ga}). The presences of these native defects may act as sources of doping, and also sources of compensation for intentional doping. These native defects usually have a high formation energy,[30] which makes them difficult to form spontaneously during the growth.

Impurities are another type of point defects. The most common impurities in GaN are O, C, and Si, and they are mainly incorporated into GaN layers, usually non-intentionally, during the growth. The impurities may also influence the electronic properties of the epitaxial layer. For example, Si and O, which act as donors in GaN, can lead to a non-intentional *n*-type conductivity and compensate the intentional *p*-type doping in the epitaxial layer.

I.1.4.b. line defects

A dislocation is a typical line defect, which can be divided into two groups: threading dislocation and misfit dislocation. For GaN, they can be generated from the coalescence of islands or relaxation processes during growth, although there is no low energy relaxation process when growing along polar orientation.[31,32,33] The typical threading dislocation density of a GaN layer grown on sapphire (by MOCVD or MBE) is between 10^8 and 10^{10}/ cm^2.[31,34] Thick GaN layers (>300µm) with a dislocation density of mid-$10^6/cm^2$ can be grown by HVPE[35]. The surface terminations of dislocations may lead to the formation of depressions due to the surface energy and the strain energy associated with the dislocations.[36] Figure I. 7 shows the scheme of a surface generated from the force balance between the surface tension and the dislocation line tension, at the termination of a dislocation. These depressions may finally result in 'V-shape' defects observed, for instance, in InGaN / GaN multi quantum well (MQW) structures.[37] The presences of dislocations may influence the electrical and optical properties of GaN, *i.e.* they may act as localized non-radiative recombination centres of excitons.[37]

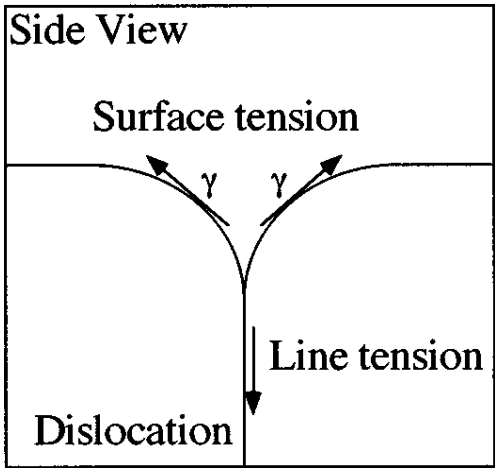

Figure I.7. Scheme of a surface depression generated at the termination of a dislocation (adapted from ref. 34).

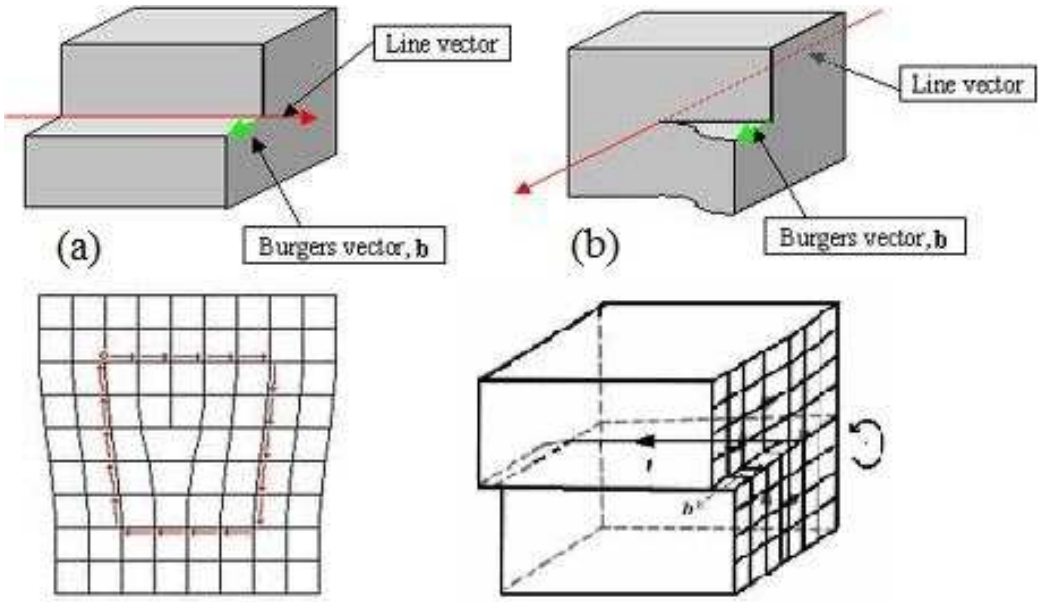

Figure I.8. Schematic representations of (a) an edge dislocation and (b) a screw dislocation.

A dislocation is defined by a Burgers vector **b** and a line direction **L**. The burgers vector describes the lattice displacement within the crystal, and **L** represents the line direction of the dislocation. For a perfect dislocation, **b** equals a unit lattice vector. When the Burgers vector is perpendicular to the line direction, the dislocation is defined as an edge dislocation, as shown in Figure I. 8 (a). When the Burgers vector is parallel to the line direction, as shown in Figure I. 8 (b), the dislocation is called a screw dislocation. When a dislocation has components from both edge and screw dislocations, it is called a mixed dislocations. In this case, the angle between **b** and **L** is in between 0° and 90°.

I.1.4.c. planar defects

The most commonly observed planar defects in wurtzite GaN are stacking faults (SFs) and inversion domain boundaries (IDBs). Basal plane stacking faults (BSFs) correspond to the disordered stacking sequence of a crystal in the (0001) plane of GaN, while prismatic stacking faults (PSFs) refer to stacking faults in prism planes. In a perfect wurtzite crystal, the stacking sequence is ABABABAB, as show in Figure I. 9 (a) and (c). The stacking sequence is ABCABCABC for a zinc blende structure (Figure I. 9 (b) and (d)). For type I BSF, the stacking sequence is switched to ABABCBCB, as all the A sites are replaced by the C sites above the fault plane. A type II fault represents a stacking sequence of ABABCACA, and an extrinsic fault is characterized by a stacking sequence of ABABCABAB.

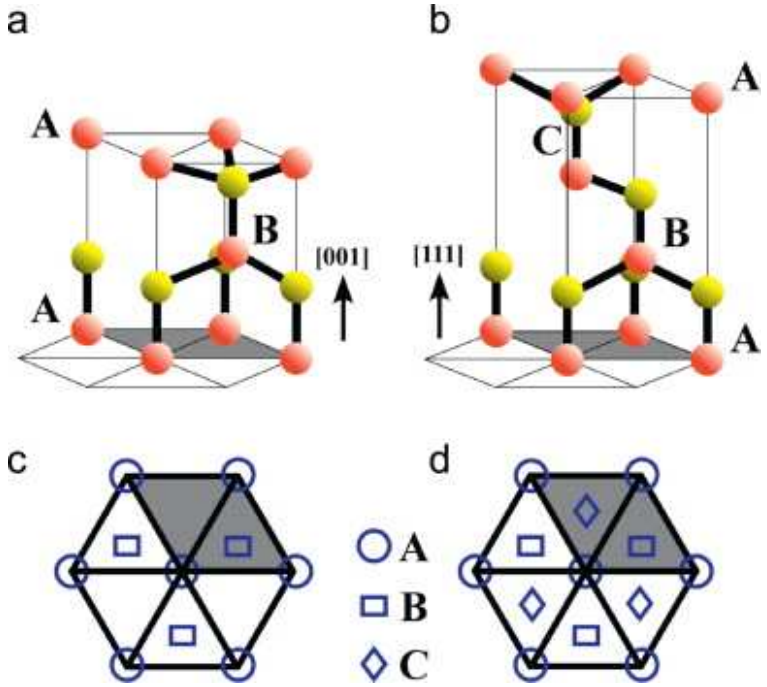

Figure I.9. Schematic representations of A, B, C sites in (a) wurtzite and (b) zinc blende structure; (c) and (d) shows the projection on the *c* plane (0001) (adapted from ref. 38).

An IDB represents a fault plane which acts as an inversion centre for domains with different anion-cation bond polarity. In GaN, IDBs having (10-10), (10-11), (10-12) and (0001) faults planes have been observed.[39,40] Figure I. 10 shows an atomic model of IDB in the (11-20) plane. The dotted line indicates the bond centre site where the inversion happens. IDBs can be evidenced by the asymmetry in convergent beam electron diffraction (CEBD) patterns containing the (0002) and (000-2) reflections.[40]

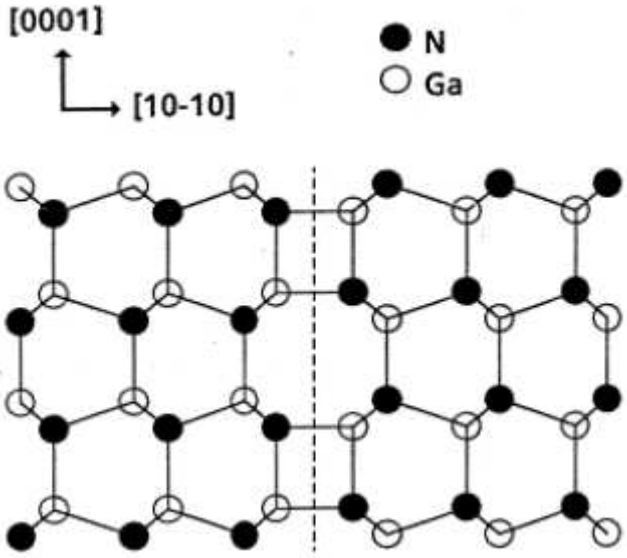

Figure I.10. Atomic model of an IDB in (10-10) plane (adapted from ref. 41).

I.2. GaN electronic band structure

I.2.1. Band structure near Γ point

GaN, like other III-nitride materials and ZnO, is a direct band gap semiconductor. Figure I. 11 shows the band structure of GaN in the first Brillouin zone. The conduction band minimum and valence band maximum locate at the center of the Brillouin zone, which is called the Γ point. The band gap E_g represents the energy difference between the conduction band minimum and the valence band maximum. The band gap energy decreases with the increasing temperature, and this behaviour is described by the Varshni equation:

$$E_g(T) = E_g(0) - \frac{\alpha T^2}{T - \beta}\ , \qquad \textbf{(I. 11)}$$

where $E_g(0)$ is the band gap at 0 K, while α and β are the Varshni parameters which can be obtained by fitting the experimental curve. The Varshni parameters differ from materials, and differ from different strain states of the same material. Take GaN for example, the band gap at room temperature is typically 70 meV lower than that at liquid helium temperature (4.2 K).

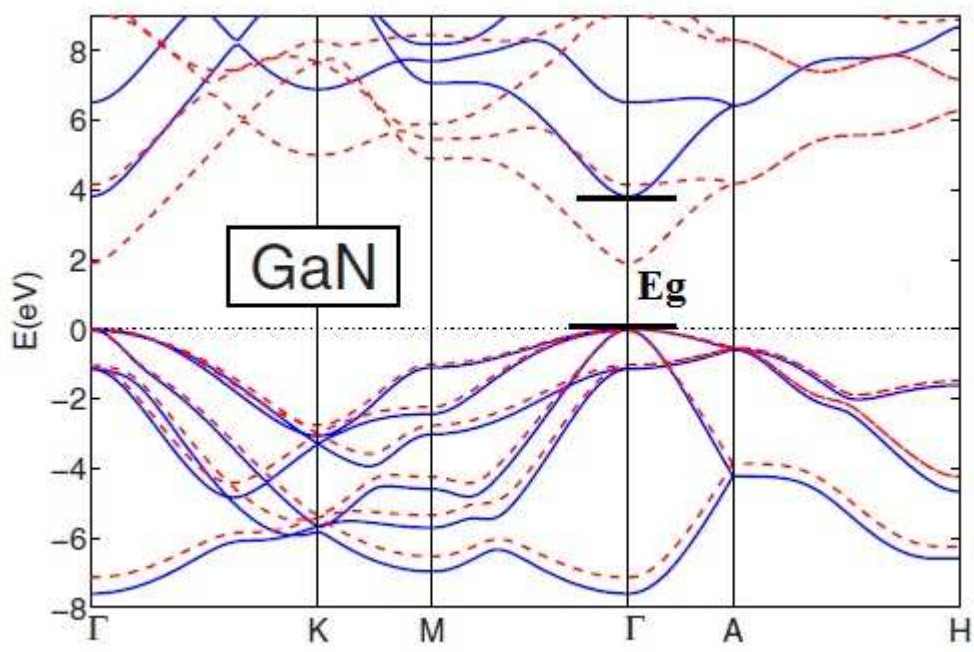

Figure I.11. GaN band structure in the first Brillouin zone, simulated using local approximation (dashed line) and quasi-particle self-consistent (solid line) approaches (adapted from ref. 42).

In the vicinity of the conduction band bottom, the electronic state mainly consists of the anti-bonding state of cation *s* state, and the energy dispersion can be expressed by a parabolic approximation model:

$$E_c(k) = E_{c0} + E^c = E_{c0} + \frac{\hbar^2}{2m_e^{\perp}}\left(k_x^2 + k_y^2\right) + \frac{\hbar^2}{2m_e^{//}}k_z^2 + a_2\left(\varepsilon_{xx} + \varepsilon_{yy}\right) + a_1\varepsilon_{zz}, \qquad \textbf{(I. 12)}$$

E_{c0} represents the original position of the conduction band minimum. The second and the third terms represent the parabolic sharp energy dispersion in the vicinity of the conduction band bottom, where $m_e^{\perp}$ and $m_e^{//}$ are the effective masses of the electron in the basal plane and along the *c* axis of the Brillouin zone, respectively. The electron and hole effective masses of nitride binaries and ZnO are listed in Table I. 4. The last two terms correspond to the energy shift due to the residual strain: a_1 and a_2 are the deformation potentials along the in-plane and out of plane directions, respectively, which are also listed in Table I. 2.

The band structure of the valence band is more complicated. There are three doubly degenerated energy levels at the top of the band, determined by the *p*-like bonding states. In an unstrained GaN layer, the three sub bands are the heavy hole band, the light hole band and

the spin orbit split off band, and the excitons related to these three bands are named as A, B and C excitons, respectively. The holes in each sub bands have different effective masses. The effective masses corresponding to the three sub bands are defined as m_A, m_B and m_C, and listed in Table I. 4. One important part of this thesis focuses on GaN layers grown along the nonpolar (11-20) orientation. In this case, possible in-plane anisotropic strains may lead to a mixing of the sub bands.[43] Therefore, the excitons corresponding to the transition between the conduction band and the three sub bands are denoted as X_1, X_2 and X_3 excitons (Figure I. 12), from the lowest to the highest transition energy, respectively.

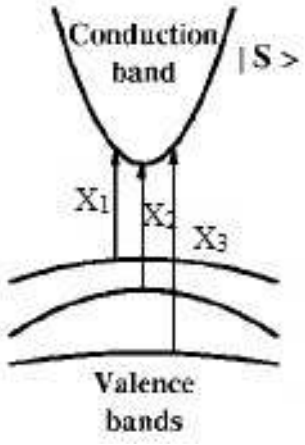

Figure I.12. Scheme of the sub valence bands and the associated exitonic transitions with the conduction band.

	$m_e^{\perp}$	$m_e^{//}$	$m_A^{\perp}$	$m_B^{\perp}$	$m_C^{\perp}$	$m_A^{//}$	$m_B^{//}$	$m_C^{//}$	$a_1(eV)^6$	$a_2(eV)^6$
GaN[44]	0.18	0.20	1.65	0.15	1.10	1.10	1.10	0.15	-4.9	-11.3
ZnO[45]	0.21	0.23	0.54	0.55	1.12	2.74	3.03	0.27		
AlN[44]	0.25	0.33	3.68	6.33	0.25	0.25	3.68	3.68	-3.4	-11.8
InN[46]	0.10	0.11	1.61	0.11	1.67	1.67	1.67	0.10	-3.5	-3.5

Table I.4. Effective mass of electrons and holes, and conduction band deformation potentials in nitride binaries and ZnO, along both in plane and out of plane directions (the unit is the free electron mass m_0).

The energy difference between the three sub bands at the vicinity of the Γ point can be related to the crystal field splitting energy Δ_{cr} and the spin-orbit split-off energy Δ_{so}. The sub-band energies and states may also be modified by the residual strain in the thin film.[47] A **k•p** perturbation approach has been developed by Bir and Pikus to describe the valence band

Hamiltonian.[44,48,49] In this method, the subband states and energies can be deduced from the eigen states and eigen values of Bir- Pikus Hamiltonian matrix:

$$H(\vec{k}) = \begin{bmatrix} F & 0 & -H^* & 0 & K^* & 0 \\ 0 & G & \Delta & -H^* & 0 & K^* \\ -H & \Delta & \lambda & 0 & I^* & 0 \\ 0 & -H & 0 & \lambda & \Delta & I^* \\ K & 0 & I & \Delta & G & 0 \\ 0 & K & 0 & I & 0 & F \end{bmatrix}, \qquad \textbf{(I. 13)}$$

where

$$F = \Delta_1 + \Delta_2 + \lambda + \theta, G = \Delta_1 - \Delta_2 + \lambda + \theta,$$
$$H = i\left(A_6 k_z k_+ + A_7 k_+ + D_6 \varepsilon_{z+}\right), I = i\left(A_6 k_z k_+ - A_7 k_+ + D_6 \varepsilon_{z+}\right),$$
$$K = A_5 k_+^2 + D_5 \varepsilon_+, \Delta = \sqrt{2}\Delta_3,$$
$$\lambda = A_1 k_z^2 + A_2 k_\perp^2 + D_1 \varepsilon_{zz} + D_2\left(\varepsilon_{xx} + \varepsilon_{yy}\right),$$
$$\theta = A_3 k_z^2 + A_4 k_\perp^2 + D_3 \varepsilon_{zz} + D_4\left(\varepsilon_{xx} + \varepsilon_{yy}\right),$$
$$\varepsilon_+ = \varepsilon_{xx} - \varepsilon_{yy} + 2i\varepsilon_{xy}, \varepsilon_{z+} = \varepsilon_{xz} + i\varepsilon_{yz},$$
$$k_+ = k_x + ik_y, k_\perp^2 = k_x^2 + k_y^2,$$
$$\Delta = \sqrt{2}\Delta_3$$

The parameters D_i (i=1 to 6) are the deformation potentials of the valence band. Two groups of GaN deformation potentials have been proposed in literature, which are listed in Table I. 5.

Deformation parameters	Ref.49 (eV)	Ref. 50 (eV)
D_1	-41.4	-38
D_2	-33.3	-33.3
D_3	8.2	4.9
D_4	-4.1	-5
D_5	-4.7	-2.8
D_6	-7.5	-3.1

Table I.5. Deformation potentials of the GaN valence band proposed by Ghosh *et al.*[49] and Ishii *et al.*[50].

A_j (j =1 to 7) are equivalent to the Luttinger parameters and determine the hole effective masses.[51] ε_{mn} and k_m (m, n =x, y, z) are the strain and wave vector components. $\Delta_1 = \Delta_{cr}$, $\Delta_2 = \Delta_3 = \Delta_{so} / 3$, where Δ_{cr} is the crystal field splitting energy, and Δ_{so} is the spin orbit split-off energy. The six basis wave functions for the matrix are:

$$
\begin{aligned}
u_1 &= \frac{1}{\sqrt{2}}\left|(X+iY),\uparrow\right\rangle, \quad u_2 = \frac{1}{\sqrt{2}}\left|(X+iY),\downarrow\right\rangle, \\
u_3 &= \left|Z,\uparrow\right\rangle, \qquad\qquad u_4 = \left|Z,\downarrow\right\rangle, \\
u_5 &= \frac{1}{\sqrt{2}}\left|(X-iY),\uparrow\right\rangle, \quad u_6 = \frac{1}{\sqrt{2}}\left|(X-iY),\downarrow\right\rangle.
\end{aligned}
\qquad \textbf{(I. 14)}
$$

where $\left|X\right\rangle$, $\left|Y\right\rangle$ and $\left|Z\right\rangle$ are the wavefunctions of the three *p*-like states, with orbital orientations along x, y and z directions, respectively (illustrated in Fig. I. 13). $\left|\uparrow\right\rangle$ and $\left|\downarrow\right\rangle$ represent the wave functions of spin up and spin down states. The eigen energies and eigen states can be deduced by diagonalizing the Bir- Pikus Hamiltonian matrix. It gives the valence energies E_j^v (j=X_1, X_2, X_3) and wave functions $\Psi_{VB}^j = \sum_{i=1}^{6} a_i u_i$ of the sub bands.

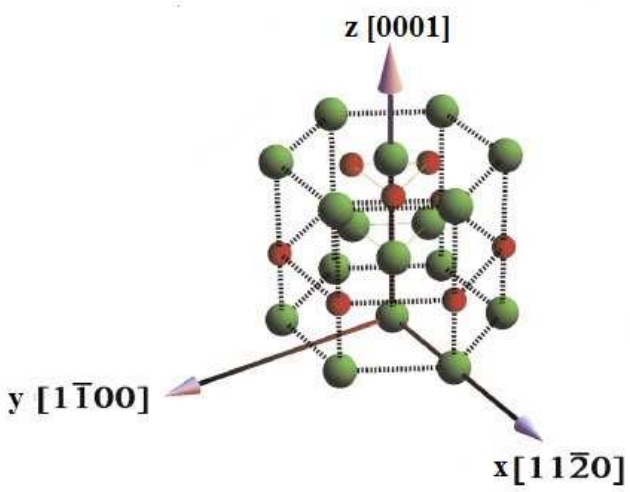

Figure I.13. Coordinate system (xyz) used in this section (adapted from ref. 52).

The excitonic transition energies can then be calculated following:

$$
E_j = E^* + E^c - E_j^v - E_{ex}^b, \qquad \textbf{(I. 15)}
$$

where $E^* = E_g + \Delta_1 + \Delta_2 =$ 3.532 eV, and E_{ex}^b is the exciton binding energy, also called Rydberg energy, which describes the coulomb interaction between electrons and holes. The exciton binding energy of GaN is 26 meV as reported in literature.[53]

The oscillator strength of the transition between the conduction band and valence band is proportional to the square modulus of the transition matrix elements:

$$f_i^{\,j} \propto \left| \left\langle \Psi_{CB} \left| p_i \right| \Psi_{VB}^{j} \right\rangle \right|^2 , \qquad \textbf{(I. 16)}$$

where f_i (i=x,y,z) represents the oscillator strength when the electric field **E** is along i direction, and p_i is the momentum operator along this direction. $\left|\Psi_{CB}\right\rangle$ is the conduction band wave function, which has a spherical shape and can be simplified as $\left|S\right\rangle$. The valence band wave function $\Psi_{VB}^{j} = \sum_{i=1}^{6} a_i u_i$ is composed of the three p-like states $\left|X\right\rangle$, $\left|Y\right\rangle$ and $\left|Z\right\rangle$. The selection rules are deduced from the wave function symmetry in the matrix element operation: $\left\langle S \left| p_x \right| X \right\rangle = \left\langle S \left| p_y \right| Y \right\rangle = I_{//}$ and $\left\langle S \left| p_z \right| Z \right\rangle = I_{\perp}$; otherwise, $\left\langle S \left| p_i \right| j \right\rangle = 0$ if $i \neq j$. At zero strain state, the two topmost sub valence bands only have components from $\left|X\right\rangle$ and $\left|Y\right\rangle$ states: $\frac{1}{\sqrt{2}}\left|\left(X \pm iY\right)\uparrow\downarrow\right\rangle$, therefore the emission from X_1 and X_2 exciton recombination is isotropic in the basal plane. The X_3 emission is polarized along the c-axis, because the corresponding valence band wave function is constructed by the $\left|Z\uparrow\downarrow\right\rangle$ states.[52]

I.2.2. Shallow and deep levels in the band gap

The doping of semiconductors is one of the fundamental steps towards the fabrication of optoelectronic devices. *N*- and *p*-type GaN layers are desired when growing nitride based LED and laser diode (LD) structures. An undoped GaN layer usually exhibits an *n*-type conductive behaviour, due to the unintentional doping of impurities such as O and Si.[30] Actually, there are two sources of GaN *n*-doping: native defects and impurities. Native defects, mainly referring to N-vacancy (V_N), may act as a shallow donor. However, the high formation energy of V_N in *n*-GaN makes it is difficult to occur in significant concentrations.[54] Si and O are the two principal impurities which are responsible for GaN *n*-type doping: Si is often used for intentional doping and O is the main source of non intentional doping. Si usually exists in GaN by substituting a Ga site and has an ionization energy of 25 meV.[54] O may occupy a N site and act as a shallow donor of GaN, with an ionization energy of 26 meV.[54]

The *p*-type doping of GaN is more difficult. Mg has become the dopant of choice to obtain *p*-GaN layers. Mg may occupy several sites in GaN, including the replacement of a Ga site (Mg_{Ga}), an antisite (Mg_N) and an interstitial site (Mg_i). Usually, Mg_{Ga} has a lower formation energy than Mg_N and Mg_i, so the Mg_{Ga} configuration is favoured in energy.[54] The ionization energy of the Mg acceptor is determined experimentally to be between 200 - 250 meV in GaN.[55,56,57] This high activation energy results in a low hole concentration compared with the Mg concentration. Currently, the typical hole concentration achieved in *p*-GaN layers for the fabrication of LEDs is in the order of ~ 10^{18} / cm^3.[58]

The transition of an electron from the donor level to the acceptor level may lead to the donor acceptor pair (DAP) emission in the photoluminescence spectrum of GaN (see Figure I. 14). The DAP emission energy can be calculated by:

$$h\nu_{DAP} = E_g - (E_D + E_A) + \frac{e^2}{4\pi\varepsilon r}, \qquad \textbf{(I. 17)}$$

where E_D and E_A represent the ionization energies of donors and acceptors, respectively. The last term corresponds to the Columb interaction between the donor and acceptor pair, and *r* is the distance between the donor and the acceptor.

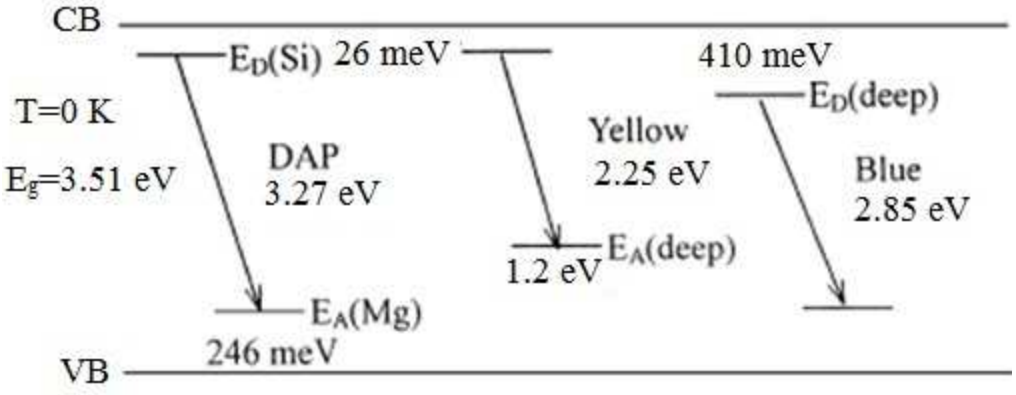

Figure I.14. Schematic representation of the transitions in the band gap of a *p*-type GaN layer (adapted from ref. 59).

Besides shallow levels, native point defects may also create deep levels in the band gap. The Ga vacancy may introduce a triple acceptor level (V_{Ga}^{3-}) due to its low formation energy in *n*-type GaN layer.[30] The V_{Ga}^{3-} level is about 1.1 ~ 1.2 eV (2-/3- transition) above the valence band, where it acts as a deep level acceptor.[60] This deep level can act as a compensation centre for the *n*-type doping of GaN, which has been demonstrated

experimentally by Yi and Wessels.[61] The transition between a shallow donor level and this deep level (Figure I. 14) has been generally accepted as the origin of yellow luminescence (~ 2.25 eV at room temperature), which has been observed in GaN layers grown by several techniques.[59,62]

The complex between the Mg_{Ga} acceptor and the N vacancy may introduce a deep donor level in GaN ($Mg_{Ga}V_N$), which is about 0.4 eV below the conduction band. The blue band observed in GaN PL spectrum (~ 2.8 eV) has been attributed to the transition between this deep donor level and the acceptor level.[63]

I.3. III-Nitride heterostructures and applications

I.3.1. Nitride bandgap engineering

There has been an increasing interest in fabricating opto-electronic devices based on III-nitrides during the last two decades. One important reason is that the band gap of nitrides and their alloys cover a broad range from 0.7 to 6.0 eV. In addition, the wurtzite phases of nitrides are direct band gap materials. These unique optical properties make nitrides suitable for a large range of opto-electronic applications, such as LEDs, LDs and photo-detectors operating in the UV-visible range.[64,65]

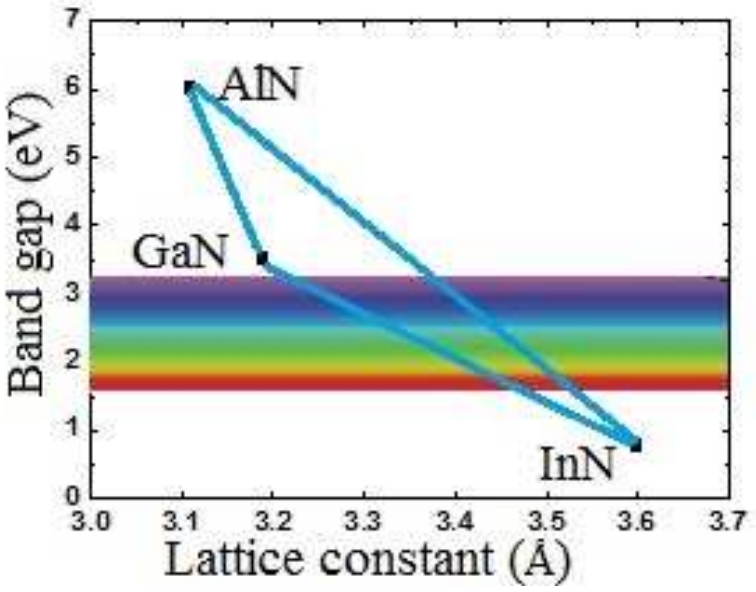

Figure I.15. Band gap energies, at room temperature of wurtzite III-nitrides as a function of the lattice constant a.

Figure I.15 shows the band gap energies of nitride binaries and their lattice constant values a. GaN and AlN have closer lattice constants than InN. The band gap energies of nitrides have been summarized by Vurgaftman and Meyer[6] and are listed in Table I. 6.

material	InN	GaN	AlN
structure	wurtzite	wurtzite	wurtzite
band gap (eV)	0.78	3.51	6.0

Table I.6. Band gap energies of nitride binaries at 0 K.

A nitride based alloy with a band gap energy in the range of 0.7-6.0 eV can be achieved by adjusting the content of InN, GaN and AlN. The band gap energy of an $A_{1-x}B_xN$ alloy can be calculated approximately by:

$$E_g(x) = (1-x)E_g^{AN} + xE_g^{BN} - bx(1-x), \quad \textbf{(I. 18)}$$

where *b* is the bowing parameter. Table I. 7 lists the bowing parameters of different nitride alloys summarized by Vurgaftman and Meyer:[6]

Alloy	AlGaN	GaInN	AlInN
b (eV)	0.7	1.4	2.5

Table I.7. Bowing parameters of AlGaN, GaInN and AlInN alloys.

I.3.2. Polar heterostructures

There is a strong polarization field along the *c* axis ([0001]) in a wurtzite crystal. The polarization field in nitrides consists of spontaneous and piezoelectric polarization. The total polarization can be obtained from the sum of spontaneous and piezoelectric polarizations:

$$\vec{P}_{total} = \vec{P}_{SP} + \vec{P}_{PZ}. \quad \textbf{(I. 19)}$$

The spontaneous polarizations in nitrides arise from the distortion of the tetrahedron structure (Fig I.16 (a)), which leads to the separation of cation (Ga) and anion (N) centers. The spontaneous polarizations have been calculated by Bernardini *et al.* and listed in

Table I. 8.[15]. Among nitrides, AlN has the largest spontaneous polarization. All the polarization values are negative, which means that the spontaneous polarizations of nitrides points along the –*c* $[000\bar{1}]$direction (Figure I. 16 (b)).

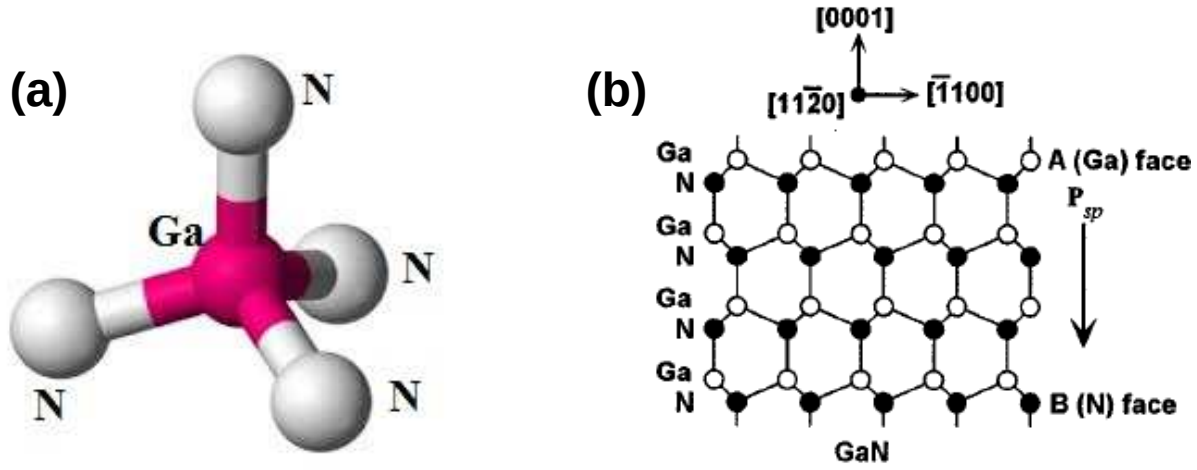

Figure I.16. Schematic representation of (a) the GaN tetrahedron structure ; (b) the relation between the direction of the spontaneous polarization and the crystal orientation of GaN (adapted from ref. 66).

The piezoelectric polarization is induced by the crystal deformation and can be calculated by:

$$\vec{P}_{PZ} = e_{ij}\varepsilon_j = d_{ij}\sigma_j,\ j = xx, yy, zz, yz, zx, xy, \qquad \textbf{(I. 20)}$$

where e_{ij} are the piezoelectric coefficients and ε_j is the strain tensor. d_{ij} are the piezoelectric coefficients which connects the piezoelectric polarization with the stress tensor σ_j. In the absence of shear strain, the expression of $\mathbf{P_{pz}}$ along the *c* axis can be simplified to:

$$\vec{P}_{PZ} = e_{31}\left(\varepsilon_{xx} + \varepsilon_{yy}\right) + e_{33}\varepsilon_{zz}. \qquad \textbf{(I. 21)}$$

In this case, only two piezoelectric coefficients e_{31} and e_{33} are responsible for the determination of the piezoelectric polarization. The calculated values of e_{31} and e_{33} are listed in Table I. 8.

material	$\mathbf{P_{SP}}$ [15]	e_{31}	e_{33}	e_{15}
InN	-0.032	-0.41	0.81	-0.11
GaN	-0.029	-0.34	0.67	-0.22
AlN	-0.081	-0.60	1.46	-0.48

Table I.8. Spontaneous polarizations and piezoelectric coefficients of nitride binaries, the units are C / m^2 (adapted from ref. 67).

When the nitride layers exhibit a biaxial tensile strain ($\varepsilon_{xx} = \varepsilon_{yy} > 0$), the strain along the *c* axis is compressive due to Poisson effect ($\varepsilon_{zz} < 0$). Considering the negative value of e_{31} and the positive value of e_{33}, the piezoelectric polarization is negative in this case, same as the direction of the spontaneous polarization. An opposite situation can be deduced when the layers exhibit a compressive strain.

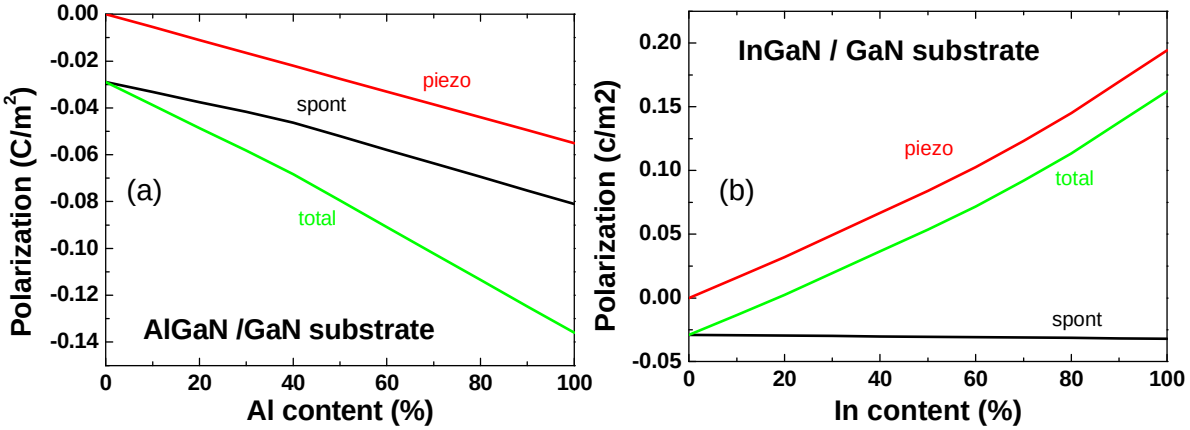

Figure I.17. Simulated total, spontaneous and piezoelectric polarizations in (a) $Al_{1-x}Ga_xN$ and (b) $In_{1-x}Ga_xN$ layers grown on GaN, with different Al and In contents (courtesy of Dr. Jean-Yves Duboz).

In the practical case, nitride based heterostructures are usually grown on the *c* (0001) plane. When an (Al,Ga)N layer is grown on GaN, there is an in-plane biaxial tensile strain in the (Al,Ga)N thin film, then the absolute value of the total polarization in the (Al,Ga)N layer is increased, as shown in Figure I. 17 (a). When an (In,Ga)N layer is grown on GaN, a compressive strain in the (In,Ga)N thin film may lead to a piezoelectric polarization along the +*c* direction, while the spontaneous polarization has an opposite direction. In this case, the total strain is determined by the difference between the piezoelectric and the spontaneous polarization values, as shown in Figure I. 17 (b).

The discontinuity of the polarization may lead to the accumulation of charges at the interface of the heterostructure, according to the boundary condition:

$$\sigma = \vec{n} \bullet \left(\vec{P}_1 - \vec{P}_2 \right), \qquad \textbf{(I. 22)}$$

where σ is the sheet charge density at the interface, n is the unit vector along the normal of the interface, $\mathbf{P_1}$ and $\mathbf{P_2}$ represent the polarization at the two sides of the interface. This property has been adapted in the application of GaN high electron mobility transistors (HEMTs), to increase the density of the 2 dimension electron gas (2DEG) at the interface of (Al,Ga)N / GaN.[68]

On the other hand, in QW based light emitting devices, the existence of interfacial charges may induce the well known quantum confined Stark effect (QCSE),[69,70,71] which may limit the performance of devices. The typical growth direction of GaN is *c* [0001], along which there is a strong polarization field, which leads to the accumulation of charges at the interface of the heterostructures. In the absence of free charges, the displacement field **D** in all the layers should satisfy:

$$\nabla \bullet \vec{D} = 0 . \qquad \textbf{(I. 23)}$$

It suggests that the displacement field over the whole structure is continuous. We recall the well known electrostatic equation:

$$\vec{D} = \varepsilon \vec{E} + \vec{P} . \qquad \textbf{(I. 24)}$$

In the MQW structures, there is:

$$\varepsilon_w \vec{E}_w + \vec{P}_w = \varepsilon_b \vec{E}_b + \vec{P}_b , \qquad \textbf{(I. 25)}$$

where the footnote *w* represents the well, and *b* represents the barrier. It has been pointed out by Bernardini and Fiorentini that the electric field **E** vanishes in large or massive materials.[72] Therefore, we assume that the electric field in the barrier $\mathbf{E}_b$ equals zero. Then, the electric field in the well can be deduced by:

$$\vec{E}_w = \left(\vec{P}_b - \vec{P}_w \right) / \varepsilon_w \qquad \textbf{(I. 26)}$$

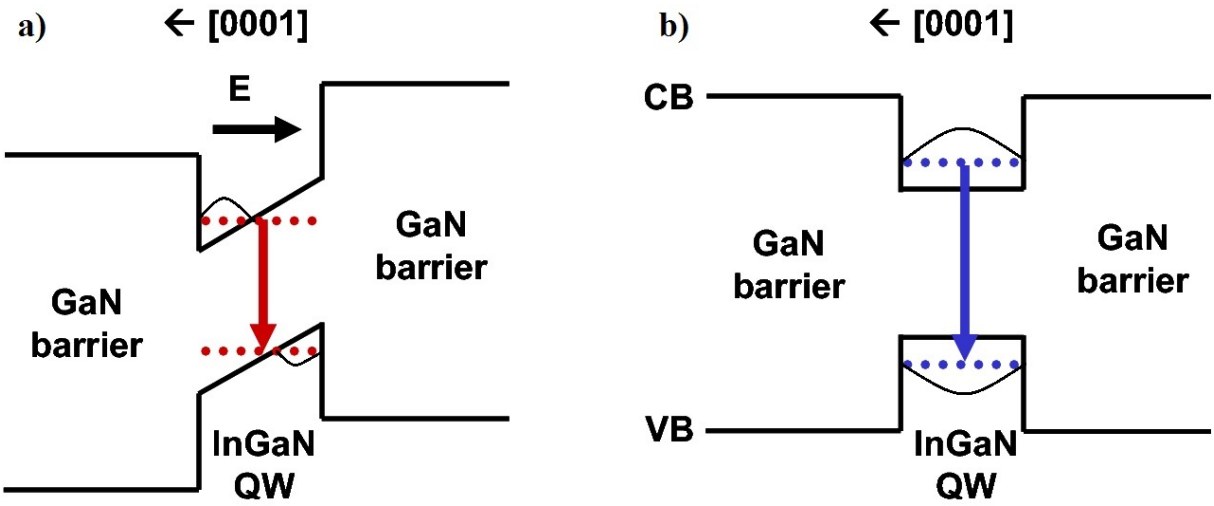

Figure I.18. Band structure of an (In,Ga)N / GaN QW (a) with and (b) without quantum confined Stark effect.

Figure I. 18 shows the band structure diagram of an (In,Ga)N / GaN QW. In the presence of QCSE, the internal electric field in the QW separates the wave functions of the electrons and the holes, reducing the transition rate of the exciton recombination. The QCSE is more pronounced in the green and yellow spectral ranges, due to the larger polarization discontinuity created by the higher In content in the QW (Figure I. 15) and consequently the larger piezoelectric polarization in the (In,Ga)N layer (Figure I. 17 (b)). This feature is the main origin of the well known ‘‘green gap’’ in nitride LEDs and LDs.[73] As shown in Figure I. 19, the external quantum efficiency (EQE) of LED devices decreases rapidly when the emission wavelength increases towards the green range.

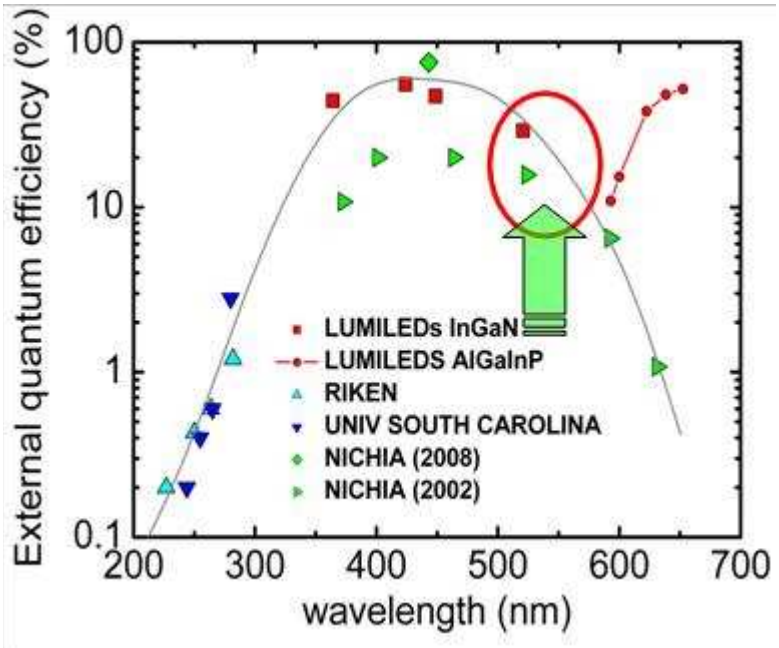

Figure I.19. External quantum efficiency of light emitting diodes as a function of the emission wavelength (courtesy of Dr. Benjamin Damilano).

In the presence of an internal electric field, the transition energy may red-shift due to the band bending caused by the internal electric field (Figure I. 18 (a)), and it can be expressed by:

$$E = E_g + E_e + E_h - R_y - qE_w L_w, \quad \textbf{(I. 27)}$$

where E_e and E_h are the confinement energies of electrons and holes in the QW. The last term corresponds to the energy drop due to the QCSE, L_w is the well thickness.

I.3.3. Nonpolar heterostructures

One solution to avoid the QCSE is to grow GaN on a nonpolar plane, *i.e.*, the *a*-plane $(11\bar{2}0)$ or the *m*-plane $(1\bar{1}00)$. In this case, there is no polarization field along the growth direction, and as a consequence no internal electric field in heterostructures.[74] Therefore, there is no band bending in the band structure. When calculating the transition energy in a nonpolar heterostructure, the last term in Eq. (I. 27) should be omitted. Therefore, growing GaN on a nonpolar plane has been proposed to be a way to achieve a flat band structure such as in Figure I. 18 (b). A higher excitonic recombination rate, as well as a higher radiative recombination efficiency compared with polar structures, is expected as there is no spatial separation of electrons and holes, especially for thick (well thickness > 4nm) and high In content QWs.

Another characteristic of nonpolar heterostructures is the optical polarization of the emitted light. The light emitted from a polar structure is isotropic, which can be explained by the hexagonal symmetry of the wurtzite structure. The rotational symmetry in the *c* basal plane (0001), which is the growth plane of the polar case, gives rise to the isotropic nature of the two top most sub-valence bands in the *x*-*y* plane, as discussed in Section I.2.1. In the nonpolar case, the rotational symmetry in the growth plane is broken mainly by the inclination of the c-axis in the growth plane. In addition, the possible anisotropic strain (discussed in Section I.1.2) in the nonpolar plane may also enhance the anisotropy. The variation of the sub-valence band structure from the polar to a nonpolar orientation has been studied by Schade *et al*[52]. In this study, a new coordinate system *x'y'z'* is defined, with the QW plane lying in the *x'*-*y'* plane and the growth direction set along *z'* (Figure I. 20). The axes of the *xyz* coordinate system always point along the crystal axes, as defined in Figure I. 13.

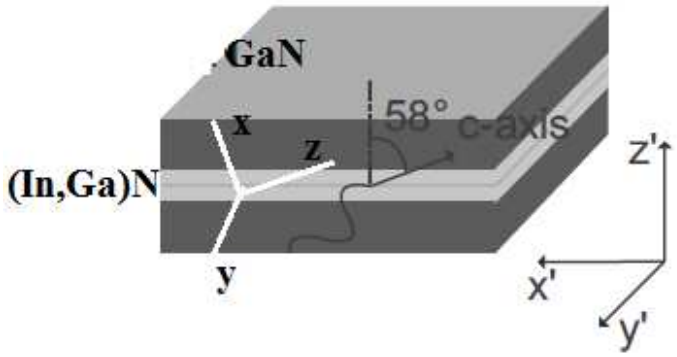

Figure I.20. Illustration of a *xyz* and *x'y'z'* coordinate system in a QW structure (adapted from ref. 52).

y' (*y*) axis is fixed as the rotation axis and θ represents the angle between the *c* axis (*z*) and the growth direction (*z'*). When θ = 90°, the *c* axis lies in the growth plane, representing a nonpolar structure. The polarization degree of a given sub band is given by:

$$P = \frac{\left|M_{y'}\right|^2 - \left|M_{x'}\right|^2}{\left|M_{y'}\right|^2 + \left|M_{x'}\right|^2}, \qquad \textbf{(I. 28)}$$

where $M_{x'}$ and $M_{y'}$ represent the transition matrix elements along *x'* and *y'* directions, respectively. Figure I. 21 represents the variation of the polarization degree of the two top most valence bands as a function of the inclination angle θ.[52] In the polar case, both X_1 band and X_2 band are unpolarized (the polarization degree equals zero). In the nonpolar case ($\theta = 0$), the X_1 band is almost totally polarized along the y' direction (perpendicular to [0001]), while the X_2 band is almost totally polarized along the x' direction (parallel to [0001]).

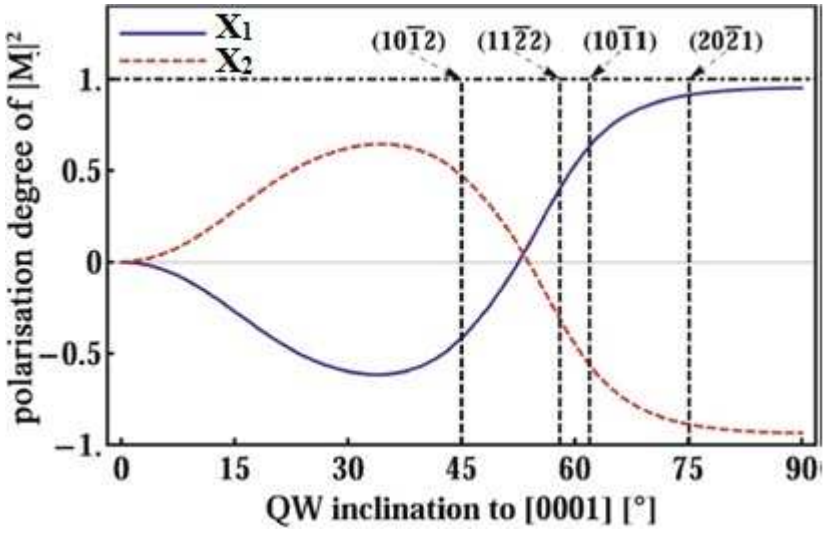

Figure I.21. Variation of the polarization degree of the two top most valence bands as a function of the inclination angle θ (adapted from ref. 52).

The X_1 exciton recombination is lower in energy, therefore it is more favoured than the X_2 exciton recombination. Then, the observed emission should be mainly polarized along the *y'* direction, *i.e.*, perpendicular to [0001] in the nonpolar case.

Many applications could be developed based on the polarization properties of nonpolar devices. Polarization sensitive photo-detectors have been demonstrated based on *m*-plane GaN.[75] Nonpolar LEDs could be used as back lighting for a liquid crystal display (LCD) panel. Indeed, a polarized light source can improve the extinction ratio between zero and an applied bias voltage to the liquid crystal cells.[76] Therefore, a polarizer is not necessary if a nonpolar LED back lighting is adapted and a thinner LCD panel can be fabricated.

MQW based waveguide (WG) laser diodes may also be fabricated on the nonpolar planes due to several advantages. Lasing originates from the stimulated emission in the active region, and the gain of the active region is proportional to the square of the modulus of the transition matrix elements between the initial and final states:

$$G^j \propto \left| \left\langle \Psi_{CB} \left| \vec{A} \bullet \vec{p} \right| \Psi_{VB}^j \right\rangle \right|^2, \qquad \textbf{(I. 29)}$$

where **A** is the vector potential of the optical mode in the WG structure with $\vec{E} = -\frac{\partial}{\partial t}\vec{A}$, and j represents the different sub valence bands. Compared to a polar device, a nonpolar device may improve the spatial overlap between the electron and hole wave functions. Hence the optical gain of the nonpolar LD could be improved compared to the polar case. In addition, different from the spontaneous emission (Eq. I. 14) where the polarization of the transition is only determined by the orientation of the hole wave function, the intensity of stimulated emission also depends on the overlap between the WG mode direction and the orientation of the hole wave function, as indicated by Eq.I.29. If the optical mode of the WG can be designed to be oriented along the same direction with the active region emission polarization, all the emitted light can be coupled into gain; whereas, in the polar case, only about half of the emitted light may be coupled, as the emission from the active region is unpolarized. Scheibenzuber *et al*. have demonstrated theoretically that the optical gain can be improved by 10 times when swiching from *c*-plane to *a*-plane, under the same injection current density.[77]

I.3.4. State of the art of nonpolar GaN heterostructures

The research on nonpolar GaN has started in the 90s. In 1997, *m*-plane (1-100) GaN layers were grown on (1-100) SiC substrates by Domen *et al.*,[78] and the optical polarization of the emission was demonstrated. In 2000, Waltereit *et al.* have grown *m*-plane GaN on *r*-plane $LiAlO_2$, and the absence of QCSE was demonstrated in (Al,Ga)N / GaN MQWs.[74] But the low availability of nonpolar SiC substrates, and the thermal and chemical instabilities of $LiAlO_2$ have limited the development of these substrates.[79] In 2002, DenBaars *et al.* have shown that *a*-plane (11-20) GaN can be grown on *r*-plane sapphire substrates.[80]

However, before achieving high recombination efficiencies as expected in theory, there are still some problems left for nonpolar GaN layers. A-plane GaN surfaces typically present triangular and pentagonal facetted pits and stripes along the c-axis.[81] The triangular pits are quite similar to the ‘‘V-defect’’ observed in the *c*-plane GaN surface, but with the triangular/pentagonal cross sections of ‘‘V-defects’’ lying in the growth plane.[82] Figure I. 22 shows the surface images of *a*- and *c*-plane GaN layers. Triangular/pentagonal and hexagonal shape pits are observed on the surface of *a*- and *c*-GaN, respectively, corresponding to different cross sections of the hexagonal pyramids (V-defects). It is found that the growth rates along *m* [1-100] and *c* [0001] directions are different, which results in the stripes observed on the surface of an a-GaN layer. Moreover, along the *c* direction, the growth rate on Ga face is four times faster than on N face.[83] The resulting rough surface may influence the homogeneity of the MQWs grown on top, and the non-radiative recombination centres created by the fluctuation of the hetero-interface could influence the device performance.[84] The second challenge arises from the large lattice mismatch between the substrate and the epitaxial layer in heteroepitaxy (Section I.1.2). It leads to the presence of a high density of defects, mainly BSFs (~ 10^5 / cm),[85] partial dislocations (~ 10^{11} / cm^2)[85] and threading dislocations (~ 10^{10} / cm^2).[80] These defects may create non-radiative recombination centres and reduce the luminescence efficiency of QWs and light emitting devices.

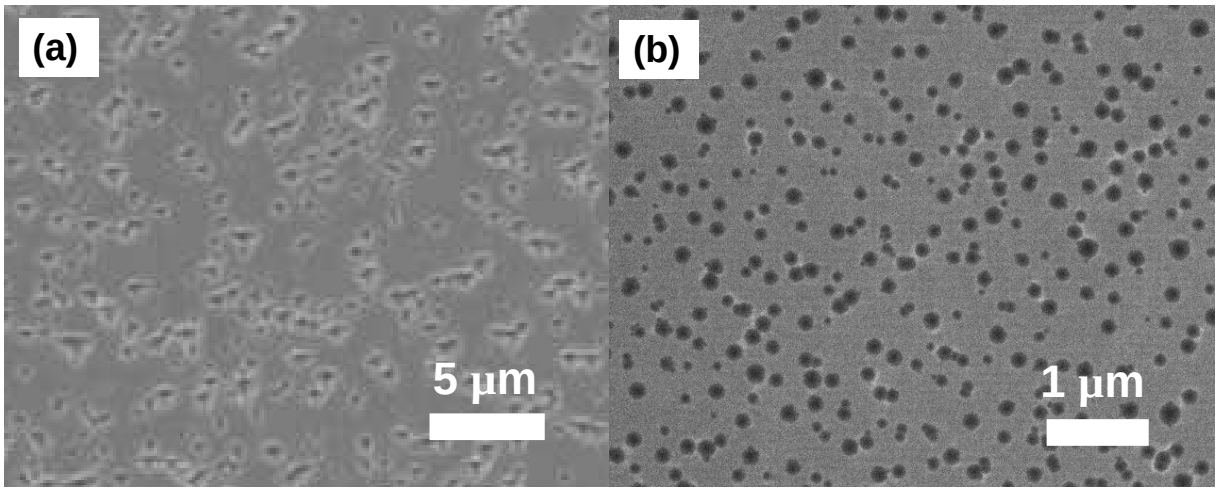

Figure I.22. Scanning electron microscopy images of ~ 1 µm thick (a) *a*-plane[81] and (b) *c*-plane GaN layers.

In the recent years, the availability of nonpolar GaN substrates has enabled the homoepitaxy of GaN, accompanied with the improvement of the GaN crystal quality. LDs[86] and high power LEDs[87] grown on GaN substrates have been demonstrated. LEDs based on m-plane (In,Ga)N / GaN MQWs have been fabricated and low efficiency droops at high injection current densities and longer emission wavelengths have been demonstrated.[88,89] Nonpolar laser diodes emitting at 405 nm, with threshold current densities as low as 7.5 kA / cm^2, have been demonstrated on *m*-plane GaN substrates.[90]

I.4. GaN grown on ZnO

I.4.1. Advantages of ZnO as a substrate

The growth of GaN is usually carried out on foreign substrates like Al_2O_3, 6H-SiC and Si, due to the lack of native substrates. In the recent years, bulk GaN substrates, in both polar and nonpolar orientations, have been fabricated by several companies, making the homoepitaxy growth of GaN possible. However, the size of bulk GaN substrates is limited, and the price is very high, e.g., ~ 1000 euro / cm^2 for nonpolar substrates.[91] Furthermore, GaN substrates in semipolar orientations have only been used at a research level and are not commercially available.

The aim of this work is to investigate if ZnO can be a substrate for the growth of GaN. ZnO substrates, prepared by hydrothermal method,[92] are commercially available for polar (*c*-plane), semipolar (*r*-plane) and nonpolar (*m*- and *a*-plane) orientations, at a much lower price than GaN substrates (~50 euro / cm^2). Figure I. 23 shows the photograph of a 2-inch ZnO wafer fabricated by Tokyo Denpa CO., LTD in Japan. In France, a chemical vapour transport

(CVT) method has been developed in LETI to grow ZnO crystals and 2-inch ZnO wafers have been demonstrated.[93]

Figure I.23. 2-inch ZnO crystal of Tokyo Denpa CO., LTD.[94]

ZnO as a substrate for GaN has many advantages, including the same crystal structure (wurtzite) and close lattice constants with GaN. Figure I. 24 (a) shows the lattice mismatch between commonly used substrates and GaN. Compared with Si, 6H-SiC and sapphire, ZnO has the closest lattice parameters with GaN along both *a*- and *c*-axes, which is important for the reduction of defects generated during the heteroepitaxial growth. Figure I. 24 (b) shows the differences of the thermal expansion coefficients (TECs) between GaN and different substrates. The TEC of ZnO is very close to GaN along the *c*-axis, and is lower than GaN along the *a*-axis. It means that the thermal strain is compressive in the GaN epi-layer when cooling down the sample from growth temperature to room temperature, which may avoid the generation of cracks. In particular, the latest point plays a very important role in the design of nitride heterostructures grown on Si.[95]

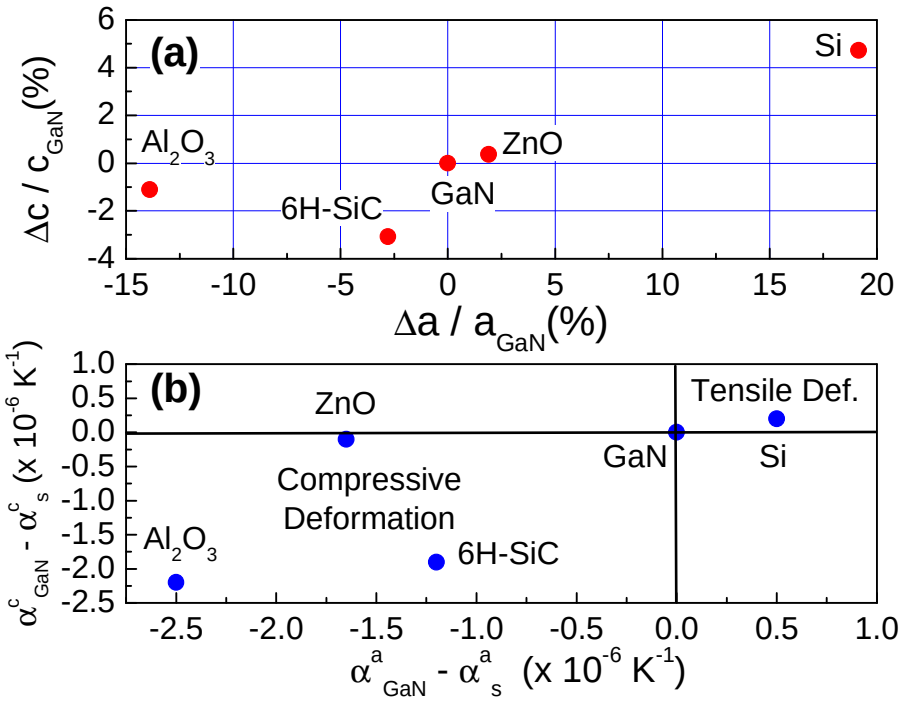

Figure I.24. (a) Lattice mismatch and (b) thermal expansion coefficient differences between Al_2O_3, 6H-SiC, Si, ZnO and GaN (300 K) , along *a* [11-20] and *c* [0001] directions, respectively.

Figure I. 25 shows the calculated temperature dependence of the lattice mismatches (LMs) between GaN and ZnO, along *a* [11-20] and *c* [0001] directions. At room temperature, the LMs are $\Delta a / a_{ZnO} = -1.87\%$ along *a* [11-20] and $\Delta c / c_{ZnO} = -0.42\%$ along *c* [0001] directions. These values are much smaller than the LMs between GaN and sapphire (16.51% along [11-20] and 1.13% along [0001]). The small value of LMs could be maintained in a wide range of temperatures, from 300 K to 1000 K, and is attributed to the small thermal expansion coefficient differences between GaN and ZnO. In particular, when the temperature decreases from 1000 K to 300 K, the LM along the *a*-axis decreases from ~ -2.1% to ~ -1.9%.

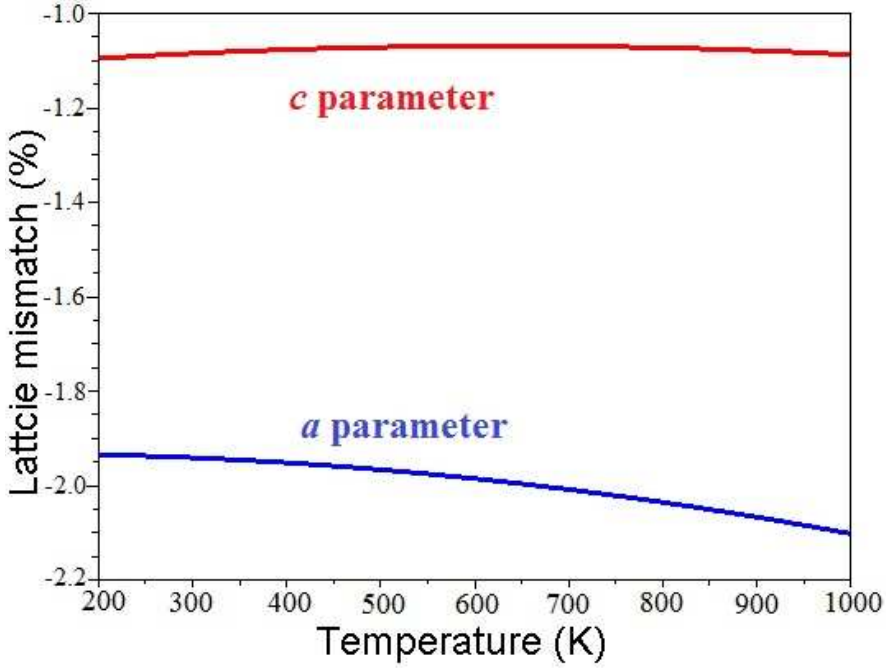

Figure I.25. Lattice mismatch of *a* and *c* parameters between GaN and ZnO, as a function of temperature.

In addition, $In_xGa_{1-x}N$ can be lattice-matched with a [0001]-oriented ZnO substrate for an In composition of $x = 0.18$. This could lead to the fabrication of (In,Ga)N templates that are more adapted to the growth of $In_xGa_{1-x}N$ / GaN based LEDs with high In content (i.e. emitting above 500 nm), as the crystal quality degradation at high In contents[96] is one of the reasons leading to the efficiency drop at the green-yellow emitting range.[97]

Furthermore, there is a high chemical selectivity between ZnO and nitrides. Based on this property, ZnO can be used as a compliant layer in the fabrication of light emitting devices. Nowadays, most of the nitride-based LEDs are grown on sapphire. The poor thermal conductivity of sapphire and the high operating power of the LED devices require the separation of the nitride layers from the substrate. This process is usually performed by a laser lift-off technique.[98] In order to avoid this costly technological step, several alternative approaches have been proposed for the thin film engineering of nitrides, including mechanical release from graphene or boron nitride layers,[99,100] chemical release by etching a sacrificial layer,[101] and wet chemical etching.[102] However, growing high quality nitride layers on large and affordable substrates which can be adapted to these low cost techniques is still an important practical challenge. ZnO fulfils all these requirements, and it can be removed by a simple chemical etching process.[103] Therefore, this approach may help to reduce the fabrication

cost of LEDs. Finally, the *n*-type conductivity of ZnO substrates opens a way to the fabrication of vertical GaN / ZnO based LED devices.

I.4.2. Challenges

There are still several difficulties left concerning the growth of GaN on ZnO. The first problem arises from the formation of an interfacial layer during the growth. It has been reported that Ga can react with ZnO, forming a thin layer of zinc gallate ($ZnGa_2O_4$) at the interface between GaN and ZnO.[104,105] $ZnGa_2O_4$ is a spinel oxide, which has a close-packed face-centred-cubic structure with $Fd\bar{3}m$ space group symmetry. It is a cubic phase crystal with a lattice parameter of 8.3376 Å.[106] The existence of such an interfacial layer, which has a different stacking sequence and a large lattice mismatch with both ZnO and GaN, may limit the advantage of using ZnO as a substrate for the growth of GaN.

The second problem lies in the fact that ZnO becomes unstable at high temperatures (> 600°C), while the growth of high quality GaN crystals requires high growth temperatures. When using NH_3 as the nitrogen source, the back etching of ZnO substrates by H_2, as well as the out diffusion of Zn and O from ZnO to GaN, may lead to the incorporation of impurities at significant concentrations and to the degradation of the crystal quality. It may become a problem when growing intentionally doped *p*-GaN layers, as the impurities may compensate the intentional doping levels, adding difficulties in the achievement of high doping concentrations.

I.4.3. State of the art

The attempt of growing GaN on ZnO substrates has started from the beginning of the 90s. In 1992, Matsuoka *et al*. tried to grow lattice matched $In_{0.23}Ga_{0.77}N$ layer on ZnO substrate, and a InGaN layer with 20% lower x-ray diffraction (XRD) peak line width than that grown on sapphire was obtained.[107] The use of ZnO as a buffer layer for the growth of GaN on sapphire has been explored by several groups, using various techniques including MOCVD, HVPE and MBE.[108,109,110,111] Gu *et al.* showed that the formation of $ZnAl_2O_4$ layer at the interface of ZnO and sapphire can improve the initial growth of GaN,[110] and a GaN layer with a FWHM of XRD (002) peak lower than 500 arcsec has been demonstrated by Lee *et al.* in 2007.[111] There has been an intense interest towards bulk ZnO substrates after 2000, and improved crystal quality of GaN grown on c-plane ZnO was demonstrated.[112,113] From 2005, Fujioka's group in the University of Tokyo has been showing a series of results of

growing GaN on bulk ZnO substrates. They use the pulsed laser deposition (PLD) technique to grown GaN on polar, semipolar and nonpolar planes of ZnO, taking advantage of the low growth temperature of PLD to avoid interfacial reactions between GaN and ZnO. GaN layers with atomic flat surfaces and low FWHM values of x-ray rocking curves (< 0.1°) have been grown at room temperature, on *c*-plane (0001) and *r*-plane (1-102) orientations.[114,115,116] However, the FWHM of the symmetric XRD peak of a-plane GaN is larger than others (> 0.3°).[117] In 2011, Izawa *et al.* showed that high quality polar and nonpolar (*m*-plane) GaN layers can be grown on ZnO substrates using MBE, by employing migration enhanced epitaxy (MEE).[118] In this technique, the Ga atoms are periodically deposited on the GaN surface under a N free atmosphere. The migration of Ga atoms can be enhanced, and therefore the growth can be carried out at very low temperature (~ 150 °C).

References

[1] http://www.monocrystal.com/en/production.

[2] V. Y. Shvidko, M. Lucht, and E. Gerdau, J. Synchr. Rad. **9**, 17 (2002).

[3] E. R. Dobrovinskaya, L. A. Lytvynov, and V. Pishchik, Springer, Berlin (2009).

[4] R. E. Krzhizhanovskiy and Z. Y. Sthtern, Leningrad : Energia, 333 (1973).

[5] I. Akasaki and H. Amano, Jpn. J. Appl. Phys. **36**, 5393 (1997).

[6] I. Vurgaftman and J. R. Meyer, J. Appl. Phys. **94**, 3675 (2003).

[7] J. Zou, D. Kotchetkov, A. A. Balandin, D. I. Florescu, and Fred H. Pollak, J. Appl. Phys. **92**, 2534 (2002).

[8] I. Z.-Tomaszkiewicz, E. Utzig, and P. Gierycz, J. Therm. Anal. Calorim. **91**, 329 (2008).

[9] M. Leszczynski and J. F. Walker, Appl. Phys. Lett. **62**, 1484 (1993).

[10] S. F. Chichibu, T. Sota, G. Cantwell, D. B. Eason, and C. W. Litton, J. Appl. Phys. **93**, 756 (2003).

[11] D. I. Florescu, L. G. Mourokh, Fred H. Pollak, D. C. Look, G. Cantwell, and X. Li, J. Appl. Phys. **91**, 890 (2002).

[12] O. Madelung, U. Rössler, and M. Schulz, II-VI and I-VII Compounds; Semimagnetic Compounds **41B**, 1 (1999).

[13] H. Ibach, Physica Status Solidi **33**, 257 (1969).

[14] S. Stølen, R. Glöckner, and F. Grønvoldf, J. Chem. Thermodyn. **28**, 1263 (1996).

[15] F. Bernardini, V. Fiorentini, and D. Vanderbilt, Phy.Rev. B **56**, R10024 (1997).

[16] H. Karzel, W. Potzel, M. Köfferlein, W. Schiessl, M. Steiner, U. Hiller, G. M. Kalvius, D. W. Mitchell, T. P. Das, P. Blaha, K. Schwarz, and M. P. Pasternak, Phys. Rev. B **53**, 11425 (1996).

[17] H. Iwanaga, A. Kunishige, and S. Takeuchi, J. Mater. Sci. **35**, 2451 (2000).

[18] X. W. Sun, R. F. Xiao, and H. S. Kwok, J. Appl. Phys. **84**, 5776 (1998).

[19] J. Narayan and B. C. Larson, J. Appl. Phys. **93**, 278 (2003).

[20] J. Narayan, Punam Pant, A. Chugh, H. Choi, and J. C. C. Fan, J. Appl. Phys. **99** (5), 054313 (2006).

[21] C. R. Gorla, N. W. Emanetoglu, S. Liang, W. E. Mayo, Y. Lu, M. Wraback, and H. Shen, J. Appl. Phys. **85**, 2595 (1999).

[22] J.-M. Chauveau, J. Vives, J. Zuniga-Perez, M. Laügt, M. Teisseire, C. Deparis, C. Morhain, and B. Vinter, Appl. Phys. Lett. **93**, 231911 (2008).

[23] J.-M. Chauveau, P. Vennéguès, M. Laugt, C. Deparis, J. Zuniga-Perez, and C. Morhain, J. Appl. Phys. **104**, 073535 (2008).

[24] P. Pant, J. D. Budai, R. Aggarwal, R. J. Narayan, and J. Narayan, Acta Materialia **57**, 4426 (2009).

[25] P. Vennéguès and Z. Bougrioua, Appl. Phys. Lett. **89**, 111915 (2006).

[26] Y. Xia, J. Brault, M. Nemoz, M. Teisseire, B. Vinter, M. Leroux, and J.-M. Chauveau, Appl. Phys. Lett. **99**, 261910 (2011).

[27] A. E. Romanov, J. Appl. Phys. **100** (023522) (2006).

[28] A. Polian, M. Grimsditch, and I. Grzegory, J. Appl. Phys. **79**, 3343 (1996).

[29] T. B. Bateman, J. Appl. Phys. **33**, 3309 (1962).

[30] J. Neugebauer and C. G. Van de Walle, Phy.Rev. B **50**, 8067 (1994).

[31] W. Qian, M. Skowronski, M. De Graef, K. Doverspike, L. B. Rowland, and D. K. Gaskill, Appl. Phys. Lett. **66**, 1252 (1995).

[32] L. T. Romano, B. S. Krusor, and R. J. Molnar, Appl. Phys. Lett. **71**, 2283 (1997).

[33] Y. Wang, P. Ruterana, S. Kret, J. Chen, S. El Kazzi, L. Desplanque, and X. Wallart, Appl. Phys. Lett. **100**, 262110 (2012).
[34] B. Heying, E. J. Tarsa, C. R. Elsass, P. Fini, S. P. DenBaars, and J. S. Speck, J. Appl. Phys. **85**, 6470 (1999).
[35] Y. Andre, A. Trassoudaine, J. Tourret, R. Cadoret, E. Gil, D. Castelluci, O. Aoude, and P. Disseix, J. Crystal Growth **306**, 86 (2007).
[36] F. C. Frank, Acta Cryst. **4**, 497 (1951).
[37] X. H. Wu, C. R. Elsass, A. Abare, M. Mack, S. Keller, P. M. Petroff, S. P. DenBaars, J. S. Speck, and S. J. Rosner, Appl. Phys. Lett. **72**, 692 (1998).
[38] A. Ghosh, S. Paul, and S. Raj, Solid State Communications **154**, 25 (2013).
[39] L. T. Romano, J. E. Northrup, and M. A. O'Keefe, Appl. Phys. Lett. **69**, 2394 (1996).
[40] B. Daudin, J. L. Rouviere, and M. Arlery, Appl. Phys. Lett. **69**, 2480 (1996).
[41] D. Cherns, J. Barnard, and H. Mokhtari, Mat. Sci. Eng. B **66**, 33 (1999).
[42] A. Svane, N. E. Christensen, Gorczyca, M. van Schilfgaarde, A. N. Chantis, and T. Kotani, Phy.Rev. B **82**, 115102 (2010).
[43] B. Gil, Phy.Rev. B **56**, (1997).
[44] M. Suzuki, T. Uenoyama, and A. Yanase, Phys. Rev. B **52**, 8132 (1995).
[45] Walter R. L. Lambrecht, Anna V. Rodina, Sukit Limpijumnong, B. Segall, and Bruno K. Meyer, Phy.Rev. B **65**, 075207 (2002).
[46] Y. C. Yeo, T. C. Chong, and M. F. Li, J. Appl. Phys. **83**, 1429 (1998).
[47] S. Ghosh, P. Misra, H. T. Grahnb, B. Imer, S. Nakamura, S. P. DenBaars, and J. S. Speck, J. Appl. Phys. **98**, 026105 (2005).
[48] S. L. Chuang, Phy.Rev. B **54**, 2491 (1996).
[49] S. Ghosh, P. Waltereit, O. Brandt, H. T. Grahn, and K. H. Ploog, Phys. Rev. B **65**, 075202 (2002).
[50] R. Ishii, A. Kaneta, M. Funato, Y. Kawakami, and A. Yamaguchi, Phy.Rev. B **81**, 155202 (2010).
[51] P. Rinke, M. Winkelnkemper, A. Qteish, D. Bimberg, J. Neugebauer, and M. Scheffler, Phy.Rev. B **77**, 075202 (2008).
[52] L. Schade, U. T. Schwarz, T. Wernicke, M. Weyers, and M. Kneissl, Phys. stat. sol. (b) **248**, 638 (2011).
[53] A. Viswanath, J. I. Lee, Dongho D. Kim, C. R. Lee, and J. Y. Leem, Phy.Rev. B **58**, 16333 (1998).
[54] C. G. Van de Walle and J. Neugebauer, J. Appl. Phys. **95**, 3851 (2004).
[55] W. Götz, R. S. Kern, C. H. Chen, H. Liu, D. A. Steigerwald, and R. M. Fletcher, Mater. Sci. Eng. B **59**, 211 (1999).
[56] F. Mireles and S. E. Ulloa, Phy.Rev. B **58**, 3879 (1998).
[57] H. Wang and A. B. Chen, Phy.Rev. B **63**, 125212 (2001).
[58] A. Dussaigne, B. Damilano, J. Brault, J. Massies, E. Feltin, and N. Grandjean, J. Appl. Phys. **103**, 013110 (2008).
[59] K. S. Ramaiah, Y. K. Su, S. J. Chang, F. S. Juang, and C. H. Chen, J. Crystal Growth **220**, 405 (2000).
[60] T. Mattila and R. M. Nieminen, Phy.Rev. B **55**, 9571 (1997).
[61] G. C. Yi and B. W. Wessels, Appl. Phys. Lett. **69**, 3028 (1996).
[62] T. Ogino and M. Aoki, Jpn. J. Appl. Phys. **19**, 2395 (1980).
[63] U. Kaufmann, M. Kunzer, M. Maier, H. Obloh, A. Ramakrishnan, B. Santic, and P. Schlotter, Appl. Phys. Lett. **72**, 1326 (1998).
[64] S. Nakamura, M. Senoh, N. Iwasa, and S. Nagahama, Appl. Phys. Lett. **67**, 1868 (1995).

[65] S. Nakamura, M. Senoh, S.-I. Nagahama, N. Iwasa, T. Yamada, T. Matsushita, Y. Sugimoto, and H. Kiyoku, Jpn. J. Appl. Phys. **36**, L1059 (1997).
[66] E. T. Yu, X. Z. Dang, P. M. Asbeck, S. S. Lau, and G. J. Sullivan, J. Vac. Sci. Technol. B **17**, 1742 (1999).
[67] P Bigenwald, B Gil, F Benharrats, K Zitouni, and A Kadri, Semicond. Sci. Technol. **27**, 024009 (2012).
[68] M. Asif Khan, A. Bhattarai, J. N. Kuznia, and D. T. Olson, Appl. Phys. Lett. **63**, 1214 (1993).
[69] T. Takeuchi, S. Sota, M. Katsuragawa, M. Komori, H. Takeuchi, H. Amano, and I. Akasaki, Jpn. J. Appl. Phys. **36**, L382 (1997).
[70] S. Chichibu, H. Okumura, S. Nakamura, G. Feuillet, T. Azuhata, T. Sota, and S. Yoshida, Jpn. J. Appl. Phys. **36**, 1976 (1997).
[71] M. Leroux, N. Grandjean, M. Laugt, J. Massies, B. Gil, P. Lefebvre, and P. Bigenwald, Phys. Rev. B **58**, R13371 (1998).
[72] F. Bernardini and V. Fiorentini, Phys. stat. sol. (b) **216**, 391 (1999).
[73] M.R. Krames, O.B. Shchekin, R. M. Mach, G.O. Mueller, L. Zhou, G. Harbers, and M.G. Craford, J. Disp. Technol. **3**, 160 (2007).
[74] P. Waltereit, O. Brandt, A. Trampert, H. T. Grahn, J. Menniger, M. Ramsteiner, M. Reiche, and K. H. Ploog, Nature **406**, 865 (2000).
[75] C. Rivera, J. L. Pau, E. Munoz, P. Misra, O. Brandt, H. T. Grahn, and K. H. Ploog, Appl. Phys. Lett. **88**, 213507 (2006).
[76] H. Masui, H. Yamada, K. Iso, J. Speck, S. Nakamura, and S. DenBaars, J Soc Inf Display. **16**, 571 (2008).
[77] W. G. Scheibenzuber, U. T. Schwarz, R. G. Veprek, B. Witzigmann, and A. Hangleiter, Phy.Rev. B **80**, 115320 (2009).
[78] K. Domen, K. Horino, A. Kuramata, and T. Tanahashi, Appl. Phys. Lett. **71**, 1996 (1997).
[79] Y. Dikme, P. van Gemmern, B. Chai, D. Hill, A. Szymakowski, H. Kalisch, M. Heuken, and R. H. Jansen, Phys. stat. sol. (c) **2**, 2161 (2005).
[80] M. D. Craven, S. H. Lim, F. Wu, J. S. Speck, and S. P. DenBaars, Appl. Phys. Lett. **81**, 469 (2002).
[81] X. Ni, Y. Fu, Y. T. Moon, N. Biyikli, and H. Morkoç, J. Crystal Growth **290**, 166 (2006).
[82] F. Wu, M. D. Craven, S. Lim, and J. S. Speck, J. Appl. Phys. **94**, 942 (2003).
[83] B. A. Haskell, F. Wu, S. Matsuda, M. D. Craven, P. T. Fini, S. P. DenBaars, J. S. Speck, and Shuji Nakamura, Appl. Phys. Lett. **83**, 1554 (2003).
[84] M. D. Craven, P. Waltereit, J. S. Speck, and S. P. DenBaars, Appl. Phys. Lett. **84**, 496 (2004).
[85] P. Vennégues, J. M. Chauveau, Z. Bougrioua, T. Zhu, D. Martin, and N. Grandjean, J. Appl. Phys. **112**, 113518 (2012).
[86] T. Obata, N. Kitajima, M. Ohta, H. Ichinokura, and M. Kuramoto, phys. status solidi (a) **205**, 1096 (2008).
[87] K. J. Vampola, N. N. Fellows, H. Masui, S. E. Brinkley, M. Furukawa, R. B. Chung, H. Sato, J. Sonoda, H. Hirasawa, M. Iza, S. P. DenBaars, and S. Nakamura, Phys. status solidi (a) **206**, 200 (2009).
[88] X. Li, X. Ni, J. Lee, M. Wu, U. Ozgur, H. Morkoc, T. Paskova, G. Mulholland, and K. R. Evans, Appl. Phys. Lett. **95**, 121107 (2009).
[89] S.-C.Ling, T.-C. Lu, S.-P. Chang, J.-R. Chen, H.-C. Kuo, and S.-C. Wang, Appl. Phys. Lett. **96**, 231101 (2010).

[90] M. C. Schmidt, K.-C. Kim, R. M. Farrell, D. F. Feezell, D.A. Cohen, M. Saito, K. Fujito, J. S. Speck, S. P. DenBaars, and S. Nakamura, Jpn. J. Appl. Phys. **46**, l190 (2007).
[91] http://ammono.com/products.
[92] L.N. Demyanets and V.I. Lyutin, J. Crystal Growth **310**, 993 (2008).
[93] J. L. Santailler, C. Audoin, G. Chichignoud, R. Obrecht, B. Kaouache, P. Marotel, D. Pelenc, S. Brochen, J. Merlin, I. Bisotto, C. Granier, G. Feuillet, and F. Levy, J. Crystal Growth **312**, 3417 (2010).
[94] http://www.tew.co.jp/e/material/01.html.
[95] F. Semond, Y. Cordier, N. Grandjean, F. Natali, B. Damilano, S. Vezian, and J. Massies, Phys. Stat. Sol. (a) **188**, 501 (2001).
[96] I. Ho and G. B. Stringfellow, Appl. Phys. Lett. **69**, 2701 (1996).
[97] S. Nakamura, Science **281**, 956 (1998).
[98] W. S. Wong, T. Sands, and N. W. Cheung, Appl. Phys. Lett. **72**, 599 (1998).
[99] K. Chung, C. H. Lee, and G.C. Yi, Science **330**, 655 (2010).
[100] Y. Kobayashi, K. Kumakura, T. Akasaka, and T. Makimoto, Nature **484**, 223 (2012).
[101] S. W. Lee, Jun-Seok Ha, Hyun-Jae Lee, Hyo-Jong Lee, H. Goto, T. Hanada, T. Goto, Katsushi Fujii, M. W. Cho, and T. Yao, Appl. Phys. Lett. **94**, 082105 (2009).
[102] A. C. Tamboli, E. D. Haberer, R. Sharma, K. H. Lee, S. Nakamura, and E. L. Hu, Nature.Photon **1**, 61 (2007).
[103] D. J. Rogers, F. Hosseini Teherani, A. Ougazzaden, S. Gautier, L. Divay, A. Lusson, O. Durand, F. Wyczisk, G. Garry, T. Monteiro, M. R. Correira, M. Peres, A. Neves, D. McGrouther, J. N. Chapman, and M. Razeghi, Appl. Phys. Lett. **91**, 071120 (2007).
[104] E. S. Hellman, D. N. E. Buchanan, D. Wiesmann, and I. Brener, MRS Internet J. Nitride Semicond. Res. **1**, 16 (1996).
[105] Y. Cho, O. Brandt, M. Korytov, M. Albrecht, V. M. Kaganer, M. Ramsteiner, and H. Riechert, Appl. Phys. Lett. **100**, 152105 (2012).
[106] P. Ravindra, D. G. Julian, K. S. Suresh, and M. R. Jose, J. Am. Ceram. Soc. **82**, 3337 (1999).
[107] T. Matsuoka, N. Yoshimoto, T. Sasaki, and A. Katsui, J. Electron. Mater. **21**, 157 (1992).
[108] T. Detchprohm, H. Amano, K. Hiramatsu, and I. Akasaki, J. Crystal Growth **128**, 384 (1993).
[109] T. Ueda, T. F. Huang, S. Spruytte, H. Lee, M. Yuri, K. Itoh, T. Baba, and J. S. Harris, J. Crystal Growth **187**, 340 (1998).
[110] S. Gu, R. Zhang, J. Sun, L. Zhang, and T. F. Kuech, Appl. Phys. Lett. **76**, 3454 (2000).
[111] S. W. Lee, T. Minegishi, W. H. Lee, H. Goto, and H. J. Lee, Appl. Phys. Lett. **90**, 061907 (2007).
[112] X. Gu, M. A. Reshchikov, A. Teke, D. Johnstone, H. Morkoc, B. Nemeth, and J. Nause, Appl. Phys. Lett. **84**, 2268 (2004).
[113] G. Namkoong, S. Burnham, K.-K. Lee, E. Trybus, W. Alan Doolittle, M. Losurdo, P. Capezzuto, G. Bruno, B. Nemeth, and J. Nause, Appl. Phys. Lett. **87**, 184104 (2005).
[114] A. Kobayashi, Y. Kawaguchi, J. Ohta, H. Fujioka, K. Fujiwara, and A. Ishii, Appl. Phys. Lett. **88**, 181907 (2006).
[115] A. Kobayashi, Y. Shirakura, K. Miyamura, J. Ohta, and H. Fujioka, J. Cryst. Growth **305**, 70 (2007).
[116] A. Kobayashi, K.i Ueno, J. Ohta, and H. Fujioka, Phys. Status Solidi A **208**, 834 (2011).

[117] A. Kobayashi, S. Kawano, K. Ueno, J. Ohta, and H. Fujioka, Appl. Phys. Lett. **91**, 191905 (2007).
[118] Y. Izawa, T. Oga, T. Ida, K. Kuriyama, A. Hashimoto, H. Kotake, and T. Kamijoh, Appl. Phys. Lett. **99**, 021909 (2011).

Chapter II. Experimental set up overview

In this chapter, a series of experimental equipments, used from the growth to the characterizations, will be introduced. All the samples were grown using Riber MBE reactors. In particular, GaN based heterostructures were grown in a Riber 32P chamber. The surface morphologies were studied by atomic force microscopy (AFM) and scanning electron microscopy (SEM). The later one was also used in some experiments to perform cross-section measurements. The structural properties were characterized by x-ray diffraction (XRD). Photoluminescence (PL) was used to investigate the electronic band structure of the heterostructures.

II.1. Molecular beam epitaxy

II.1.1. MBE reactor

Molecular beam epitaxy (MBE) is an ultra high vacuum (UHV) growth technique, which is widely used in the epitaxial growth of thin film layers. Figure II. 1 shows the scheme of an MBE chamber. The growth is carried in an UHV environment (10^{-8}-10^{-10} Torr). The substrate is fixed on a molyblock, and the molyblock can be introduced into the chamber using a transfer rod. The molyblock is then fixed on the furnace of the manipulator. The direction of the atomic fluxes used for the thin film growth reaching the substrate surface can be adjusted by varying the manipulator position. The manipulator is rotated during the growth to obtain a good homogeneity of the epitaxial layer.

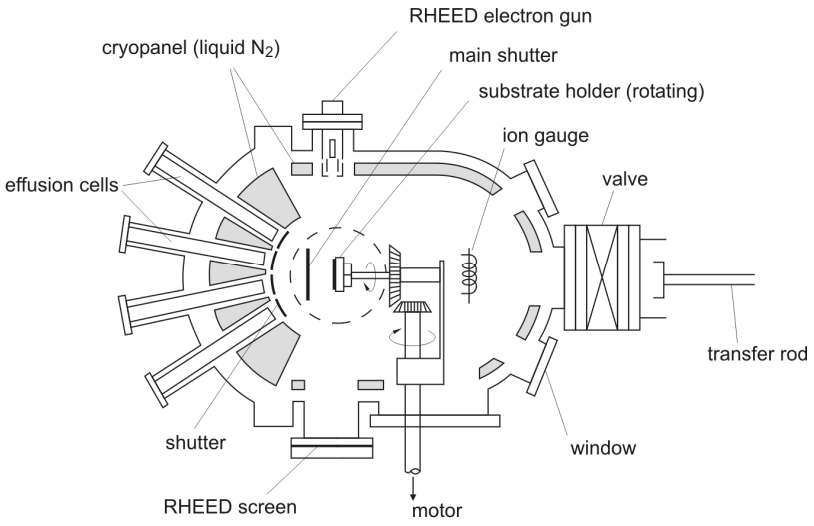

Figure II.1. Schematic representation (top view) of an MBE chamber (adapted from ref.1).

MBE growth of classical III-V compounds is based on the three temperature rule proposed by Freller and Gunther[2], in which the substrate temperature T_s should fulfil the condition $T_{III} > T_s > T_V$, where T_{III} and T_V are the effusion cell temperatures of III and V elements, respectively. For the typically used growth conditions (substrate temperatures), the desorption rate of III elements is negligible, implying that all the III element atoms are absorbed at the surface and diffuse to reach an incorporation site. The substrate is heated up to the desired temperature by the radiation of the furnace. A thermocouple, placed at the backside of the molyblock, gives a measure of the heating temperature. Besides, the substrate temperature is also monitored by a pyrometer placed in the front side of the substrate, through a window of the chamber. In this measurement, the thermal radiance from the substrate is focused by an optical system onto a detector. The thermal radiance *j* and the substrate temperature *T* are related through Stefan-Boltzmann's law:

$$j = \sigma \varepsilon T^4, \qquad \textbf{(II. 1)}$$

where σ is the Stefan-Boltzmann constant ($\sigma = 5.67x10^{-8} Wm^{-2}K^{-4}$) and ε is the emissivity of the substrate.

Atomic fluxes, coming from effusion cells placed in front of the substrate (tens of centimetres away from the substrate surface in our system), provide the elements needed for the growth. A shutter is placed in front of each effusion cell, and the atomic composition and the doping of the epitaxial layer can be adjusted by opening or closing the shutter. A general shutter is placed in front of all the individual shutters to start or stop the growth. The low growth rate, together with the fast response time of the cell shutter opening/closing, enables the growth of epitaxial layers at the atomic scale (*i.e.* the control of sub-nanometer thick layers). It is also adapted to the growth of abrupt interfacial layers in heterostructures.

MBE growth requires the mean free path of atomic fluxes to be larger than the distance between the cells and the substrate. This condition can be fulfilled when the chamber pressure is lower than 10^{-5} Torr. In addition, to obtain an epitaxial layer with high crystalline quality and low non-intentional doping levels, the background pressure in the growth chamber should be as low as possible, which is obtained by using a turbo molecular pump connected to the MBE chamber. A titanium sublimation filament is also installed to further reduce the gas pressure in the chamber. Besides, a liquid N_2 cryopanel, located in the inner wall of the chamber, is used as a sink for gases like CO, H_2O. Every time the chamber is vented for

maintenance, a bakeout process at ~200 °C for at least several days is required to achieve UHV.

II.1.2. Group III and dopant element sources

For growth of nitride based heterostructures, III-group metal elements including Ga, Al, and In are used. In addition, the Si and Mg doping elements are also prepared. The elements are placed in the crucible of an effusion cell (each cell being specifically adapted to one element). The temperature of the effusion cell is controlled by a thermocouple. The evaporated flux is related to the crucible temperature by:

$$F = A\exp\left(-\frac{H}{k_B T}\right), \qquad \textbf{(II. 2)}$$

where H is the enthalpy of evaporation, k_B is the Boltzmann constant, and T is the effusion cell temperature. According to this expression, the atomic flux increases exponentially with the increasing cell temperature. Figure II. 2 shows the measurement of the Ga beam equivalent pressure (BEP), which is proportional to the Ga flux, as a function of the Ga cell temperature. The BEP increases exponentially with the temperature, which coincides with the expression of Eq.II.2. The activation energy (evaporation enthalpy) of the Ga cell is determined to be ~ 2.33 eV by fitting the experimental data using Eq.II.2.

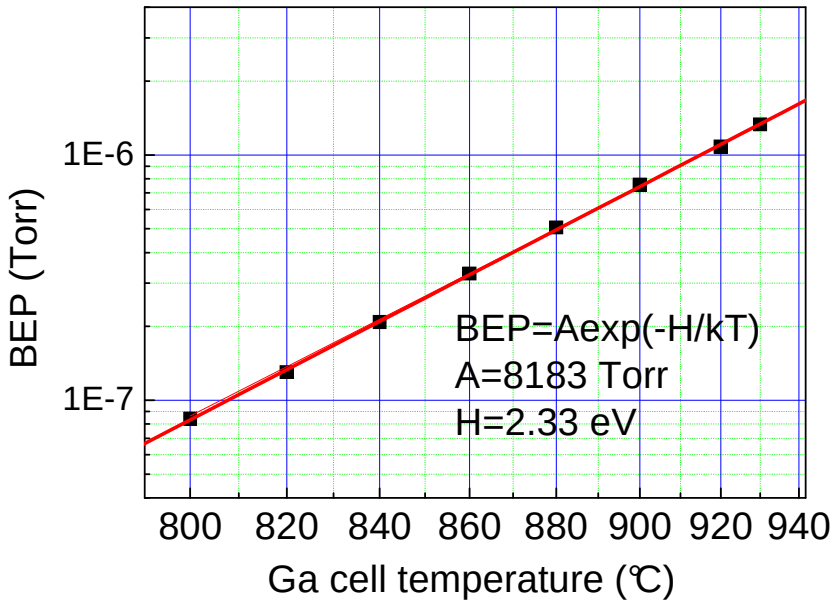

Figure II.2. Beam equivalent pressure (BEP) of the Ga flux (logarithmic scale) as a function of the Ga cell temperature (dotted line).

II.1.3. Group V element sources

II.1.3.a. Ammonia gas source

The nitrogen species are provided from the decomposition of ammonia (NH_3) at the surface of the substrate. A mass flow-meter is connected with the gas line to control the NH_3 flow rate. The decomposition efficiency of NH_3 is strongly influenced by the substrate temperature. Figure II. 3 shows the reaction efficiency of NH_3 with a pre-deposited Ga layer as a function of the substrate temperature. It indicates that the NH_3 reaction efficiency, *i.e.* the cracking efficiency of NH_3 on the substrate, is very low (almost zero)when the temperature is below 450 °C, and this value increases abruptly between 500 and 650 °C. The NH_3 efficiency reaches ~ 4% when the temperature is around 800 °C.

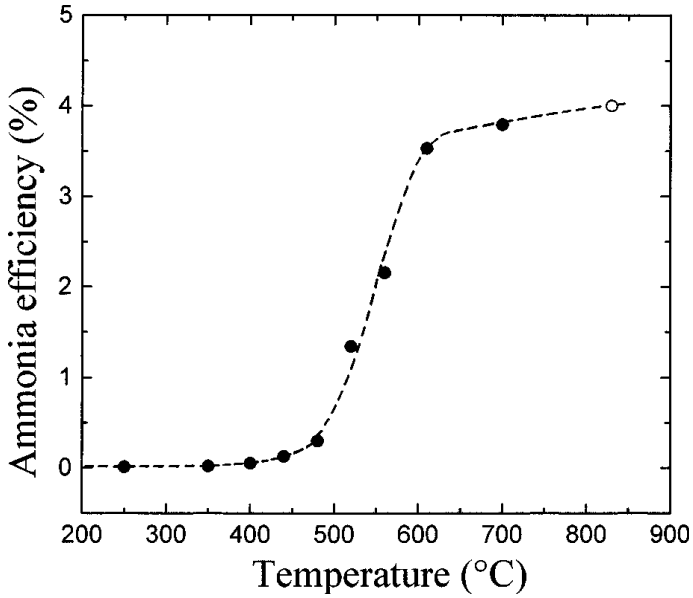

Figure II.3. Reaction efficiency of NH_3 with a pre-deposited Ga layer to form GaN, studied by Mesrine *et al.*[3]

The growth of GaN in NH_3 source MBE is usually carried out under N-rich conditions (typically with a V/III ratio ~ 4)[4]. It means that the GaN growth rate is mainly determined by the Ga flux. The relation between the GaN growth rate (µm/h) with the Ga cell temperature under this growth mode is indicated in Figure II. 4 (a) for a growth temperature of 800°C. It shows that the GaN growth rate increases exponentially from 0.2 to 1.0 µm/h, when the Ga cell temperature is increased from 860 to 945 °C. Typical growth rates are in the range of 0.1 – 1.2 µm/h.

II.1.3.b. Nitrogen plasma source

A N_2 plasma source can also be used as the N source. The N_2 plasma is generated by an ADDON RF plasma source generator at the power of 450 W. The N flux is set at a constant value of 0.5-sccm, which is controlled by a mass flow meter. When using a plasma assisted MBE (PAMBE) to grow GaN, Ga-rich conditions have been proved to grow GaN layers with best material properties[5]. Under this mode, the growth rate is determined by the N flux. Figure II. 4 (b) shows the GaN growth rates in both N- and Ga- rich conditions. By varying the Ga cell temperature from 870 to 925 °C, the GaN growth rate is found to remain a constant value of ~ 0.23 µm/h. The growth rate starts to decrease when the V / III ratio is above the stoichiometry condition (V / III > 1), and varies proportionally to the variation of Ga flux.

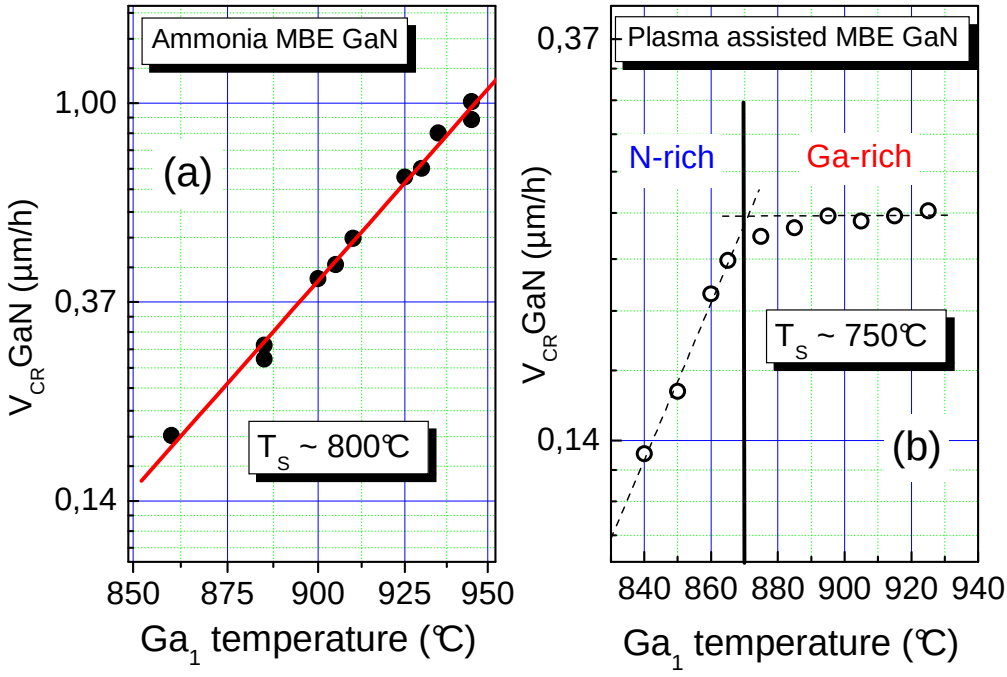

Figure II.4. Growth rate of GaN (in µm/h) as a function of the Ga cell temperature, in the case of (a) NH_3 source and (b) N plasma source MBE growth. The stoichiometric condition (V/III ~ 1) in the case of the PAMBE growth is indicated by a vertical solid line.

II.1.4. Reflection high energy electron diffraction

Reflection high energy electron diffraction (RHEED) is used to monitor *in situ* the surface of the sample during the growth. Figure II. 5 shows a schematic of the technique. It consists of a high energy electron gun and a fluorescent screen. A high energy electron beam

of 20 keV is shined to the sample surface in a grazing angle (1-2°). The electrons are diffracted by the crystal structure of the sample and captured by the fluorescent screen installed at the opposite side of the electron gun. The diffraction pattern is observed on the fluorescent screen. At the grazing incident angles, only the low order diffraction lines can be observed. The distance between streaks (*S*) reflects the periodicity along the in-plane directions. The penetration depth of the beam is only one or two atomic layers. Therefore, the RHEED pattern reflects the crystal structural information of the sample surface. A camera is installed in front of the fluorescent screen to record the RHEED pattern and monitor the time variation of some specific features (*e.g.*, the specular spot).

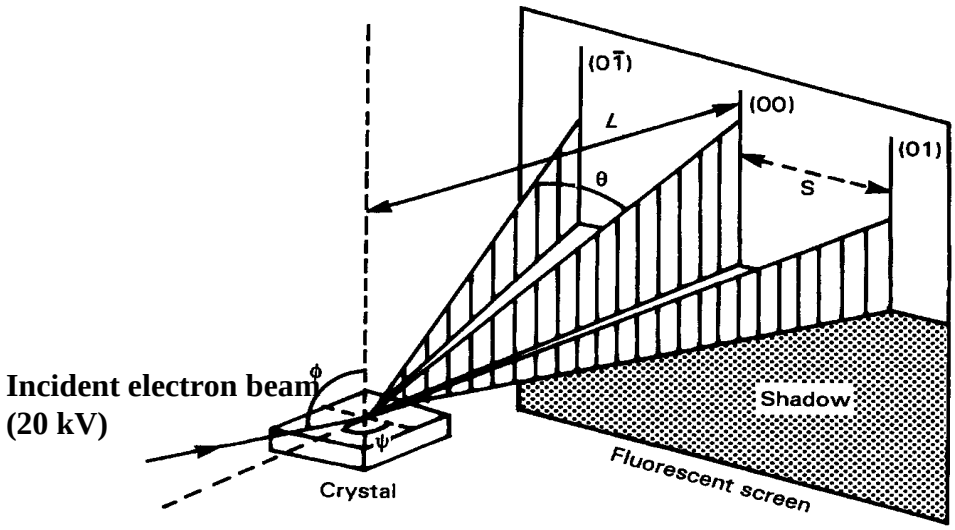

Figure II.5. Schematic diagram of the RHEED technique.

The RHEED can give qualitative information such as the morphology of the sample surface, and quantitative data such as the growth rate. **Figure II. 6** (a) shows the oscillations of the specular spot intensity of RHEED when growing GaN. During the growth, a periodic change of the surface structure happens (Fig II.6 (b)): (1) the specular spot has the highest intensity when the layer is flat; (2) after the deposition of atoms on the flat surface, the surface becomes rough and the specular spot intensity decreases, reaching a minimum for a surface coverage of ½ (3) and then increases again with the surface coverage (4); (5) after a complete monolayer (ML) of GaN is deposited, the surface becomes flat again, and the specular spot intensity reaches a new maximum. One period of intensity oscillations corresponds to one monolayer of the crystal growth. Therefore, the growth process can be monitored by recording the oscillation of the specular point intensity, and the growth rate can be estimated. The growth rate is deduced to be 0.31 ML/s in **Figure II. 6** (a).

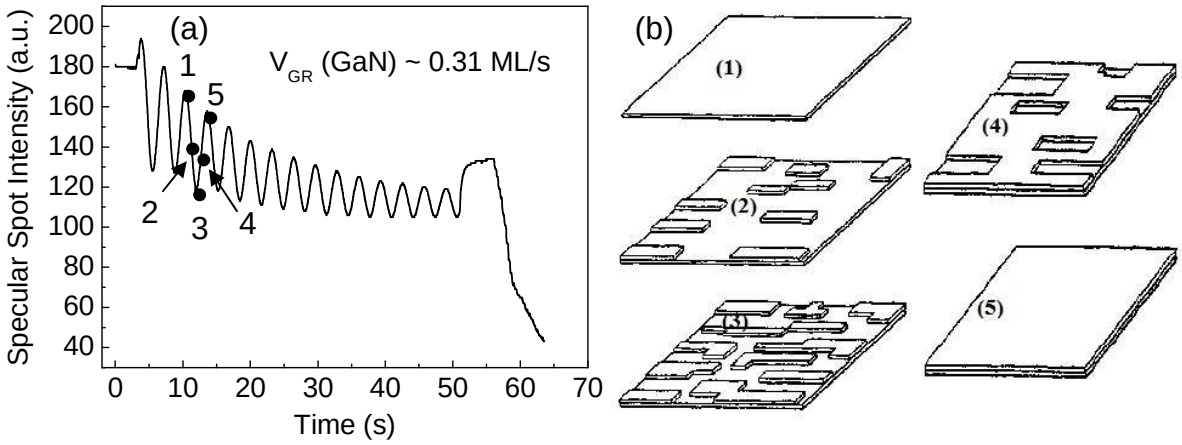

Figure II.6. (a) Oscillation of the specular spot intensity of RHEED during the GaN growth. (b) Evolution of GaN surface structure during the deposition of one monolayer; the corresponding position of each drawing in (b) with one oscillation of the curve in (a) is indicated with numbers.

In addition, surface reconstructions can be monitored from the RHEED pattern. In the case of GaN (0001) surface, a (1 x 1) RHEED pattern, composed of first order streaks, is observed when the GaN surface is exposed to NH_3 at 800 °C (Figure II. 7 (a)). When the substrate temperature is decreased, the appearance of additional lines in between the first order RHEED streaks, having a S/2 spacing with the primary lines, represents a (x 2) surface reconstruction in the <1-10> axes (Figure II. 7 (b))[6]. A similar pattern is observed in the <11-2> axes, leading to a (2 x 2) surface reconstruction on c-plane GaN surfaces. This reconstruction usually appears when the Ga-polar GaN surface is exposed to a strong N-rich environment below 600 °C[7]. Surface reconstructions can be used to calibrate the substrate temperature, as well as other growth conditions (*e.g.*, V/III ratio).

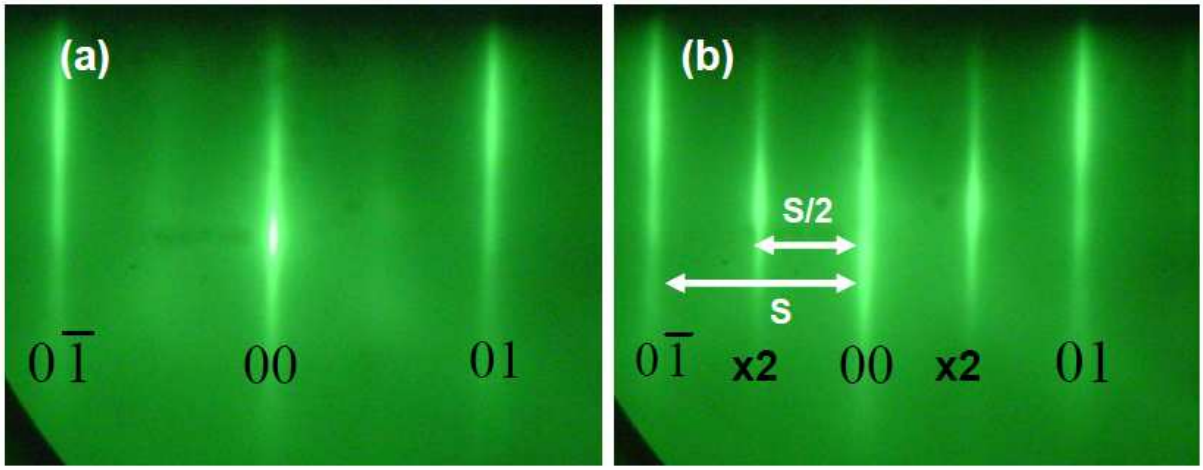

Figure II.7. RHEED pattern of the GaN surface exposed to NH_3 at (a) 800 °C and (b) 500 °C, respectively. The electron beam is along the <11-20> direction.

II. 1.5. Laser reflectivity

A laser reflectivity system is installed to monitor the growth process. An incident laser with a wavelength of 670 nm is shined to the surface of the sample at normal incidence. The laser beam oscillates in the epitaxial layer, which behaves like a cavity sandwiched between the substrate and the vacuum. The reflected signal is captured by a Si photodiode. This system is used to measure directly the growth rate during the entire deposition process. The oscillation period of the signal intensity varies with the epitaxial layer thickness. For GaN, one period of oscillation T corresponds to a layer thickness variation of 138 nm ($\lambda_{laser} / 2n$, n is the refractive index of GaN) at 800 °C. The growth rate can be deduced from the relation $v = 138 / T$ (in nm / min).

Importantly, the oscillation amplitude variation of the signal reflects the surface roughness of the epitaxial layer. Figure II. 8 shows the oscillation of the reflected signal during a two dimensional (2D) (Fig. II.8 (a)) and a three dimensional (3D) growth (Fig. II.8 (b)). In a 2D growth mode, the amplitude remains constant. In a 3D growth mode, it decreases gradually as the surface roughness increases, due to the scattering of the signal on the surface (for a roughness of characteristic size $\geq \lambda_{laser} / 4n$)[8].

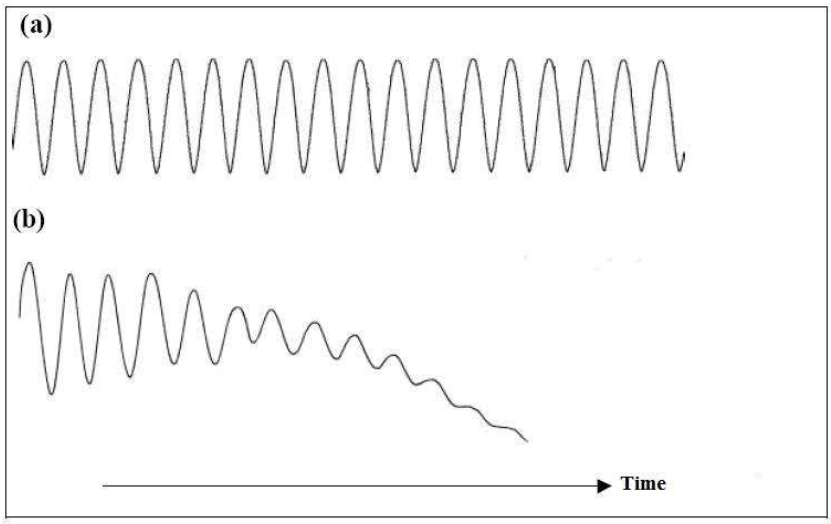

Figure II.8. Oscillation of the reflected signal during a (a) 2D and (b) 3D growth.

II.2. Atomic force microscopy

Atomic force microscopy (AFM) is a high resolution technique used to characterize the surface morphology of a sample. It can be used to characterize almost any type of surface. It consists of a cantilever with a sharp tip at the end to scan the specimen surface. In this study, the sample surface morphology is studied using an AFM working in the trapping mode. In this mode, the cantilever is driven in an oscillating mode by a piezoelectric element mounted in the tip holder, at a frequency close to its resonant frequency. When the tip approaches the surface, the atomic forces between the tip and the sample surface, including Van der Waals forces, dipole-dipole interactions, electrostatic forces, etc., may decrease the amplitude of the oscillation. An electronic servo is used to adjust the height of the cantilever to maintain a constant oscillation amplitude.

In this work, two different imaging modes are used: the topographical mode records the height variation of the tip, and the derivative mode records the perturbation of the tip oscillation amplitude when scanning the sample surface. The first mode is used to measure the surface roughness of the sample, and the second mode allows to detect sudden variations of the surface topography, and to distinguish specific surface features. Using AFM in the tapping mode may reduce the damage on the sample surface and the tip.

As an example, Figure II. 9 (a) shows the surface morphology (topographical image) of a 300 nm thick GaN layer grown on *c*-plane ZnO substrate. The black points are related to the threading dislocations[9]. The atomic steps can also be resolved. As shown in Figure II. 9 (b), a height profile of one vertical line crossing the surface (indicated in Figure.II.9 (a)) is measured. The height of the surface steps is ~ 0.25 nm, which corresponds to one monolayer of GaN. Figure II. 9 (c) shows the surface morphology of the same GaN layer recorded using the derivative mode.

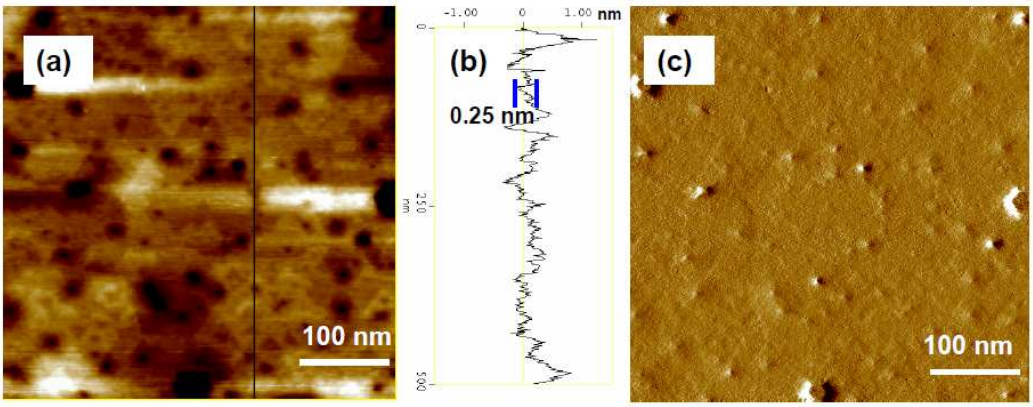

Figure II.9. (a) Surface morphology of a 300 nm thick *c*-GaN layer grown on ZnO, the vertical scale is 3 nm; (b) height profile of a vertical line crossing the surface.

II.3. Scanning electron microscopy

Scanning electron microscopy (SEM) is another technique used in this study to characterize the surface properties of the samples. The sample is placed on the sample holder and introduced into a high vacuum chamber. A focused electron beam with a high kinetic energy is sent to the sample surface and interacts with the electrons inside the sample. A series of signals are produced, including secondary electrons (SE), back-scattered electrons (BSE), characteristic X-rays, light, specimen current and transmitted electrons. The SEs are detected by SE detectors installed in the SEM chamber, and they are most commonly used for surface imaging. In addition, the thickness of the epitaxial layer can be measured by recording cross-sectional images. Figure II. 10 shows the cross sectional image of a GaN layer grown on ZnO, and the measured epiyaxial layer thickness is 0.365 µm.

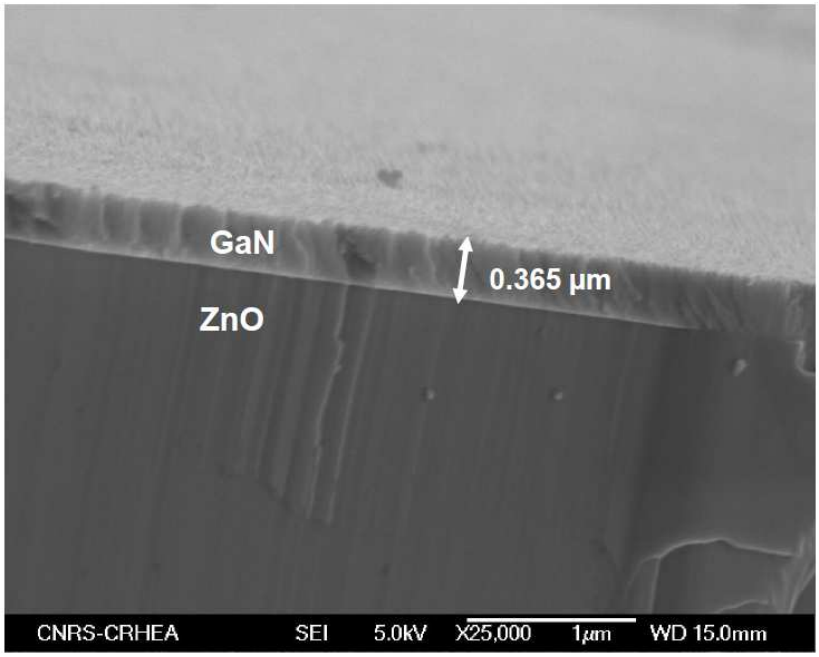

Figure II.10. Cross sectional image of a GaN layer grown on a c-plane ZnO substrate, recorded by SEM.

II.4. Photoluminescence

II.4.1. Photoluminescence Setup

Photoluminescence (PL) is the optical radiation from a physical system in excess of the blackbody radiation. In a compound semiconductor system like GaN, the thermal equilibrium is broken by the external optical excitation, from which the electrons are excited from the valence band to the conduction band. The system tends to return to its equilibrium state through the recombination of electron-hole pairs. This process is usually achieved by either band-to-band transitions, or transitions through discrete levels in the band gap related to dopants or defects. The spectrum is then recorded, and peaks with different energies are related to different recombination processes. The electronic band structure of the material can be investigated by analyzing its PL spectrum.

Figure II. 11 shows the schematic of our PL setup. The sample is placed in a cryostat to study the PL properties at different temperatures. To cool down the sample temperature, the sample needs to be isolated from the environment to avoid thermal exchanges. Therefore, the cryostat is pumped using a turbo molecular pump and a high vacuum ($< 10^{-5}$ Torr) is obtained. The temperature can be cooled down to around 10 K using a liquid helium cooling system.

The laser beam is focused on the sample surface, and different regions of the sample can be excited by moving the position of the sample with a translation stage. The emitted light

from the sample is collected through an optical system, placed in front of the sample and along the surface normal. The signal is coupled into an optical fiber connected to a multichannel photo-detector. Finally, the spectrum is analyzed by a computer.

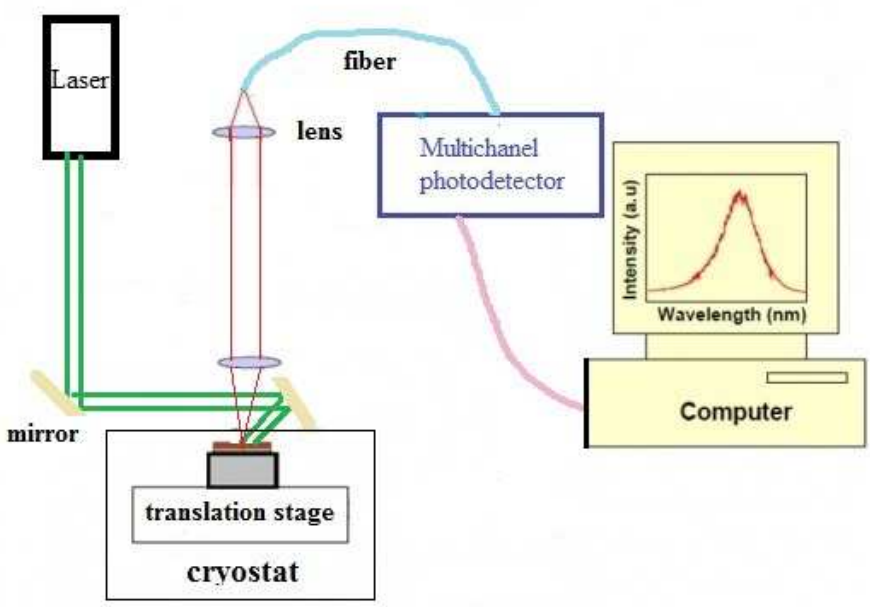

Figure II.11. Schematic of the photoluminescence setup.

II.4.2. Excitation sources

Two types of lasers are used in this work: one is a frequency-doubled argon ion (Ar^+) laser, which emits at 244 nm; the other one is a He-Cd laser emitting at 325 nm. The intensity of the laser beam penetrating into the sample is determined by:

$$I(d) = I_0 \exp(-\alpha d), \qquad \textbf{(II. 3)}$$

where I_0 and $I(d)$ are the intensity of the laser beam reaching the sample surface and in a distance *d* from the surface (inside the sample), respectively. α is the absorption coefficient of the sample, which varies with the structure of the layer, the doping levels, the wavelength of the incident beam and the temperature[10,11]. Figure II. 12 shows the absorption coefficient of GaN as a function of the incident beam energy at room temperature (295 K). The points corresponding to the frequency-doubled Ar^+ and He Cd lasers are indicated. The penetration depth, which is defined by $D = 1/\alpha$, is calculated and listed in Table II. **1**.

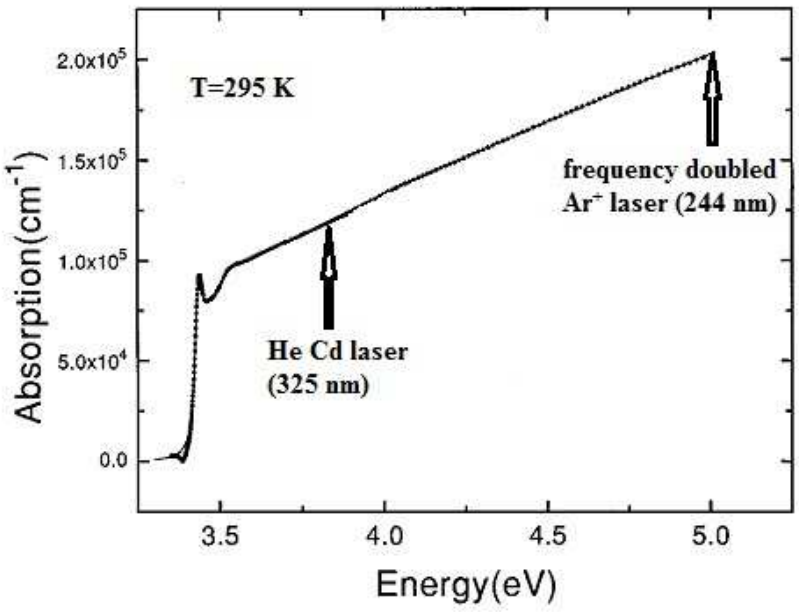

Figure II.12. Absorption coefficient of GaN as a function of the incident beam energy at room temperature (295 K) (adapted from ref. 11)

Laser	Wavelength (nm)	Temperature (K)	Absorption coefficient (cm^{-1})	Penetration depth (nm)
Frequency-doubled Ar^+ laser	244	295	$2.0x10^5$	50.0
He Cd laser	325	295	$1.2x10^5$	83.3

Table II.1. Penetration depth of two types of lasers in a GaN layer.

The penetration depth in GaN for both lasers is less than 100 nm at room temperature. It means that only a thin layer close to the sample surface is excited.

II.4.3. Measurements

The PL spectrum of a semiconductor contains a series of peaks arising from band to band, band to intermediate levels, and intermediate level to intermediate level transitions. Table II. 2 gives information on the main peaks usually observed in the PL spectrum of GaN. For a GaN layer with a high crystal quality, its spectrum is dominated by excitonic recombination, which consist of free and bound exciton recombination. The excitons related to the holes in different sub-valence bands are named as A, B, and C from the lowest to the highest energy transition. The transition energies of these excitons are very sensitive to the

strain state of the GaN layer. Therefore, it varies in a range of ~ 40 meV depending on the GaN strain states. The intensity of these transitions is proportional to $\exp(-E/kT)$, where E is the transition energy. In a typical spectrum of GaN, the intensity of A exciton recombination is ~ 10 times stronger than that of B exciton, and C exciton is very difficult to observe due to the higher transition energy. At low temperature (~ 10K), the excitons are usually bound to neutral donors, with a bonding energy of ~ 6 meV. Besides, transitions between the discrete levels in the band gap also contribute to the spectrum, including donor acceptor pairs, yellow luminescence and blue luminescence. The origins of these transitions have been analyzed in Section I.2.2. The above transitions can be possibly coupled by longitudinal optical phonons (LO), with a decrease of ~ 90 meV in energy for each LO replica.

Description	PL energy (10 K)
Free exciton A	3.477 eV (3.45 - 3.49 eV)
Free exciton B	A + ~ (7-8) meV
Free exciton C	A + ~ 20 meV
A-LO	A - 90 meV
D^0X (neutral donor bound exciton)	A - ~ 6 meV
D^0X-LO	D^0X - 87 meV
DAP (donor acceptor pair)	3.27 eV
DAP-LO	DAP – 91 meV
BSF (basal stacking fault)	3.42 eV
YL (yellow luminescence)	~ 2.25 eV
BL (blue luminescence)	~ 2.85 eV

Table II.2. Main PL peaks in GaN and their physical origins.

The optical polarization of the PL emission can be measured by placing a polarizer in front of the optical fiber. In this configuration, only the light component with the electric field (or magnetic field) oscillating along a certain direction can pass through the polarizer and be collected by the fiber. Therefore, the light polarized along different directions in the surface plane of the sample can be recorded by rotating the polarizer. Usually, these measurements are carried out by rotating the polarizer with a step of 15° and 24 spectra are recorded in a whole circle. Figure II. 13 shows the integrated PL intensity of a c-plane GaN layer when the

electric field oscillation different directions in a whole cycle. Due to the isotropic nature inside the growth plane (0001), an isotropic emission is observed.

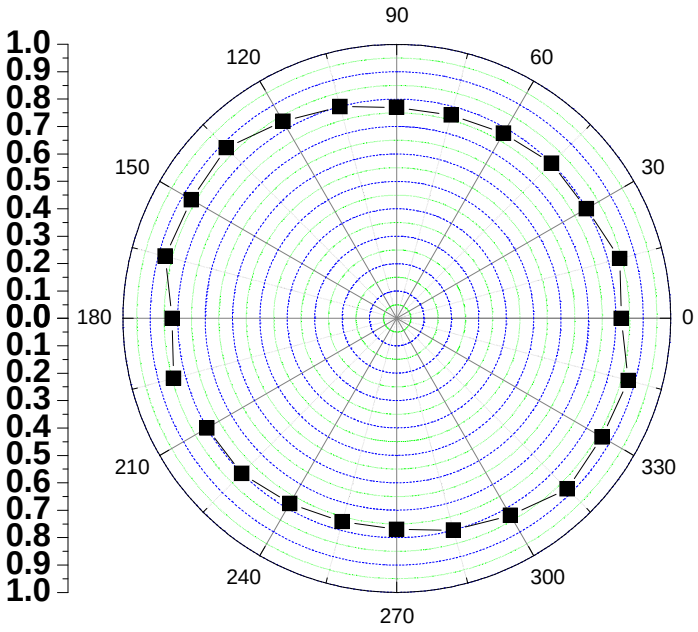

Figure II.13. Linear polarization of the integrated PL intensity of a c-plane GaN layer grown on a c-plane ZnO substrate (the electric field direction is varied by 15° steps in the surface plane).

II.5. X-ray diffraction

II.5.1. Working principle of XRD

High resolution x-ray diffraction is a non-destructive technique to explore the structural properties of the crystal. A series of structural information can be extracted from the diffraction pattern, including the crystal quality, density of defects, as well as the strain states of the epitaxial layers. The basic principle is the Bragg's law:

$$2d_{hkl}\sin\theta = n\lambda\,, \qquad \textbf{(II. 4)}$$

where d_{hkl} represents the interplanar spacing of the (*hkl*) plane, n is the order of the diffraction, θ is the Bragg's angle, and λ is the wavelength of the x-ray source. Experimentally, a crystal acts as a 3D grating, in which the x-ray beam is diffracted and a 3D diffraction pattern is produced. By varying the position of the sample, the angle of the incident beam, as well as the position of the detector, the 3D array of the diffraction pattern can be investigated.

This 3D array reflects the information of the reciprocal space. Each diffraction spot corresponds to one set of crystal planes. The position and the size of the spots are inversely related to the interplanar spacing and the crystallite size in the real space, respectively.

Figure II. 14 shows the scheme of the four cycle diffractometer used in this study. The x-ray source is generated by bombarding a Cu target using electrons in an vacuum tube. The wavelength of the source is selected by a monochromator, and the $K\alpha_1$ line of the Cu with a wavelength of 1.5406 *Å* is selected in our measurements. The typical divergence beam given by the monochromator is $\delta\omega \sim 0.005°$.

The sample is placed on a sample holder. The sample has six freedoms of movements, including three translational motions and three rotational motions. The transitional motions are represented by the orthogonal indexes X, Y, and Z. The rotational motions are represented by ω, χ and φ, and their rotation axes are illustrated in Figure II. 14. ω represents the angle between the incident beam and the sample surface, and its rotation axis is perpendicular to the diffraction plane. The χ rotation represents the rotation of the sample with respect to the intersection of the diffraction plane and the sample surface. The φ rotation represents the rotation with respect to the axis perpendicular to the sample surface.

The diffracted signal is recorded by a detector. The angle between the incident and diffracted beam is 2θ, where θ is the angle between the incident beam and the crystal plane. With an open detector, the divergence of the diffracted beam $\delta\theta$ is an arc of ~ 5°, and this value can be reduced to 0.005° by the utilisation of an analyzer crystal.

As mentioned before, the 3D array of the diffraction pattern could be investigated by moving the position of the sample or/and the detector. Each type of movement corresponds to one ‘‘scan’’. Table II. 3 gives the description and function of several types of scans which are most commonly used in the XRD measurements.

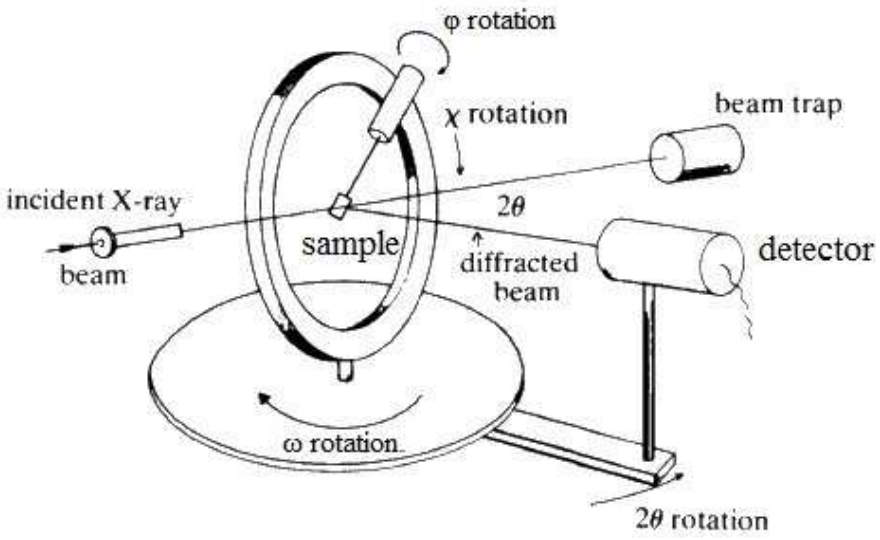

Figure II.14. Schematic diagram of the diffractometer.

Scan type	Description
2θ	The sample position remains unchanged, and only the position of the detector is changed. The zero position of the detector is usually calibrated by performing the *2θ* scan on the analyzer crystal.
ω	The detector remains stationary, and the sample is rotated around the *ω* axis. A *ω* scan is also called ‘‘rocking curve’’, as it corresponds to the rocking of the sample with respect to the *ω* axis. The *ω* scan is usually used to evaluate the crystal quality, as the line width of the rocking curve is usually broadened by the dislocations and the wafer curvature.
2θ/ ω	The sample is rotated by *ω* and the detector is rotated by 2*θ*, with an angular ratio of 1:2. It probes the diffraction spots along a direction with less broadening, thus it is used to evaluate the lattice parameters. An analyzer crystal is usually used in this measurement to reduce the divergence.
ω/2θ	Same as a *2θ* scan, but with *ω* on the *x* axis.
χ	Rotation of the sample with respect to the *χ* axis. It is used to orientate the position of the crystal planes.
φ	Rotation of the sample with respect to the *φ* axis. It is used to orientate the position of the crystal planes.

Table II.3. Introduction to the different scans available on the diffractometer.

To investigate the diffraction spots related to different planes, several diffraction geometries are adapted. Figure II. 15 shows three types of the most commonly used diffraction geometries. A symmetric geometry is used to investigate the crystal planes parallel to the sample surface. In this case, we have $2\theta = 2\omega$. An asymmetric geometry is adapted to reach spots which can not be measured by the symmetric geometry. An offset in ω is applied (offset = $\theta \pm \omega$) to obtain a grazing incidence or exit configuration. For crystal planes which have a non zero angle with the sample surface, a skew symmetric geometry is usually used. A χ offset is applied to position the measured plane perpendicular to the diffraction plane. After the χ offset is applied, a φ scan is necessary to find the diffraction spot.

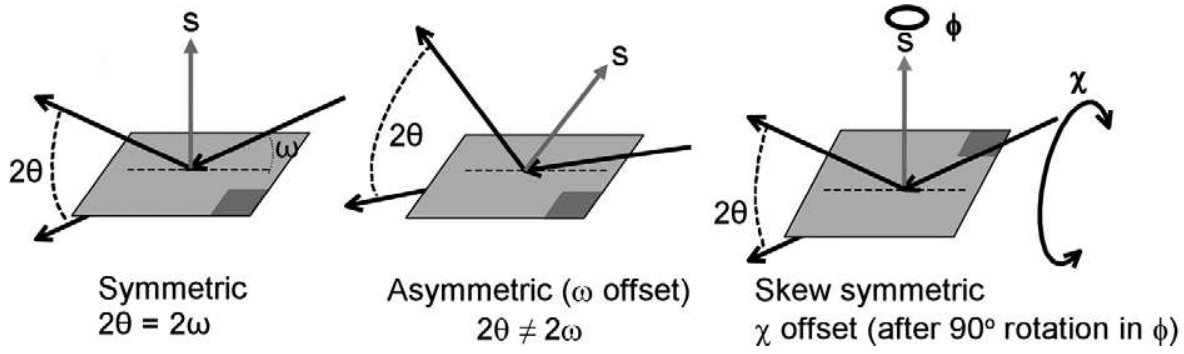

Figure II.15. Diffraction geometries commonly used in XRD measurements (adapted from ref.12).

II.5.2. Determination of lattice parameters using XRD

The lattice parameters of GaN layers can be measured by XRD. In the polar case, symmetrical reflections of the GaN (006) plane and asymmetrical reflections of the (205) and (3-13) planes are recorded using an analyzer crystal. The asymmetrical reflections are measured in grazing incidence configurations. The *2θ* positions of these reflections are obtained. Then, distances between these planes can be calculated following Eq.II.5.

In a hexagonal model, the distance between crystal planes is determined by:

$$d_{hkl} = \frac{a}{\sqrt{\frac{4}{3}\left(h^2 + k^2 + kl\right) + l^2 \frac{a^2}{c^2}}}, \qquad \textbf{(II. 5)}$$

where *a* and *c* are the lattice constants. Therefore, the distances between the (006), (205), and (3-13) planes can be expressed by:

$$d_{006} = \frac{c}{6},$$

$$d_{205} = \frac{ac}{\sqrt{\frac{16}{3}c^2 + 25a^2}}, \qquad \textbf{(II. 6)}$$

$$d_{3\text{–}13} = \frac{ac}{\sqrt{\frac{28}{3}c^2 + 9a^2}}.$$

Together with Bragg's law (Eq. II.4), the lattice constants can be obtained.

In the nonpolar case (*a*-plane), the crystal point group of GaN is reduced from hexagonal (C_v^6) to orthorhombic (C_v^2) due to the in-plane anisotropic residual strain and relaxation[13]. Therefore, an orthorhombic model of the GaN crystal structure is introduced for the calculation of the lattice parameters. The symmetrical (11-20) reflection, and the asymmetrical (20-20) and (11-22) reflections, are measured. Figure II. 16 illustrates the axes and the planes in the orthorhombic system. ***a***, ***b*** and ***c*** represents the three orthogonal crystal axes in the orthorhombic model. The blue lines represent two of the planes used in the measurements of the lattice parameters. The (11-20) (hexagonal system) plane is the growth plane. The reflections from the (11-22) plane (not illustrated in Fig. II. 16) are also measured to extract the periodic information along the ***c*** axis. The relationships of the crystal plane notations between hexagonal and orthorhombic systems can be found in Table II. 4

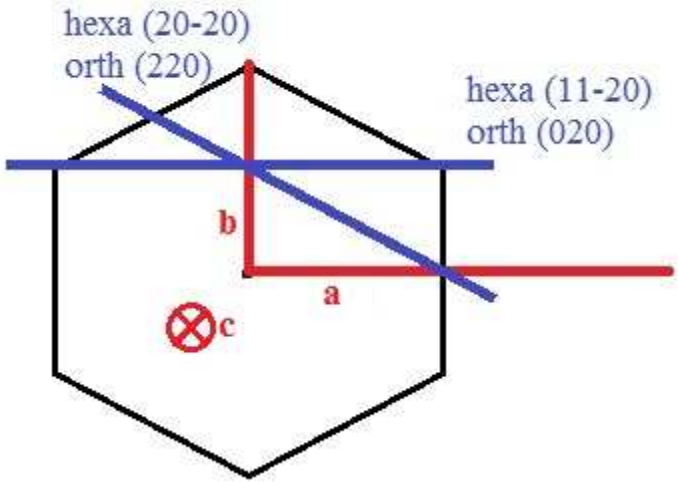

Figure II.16. Illustration of the orthorhombic crystal system and the related planes, from the top view of the basal plane.

Hexagonal system	Orthorhombic system
(11-20)	(020)
(20-20)	(220)
(11-22)	(022)

Table II.4. Comparison of the crystal plane notations between hexagonal and orthorhombic systems.

In the orthorhombic system, the plane distance is related to the Miller indexes and the lattice parameters by:

$$d_{hkl} = \frac{1}{\sqrt{\frac{h^2}{a^2} + \frac{k^2}{b^2} + \frac{l^2}{c^2}}}. \qquad \textbf{(II. 7)}$$

Then the (020), (220) and (022) plane distances can be expressed by:

$$\begin{aligned} d_{020} &= \frac{b}{2} \\ d_{220} &= \frac{1}{2\sqrt{\frac{1}{a^2} + \frac{1}{b^2}}}. \\ d_{022} &= \frac{1}{2\sqrt{\frac{1}{b^2} + \frac{1}{c^2}}} \end{aligned} \qquad \textbf{(II. 8)}$$

Together with Eq. II. 5, the orthorhombic lattice parameters of the GaN layer can be obtained.

References

[1] http://web.tiscali.it/decartes/phd_html/node4.html.

[2] H. Freller and K. G. Günther, Thin Solid Films **88**, 291 (1982).

[3] M. Mesrine, N. Grandjean, and J. Massies, Appl. Phys. Lett. **72**, 350 (1998).

[4] N. Grandjean, M. Leroux, J. Massies, M. Mesrine, and M. Laügt, Jpn. J. Appl. Phys. **38**, 618 (1999).

[5] C. Adelmann, J. Brault, D. Jalabert, P. Gentile, H. Mariette, G. Mula, and B. Daudin, J. Appl.Phys **91**, 9638 (2002).

[6] A.R. Smith, R.M. Feenstra, D.W. Greve, M.-S. Shin, M. Skowronski, J. Neugebauer, and J.E. Northrup, Surface Science **423**, 70 (1999).

[7] A. R. Smith, R. M. Feenstra, D. W. Greve, M.-S. Shin, M. Skowronski, J. Neugebauer, and J. E. Northrup, Appl. Phys. Lett. **72**, 2114 (1998).

[8] J. Massies and N. Grandjean, J. Crystal Growth **201–202**, 382 (1999).

[9] M Khoury, A Courville, B Poulet, M Teisseire, E Beraudo, M J Rashid, E Frayssinet, B Damilano, F Semond, O Tottereau, and P Vennéguès, Semicond. Sci. Technol. **28**, 035006 (2013).

[10] O. Ambacher, W. Rieger, P. Ansmann, H. Angerer, T.D. Moustakas, and M. Stutzman, Sol. State. Commun **97**, 365 (1996).

[11] J. F. Muth, J. H. Lee, I. K. Shmagin, R. M. Kolbas, H. C. Casey, B. P. Keller, U. K. Mishra, and S. P. DenBaars, Appl. Phys. Lett. **71**, 2572 (1997).

[12] M A Moram and M E Vickers, Rep. Prog. Phys. **72**, 036502 (2009).

[13] J.-M. Chauveau, P. Vennéguès, M. Laugt, C. Deparis, J. Zuniga-Perez, and C. Morhain, J. Appl. Phys. **104**, 073535 (2008).

Chapter III. Nonpolar (Al,Ga)N heterostructures grown on (Zn,Mg)O templates

In this chapter, *a*-plane (Al,Ga)N heterostructures have been grown on (Zn,Mg)O / *r*-sapphire templates. The growth conditions of GaN layers are optimized, and the influence of Mg content in templates on the GaN growth is discussed. Structural and optical properties of GaN layers are characterized, and the optical polarization behaviour of the GaN near band edge emission is analyzed. A series of a-plane $Al_{0.2}Ga_{0.8}N$ / GaN MQWs with different well thicknesses is fabricated, and the absence of QCSE in the nonpolar heterostructures is evidenced.

III.1. a-plane ZnO / sapphire templates

As introduced in Section I.1.2, *a*-plane ZnO can be grown on *r*-plane sapphire. In this chapter, *a*-plane $(11\bar{2}0)$ GaN layers have been grown on (Zn,Mg)O templates. There are three objectives of this study: 1) to investigate the possibility of growing GaN along the [11-20] orientation; 2) to study the influence of the Mg content in the templates on the structural and optical properties of the GaN epi-layers; 3) to investigate the optical properties of the QW-based heterostructures grown on nonpolar planes. The (Zn,Mg)O templates were grown on *r*-plane sapphire substrates. Actually, the (Zn,Mg)O layers can be regarded as buffer layers for the growth of GaN on *r*-sapphire. By adapting this approach, *a*-GaN layers of large area (>2 inch) could be grown.

One concept needs to be introduced before carrying out the GaN growth: the usage of (Zn,Mg)O instead of ZnO templates. In CRHEA, we have shown that the incorporation of Mg into (Zn,Mg)O can improve the smoothness of this layer.[1] Figure III. 1 shows the surface roughness variation of a-plane (Zn,Mg)O layers as a function of Mg content. The incorporation of Mg strongly decreases the surface roughness on sapphire, from 8 nm for ZnO,

to only 1.7 nm when the Mg content is 40%. The smoothing of the template surface roughness may facilitate the GaN growth and improve the crystal quality.

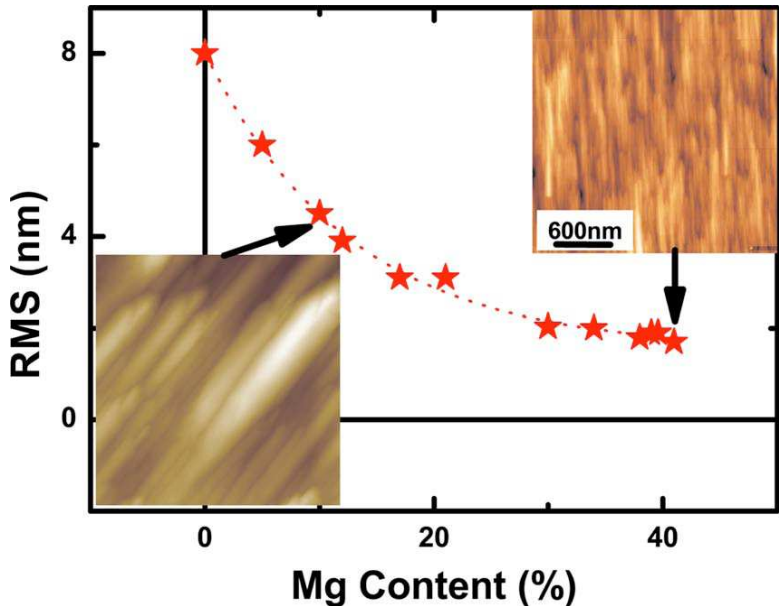

Figure III.1. Evolution of the surface roughness of 1 µm thick a-plane (Zn, Mg)O layers with the Mg content (5 x 5µm^2). In inset, the surface morphologies of $Zn_{0.9}Mg_{0.1}O$ and $Zn_{0.58}Mg_{0.42}O$ layers measured by AFM are shown (adapted from ref.1).

Therefore, besides ZnO templates, the (Zn,Mg)O templates are also used in this study. The templates were grown in a Riber Epineat MBE chamber. The oxygen atomic species were provided by a radio frequency (RF) plasma source, and the zinc (Zn) was evaporated from a double-filament effusion cell. The (Zn, Mg)O layers were grown at 400°C under metal rich conditions, and the growth rate was 0.3 µm/h. More information about the growth can be found in ref.2.

The surface morphologies of the (Zn,Mg)O layers are characterized by the presence of stripes. The stripes are along the *c* [0001] direction, and the formation of these stripes is attributed to the faster growth rate of (Zn,Mg)O along the *c* direction compared to the *m* direction. This feature is a characteristic of a-plane surfaces as introduced in Section I.3.3.

Figure III. 2 displays the lattice mismatch between GaN and unstrained (Zn,Mg)O as a function of the Mg content,[3] along both [0001] and [1-100] directions. The lattice parameters of (Zn,Mg)O could be tailored by modifying the Mg content. When the Mg content increases, GaN has an increasing compressive mismatch along the *m* [1-100] direction. Along the *c* [0001] direction, the lattice mismatch is tensile at low Mg contents, and it switches to be compressive when the Mg content is above 20%. When the Mg content equals 20%, there is a

lattice match between GaN and $Zn_{0.8}Mg_{0.2}O$ along the *c* [0001] direction. The density of defects generated from the lattice misfit can be expected to be reduced by growing GaN on such a lattice matched layer, at least along one direction.

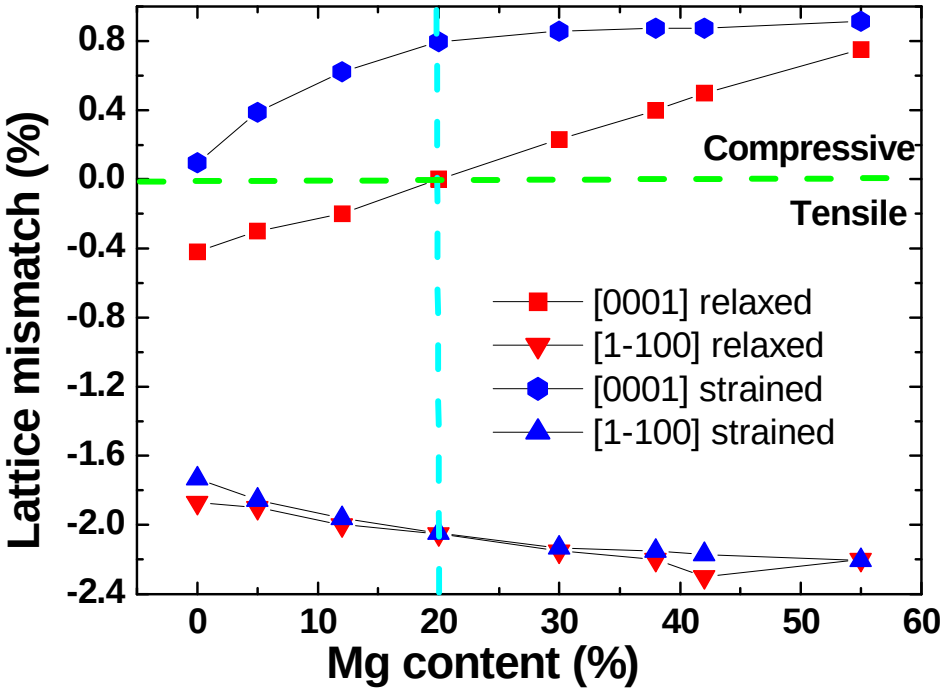

Figure III.2. Calculated lattice mismatch between GaN and (Zn, Mg)O as a function of the Mg content, when the (Zn,Mg)O layers are relaxed and strained on sapphire.

X-ray diffraction (XRD) measurements have been carried out to characterize the structural properties of the (Zn,Mg)O layers.[1] The 2θ/ω diagram was recorded. Except peaks arising from the sapphire substrates, only peaks from the (Zn,Mg)O (11-20) and (22-40) planes were detected (Figure III. 3). It indicates that the layers were grown in a unique *a*-orientation. The symmetric (11-20) diffraction peaks have been recorded at different azimuthal angles. The FWHM of the (11-20) reflection is ~ 1000 arcsec when the incident beam is parallel to the *c* axis of the ZnO layer, and this value was found to be ~ 1260 arcsec when the beam is perpendicular to the *c* axis, *i.e.* along the [1-100] direction.

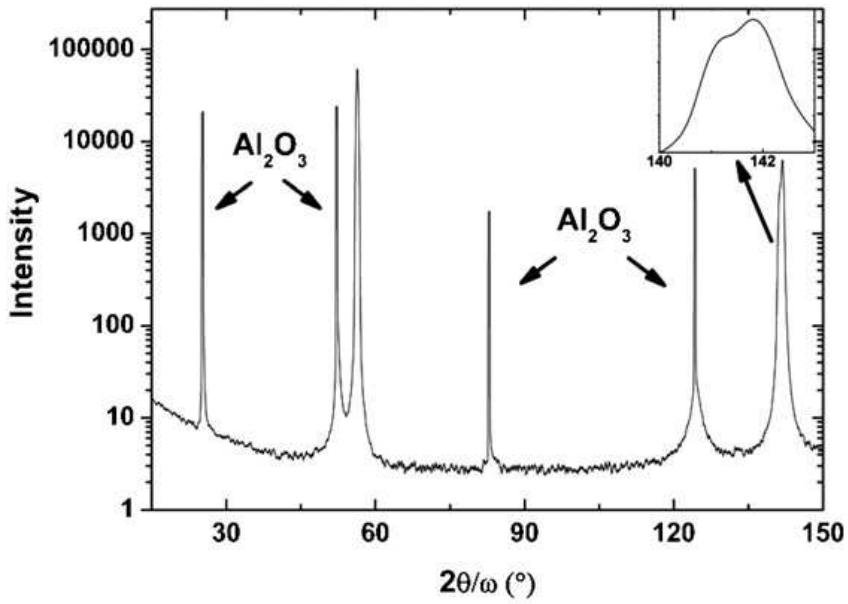

Figure III.3. *2θ-ω* diagram of a $Zn_{0.85}Mg_{0.15}O$/ZnO MQW structure, the inset the (22-40) reflection peak (ref. 2).

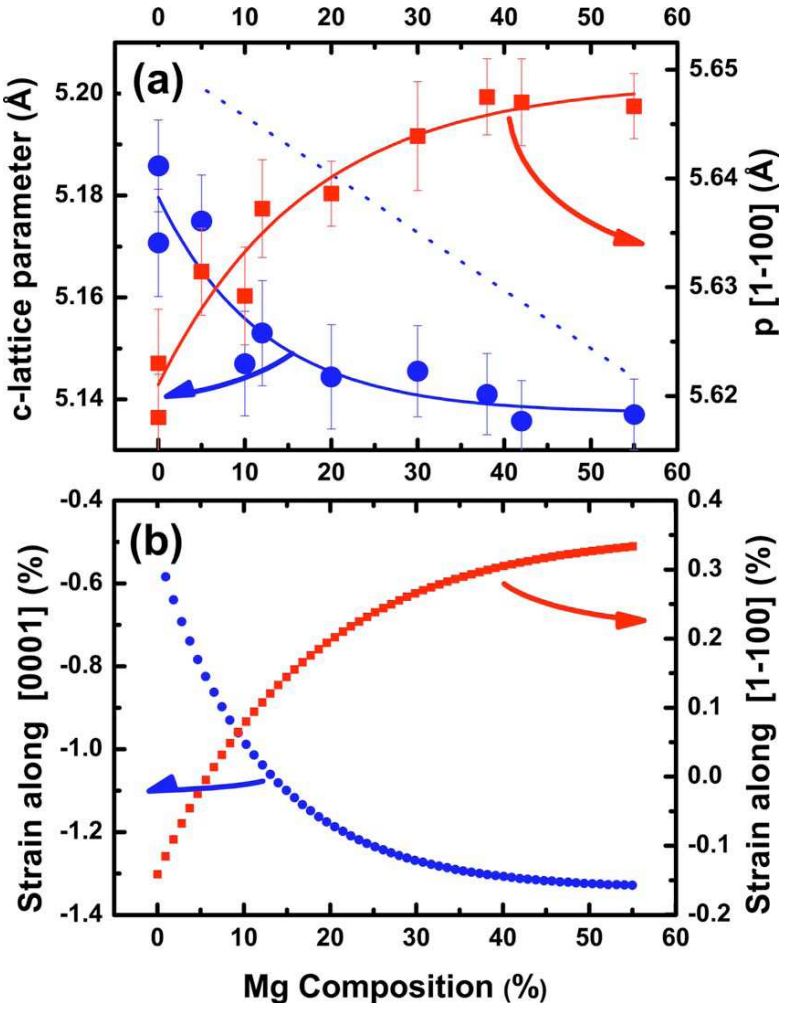

Figure III.4. Evolution of (Zn, Mg)O lattice parameters and strains with respect to the Mg content (adapted from ref.1).

Figure III. 4 shows the lattice parameters of (Zn,Mg)O layers strained on sapphire substrates as a function of Mg content, measured by XRD. In these measurements, an orthorhombic model was adapted. The in-plane periodicity along *m* [1-100] direction has a theoretical value of $\sqrt{3}a$ (Figure III. 4), where ***a*** is the lattice constant in the hexagonal system. When the Mg content is zero, *i.e.* a ZnO template, the lattice periodicity along *c* and *m* axis are 5.18 Å and 5.62 Å respectively, while those of a bulk ZnO are 5.207 Å and 5.629 Å. Therefore, compressive strains exist in the ZnO layer along both directions, which is desired to accommodate the compressive lattice mismatch with the sapphire substrate. In this case, the lattice mismatch between GaN and (Zn,Mg)O is shifted to higher values along both [0001] and [1-100] directions (Fig. III.2), owing to the compressive residual strain. Actually, the *c* lattice constant of the ZnO template (5.180 Å) is close to that of GaN (5.185 Å). When increasing the Mg content, the *c* lattice parameter continues to decrease, which leads to an even higher compressive lattice mismatch with GaN. On the other hand, the lattice parameter along [1-100] increases with the increasing Mg content, which leads to an increasing tensile lattice mismatch with GaN layer. Therefore, the lattice matching relation in the unstrained case (Fig. III. 2) is not valid anymore in the case of our (Zn,Mg)O templates, which are compressively strained on *r*-sapphire substrates along the [0001] direction, independent of the Mg concentration.

III.2. GaN layers grown on (Zn,Mg)O templates

III.2.1. Growth conditions of GaN

GaN layers have been grown by MBE on *a*-plane ($11\bar{2}0$) $Zn_xMg_{1-x}O$/*r*-sapphire templates. Ammonia (NH_3) is used as N source and the growths were carried out under N rich conditions.

The influence of the nucleation layer growth temperature on the GaN properties has been investigated. In this study, a series of identical (2x1) cm^2 ZnO templates were obtained from cutting a whole 2-inch wafer, consisting of a 200 nm thick ZnO layer grown on a *r*-sapphire substrate. 20 nm thick GaN layers were deposited on the ZnO templates at different growth temperatures, ranging from 525 to 725 °C.

Table III. **1** lists the structures and growth conditions of the samples investigated in this study. The surface morphologies of the GaN layers were studied by RHEED and AFM.

Sample	Template	GaN thickness	Growth temperature
N1636	200 nm ZnO /*r*-Sapphire	20 nm	525 °C
N1637	200 nm ZnO /*r*-Sapphire	20 nm	625 °C
N1638	200 nm ZnO /*r*-Sapphire	20 nm	700 °C
N1651	200 nm ZnO /*r*-Sapphire	20 nm	720 °C

Table III.1. Structures and growth conditions of GaN layers grown on ZnO / *r*-sapphire templates.

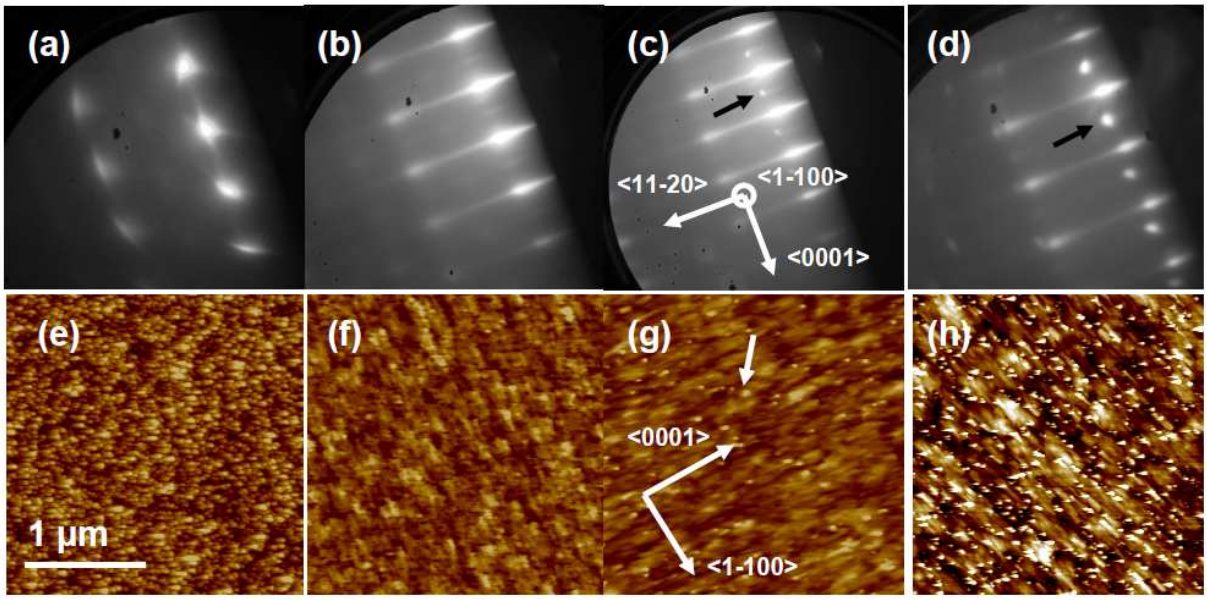

Figure III.5. RHEED patterns and surface morphologies of 20 nm thick GaN layers measured by AFM. The growth temperature were (a) (e) 525 °C, (b) (f) 625 °C, (c) (g) 700 °C and (d) (h) 720 °C, respectively. The vertical scales of the AFM image are 20 nm for (e) (h) and 10 nm for (f) (g).

Figure III. 5 shows the evolution of the GaN surface morphology with growth temperature. When the GaN layer was grown at 525 °C (sample N1636), the growth started and remained in a 3D mode, characterized by a spotty RHEED pattern (Fig III.6 (a)). Islands, with a diameter of ~ 20 nm are observed on the AFM image (Fig III.6 (e)), which leads to a surface *rms* roughness of ~ 4 nm. When the growth temperature was increased to 625 °C (sample N1637), the RHEED pattern gradually changed from a spotty pattern to streaky lines

after the initial growth of a 5 nm thick GaN layer. After the deposition of 20 nm, clear streaky lines are observed (Fig III.6 (b)), indicating that a 2D growth mode of the GaN layer was obtained. The *rms* roughness is reduced to ~ 1 nm (Fig III.6 (f)). When the growth temperature was increased to 700 °C (sample N1638), additional points progressively appeared in between the regular streaks in the RHEED pattern, which suggest the formation of disoriented GaN phases in the *a*-GaN matrix (Fig III.6 (c)). In the AFM image, small dots are observed on the GaN surface as indicated by the arrow in Fig III.6 (g). These grains are the origin of the additional points observed in the RHEED pattern. When the growth temperature was further increased to 720 °C, the intensity of the additional points in the RHEED pattern became higher (Fig III.6 (d)). Indeed, as shown in the AFM image, the density of grains increases significantly compared to the GaN layer grown at 700 °C, and the *rms* roughness increases to ~ 4 nm (Fig III.6 (h)). The average diameter of the grains is ~ 20 nm, which equals the GaN film thickness. The presence of these grains in the GaN layers will be discussed in detail in Section III.2.2.

Figure III. 6 shows the evolution of the GaN surface roughness as a function of the growth temperature. Surface areas of 5 x 5, and 10 x 10 μm^2 were scanned and the measured roughness is plotted with respect to the growth temperature. It is found that the roughness rms processes an ‘‘U’’ shape variation as the growth temperature increases. At low growth temperature, the GaN surface is rough due to the 3D growth and the formation of islands. The roughness reaches a minimum value of ~1 nm when the GaN layer is grown at 625 °C. If the temperature continues to increase, the roughness increases again due to the formation of disoriented phases. Therefore, a temperature range of 600 – 650 °C is found to be the growth window for the nucleation of GaN on *a*-plane ZnO layers.

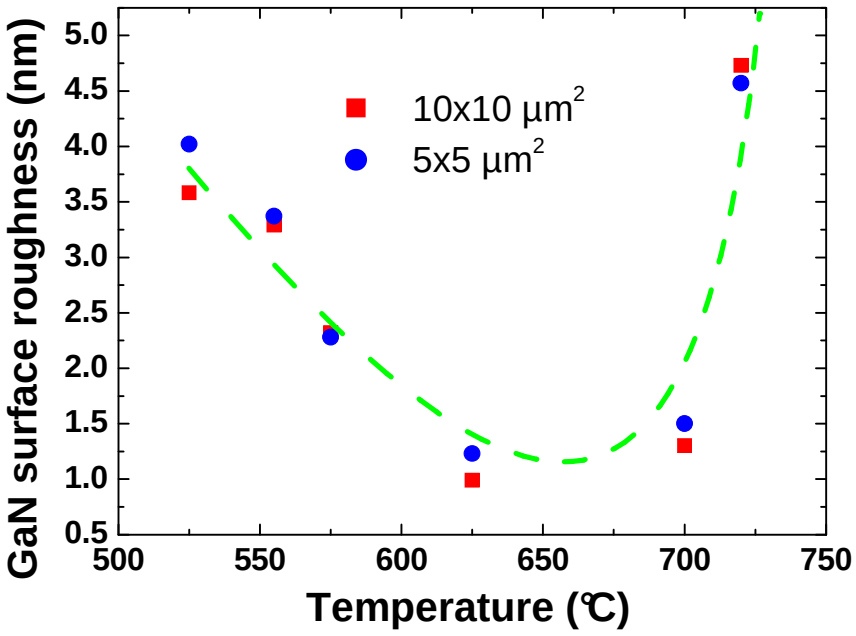

Figure III.6. Evolution of the GaN surface roughness rms as a function of the growth temperature.

Based on this study, a two step growth process was developed for the growth of thick GaN layers, and the scheme of the growth is shown in Figure III. 7. At first, a 100 nm thick GaN nucleation layer was deposited at low temperature (~600°C), to grow in a 2D growth mode and suppress the formation of disoriented phases. In the second step, a 900 nm thick GaN layer was deposited at 780 °C with a growth rate of ~ 0.3 µm/h, as a high temperature growth (~ 800 °C) is needed to grow GaN of high crystal quality[4].

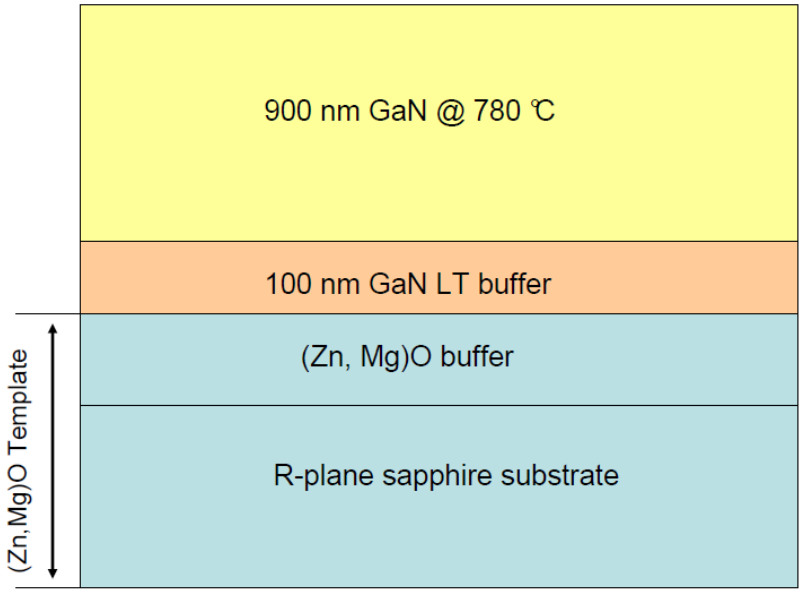

Figure III.7. Scheme of the two step growth of GaN on $Zn_{1-x}Mg_xO$/sapphire templates.

III.2.2. Structural properties of a-plane GaN layers grown on ZnO / Sapphire templates

After the growth, the surface morphologies of GaN layers were characterized by SEM and AFM. Figure III. 9 (a) shows a SEM image of a 1 µm thick GaN layer grown on a ZnO template. Stripes along the *c* [0001] direction are observed, and consequently a surface undulation is found along the *m* [1-100] direction. It is typical of *a*-GaN surfaces, and the formation of these stripes is due to the different GaN growth rates along the *c* [0001] and *m* [1-100] directions, as the growth rate along *c*-axis has been reported to be 2 – 4 times higher than that along *m*-axis.[5,6] Figure III. 9 (b) shows the surface morphology of the same GaN layer measured by AFM. Two grains are observed in the image. The surface *rms* roughness is 13 nm for a (10x10) μm^2 scan, which is directly related to the stripes on the surface. These stripes have an average length, width and height of 1.5 µm, 0.4 µm and 50 nm, respectively.

In addition, some cracks are also observed. They are all aligned along the *c* [0001] direction. This characteristic can be explained by the tensile lattice mismatch between GaN and ZnO templates along the *m* [1-100] direction (Fig.III.2). As a result, GaN layers are grown under tensile strain along this direction, which leads to the generation of cracks along the *c*-axis, as observed for $Al_xGa_{1-x}N$ grown on GaN.[7]

Besides the cracks, there is also the presence of microscopic defects on the surface. These defects are indicated by a cycle in Figure III. 9 (a) and (b). The density of these grains is as high as 5 x 10^6 / cm^2. The average size of these grains is ~ 1 µm, which is the same as the thickness of the GaN layer. The surface of GaN layers with thicknesses ranging from 20 nm to 1 µm have been systematically investigated by SEM, and Figure III. 8 shows the average diameter of the grains as a function of the GaN layer thickness. It indicates that the size of the grains increases linearly with the GaN thickness, with a coefficient of ~ 1. It suggests that they are formed during the nucleation stage of the GaN layer (Fig.III.5 (c)), and the growth rates of these grains along the in-plane directions and the growth direction are the same.

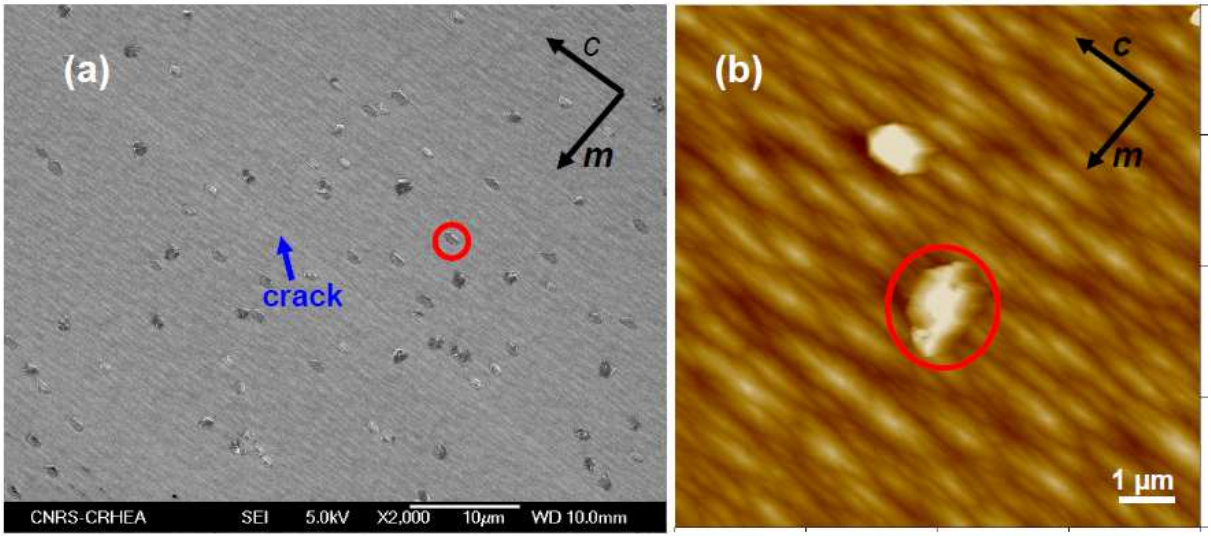

Figure III.8. (a) SEM image of an a-plane GaN surface; (b) surface morphology of GaN measured by AFM, the scan size is (10x10) μm^2 and the vertical scale is 150 nm.

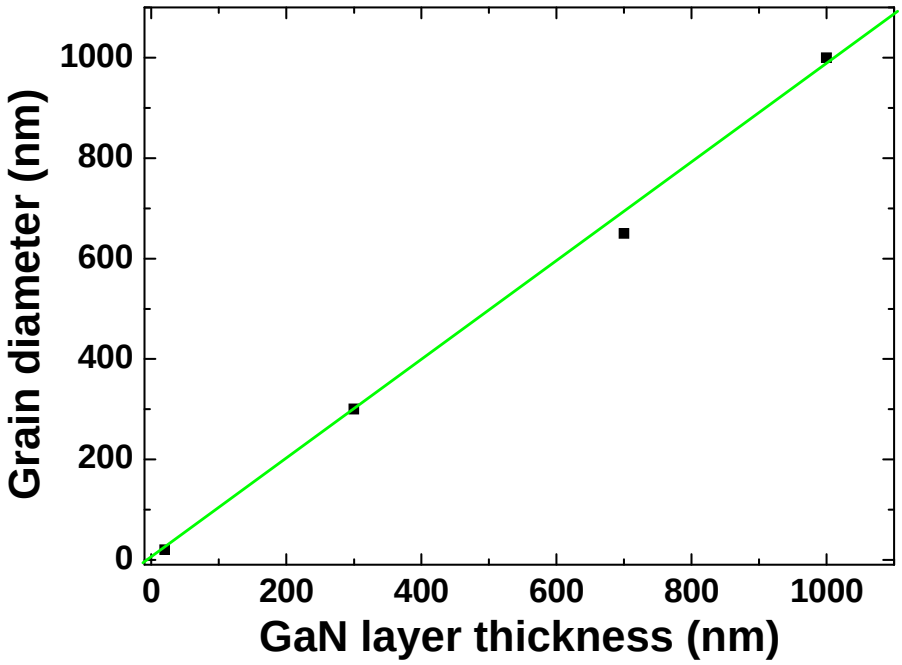

Figure III.9. Average diameter of the grains as a function of the GaN layer thickness. The solid line is a linear fitting curve.

To investigate the origin of these grains, as well as other structural properties of the GaN layer, TEM characterizations were carried out. Taking advantages of the same stacking sequence and very close lattice parameters between GaN and ZnO, their epitaxial relations is found along the same crystal axis: : $(0001)_{GaN} \parallel (0001)_{ZnO}$, $(11\bar{2}0)_{GaN} \parallel (11\bar{2}0)_{ZnO}$ and

$(10\bar{1}0)_{GaN} \| (10\bar{1}0)_{ZnO}$. Different types of defects can be identified in the high resolution plan view (zone axis [11-20]) image of the *a*-GaN layer. As shown in Figure III. 10, basal stacking faults (BSFs), prismatic stacking faults (PSFs), inversion domain boundaries (IDBs) and partial dislocations (PDs) are observed. The densities of these defects collected from different samples are listed in Table III. 2. The IDBs are formed along the c axis, and two domains with opposite polarities were identified at the two sides of the IDB. BSFs, with a density ranging from 4 x 10^5 to 1 x 10^6 / cm, are observed, and the defect planes are oriented perpendicular to the ***c*** axis. Vénneguès *et al* have analyzed the formation mechanism of BSF in wuztite layers grown along the *a* orientation (*a*-ZnO and *a*-GaN). The origin of the BSF has been mainly attributed to a Volmer Weber growth mode[8]:

-step 1: 3D nuclei are formed during the nucleation stage at least along one direction.

-step 2: BSFs are created in the coalescence boundaries of the islands in order to compensate translations between neighbouring islands.

The BSF planes have the same orientation with the coalescence boundaries, which is perpendicular to the growth plane.

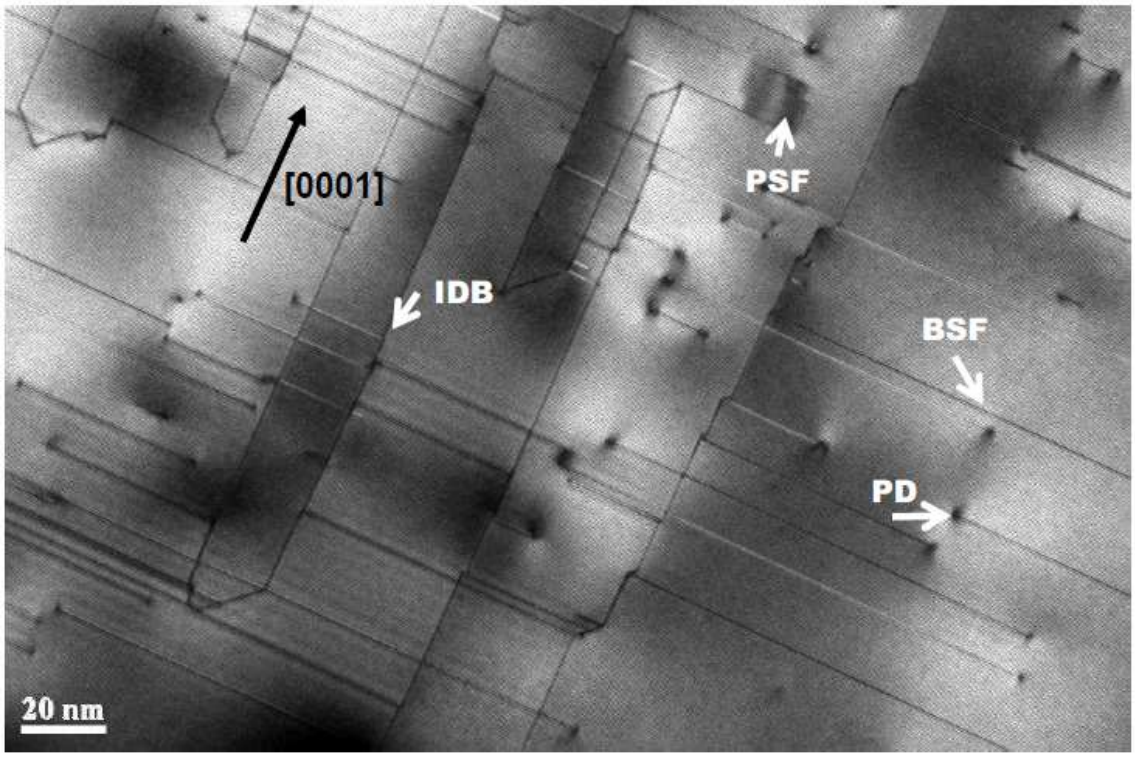

Figure III.10. TEM plan view image of an a-GaN layer grown on ZnO / sapphire (10-12).

Defect	ZnO template	GaN layer
BSF	1-2x10^5 cm^{-1}	4-10x10^5 cm^{-1}
PD	4-7x10^{10} cm^{-2}	9-20x10^{10} cm^{-2}
PSF		5-20x10^3 cm^{-1}
IDB		1.5x10^5 cm^{-1}

Table III.2. Summary of the average defect densities in the ZnO templates and the GaN epitaxial layers grown on top, measured by TEM.

Figure III. 11 displays a cross sectional TEM image of an *a*-GaN layer, where the microscopic grains observed on the GaN surface (Fig. III.9) can be identified more clearly. These grains are crystalline domains disoriented with the GaN epitaxial layer. Therefore, these defects will be referred as ‘‘disorientated grains’’ (DGs) in the following text. According to Fig. III.9, DGs are formed from the starting stage of the growth. Moreover, it is the growth conditions of the nucleation layer, in particular the growth temperature (Figure III. 5), which is the critical factor influencing the formation of DGs. It is worth noting that similar DG have also been observed in *a*-plane GaN layers grown on *a*-GaN / *r*-sapphire templates grown by MOCVD. The exact formation mechanism of the DGs is still not clear. Some semipolar oriented phases, which are also energetically favourable on *a*-ZnO (GaN) surfaces, may be an explanation. Further investigations are needed to understand their exact formation mechanism.

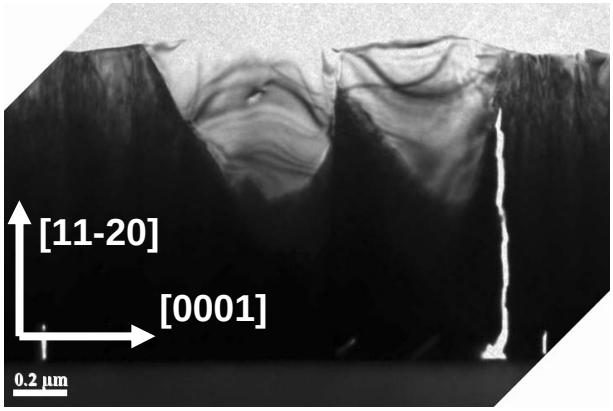

Figure III.11. Cross sectional TEM image of an *a*-GaN layer, observed along the [0001] direction.

XRD has also been used to investigate the GaN structural properties. Figure III. 12 shows the GaN 2θ/ω diagram. Only peaks related to GaN (11-20), ZnO (11-20) and sapphire (10-12) planes are observed. No peaks related to the presence of DGs are observed, which

suggests that they exhibit no particular crystal orientation close the [11-20] orientation of GaN. It indicates that the GaN layer is mainly *a* $[11\bar{2}0]$ oriented.

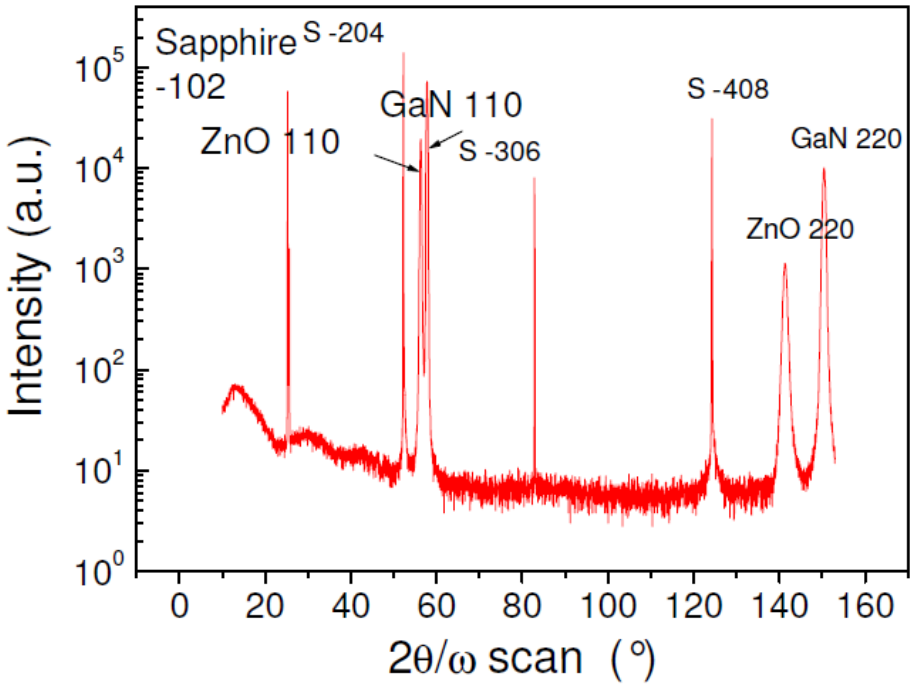

Figure III.12. GaN 2θ/ω diagram of an *a*-GaN layer grown on a ZnO / *r*-sapphire template.

Figure III. 13 shows the FWHM of the x-ray rocking curve (XRC) of the symmetric (11-20) diffraction of an *a*-GaN layer. Considering the in plane anisotropic characteristics of the layers, the XRC was recorded by varying the φ azimuthal angle of the sample from 0° to 360°, with a step of 15°, to perform a series of ω-scan on the GaN (11-20) reflection. When the incident x-ray beam is along the *c* [0001] direction of the GaN layer, the XRC has a minimum FWHM of 1550 arcsec; and when the incident beam is along the *m*-[1-100] direction, the XRD has a maximum FWHM of 2310 arcsec. This feature is observed in all the GaN layers grown along the [11-20] direction, independently of the growth conditions. It suggests that this anisotropic behaviour is related to the anisotropic nature of the growth, including the anisotropy of the lattice mismatch and the growth rate.

Several factors may contribute to the FWHM anisotropy of the GaN XRC. The first one is related to the tilt of the microstructures in *a*-GaN layer.[9] Different domain sizes along *m*- and *c*- axes is another important factor,[10] as the lateral coherence length is larger along *c*-axis than along *a*-axis. This anisotropy can be attributed to the formation of nuclei elongated along c-axis, due to the faster growth rate along *c* than along *m* direction. Besides, the presence of BSFs, which can be treated as boundaries between domains,[11] also contributes to

the shorter lateral coherence length along *m*, leading to the broadening of GaN XRCs along this direction.

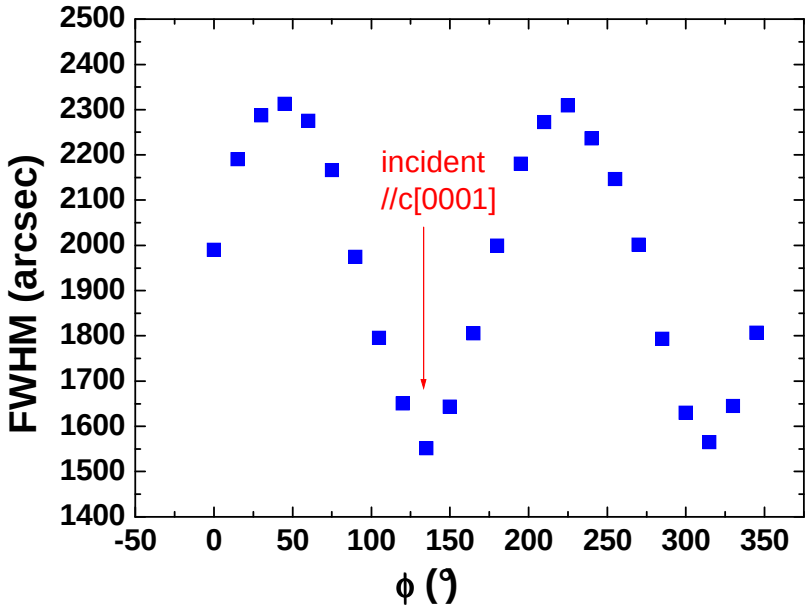

Figure III.13. X-ray rocking curve FWHM of the symmetric (11-20) diffraction of an *a*-GaN layer as a function of the φ azimuthal angle.

III.2.3. Influence of the Mg content in (Zn,Mg)O templates on the growth of GaN

To study the influence of the Mg content in (Zn,Mg)O templates on the growth of GaN layers, 1 µm thick GaN layers have been grown on a series of (Zn,Mg)O templates with a Mg content ranging from 0 to 52%. All the samples were grown under similar conditions, and the optimized two step growth mode was employed. It the first step, a 100 nm thick GaN layer was grown at ~ 620°C, followed by a 900 nm thick GaN layer grown at 780°C. However, the growth of GaN on a $Zn_{0.48}Mg_{0.52}O$ template was stopped at 600 nm, due to the observation of a completely spotty RHEED pattern.

After the growth, the surfaces of the GaN layers were characterized by SEM. All the layers exhibit similar morphologies, which correspond to the morphology observed on GaN layers grown on ZnO templates (Figure III. 8). However, in the particular case of the GaN layer grown on the $Zn_{0.48}Mg_{0.52}O$ template, the surface is covered by a high density of non-coalesced islands and no clear structural orientation preference can be observed (Figure III.

14). Therefore, it indicates that (Zn,Mg)O templates with too high Mg content ([Mg] >50%) are not suitable for the growth of GaN.

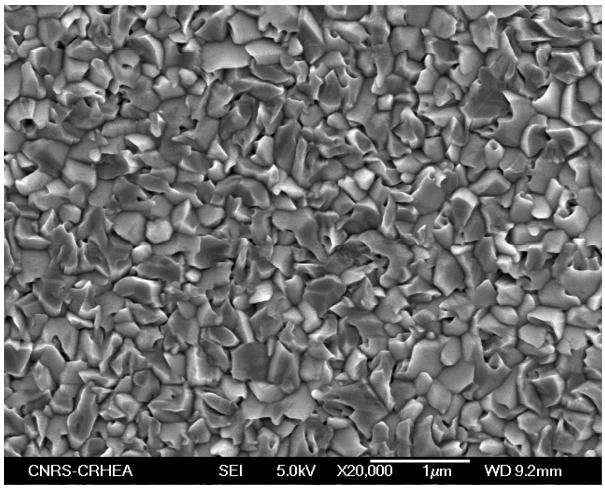

Figure III.14. SEM image of a 600 nm thick GaN layer grown on a $Zn_{0.48}Mg_{0.52}O$ template.

Figure III. 15 shows the surface morphologies of the (Zn,Mg)O templates and GaN layers grown on top. The comparison between Fig. III. 15 (a) and (c) indicates that the (Zn,Mg)O surface roughness is strongly improved for a $Zn_{0.64}Mg_{0.36}O$ template (rms ~ 3.4 nm) compared to a ZnO template (rms ~ 8.1 nm). As a result, a GaN layer with an improved surface roughness was obtained when growing on a $Zn_{0.64}Mg_{0.36}O$ template (Figure III. 15 (d)).

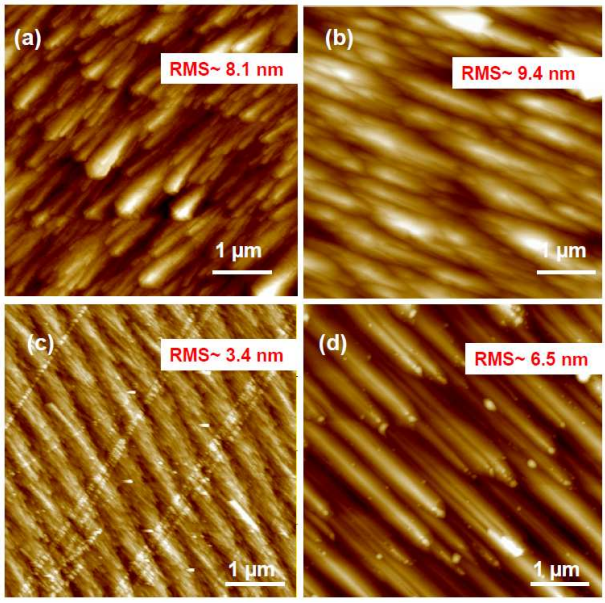

Figure III.15. AFM images of (a) a ZnO / r-sapphire template and (b) a GaN layer grown on the ZnO / r-sapphire template ; (c) a $Zn_{0.64}Mg_{0.36}O$ / r-sapphire template and (d) a GaN layer grown on the $Zn_{0.64}Mg_{0.36}O$ / r-sapphire template. The scan size is (5 x 5) µm^2, and the vertical scales are 80 and 40 nm for (a), (b) and (c), (d), respectively.

Figure III. 16 shows the density of the DGs observed on the GaN surfaces as a function of the Mg content in the (Zn,Mg)O templates. The use of (Zn,Mg)O templates, instead of ZnO, could strongly reduce the density of DGs in the GaN layers. Among the samples we have investigated, the GaN layer grown on the $Zn_{0.74}Mg_{0.26}O$ template has shown a minimum DG density of ~ 3 x 10^5 / cm^2. Yet, the reason why the DG density is reduced on (Zn,Mg)O templates is still not clear, but the difference in the lattice mismatch between GaN and (Zn,Mg)O, as well as the better thermal stability of (Zn,Mg)O alloys for increasing Mg concentrations, could be possible explanations.

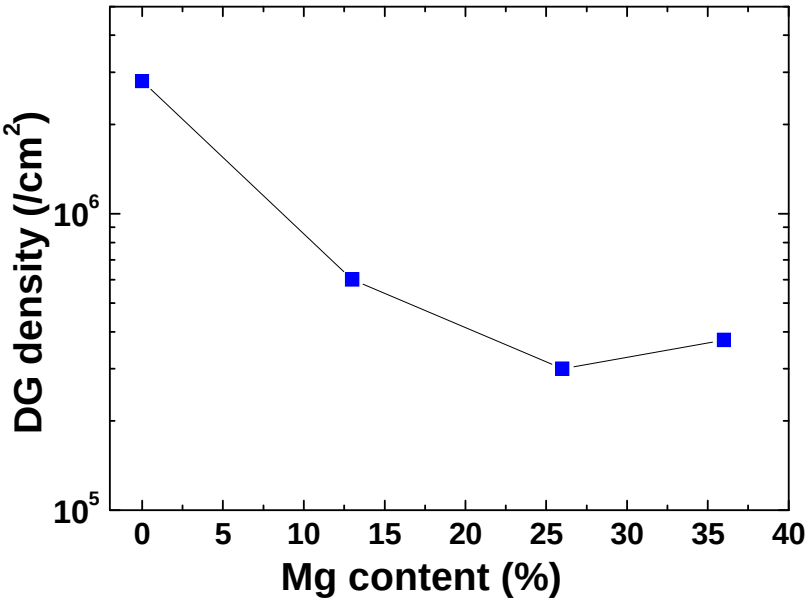

Figure III.16. Density of disorientated grains observed on GaN surfaces as a function of the Mg content in the (Zn,Mg)O templates.

Figure III. 17 compares the XRC FWHM of the (11-20) reflection for GaN layers grown on (Zn,Mg)O templates. The FWHM values decrease with increasing Mg content, for a Mg content lower than 36%. The GaN layer grown on $Zn_{0.64}Mg_{0.36}O$ has a minimum FWHM value for XRC of 960 arcsec when the incident beam is parallel to the *c* axis. It indicates that the crystal quality of GaN can be improved by the use of a (Zn,Mg)O template with a Mg content between 25 and 40%. However, the GaN layer grown on the $Zn_{0.48}Mg_{0.52}O$ template shows much larger XRC FWHM values. It means that the crystal quality is degraded if the Mg content is too high. It can be explained by the degraded (Zn,Mg)O crystal quality and the large lattice mismatch with GaN (Figure.III.2), for Mg concentrations above 50%.

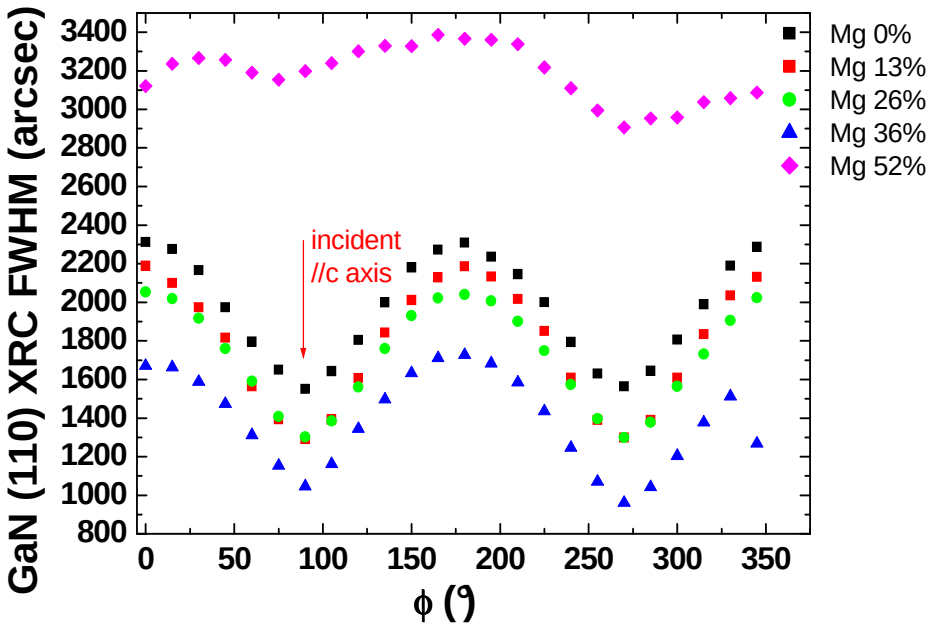

Figure III.17. XRC FWHM values of the symmetric (11-20) diffraction of a-GaN layers as a function of the φ azimuthal angle, grown on a series of (Zn,Mg)O templates with different Mg content.

To conclude, GaN layers have been grown on a series of (Zn,Mg)O templates, and the surface morphologies, as well as the structural properties have been characterized by AFM, SEM, and XRD. The use of (Zn,Mg)O templates could help reduce the DG density, improve the surface morphology and the overall quality of the crystal. However, it is not suitable for the growth of GaN when the Mg content is higher than 50%. (Zn,Mg)O templates with a Mg content ranging from 25% to 40% are found to be the best suited for the growth of GaN.

III.2.4. GaN lattice parameters

The lattice parameters of the GaN layers could be measured by XRD. In this measurement, the *2θ* positions of a series of reflections, including the symmetrical (11-20) plane, and the asymmetrical (20-20) and (11-22) planes, were measured precisely using an analyzer crystal.

Due to the in-plane anisotropic lattice mismatch between ZnO and sapphire (introduced in Section I.1.2.b) and anisotropic relaxation mechanisms,[12] there is an anisotropic residual strain in the (Zn, Mg)O layers.[1] As a consequence, the GaN layers grown on these templates exhibit anisotropic in-plane strain, induced by the compressive lattice mismatch along *c* [0001] and the tensile lattice mismatch along *m* [1-100] (Section III.1).

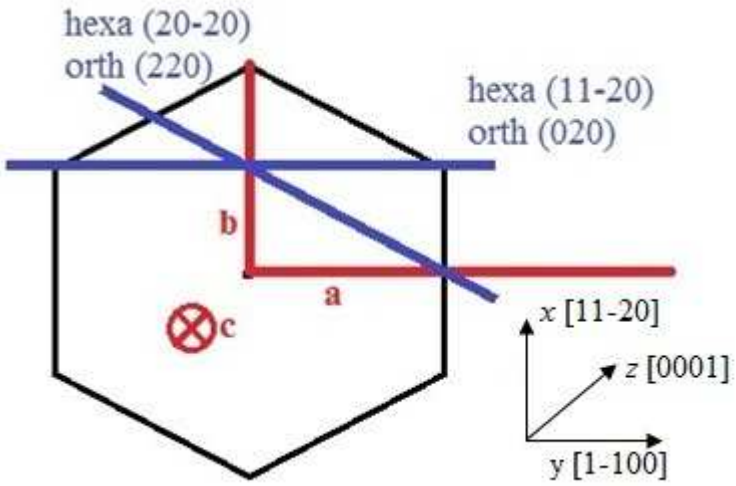

Figure III.18. Illustration of the orthorhombic crystal system and the coordinate system used in this chapter, from the top view of the basal plane.

As the crystal point group of GaN is reduced from hexagonal (C_v^6) to orthorhombic (C_v^2), the lattice parameters of the a-GaN layers are calculated based on the orthorhombic model, following the method introduced in Section II.5.2. The coordinate system is illustrated in Figure III. 18: the ***x*** axis is along the growth direction, ***y*** and ***z*** are two in-plane directions, with ***z*** along the c axis of GaN. Table III. 3 lists the lattice parameters (LPs) of the GaN layer grown on three different types of templates. The average LPs of the GaN layers were calculated to facilitate the discussion. By comparing the measured LPs with the standard values of GaN bulk crystals and $Zn_{0.8}Mg_{0.2}O$ templates, a tensile strain of $\varepsilon_{yy} = 0.2\%$ along the ***a*** axis (*i.e.*, *m* [1-100] direction in the hexagonal system) and a compressive strain of $\varepsilon_{zz} = -0.06\%$ along the ***c*** axis are found in the GaN layers. The strains along these two in-plane directions are directly related to the lattice mismatch between GaN and the (Zn, Mg)O templates (Figure.III.2).

According to the in-plane strain values ε_{yy} and ε_{zz}, a compressive strain of $\varepsilon_{xx} = -0.06\%$ along the ***b*** axis (the growth direction) can be deduced from Eq I.10. Based on the XRD measurements, a compressive strain of $\varepsilon_{xx} = -0.08\%$ is detected, which is very close to the calculated results. It indicates that the compressive strain along the growth direction mainly arises from Poisson effect.

Sample	Template structure	GaN structure	$\boldsymbol{a}$ ($\overset{o}{A}$) (in plane)	$\boldsymbol{c}$ ($\overset{o}{A}$) (in plane)	$\boldsymbol{b}$ ($\overset{o}{A}$)	$\boldsymbol{b}$ ($\overset{o}{A}$) calculated
N1606	ZnO 180 nm /sapphire	1µm GaN	5.5341	5.1839	3.1860	3.1875
N1653	$Zn_{0.74}Mg_{0.26}O$ 1,4µm/ sapphire	1µm GaN	5.5327	5.1811	3.1870	3.1877
N1704	$Zn_{0.87}Mg_{0.13}O$ 200nm/ sapphire	1µm GaN	5.5384	5.1817	3.1864	3.1863
GaN layer average values			5.5351	5.1822	3.1865	
Bulk GaN[13]			5.5235	5.185	3.189	
$Zn_{0.8}Mg_{0.2}O$/ sapphire[1]			5.64	5.14		
Bulk ZnO[14]			5.6292	5.207	3.250	

Table III.3. Lattice parameters of the GaN layers grown (Zn,Mg)O templates. The lattice parameters of bulk GaN, ZnO and $Zn_{0.8}Mg_{0.2}O$ template[1] are also listed for comparison.

III.2.5. Optical properties of a-plane GaN layers grown on (Zn,Mg)O / r-sapphire templates

The optical properties of the GaN layers were investigated by photoluminescence measurements. The low temperature (14 K) PL spectrum of a 1 µm GaN layer grown on a $Zn_{0.7}Mg_{0.3}O$ template, excited by a He Cd laser at 325 nm, is shown in Figure III. 19. The main emission peak at 3.477 eV is attributed to the near band edge (NBE) emission of GaN. At low temperature, the NBE is dominated by the donor bound exciton (DBE) emission, with a FWHM of 15 meV.

The peak at 3.42 eV is related to the basal stacking faults (BSFs) in the GaN layer.[15,16,17] There are usually a high density of BSFs in a-plane GaN layers.[16] In the GaN layers grown on (Zn,Mg)O templates, the density of BSF is found to be in the range of 4-10 x 10^5 / cm (Table III. 2). The BSF can be regarded as a thin zincblende layer embedded in the wurtzite crystal. The 3.42 eV emission is attributed to the recombination between the electrons confined in the zincblende layer with the holes in the wurtzite structure.[16]

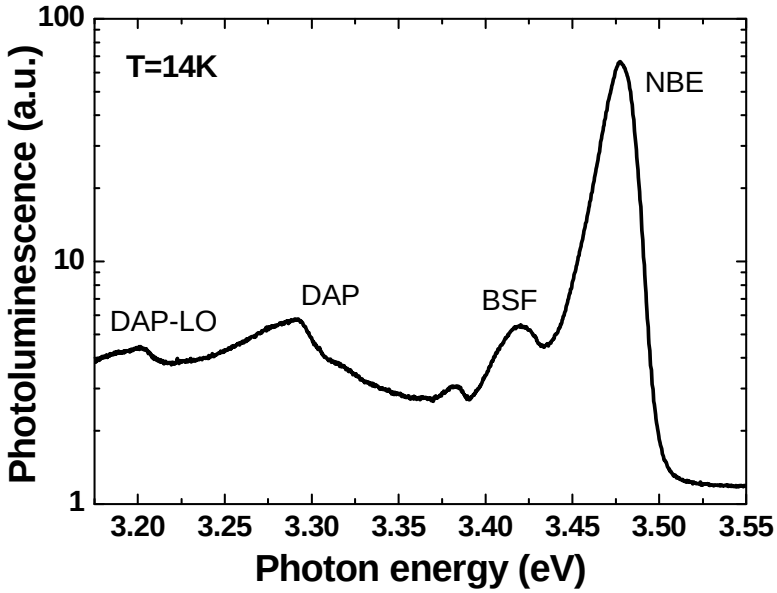

Figure III.19. PL spectra of a 1 µm thick GaN layer grown on a $Zn_{0.7}Mg_{0.3}O$ template. The sample was excited by a 325 nm He Cd laser at 14K.

The emission peak at 3.285 eV arises from the recombination of donor acceptor pairs (DAPs). The large line width of this peak is due to a wide range of spatial distribution of the donors and acceptors. In addition, the DAP emission is accompanied by a sub-peak of ~ 90 meV lower in energy, which comes from the longitudinal optical (LO) phonon replica of the DAP emission. The Huang-Rhys factor of this coupling is ~ 0.58. This is a typical characteristic of the DAP emission, as the localized carriers recombination is always accompanied with a strong lattice phonon coupling.[18]

Figure III. 20 shows the variation of the band edge emission energy of the GaN layer as a function of temperature. In the low temperature range (T < 50 K), the emission energy increases with temperature, and it can be explained by the thermal activation of the donor bound exciton to free exciton. When the temperature is above 50 K, the evolution of the emission energy obeys to the Varshni equation (Eq. I.9). The energy variation curve was fitted using the Varshni equation: the FE emission energy at 0 K was found to be 3.484 eV, and the fitting parameters are α = 1 x 10^{-3} and β = 1068.5. These values are within the range of the reported values for GaN grown on sapphire.[16,19] The neutral donor binding energy of 6 meV can be deduced by comparing the low temperature emission energy with the fitting curve. This value coincides with the reported values from both *a*- and *c*-plane GaN.[16,19]

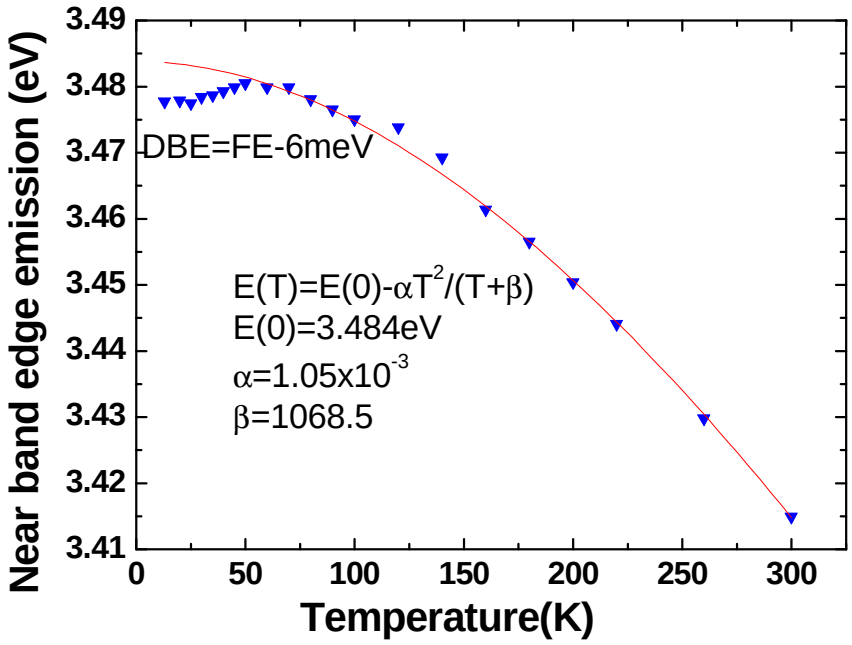

Figure III.20. Temperature dependence of the GaN near band edge emission energy, fitted by the Varshni equation (solid line).

As introduced in Section I.3, due to the broken in-plane rotational symmetry by the inclination of the *c* axis in the growth plane, the band edge emission of the nonpolar GaN layer is usually polarized. Therefore, two GaN layers grown on (Zn,Mg)O templates, N1653 and N1704, were chosen for the optical polarization study. Figure III. 21 shows the integrated PL intensity of the GaN NBE emission as a function of the **E** polarization angle, and these values have been averaged between each two polarization directions with 180° difference in angle, in order to limit the artifacts due to the polarizer.. The GaN NBE emissions of N1653 and N1704 are both polarized with **E** parallel to *c* axis ([0001]). According to Eq I.28, the polarization degree along **E**//c is deduced to be $P_{//c} = 0.23$ for sample N1704, which is higher than that of sample N1653 ($P_{//c} = 0.08$).

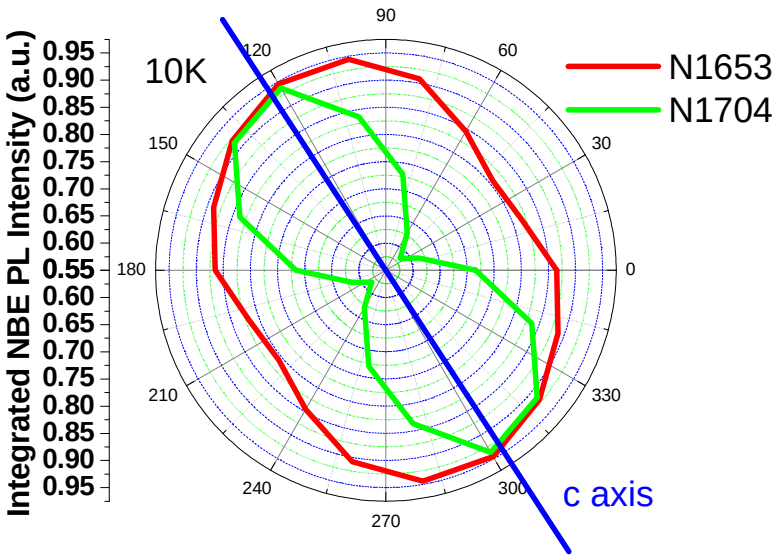

Figure III.21. Integrated PL intensity of the GaN near band edge emission as a function of the polarization angle. The integration range for the PL spectra is 3.45eV-3.54eV.

To understand the polarization behaviour of the GaN NBE emission, the oscillator strengths between the conduction band and the three sub-valence bands have been simulated using the **k•p** method introduced in Section I.2.[20] It deserves to be noticed that due to the reduced crystal symmetry, the common optical selection rules for unstrained or strained GaN layers grown on *c*-plane are no longer valid for *a*-plane GaN layers.

The residual strains in GaN layers have been measured in Section III.2.4. Deformation potentials provided by Ishii *et al.*[21] are adapted for the calculation of the transition matrix elements (Table I. 3). The simulated transition matrix elements along the three orthogonal directions are listed in Table III. 4 (the orientations of ***x***, ***y*** and ***z*** axes are illustrated in Fig. III. 18). It is found that the polarization properties of each exciton are very sensitive to the strain values. N1653 and N1704 show very similar polarization behaviours.

Exciton	N1653 (GaN/ $Zn_{0.74}Mg_{0.26}O$)				N1704 (GaN/ $Zn_{0.87}Mg_{0.13}O$)			
	Energy (eV)	*x* <11-20>	*y* <1-100>	*z* <0001>	Energy (eV)	*x* <11-20>	*y* <1-100>	*z* <0001>
X_1	3.474	0.857	0.053	0.089	3.464	0.859	0.023	0.118
X_2	3.483	0.005	0.451	0.544	3.475	0.046	0.283	0.671
X_3	3.450	0.138	0.495	0.368	3.492	0.095	0.694	0.211

Table III.4. Simulated oscillator strengths and transition energies of X_1, X_2, and X_3 excitons of samples N1653 and N1704, along three orthogonal directions, respectively.

The main component of X_1 exciton is polarized along the growth direction (***x*** axis). When the electric field **E** is oscillating along the ***x*** direction, the emitted light is hardly detected along the surface normal as the wave propagates along the in plane directions.[22] Therefore, the X_1 exciton should have a very weak contribution to the PL emission. The X_2 exciton has the highest oscillator strength when **E** is oscillating along the ***z*** direction. It means that the emission from X_2 recombination is polarized parallel to the *c* axis. Together with the experimental observations, it can be concluded that the GaN NBE emission mainly arises from the X_2 exciton recombination, which is polarized parallel to the *c* axis. The polarization degree of X_2 exciton along **E** // c are 0.09 and 0.40 for N1653 and N1704, respectively, which are very close to the experimental observations.

The measured NBE energies are 3.474 eV for N1653 and 3.477 eV for N1704, respectively. Taking into account the donor binding energy, which is ~ 6 meV according to Fig. III. 20, the free exciton emission energies are deduced to be 3.480 eV for sample N1653 and 3.483 eV for sample N1704. These values are very close to the simulated X_2 exciton recombination energies for both samples, which support the conclusion that the NBE mainly arises from the X_2 exciton.

III.3. a-plane (Al, Ga)N / GaN MQWs grown on (Zn,Mg)O / r-sapphire templates

III.3.1. Growth conditions and structural characterizations

Six MQWs were grown on (Zn, Mg)O / sapphire templates. Three different types of templates were used, with different (Zn, Mg)O buffer layer thicknesses and Mg contents. Following the growth of the 1-µm thick GaN buffer layer (Section III.2.1), a series of $Al_{0.2}Ga_{0.8}$ N / GaN MQWs were fabricated. The MQW structure consists of three identical GaN QWs separated by 30 nm-thick $Al_{0.2}Ga_{0.8}N$ barriers. The GaN well widths range from 0.5 to 7 nm. Table III. 5 lists the structures of the six MQWs.

Sample name	Template structure	GaN structure	MQW barrier	Well thickness
N1608	ZnO 180 nm /sapphire	1µm GaN	$Al_{0.2}Ga_{0.8}N$ 30 nm	GaN 1 nm
N1660	$Zn_{0.74}Mg_{0.26}O$ 1,4µm/ sapphire	1µm GaN	$Al_{0.2}Ga_{0.8}N$ 30 nm	GaN 2 nm
N1662	$Zn_{0.74}Mg_{0.26}O$ 1,4µm/ sapphire	1µm GaN	$Al_{0.2}Ga_{0.8}N$ 30 nm	GaN 3 nm
N1690	$Zn_{0.87}Mg_{0.13}O$ 200nm/ sapphire	1µm GaN	$Al_{0.2}Ga_{0.8}N$ 30 nm	GaN 7 nm
N1692	$Zn_{0.87}Mg_{0.13}O$ 200nm/ sapphire	1µm GaN	$Al_{0.2}Ga_{0.8}N$ 30 nm	GaN 5 nm
N1693	$Zn_{0.87}Mg_{0.13}O$ 200nm/ sapphire	1µm GaN	$Al_{0.2}Ga_{0.8}N$ 30 nm	GaN 0.5 nm

Table III.5. Structures of (Al,Ga)N / GaN MQWs grown on (Zn,Mg)O templates.

Sample N1608 is grown on a template made of a 180 nm thick ZnO buffer layer. Samples N1660 and N1662 are grown on templates made of 1.4 µm thick $Zn_{0.74}Mg_{0.26}O$ buffer layers, and samples N1690, N1692 and N1693 are grown on templates made of 200 nm thick $Zn_{0.87}Mg_{0.13}O$ buffer layers.

The Al content in the barrier is measured by energy-dispersive X-ray spectroscopy (EDX). An average Al content of 20% was measured, with a variation of ± 3%.

The surface morphologies of the MQWs were characterized by SEM and AFM. Figure III. 22 (a) shows the image of the surface of sample N1692 recorded by SEM. Cracks oriented along the *c* [0001] direction are observed, and the average distance between them is 15 µm. There is also presence of the DGs, with an average diameter of ~ 1 µm. From the AFM image (Figure III. 22 (b)), stripes oriented along the [0001] direction are observed, and the surface *rms* roughness is 8.6 nm.

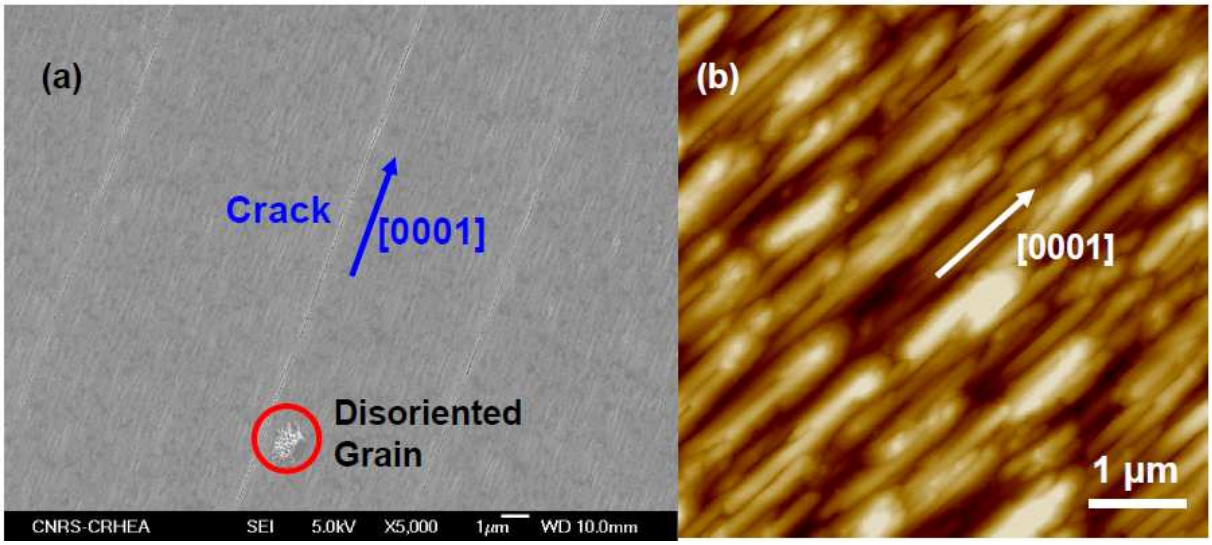

Figure III. 22. (a) SEM and (b) AFM images of the surface of sample N1692. The scan size for the AFM image is 5 x 5 µm2, and the vertical scale is 50 nm.

The lattice parameters of the GaN layers in the MQW heterostructures have been calculated following the method introduced in Section III.2.3 and listed in Table III. 6. The crystal axes related to the lattice constants ***a***, ***b***, and ***c*** are illustrated in Figure III. 18.

sample	layer	a ($\overset{o}{A}$) (in plane)	c ($\overset{o}{A}$) (in plane)	b ($\overset{o}{A}$)
N1608	GaN 1µm +MQWs	5.5234	5.1752	3.1889
N1662	GaN 1µm +MQWs	5.5132	5.1734	3.1909
N1692	GaN 1µm +MQWs	5.5248	5.1837	3.1884
N1693	GaN 1µm +MQWs	5.5154	5.1807	3.1885
N1690	GaN 1µm +MQWs	5.5252	5.1904	3.1883
MQW layers average values		5.5204	5.181	3.189
GaN layers average values		5.5351	5.1822	3.1865
$Al_{0.2}Ga_{0.8}N$		5.496	5.1444	3.173
Bulk GaN		5.5235	5.185	3.189

Table III. 6. Lattice parameters of the (Al,Ga)N / GaN heterostructures.

To facilitate the discussion, the lattice parameters (LPs) of the GaN layers in the MQWs have been averaged, and they are compared with the averaged 1 µm thick GaN layer LPs listed in Table III. 6. The LPs of $Al_{0.2}Ga_{0.8}N$ are deduced from Vegard's law and bulk GaN LPs are also listed as references. Contrary to thick GaN layers, GaN layers in the MQWs

have an average compressive strain of - 0.06% along the *m* [1-100] direction. This result indicates that the GaN QW layers are strained on the relaxed $Al_{0.2}Ga_{0.8}N$ barriers, which have smaller LPs than GaN.

III.3.2. Optical properties of the (Al,Ga)N / GaN MQWs

Photoluminescence (PL) spectra of the MQW heterostructures were recorded by a multi channel Si detector, under the excitation of a double frequency Ar^+ laser at 244 nm. Figure III. 23 shows the normalized PL spectra of the MQWs. The barrier luminescence is observed at 3.81 eV, which indicates an Al composition of ~ 20%,[19] coinciding with the measured Al content using EDX. The main emission peak originates from the recombination of carriers in the MQWs. The peaks arising from the MQWs with different well thicknesses are well resolved. Their transition energies increase when the QW width decreases. The 0.5 nm MQW exhibits a total confinement energy of 290 meV. The FWHM of the PL peaks ranges from 50 meV to 90 meV. Moreover, the MQW PL peaks are all found at energies larger than the energy of a reference 1-µm thick GaN layer grown on a (Zn,Mg)O / r-sapphire template.

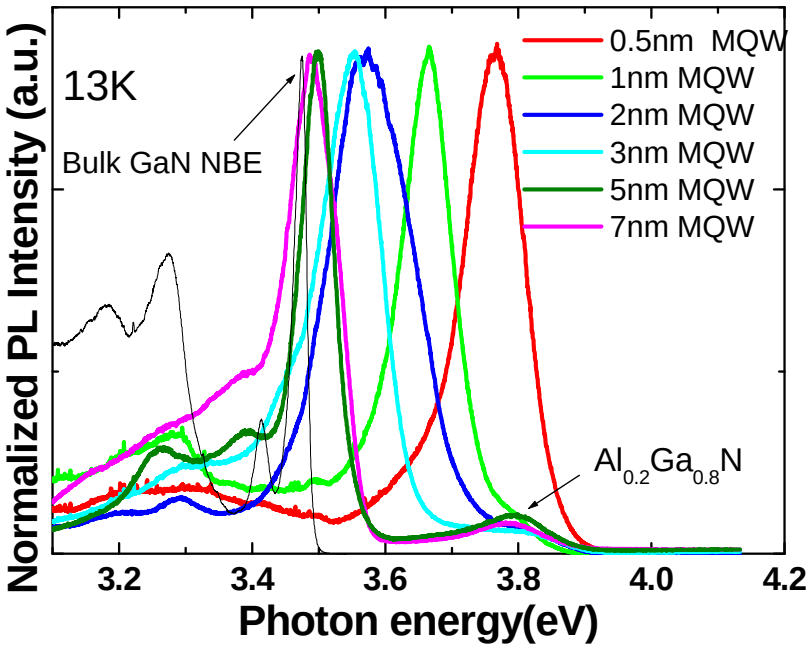

Figure III. 23. PL spectra at 13 K of a-plane Al0.2Ga0.8N / GaN MQWs for various well widths. The black line indicates the near band edge (NBE) emission of a 1-µm thick GaN layer.

Excitation power dependent PL measurements were performed on the MQWs, and an optical density was placed in front of the laser beam to adjust the excitation power. Figure III. 24 shows the excitation dependence of the PL spectrum of sample N1692. In our *a*-plane MQWs, no emission energy shift was detected when varying the excitation power from 20 mW to 20 µW. It indicates that there is no carrier screening effect, which is a further evidence of the absence of internal electric field along the growth direction. Indeed, in the polar case, a blue shift of the QW emission is observed when the PL excitation power increases, due to the screening of interfacial charges by the increasing carrier density.[23] These results indicate the absence of QCSE in the $Al_{0.2}Ga_{0.8}N$ / GaN MQWs grown on a-plane (Zn, Mg) O templates.

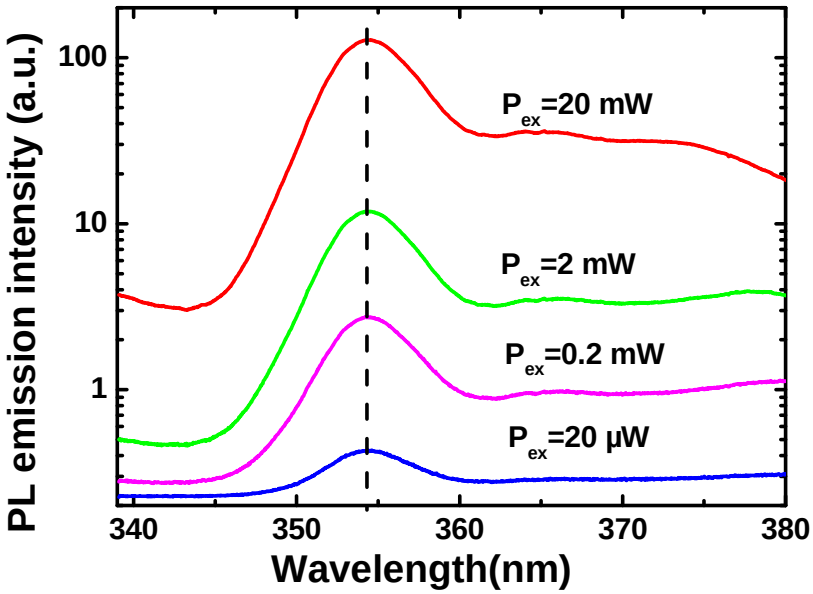

Figure III. 24. Excitation dependence of the MQW PL spectra from sample N1692.

Figure III. 25 shows the MQW transition energies as a function of the well width. The results from $Al_{0.17}Ga_{0.83}N$ / GaN QWs grown on *c*-plane sapphire substrates (Ref. 24) are also shown for comparison. For thick polar QWs (thickness > 3nm), the polar QW emission lies below the GaN band gap owing to the QCSE while the non-polar QW emissions are always measured above it. Therefore, it suggests that the internal electric field is absent in the *a*-plane MQWs.

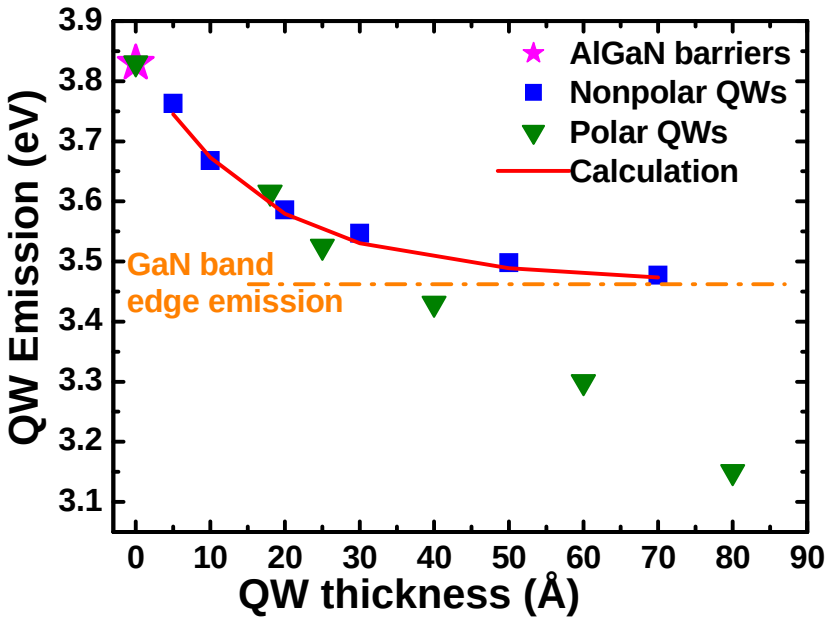

Figure III. 25. Transition energies of a-plane Al0.2Ga0.8N/GaN MQWs versus the well width (full squares), compared with c-plane Al0.17Ga0.83N/GaN QWs from [24] (full triangles) and square well calculations (continuous line).

The QW confinement energies of electrons (E_e) and holes (E_h) as a function of the quantum well thickness are calculated based on the analytical solutions of a 1D finite barrier QW model, and the detailed calculations can be found in Appendix I.

The non-homogeneities of Al content, well thickness, and/or strain lead to localized states, which are important to be taken into account in the calculation. Figure III. 26 shows the temperature dependence of the MQW transition energy of sample N1692. In the low temperature range, the transition energy raise with the increasing temperature, up to 120 K, which is attributed to the thermal activation of excitons from localized states to free states. The other MQWs have similar temperature dependent behaviours. The localization energy (E_L) was measured in the range of ~ 30 ± 5 meV in the MQWs.

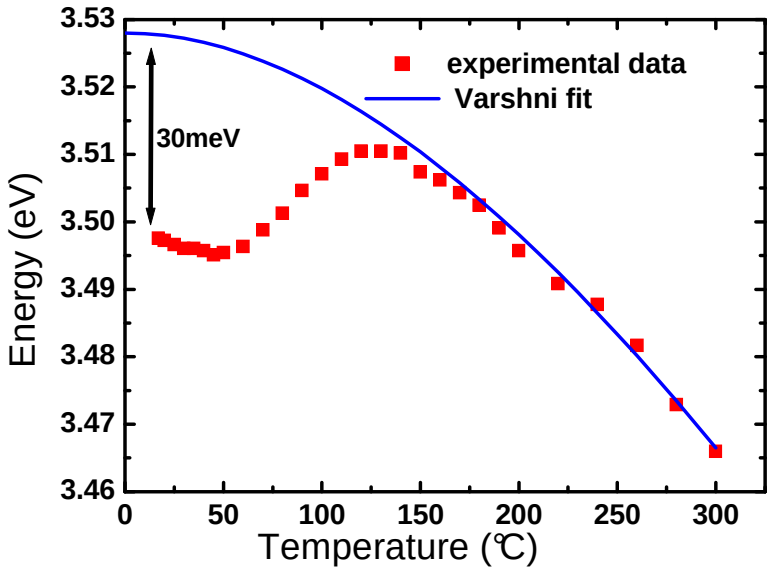

Figure III. 26. MQW transition energy of the 5 nm well thickness sample (N1692) as a function of temperature (dotted line). The experimental curve is fitted using Varshni's equation (solid line).

The quasi-2D exciton binding energy (E_{Ry}) was calculated following the approach developed by Leavitt and Little.[25]

Finally, the QW transition energy is determined by:

$$E = E_{GaN} + E_e + E_h - E_L - E_{Ry}. \qquad \textbf{(III. 1)}$$

where E and E_{GaN} are the final transition energy and the GaN band gap energy, respectively. Note that when an internal electric field is present in the QW, an additional term ($-eE_{\text{int}}L$) corresponding to the QCSE related energy drop has to be considered in Eq. III. 1. The calculated results are plotted in Figure III. 25 (solid line). One can notice the very good agreement between the experimental data and the calculated transitions, which provides another evidence of the absence of QCSE in the non-polar heterostructures.

III.4. Conclusions

A series of a-plane GaN layers are grown on (Zn,Mg)O / *r*-sapphire templates. The a-GaN layers show anisotropic structural and optical properties. (Zn,Mg)O templates with Mg content ranging from 25% to 40% are found to be most suitable for the growth of GaN. The GaN NBE emission dominates the PL spectrum and the emission is polarized parallel to the [0001] direction, which mainly arises from the X_2 exciton recombination. A group of

$Al_{0.2}Ga_{0.8}N$ / GaN MQWs are fabricated based on the *a*-GaN layers. The QW transitions are studied by PL, and the absence of QCSE is demonstrated.

References

[1] J.-M. Chauveau, J. Vives, J. Zuniga-Perez, M. Laügt, M. Teisseire, C. Deparis, C. Morhain, and B. Vinter, Appl. Phys. Lett. **93**, 231911 (2008).

[2] J-M Chauveau, M Laugt, P Vennégues, M Teisseire, B Lo, C Deparis, C Morhain, and B Vinter, Semicond. Sci. Technol. **23**, 035005 (2008).

[3] W. I. Park, Gyu-Chul Yi, and H. M. Jang, Appl. Phys. Lett. **79**, 2022 (2001).

[4] N. Grandjean, J. Massies, P. Vennégues, M. Leroux, and F. Demangeot, J. Appl. Phys. **83**, 1379 (1998).

[5] C.Q. Chen, J.W. Yang, H.M. Wang, J.P. Zhang, V. Adivarahan, M. Gaevski, E. Kuokstis, Z. Gong, M. Su, and M.A. Khan, Jpn. J. Appl. Phys. **42**, L640 (2003).

[6] X. Ni, Y. Fu, Y. T. Moon, N. Biyikli, and H. Morkoç, J. Crystal Growth **290**, 166 (2006).

[7] J. M. Bethoux, Ph. D thesis. CRHEA (2004).

[8] P. Vennégues, J. M. Chauveau, Z. Bougrioua, T. Zhu, D. Martin, and N. Grandjean, J. Appl. Phys. **112**, 113518 (2012).

[9] Q. Sun, T.-S. Ko, C. D. Yerino, Y. Zhang, I.-H. Lee, J. Han, T.-C. Lu, H.-C. Kuo, and S.-C. Wang, Jpn. J. Appl. Phys. **48**, 071002 (2009).

[10] R. Chierchia, T. Bottcher, H. Heinke, S. Einfeldt, S. Figge, and D. Hommel, J. Appl.Phys **93**, 8918 (2003).

[11] M. B. McLaurin, A. Hirai, E. Young, F. Wu, and J. S. Speck, Jpn. J. Appl. Phys. **47**, 5429 (2008).

[12] J.-M. Chauveau, P. Vennégues, M. Laugt, C. Deparis, J. Zuniga-Perez, and C. Morhain, J. Appl. Phys. **104**, 073535 (2008).

[13] I. Vurgaftman and J. R. Meyer, J. Appl. Phys. **94**, 3675 (2003).

[14] H. Karzel, W. Potzel, M. Köfferlein, W. Schiessl, M. Steiner, U. Hiller, G. M. Kalvius, D. W. Mitchell, T. P. Das, P. Blaha, K. Schwarz, and M. P. Pasternak, Phys. Rev. B **53**, 11425 (1996).

[15] R. Liu, A. Bell, F. A. Ponce, C. Q. Chen, J. W. Yang, and M. A. Khan, Appl. Phys. Lett. **86**, 021908 (2005).

[16] P. P. Paskov, R. Schifano, B. Monemar, T. Paskova, S. Figge, and D. Hommel, J. Appl. Phys. **98**, 093519 (2005).

[17] T. Gühne, Z. Bougrioua, P. Vennégues, M. Leroux, and M. Albrecht, J. Appl. Phys. **101**, 113101 (2007).

[18] H. Zhao and H. Kalt, Phy.Rev. B **68**, 125309 (2003).

[19] M. Leroux, N. Grandjean, B. Beaumont, G. Nataf, and F. Semond, J. Appl. Phys. **86**, 3721 (1999).

[20] S. Ghosh, P. Waltereit, O. Brandt, H. T. Grahn, and K. H. Ploog, Phys. Rev. B **65**, 075202 (2002).

[21] R. Ishii, A. Kaneta, M. Funato, Y. Kawakami, and A. Yamaguchi, Phy.Rev. B **81**, 155202 (2010).

[22] K. Hazu, T. Hoshi, M. Kagaya, T. Onuma, and S. F. Chichibu, J. Appl. Phys. **107**, 033701 (2010).

[23] A. Reale, G. Massari, A. Di Carlo, P. Lugli, A. Vinattieri, D. Alderighi, M. Colocci, F.Semond, N. Grandjean, and J. Massies, J. Appl. Phys. **93**, 400 (2003).

[24] N. Grandjean, B. Damilano, S. Dalmasso, M. Leroux, M. Laugt, and J. Massies, J. Appl. Phys. **86**, 3714 (1999).

[25] R. P.Leavitt and J. W.Little, Phys. Rev. B **42**, 11774 (1990).

Chapter IV. GaN grown on c-plane ZnO substrates

In this chapter, the growth and characterizations of (Ga,In)N heterostructures on c-plane ZnO substrates are discussed. In the first part, the preparation of the ZnO substrates is introduced. The second part focuses on the growth of GaN layers, especially on the polarity control of GaN on O- and Zn- face ZnO substrates. In the third part, the structural and optical properties of GaN layers are studied. Finally, light emitting devices based on (In,Ga)N/GaN quantum wells are fabricated, and the optical and electrical properties are studied and discussed.

IV.1. Preparation of epi-ready ZnO substrates

ZnO substrate is now commercially available, and 3-inch c-plane ZnO wafers have been demonstrated using the hydrothermal growth method.[1] Due to a mechanical polishing process of the surface preparation, a high density of colloidal silica is usually present on the surface of the as-received ZnO substrates (Figure IV. 1 (a)). In addition, scratches are also observed. An annealing process is needed to obtain a substrate in an epi-ready state, which is important to take advantage of the low lattice mismatch between GaN and ZnO. The substrates are annealed under O_2 atmosphere at 1000 °C. After annealing, the substrate surface is characterized by AFM, and a smooth surface with a rms roughness as low as 0.2 nm is obtained. Atomic steps can be observed, and the height of the step is ~0.26 nm, corresponding to one monolayer of ZnO.

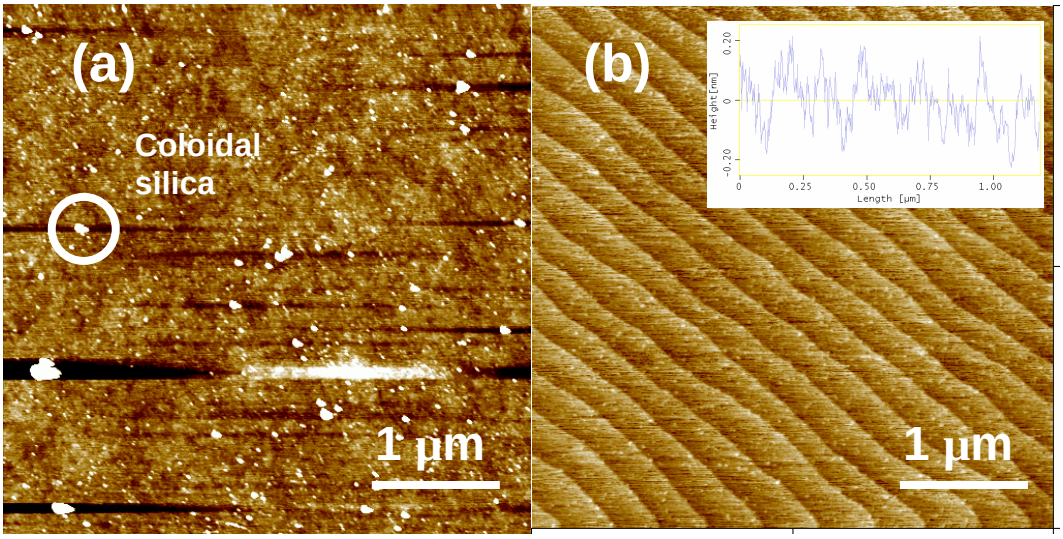

Figure IV. 1. AFM images of a ZnO substrate (a) before and (b) after annealing. The inset shows the height profile over 1 µm on the surface. The vertical scale of the images is 5 nm.

The substrate was then introduced into the MBE chamber. The substrate temperature was raised to 450 °C under vacuum, and the background pressure was ~10^{-9} Torr. Figure IV. 2 shows RHEED patterns of the ZnO surface when the incident electron beam is parallel to (a) a <11-20> and (b) m <1-100> directions. Streaky lines can be observed from both directions, which indicate a flat ZnO surface. Kikuchi lines, which are formed by the diffuse scattered electrons, are also observed. The lines underlined by a dashed line in Figure IV. 2 (b) arise from the reflection of the electron beam by atomic steps. These lines are perpendicular to the diffraction patterns of the substrate surface, as the atomic step planes are perpendicular to the substrate surface.

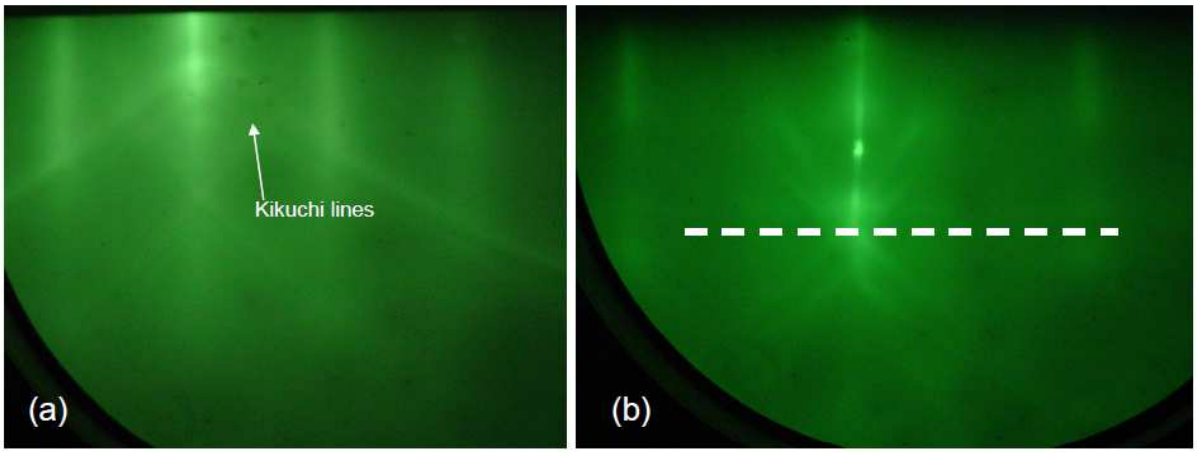

Figure IV. 2. RHEED patterns of the ZnO surface when the incident electron beam is parallel to (a) a <11-20> and (b) m <1-100> directions.

IV.2. Polarity control of the GaN epi-layers on ZnO

IV.2.1. General introduction

GaN based light emitting diodes (LEDs) and laser diodes (LDs) have reached outstanding performances in the near UV-blue range.[2,3] Most of these devices are fabricated along the $+c[0001]$ direction of GaN (Ga-polar), due to the higher crystal quality and smoother surface morphology achieved compared with the N-polar crystals.[4] However, devices fabricated on N-polar GaN may have some advantages: it has been shown that the N-polar (In,Ga)N/GaN multiple quantum wells (MQWs) may facilitate the electron-hole injection in a LED structure, and the recombination efficiency could be improved as the MQW band structure is flattened under high forward voltages.[5] Therefore, it is of technological importance to understand and control the growth of GaN layers in both gallium and nitrogen polarities.

Actually, the polarity of GaN grown on c-plane ZnO substrates has been discussed by several groups. Gu *et al.* have shown that Ga-polarity GaN layers are obtained when growing on both Zn and O terminated ZnO substrates.[6] Whereas, Namkoong *et al.* have argued that growing GaN on O face ZnO leads to a mixed polarity surface dominated by the Ga polarity, as ‘‘O-Ga’’ bonding is electro-statically favourable while ‘‘O-N’’ shows a stronger chemical bonding. On the other hand, when growing on Zn face ZnO substrates, Ga polarity GaN films are obtained as ‘Zn-N’ bond is more stable than the ‘Zn-Ga’ bond.[7] Actually, the existence of an interfacial layer, which results from the reactions between Ga and the ZnO substrate, could also play an important role in the determination of the GaN polarity. Indeed, Kobayashi *et al.* have showed that the interfacial layer may act as polarity inversion center:[8] a Ga polarity layer is obtained when growing on O face ZnO substrates at room temperature (i.e. without an interfacial layer), and the GaN layer is N-polar when growing at 700°C (i.e. with the existence of an interfacial layer between GaN and ZnO). When the same study was performed on Zn face ZnO substrates, an opposite result was obtained.[9] In the contrary, Ohgaki indicated that Ga- and N- polar GaN layers were grown on O and Zn face ZnO substrates, respectively, due to a very thin Ga_2O_3 interfacial layer (a few nm thick), which acts as a polarity inversion center[10]. Therefore, there is still no clear conclusion concerning the polarity determination mechanism of a GaN layer grown on ZnO substrates. Table IV. 1 summarizes the reports which discuss the polarity of GaN films grown on ZnO substrates.

Year	Author	Growth technique	GaN polarity		Interfacial layer
			O face (c-)	Zn face (c+)	
2004	Gu[6]	N_2 plasma /NH_3- MBE	c+	c+	unclear
2005	Namkoong[7]	N_2 plasma-MBE	c+/c-	c+	with interfacial layer
2006-2007	Kobayashi[8,9]	PLD	c+	c-	without interfacial layer
2006-2007	Kobayashi[8,9]	PLD	c-	c+	with interfacial layer
2009	Ohgaki[10]	N_2 plasma-MBE	c+	c-	few nm Ga_2O_3 interfacial layer
2009	Ohgaki[10]	N_2 plasma-MBE	c+	c+	with (In,Ga)N buffer

Table IV. 1. Summary of reported results concerning the polarity of GaN films grown on c-plane ZnO substrates.

In this section, GaN layers with either Ga or N polarity grown on c-plane ZnO substrates by molecular beam epitaxy (MBE) are demonstrated. The GaN polarity is determined *in situ* by using reflection high-energy electron diffraction (RHEED), and the results are correlated by complementary analyses including chemical etching and convergent beam electron diffraction (CBED). The structural and optical properties of the GaN layers with different polarities are investigated and compared.

IV.2.2. Growth of Ga- and N- polar GaN layers

The GaN layers were grown by molecular beam epitaxy (MBE). The growth rate is set as 0.1 µm/h. Different growth conditions are set to fabricate two groups of GaN layers (group S1 and S2) (illustrated in Figure IV. 3). The nucleation stage of S1 samples was performed at low temperatures with a 10 nm GaN buffer layer deposited between 500 and 550 °C; on the other hand, the growth was initiated between 600 and 700 °C for S2 samples. The following steps are similar for both series of samples: the substrate temperature was raised to ~ 700-750 °C to grow a 10 nm thick GaN layer, and then, GaN layers with thicknesses ranging from 300 to 600 nm were deposited at 800 °C.

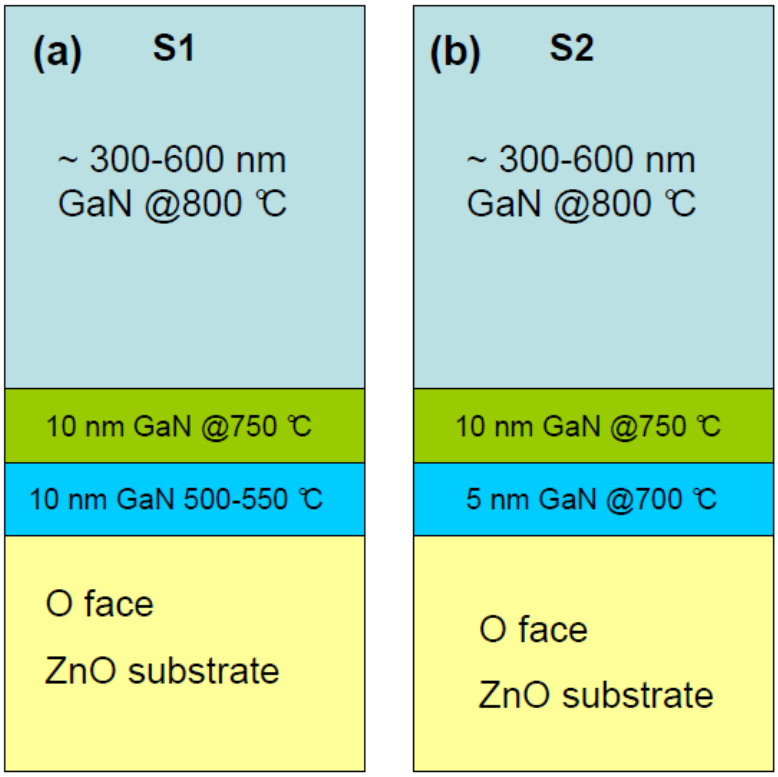

Figure IV. 3. Schematic representation of growth conditions of (a) S1 and (b) S2 samples.

For the S1 samples, the low initial growth temperatures (~ 500 °C) result in a limited NH_3 decomposition rate.[11] This led to a metal rich growth mode (*i.e.* III/V>1) during the initial nucleation stage, as indicated by a diffuse RHEED pattern with a decreased intensity (Fig. IV.4 (a)). As the temperature was increased progressively to 750 °C after the nucleation stage, the RHEED pattern got stronger and turned from streaky to spotty, which indicated a 3D morphology of GaN layer (Fig. IV.4 (b)). At this temperature, the growth condition was switched from Ga to N rich, since the decomposition rate of NH_3 increases abruptly between 500 and 700°C[11]. After the growth temperature was raised to 800 °C, the RHEED pattern turned from spots to clear streaky lines, implying that a 2D growth mode was achieved after the complete coalescence of the initial 3D islands. The streaky lines in the RHEED pattern were maintained until the end of the growth (Fig. IV.4 (c)). After the growth of a 300 – 600 nm thick GaN layer, when the substrate temperature was decreased to 500°C under NH_3 flux, a strong (2x2) surface reconstruction was observed (Fig. IV.4 (d)), indicating that a Ga polar GaN layer was grown.[12] The growth of the S2 samples was carried out in a different way: the growth was initiated at higher temperatures (~ 600 - 700°C), under N rich conditions (III/V < 1). During the first 5 nm of GaN nucleation step, the RHEED pattern became modulated, indicating a progressive roughening of the surface (Figs. IV.4 (e) and (f)). However, contrary

to the S1 sample series, diffraction lines were still observed, suggesting that the growth front remained mainly 2D. After the deposition of a 5 nm GaN nucleation layer, the substrate temperature was decreased to 500 °C and a (1x1) RHEED pattern was observed, which suggested that a N-polar GaN layer was grown from the nucleation stage.[12] Then, a 300 - 600 nm thick GaN layer was grown following a procedure similar to that of the S1 samples, and the RHEED diagram showed a streaky pattern during the whole growth process (Fig. IV.4 (g)). In addition, it should be noted that a dim V-shaped pattern gradually appeared on the RHEED diagram during the growth, which is related to the electron reflection on tilted planes or facets. Finally, after the growth, the (1x1) RHEED pattern remained when the samples were cooled down to 500°C under NH_3 flux (Fig. IV.4 (h)), meaning that the N polarity was maintained during the growth.

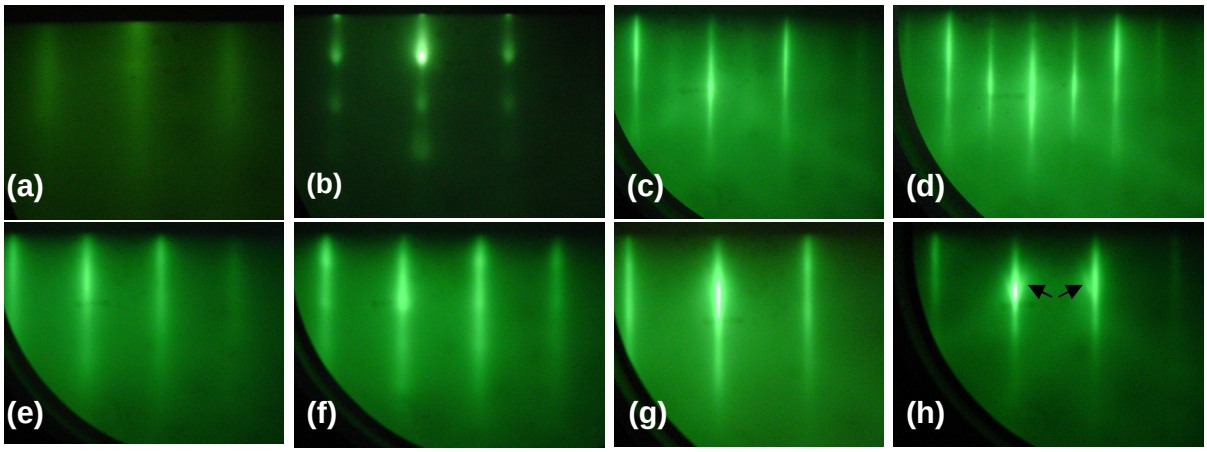

Figure IV. 4. Typical RHEED patterns (along the <11-20> azimuth) of: (a) (e) 2 nm, (b) (f) 5 nm, (c) (g) 300 to 600 nm thick GaN layers grown on O face ZnO substrates, in the case of a sample from the S1 series and the S2 series , respectively. (d) and (h) images have been taken after the end of the growth, when the temperature was decreased to 500 °C under NH_3, in the case of a sample from the S1 series and the S2 series , respectively. The arrows in (h) indicate the V-shape patterns.

IV.2.3. Comparison of the structural and optical properties of GaN layers with Ga- and N polarities

Each group of samples shows particular structural and optical properties, and one representative sample from each group is chosen for illustration. Figure IV. 5. shows the typical surface morphologies obtained for each series of sample measured by AFM. The S1 samples show a smooth surface with a root mean squared (rms) roughness of ~ 1 nm for (10 x

10) μm^2 areas, and hexagonally shaped pits with a density of 0.5 - 2 x 10^9 / cm^2 are observed (Fig. IV. 5 (a)). The formation of pits is attributed to the surface energy and the strain energy associated with dislocations.[13,14] The S2 sample exhibits a quite different surface morphology (Fig. IV. 5 (b)): it is free of pits, but the *rms* roughness is much larger (~20 nm) due to the presence of hexagonally-shaped pyramidal islands with a height of ~ 120 nm, a diameter of ~ 1.5 µm and a density of ~ 1 - 3 x 10^7 / cm^2. The presence triangular shape patterns is due to the rubbing of the AFM tip with the top of the hexagonal structures. The angle between the facets of the pyramidal islands and the growth plane is ~ 10°, which equals the angle between the dim V-shaped pattern and the main diffraction line in Fig. IV. 4 (d). Therefore, the facets of the pyramids are responsible for the dim V-shaped patterns observed by RHEED during the growth. Actually, this is the typical surface morphology of N polarity GaN layers[15].

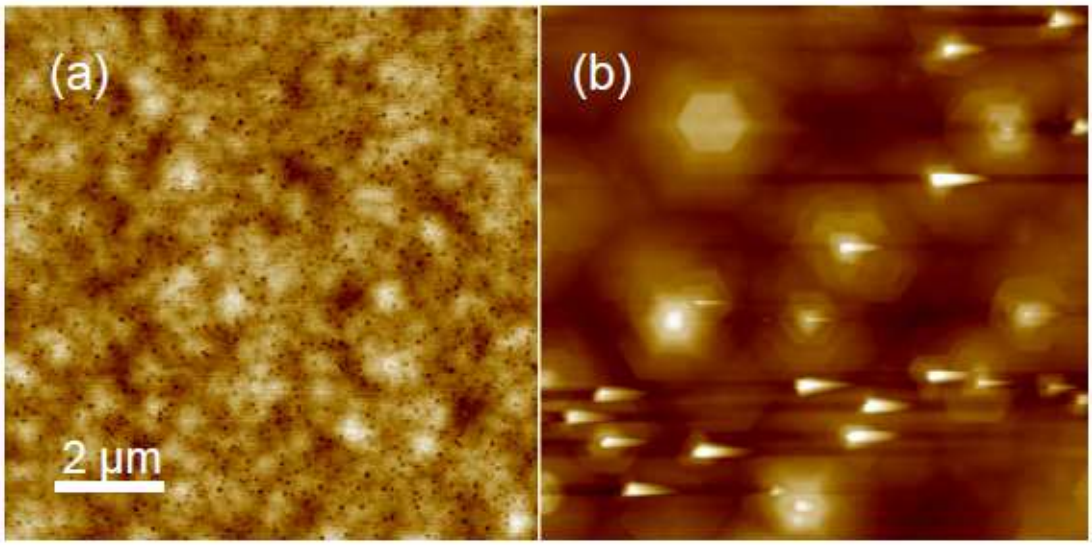

Figure IV. 5. Surface morphologies of sample (a) S1 and (b) S2. The AFM scan sizes for both samples are 10 x 10 μm^2. The vertical scales are 10 nm and 300 nm, respectively.

To confirm the polarity of the grown layers, both series of sample are etched in boiling 10% KOH solution for one minute. Figure IV. 6 shows the surface images of two samples from S1 and S2 series recorded by SEM, before and after KOH etching. While no significant change in the S1 sample morphologies can be found (Fig. IV. 6 (b)), the surface morphology of S2 sample is significantly modified after the etching (Fig. IV. 6 (d)). In the later cases, the GaN layer is strongly etched off. It is well known that GaN layers with Ga polarity are resistant to alkali solutions, while N polarity GaN layers can be easily etched.[16,17] These results confirm that the S1 samples exhibit a Ga polarity, while the S2 samples have an N polarity.

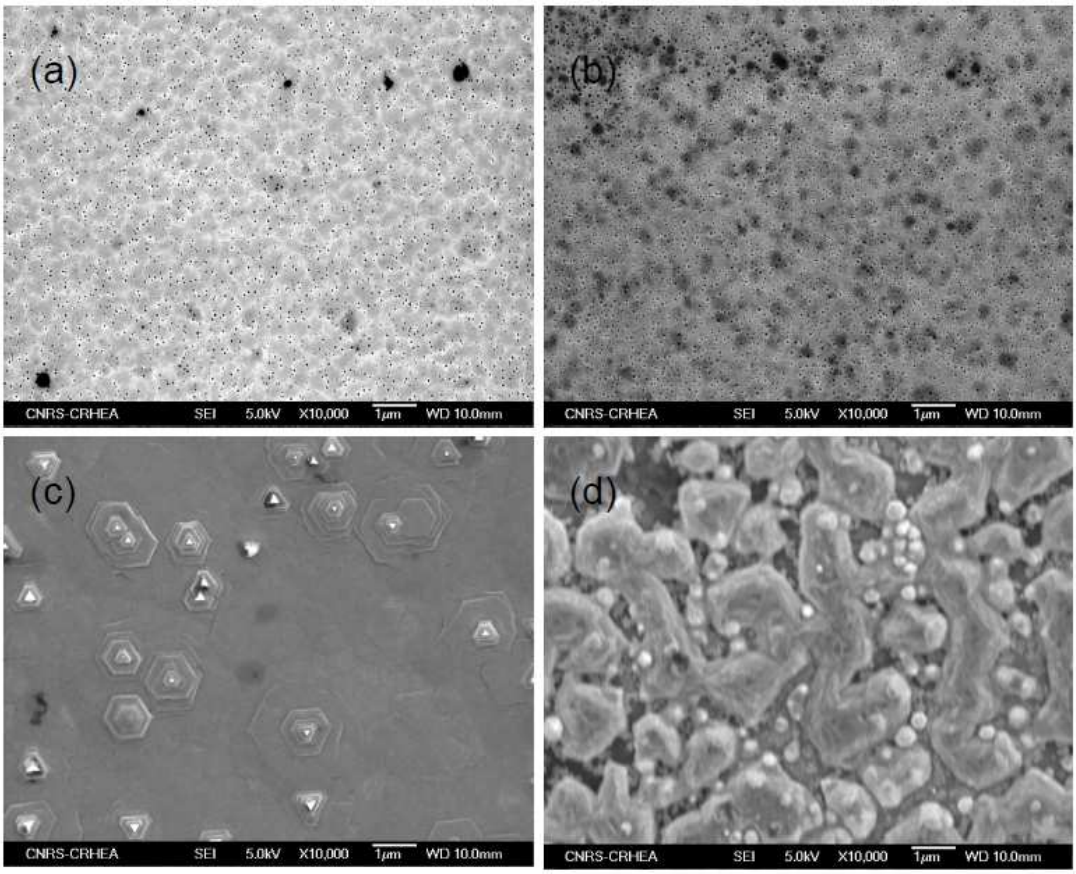

Figure IV. 6. SEM images of the surfaces of samples S1 and S2, before ((a) and (c), respectively) and after ((b) and (d), respectively) KOH etching.

Figure IV. 7 shows the typical XRD $2\theta/\omega$ scans of the GaN (002) plane of samples S1 and S2. The two samples show quite similar diffraction diagrams. They consist of six main peaks related to GaN {0002} and ZnO {0002} plane families. The peaks related to GaN (0002) (2θ~34.57°) and ZnO (0002) (2θ~34.42°) planes are difficult to resolve owing to the very close diffraction angles. The observation of the GaN (0005) reflection, which is forbidden for the wurtzite structure, is due to the multiple scattering.[18] There are also four additional peaks (labelled X_1-X_4, with 2θ positions at 37.3°, 57.5°, 79.9° and 106.6°, respectively) not related to either GaN or ZnO. These peaks are ascribed to the diffraction of the {111} plane family of zinc gallate ($ZnGa_2O_4$).[19] The formation of $ZnGa_2O_4$ is the result of the interfacial reaction between GaN and ZnO. It shows that a $ZnGa_2O_4$ single crystal phase is present in both samples, probably at the interface of ZnO and GaN layers. However, the intensities of the $ZnGa_2O_4$ related peaks in S2 samples are five to eight times weaker than those of the S1 samples.

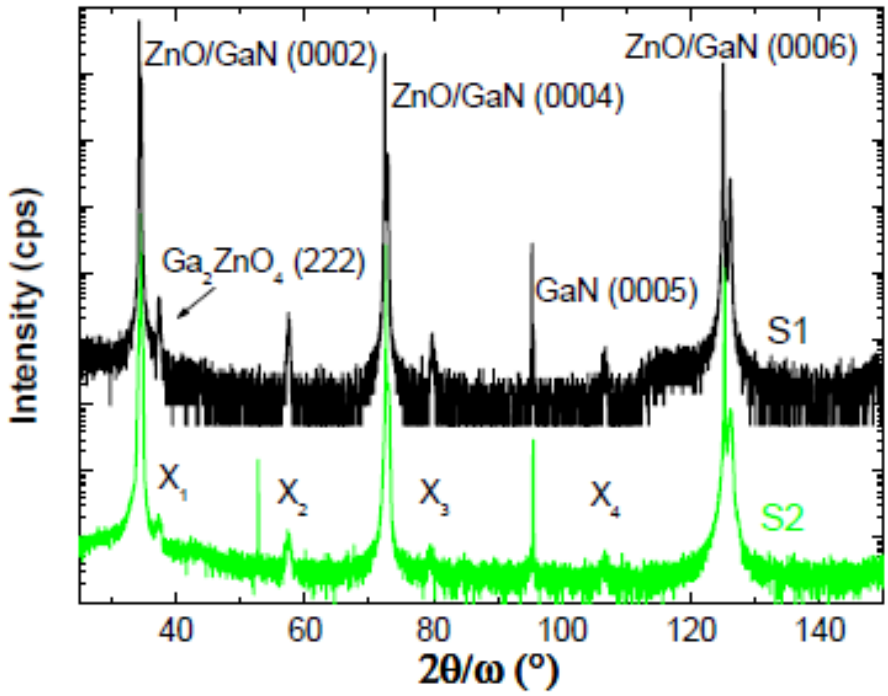

Figure IV. 7. XRD GaN $2\theta/\omega$ diagrams of samples from the S1 (upper curve) and the S2 (lower curve) series.

TEM measurements are carried out to investigate the structural properties. In the first step, the sample polarities are verified by convergent beam electron diffraction (CBED) measurements. Figure IV. 8 shows the CBED patterns of samples S1 and S2, and they are compared with the simulated diffraction patterns of Ga- and N- polar GaN layers, respectively. The matching between experimental and simulated patterns confirm that S1 samples have a Ga polarity, whereas the polarity of S2 samples is N. Some inversion domains, with a very low density, can be observed in the Ga-oriented matrix (S1 samples).

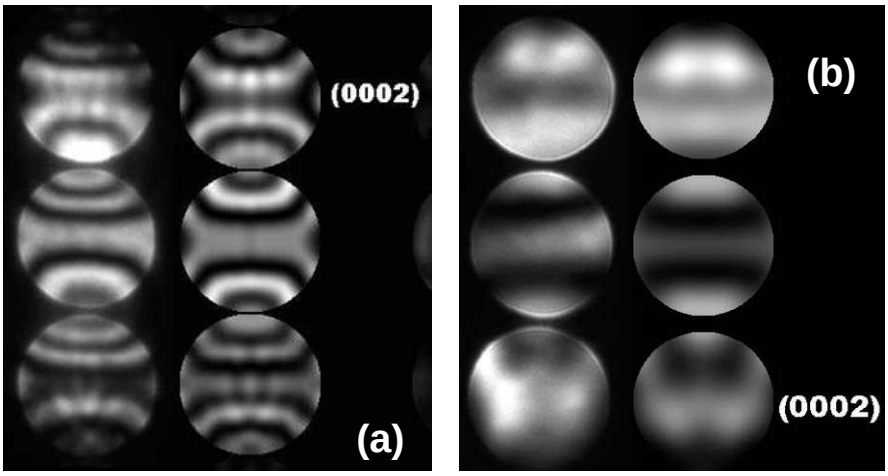

Figure IV. 8. Convergent beam electron diffraction patterns of samples (a) S1 and (b) S2 (on the left side of each images), compared to the simulated images (on the right side of each images) determined for a (a) Ga- and (b) N- polar GaN layer.

Figure IV. 9 shows TEM images of the interfacial structures between GaN and ZnO studied by high-resolution TEM (HRTEM). The S1 interface is mainly constituted of a 25 nm thick single crystalline phase sandwiched between the ZnO and the GaN layers, while the S2 interface is dominated by the GaN / ZnO junction, *i.e.* the direct growth of GaN on the bare ZnO surface. The single crystalline phase is assumed to be $ZnGa_2O_4$ according to the XRD measurements (Fig. IV. 7). To confirm this assumption, the diffraction patterns of both GaN and $ZnGa_2O_4$ crystalline structures are simulated for the incident beam along the GaN $<1\bar{1}00>$ and $<11\bar{2}0>$ directions, assuming that the (0001) plane of GaN is parallel to the (111) plane of $ZnGa_2O_4$.

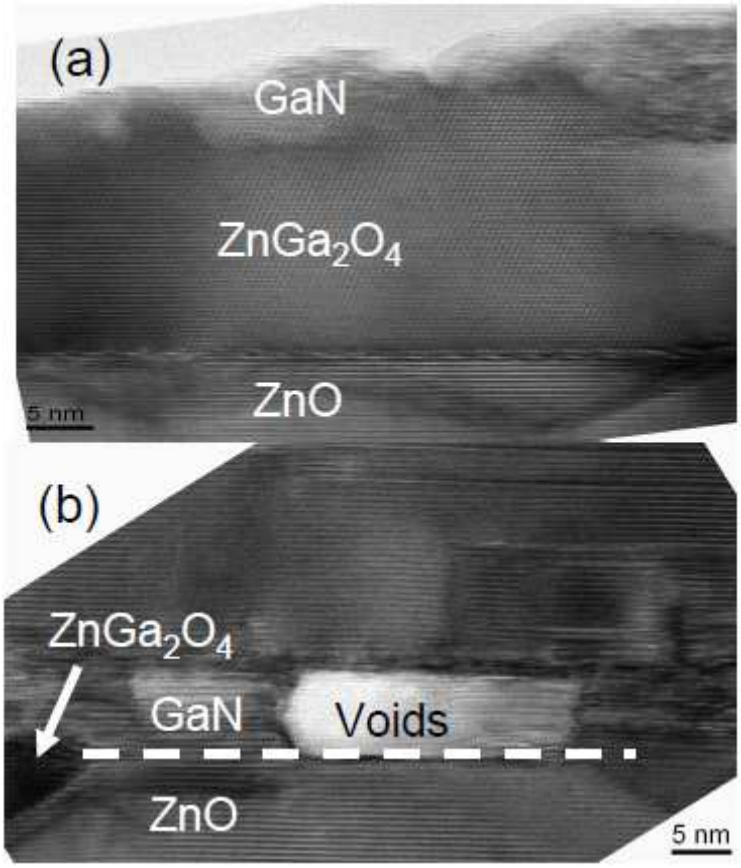

Figure IV. 9. Cross sectional HRTEM images taken along the $[11\bar{2}0]$ direction showing the GaN/ZnO interfaces of samples from (a) the S1 and (b) the S2 series.

Figure IV. 10 shows the comparison between the simulated diffraction pattern and the experimental pattern. The perfect match between the two patterns confirms our assumption, indicating that the $ZnGa_2O_4$ phase is grown pseudomorphically with both GaN and ZnO materials. The epitaxial relations between GaN (ZnO) and $ZnGa_2O_4$ are then determined to be: $[11\text{-}20]_{ZnO/GaN} \,||\, [110]_{ZnGa2O4}$, $[1\text{-}100]_{ZnO/GaN} \,||\, [11\text{-}2]_{ZnGa2O4}$ and $[0001]_{ZnO/GaN} \,||\, [111]_{ZnGa2O4}$. The above observations clearly demonstrate that the direct epitaxy of GaN on O polarity ZnO substrates leads to a N-polar layer, which is reasonable as the orientation of the 'anion-cation' bond is repeated in the epitaxial layer. On the contrary, the formation of a cubic interfacial layer during the growth leads to a film with the polarity having the lowest surface energy, *i.e.*, the Ga-polarity[20].

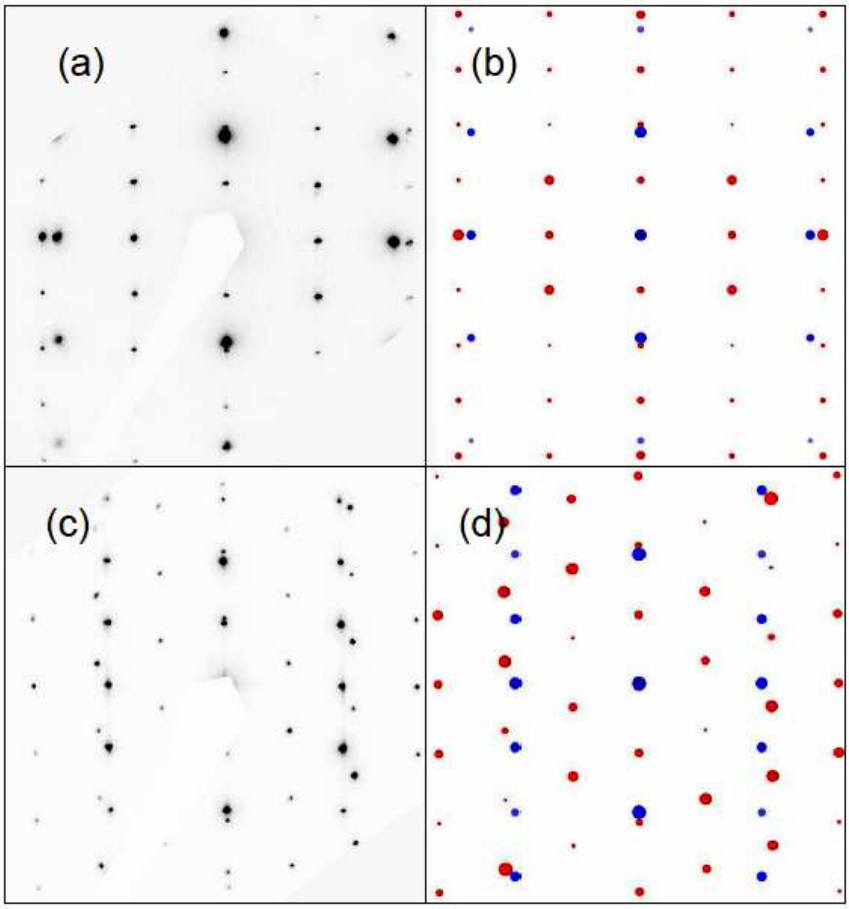

Figure IV. 10. (a) Experimental and (b) simulated diffraction patterns of GaN and $ZnGa_2O_4$ crystalline structures, when the incident beam is along the GaN $[1\bar{1}00]$ axis; (c) and (d) are the experimental and the simulated diffraction patterns when the incident beam is along the $[11\bar{2}0]$ axis, respectively. The blue points correspond to the diffraction pattern of GaN and the red points correspond to the diffraction pattern of $ZnGa_2O_4$.

The presence of a continuous $ZnGa_2O_4$ interfacial layer (*i.e.* above the ZnO surface) is observed in S1 samples. It can be explained by the Ga rich growth condition of the nucleation stage resulting from the low growth temperature. In other words, the growth of $ZnGa_2O_4$ at the interface is favoured by the excess of Ga atoms. Therefore, the III / V ratio is another important factor influencing the formation of the $ZnGa_2O_4$ phase along with the growth temperature. In S2 samples, the $ZnGa_2O_4$ phase is discontinuous (Figure IV. 9 (b)), which coincides with the low intensity of the $ZnGa_2O_4$ peaks observed in the XRD diagram (Figure IV. 7). Note that this layer is mainly localized below the GaN / ZnO interface, therefore the $ZnGa_2O_4$ formation in S2 samples occurred after the growth of the GaN nucleation layer. In addition, the N polarity of the layer was determined *in-situ* by RHEED immediately after the

growth of the 5 nm-thick GaN nucleation layer. These two results suggest that this phase is formed by the inter-diffusion of Ga into ZnO substrate after the GaN nucleation layer growth. The diffusion of Zn and O atoms from the ZnO substrate are expected to be at the origin of the voids present at the heterostructure interface (Figure IV. 9 (b)).

Finally, the optical properties are characterized by photoluminescence (PL) at 12K, under the excitation of a He-Cd laser at 325 nm. The typical spectra of S1 and S2 samples are presented in Figure IV. 11. Near band edge (NBE) emissions with similar intensities are observed at 3.461 and 3.467 eV for S1 and S2 samples, respectively, which indicates either a lower tensile strain or a higher free electron concentration in S2 sample.[21] However, the N polar sample shows a significantly enhanced emission from donor acceptor pairs (DAPs) at 3.285 eV, 30 times stronger than the DAP emission from the Ga polar sample. One reason can be attributed to the stronger diffusion of O atoms from the ZnO substrate to the GaN epitaxial layer in the N polar sample, due to a higher initial growth temperature. Another reason is related to the stronger impurity incorporation when growing GaN along the $-c$ direction.[22] The emission energy of the DAP related peak of S2 sample is 15 meV higher than that of S1 sample, and several factors may contribute to this energy difference. The first factor can be the different strain states in the two samples (discussed in Section IV.3.1), indicated by the different peak positions of the GaN NBE emission. Higher acceptor/donor incorporation in S2 sample is another reason, which can lead to the reduced average distance between the acceptors and the donors, and even to the appearance of the free electron to acceptor transition (eA^0). Furthermore, an emission peak at 3.42 eV is observed in the spectrum of the N polar sample. This emission is ascribed to the presence of I_1 type basal stacking faults (BSFs) in the GaN layer,[23,24] which have also been observed from the TEM characterization. These results agree with the study of Gühne *et al.* which shows that GaN grown along the $-c$ direction presents a higher density of BSFs than that grown along the $+c$ direction.[25]

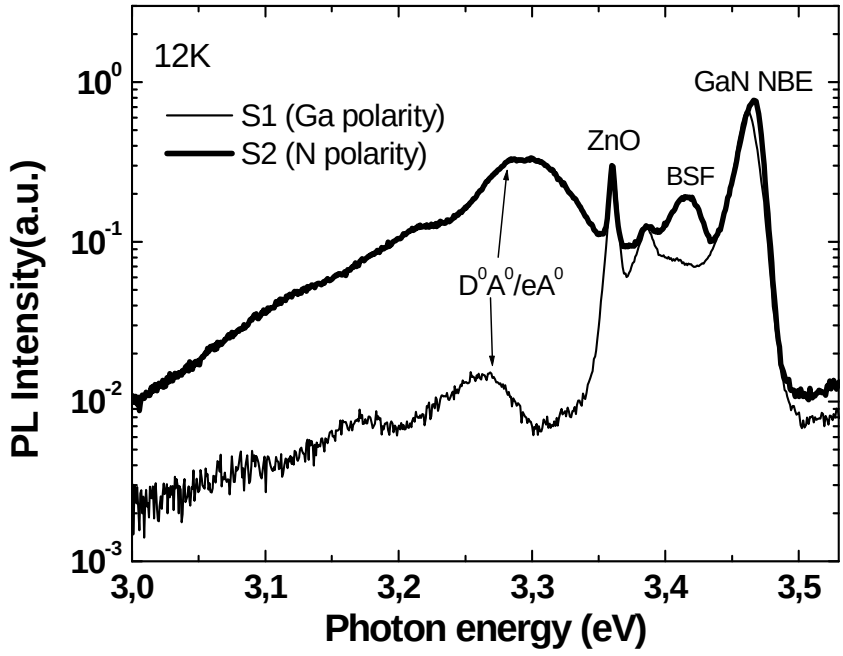

Figure IV. 11. Low temperature (12K) PL spectra of sample S1 (thin curve) and S2 (thick curve).

In addition, similar experiments have been performed on Zn face ZnO substrates. In this study, two groups of GaN layers are grown with different buffer layer growth temperatures: 550 °C for the first group and 700 °C for the second group, following the same growth procedures as those of S1 and S2 samples. The polarities of the GaN layers are determined *in situ* by RHEED, following the methods introduced in Section IV.2.2. As shown in Figure IV. 12, (2x2) reconstructions were observed on both groups of samples when the temperature was decreased to 500 °C under NH_3 flux. It implies that both groups of GaN have Ga polarity. The growth information and obtained results are summarized in Table IV. 2. According to the conclusions obtained from the growth of S1 sample series, if the buffer layer growth is initialized at 550 °C, a $ZnGa_2O_4$ interfacial layer is formed and a Ga-polar GaN layer will be grown on this cubic interfacial layer as it has a lower surface energy. When the buffer layer is grown at 700 °C, where no interfacial layer is formed, the direct growth of GaN on Zn face ZnO would also lead to a Ga-polar layer, as the 'Zn-N' bond is energetically favourable than the 'Zn-Ga' bond. Therefore, Ga-polar GaN layers are obtained in both cases, as observed in experiments.

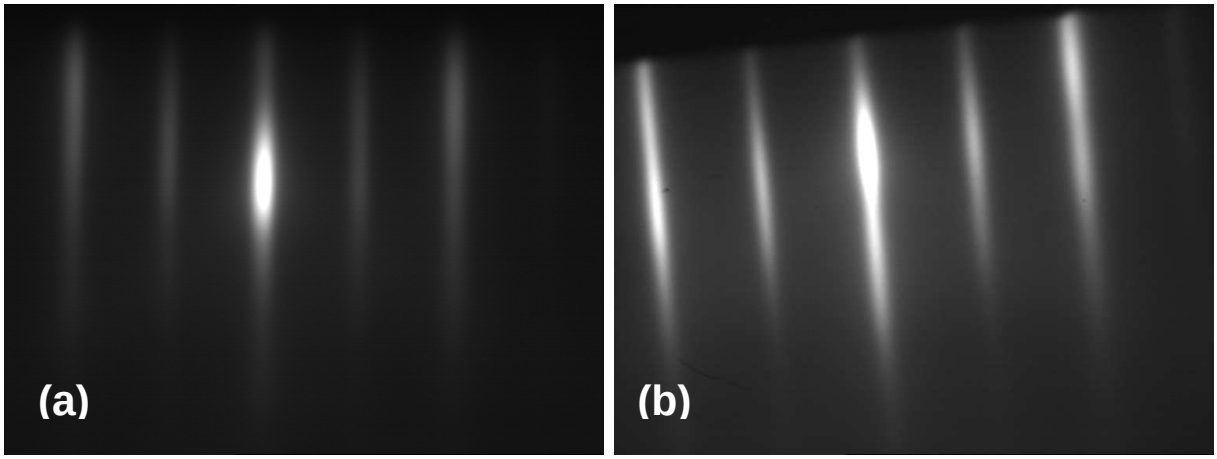

Figure IV. 12. RHEED patterns at 500 °C under NH_3 flux of GaN layers grown on Zn face ZnO substrates following the growth conditions of (a) S1 and (b) S2. The incident beam is along the <11-20> direction.

Sample series	Substrates	Growth technique	Buffer layer temperature	GaN polarity
S1	O face ZnO	NH_3-MBE	~ 500 °C	Ga-polar
S2	O face ZnO	NH_3-MBE	~ 700 °C	N-polar
$S1_{Zn\ face}$	Zn face ZnO	NH_3-MBE	~ 500 °C	Ga-polar
$S2_{Zn\ face}$	Zn face ZnO	NH_3-MBE	~ 700 °C	Ga-polar

Table IV. 2. Summary of polarities and growth conditions of GaN layers grown on ZnO substrates.

IV.2.4. Conclusions

GaN epitaxial layers with either Ga or N polarities have been grown on O face ZnO substrates. We show that the direct growth of GaN on the ZnO surface leads to an N-polar layer, whereas the formation of an interfacial alloy leads to a Ga-polar layer. This alloy has been identified as $ZnGa_2O_4$ by XRD and TEM measurements. Furthermore, the $ZnGa_2O_4$ layer has been found to be coherently grown with ZnO and GaN materials and the epitaxial relations have been determined. The polarity of the GaN layer can be switched by varying the growth temperature and the III / V ratio when growing the GaN nucleation layer. Finally, the morphological, structural and optical properties of the GaN layers are investigated and compared, showing strong differences between GaN layers with opposite polarities. On the

other hand, Ga polar GaN layers are always obtained on Zn face ZnO substrates. It is attributed to the fact that a Ga-polar GaN can be grown on both Zn face ZnO and $ZnGa_2O_4$ surfaces, independently of the presence of an interfacial layer.

IV.3. Characterization of the GaN layers

IV.3.1. Structural properties

Figure IV. 13 shows the x-ray rocking curve (XRC) of the GaN (0002) reflection. Due to the very close diffraction angle, the XRC of ZnO (0002) is also observed. The FWHM of the XRCs are ~0.2° and ~0.36° for the GaN (0002) reflection and the skew symmetric $(30\bar{3}2)$ reflection, respectively. These results are comparable to those obtained from a similar structure grown on sapphire by MBE.[24]

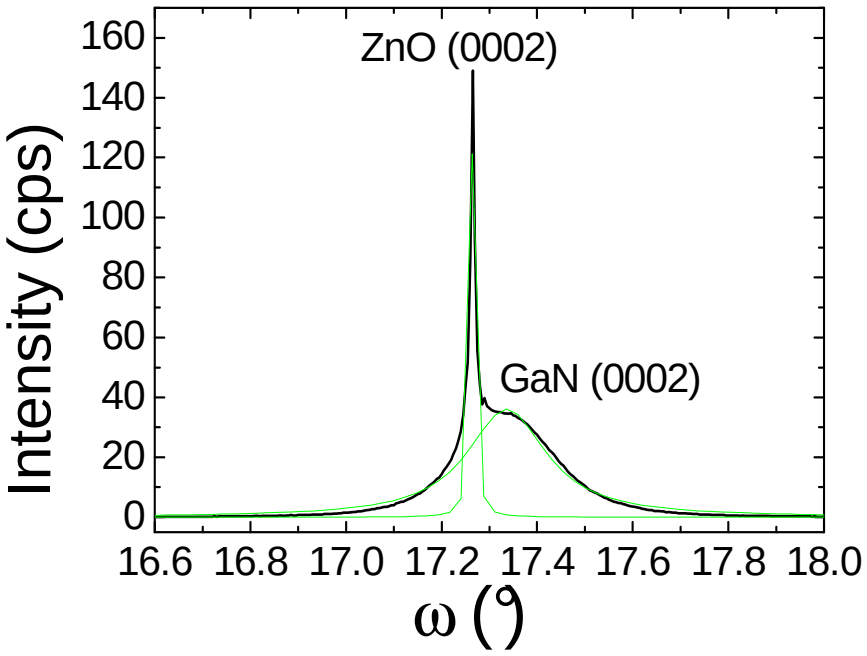

Figure IV. 13. X-ray rocking curve of GaN (0002) reflection.

The lattice parameters of the GaN layer are determined from the XRD measurements. The measurements have been carried out on two 600 nm thick GaN layers with Ga and N polarities. The symmetrical reflections of the GaN (006) plane and the asymmetrical reflections of the (205) and (3-13) plane are recorded and the 2θ positions are listed in Table IV. 3.

Sample	GaN thickness	GaN polarity	(006)	(205)	(3-13)
S1	0.6 µm	Ga	126.178°	136.446°	118.988°
S2	0.6 µm	N	126.148°	136.536°	119.122°

Table IV. 3. *2θ* positions of the GaN (006), (205), and (3-13) reflections, for GaN layers with Ga and N polarities.

Unlike the *a*-plane GaN layers, where the hexagonal symmetry is broken by the anisotropic in-plane strain, the hexagonal symmetry of the GaN layer is maintained in the polar case. Following the method introduced in Section II.5.2, lattice constants are calculated and the results are listed in Table IV. 4.

Sample	GaN polarity	a (Å)	c (Å)
N1800	Ga-polar	3.192	5.183
N1827	N-polar	3.191	5.184
Bulk GaN		3.189	5.185

Table IV. 4. Lattice parameters (LPs) of two 600 nm thick GaN layers of opposite polarities grown on O face ZnO substrates. Bulk GaN LPs are also reported for comparison.

By comparing the in-plane parameter of the epitaxial layers with that of bulk GaN, the GaN layers are found to be tensilely strained on the ZnO substrates, with a strain value of ε_{xx} ~ 0.06 - 0.09%. This result is the consequence of larger lattice constants of ZnO compared to those of GaN. It indicates that epitaxial layer is not completely relaxed after a deposited thickness of 600 nm.

IV.3.2. Optical properties

The optical properties of GaN layers grown on O face ZnO substrates have been studied by photoluminescence. The samples were excited by a double-frequency Ar^+ laser at 244 nm. Temperature dependent measurements were also carried out.

Figure IV. 14 shows the low temperature PL spectrum of a 1 µm thick GaN layer. The dominant peak at 3.47 eV is related to the near band edge emission (NBE) of GaN, with a

FWHM of 12 meV. Due to the reduced line width of this peak, the emission related to the donor bound exciton (DBE) and free exciton (FE) can be resolved.

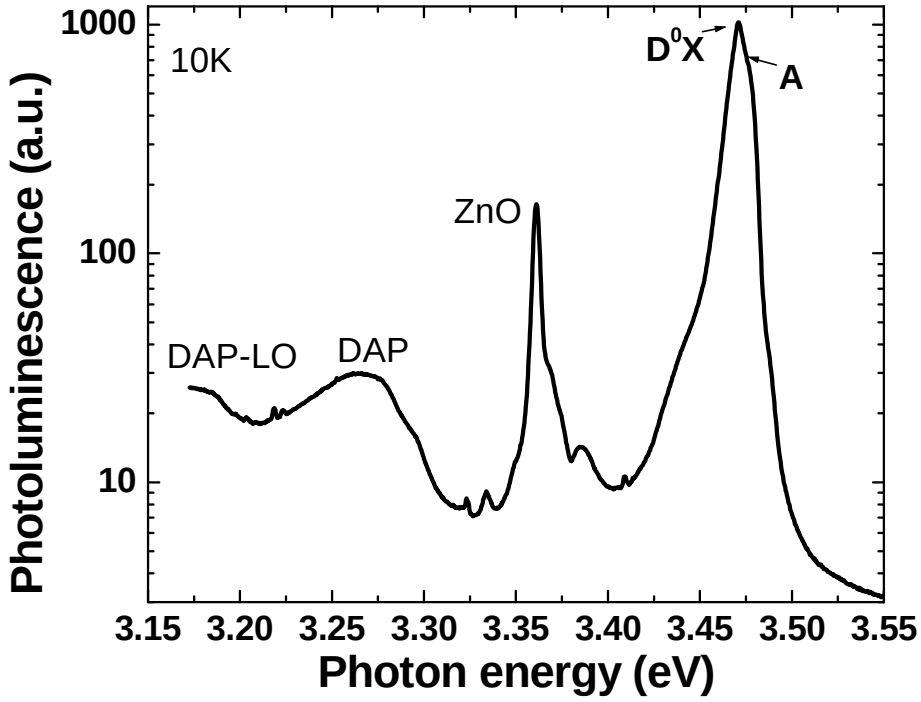

Figure IV. 14. PL spectrum of 1 µm Ga-polar GaN layer grown on a O face ZnO substrate. The sample is excited using a frequency doubled Ar^+ laser (244 nm) at 10 K.

The emission arising from the ZnO substrate can be observed at 3.36 eV. Considering the thickness of the GaN layer (1 µm) and the penetration depth of the laser beam (~0.1 µm), the ZnO substrate is assumed to be excited by the emission from the GaN layer. The broad emission peak at 3.27 eV is attributed to the recombination of donor acceptor pairs (DAPs).

Temperature dependent measurements have been performed on the same layer. Figure IV. 15 shows the PL spectra at different temperatures. As the temperature increases, the peak related to the donor bound exciton diminishes rapidly, and the free exciton recombination starts to dominate the peak when the temperature is above 30 K. It suggests that the DBE is thermally activated from the neutral donor bound states (D^0X) to the free states. The emission peak at 3.38eV blue-shifts with the increasing temperature, and red-shifts when the temperature is above 100 K, showing the same behaviour as the band edge emission. The energy difference between this peak and the NBE is ~90 meV. Together with the above observations, this emission is ascribed to the longitudinal optical phonon (LO) replica of the NBE.

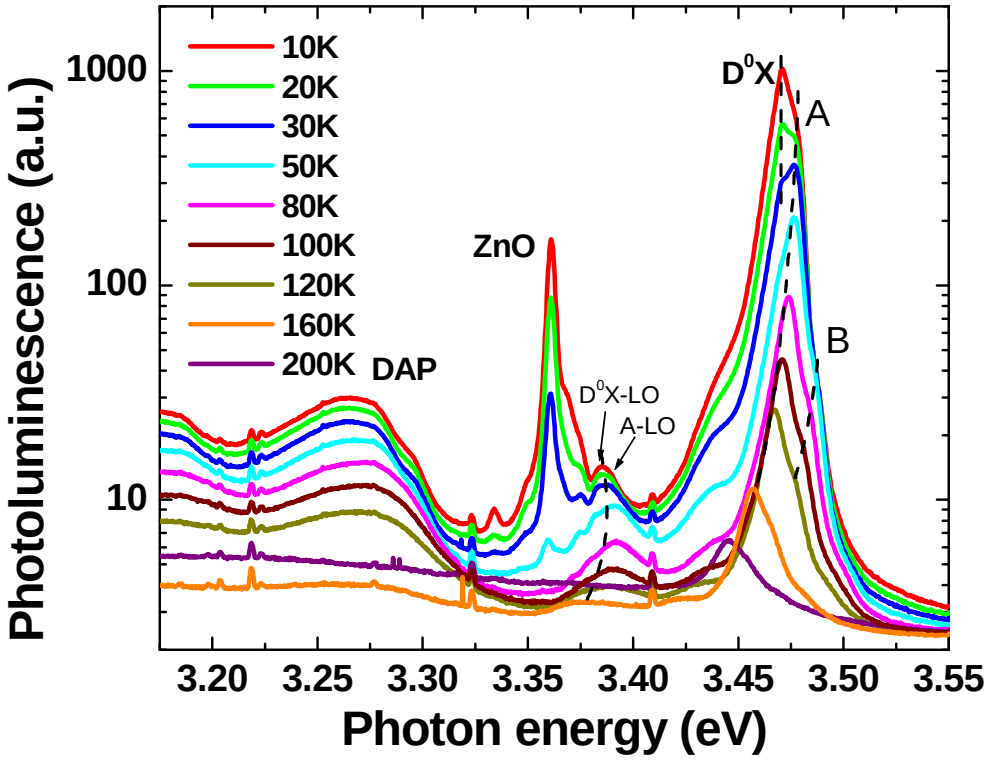

Figure IV. 15. Evolution of the GaN layer PL spectra with temperature.

The variation of the NBE and DAP emission energies with the temperature has been plotted in Figure IV. 16. The energy of the FE peak obeys to the Varshni equation. The evolution of FE peak is fitted using Eq.I.11, and it gives:

$$E(T) = E(0) - 1.9\times10^{-3}T^{2}/(2235+T) \qquad \textbf{(IV. 1)}$$

The FE transition energy at 0 K is 3.478 eV, which is 11meV lower than that of a GaN layer strained on a sapphire substrate.[26] It could be attributed to the fact that the GaN layer is tensilely strained on the ZnO substrate, and therefore, the band gap energy is lower. The fitting parameters of $\alpha = 1.9x10^{-3} eV/K$ and $\beta = 2235K$ are obtained, and these values are more than twice larger than those of GaN grown on sapphire.[26] The variation of the DBE line follows that of the FE, but is 6 meV lower in energy. It corresponds to the binding energy of the exciton on the neutral donor.

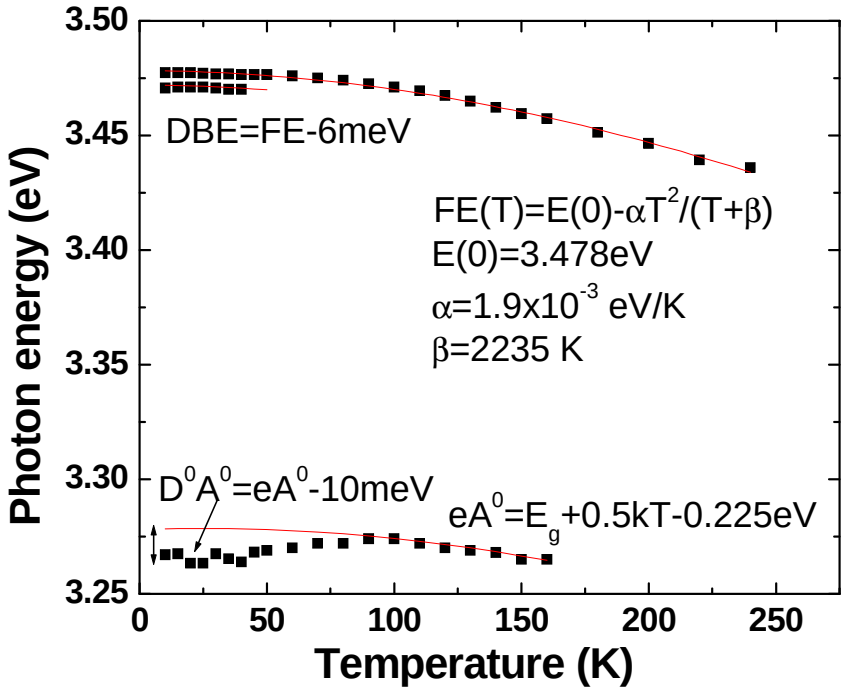

Figure IV. 16. Variation the NBE and DAP emission energies with temperature (dotted line). The curves are fitted using the Varshni equation (solid line).

Figure IV. 17 shows the Arrhenius plot of the temperature dependence of the GaN NBE emission intensity (including emission from both DBE and FE). The integrated intensity decreases as the temperature increases, due to the quenching by the other recombination channels. To study the nature of quenching channels, a two-recombination-channel model is proposed and the experimental curve is fitted using Eq.IV.4:

$$I(T) = \frac{I_0}{1 + P_A \exp\left(-\frac{E_A}{kT}\right) + P_B \exp\left(-\frac{E_B}{kT}\right)}, \qquad \textbf{(IV. 4)}$$

where I_0 is the NBE emission intensity at low temperature, and E_A and E_B are the activation energies of two quenching channels, respectively. The activation energy of quenching channel A is found to be $E_A = 4.7 \pm 0.15 meV$, and this value is close to the binding energy of DBE (6 meV). When the DBE is activated to FE, it may be captured by the defect related non-radiative recombination centers, like the threading dislocations. As a result, the radiative recombination intensity is reduced. The activation energy of quenching channel B is deduced

to be $E_B = 25.4 \pm 1.75 meV$, which is close to the GaN exciton binding energy ($E_{Ry} = 25 meV$). This channel is attributed to the release of the exciton.[26]

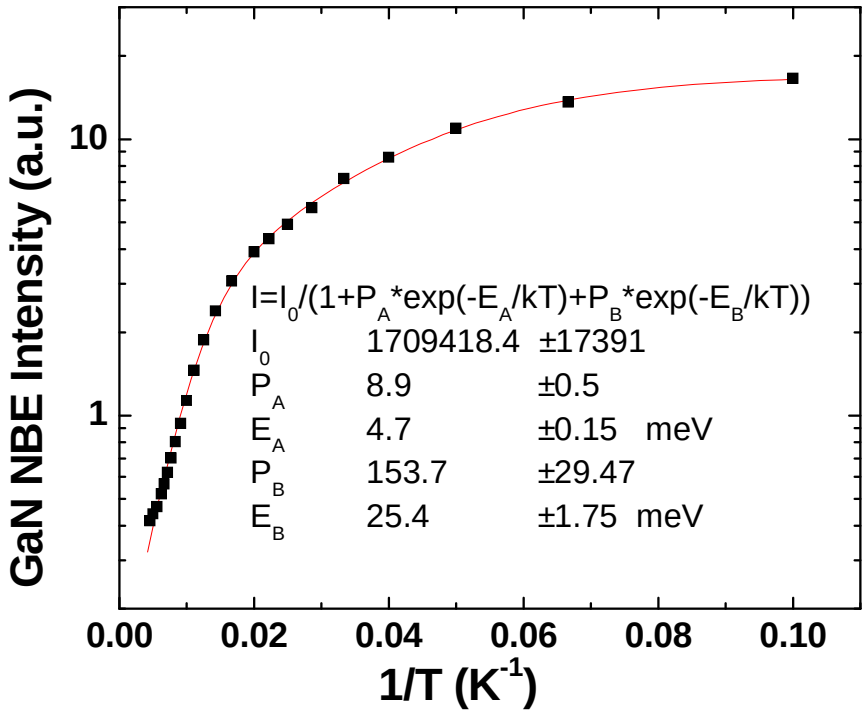

Figure IV. 17 Arrhenius plot of the temperature dependence of the GaN NBE emission intensity (dotted line). The integration range is from 3.43 to 3.50 eV. The horizontal axis is the inverse of the temperature, and the vertical axis is the integrated intensity in logarithmic scale. This curve is fitted by Eq. IV.4.

The variation of the DAP emission energy with temperature is also plotted in Figure IV. 16. In the low temperature range, the emission mainly arises from the neutral donor-neutral acceptor (D^0A^0) recombination. When the temperature is above 50 K, the emission gradually switches to the free electron-neutral acceptor recombination (eA^0), due to the donor ionization. The variation of the eA^0 line follows:[27]

$$eA^0 = E_g + 0.5kT - E_A, \qquad \textbf{(IV. 5)}$$

where the band gap energy E_g can be deduced from: $E_g = E_{FE} + E_{Ry}$, and $E_{Ry} = 25 meV$ is the Rydberg energy of the exciton. E_A represents the residual acceptor binding energy, and it is fitted to be 225 ± 1 meV. This value coincides with most findings, which is very close to the binding energy of Mg (200 - 250 meV)[26,27,28]. The origin of this shallow acceptor level is not

clear. Some researchers have simply attributed it to the non-intentional Mg doping.[29] Actually, Mg is used to grown *p*-type GaN layers, which gives rise to memory effects.[30] Fischer *et al* attributed it to a shallow acceptor induced by carbon contamination, which has a binding energy (230 meV) slightly lower than that of Mg[27].

The variation of the DAP emission energy with the excitation power is also studied. An optical density is placed in front of the incident laser beam and the excitation power reaching the sample surface is varied over three decades. Figure IV. 18 shows the PL spectrum of the GaN layer in the DAP emission range, including the DAP emission and its first order photon replica (DAP-LO). The DAP peak energy increases from 3.25 to 3.27 eV when the excitation power increases from 20 µW to 20 mW. This is a typical behaviour of a DAP emission.[31] The broad emission peak of the DAP is contributed by donors and acceptors distributed in a wide distance range. The recombination between donors and acceptors distributed in longer distances, which has lower emission energies according to Eq. I.17, have longer lifetimes. When the excitation power increases, the recombination from these donor-acceptor pairs saturates easily. Then, the recombination between DAPs with shorter distances, which has higher emission energies, become more pronounced in the spectrum, which finally leads to the blue-shift of the DAP peak.

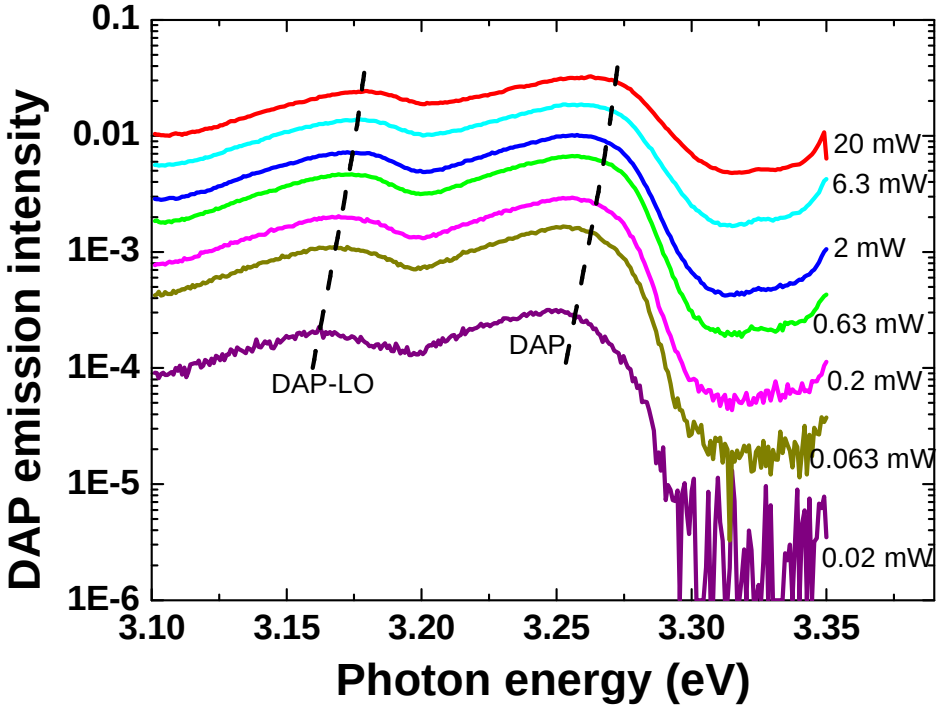

Figure IV. 18. DAP emission and its LO phonon replica under different excitation powers.

IV.4. (In, Ga)N/GaN MQW based LEDs

IV.4.1. Introduction to the LED structure

Light Emitting Diode (LED) structures, as illustrated in Figure IV. 19, have been grown on c-(0001) ZnO substrates using MBE. Following the growth conditions of S1 samples presented in Section IV.2.2, a 700-nm-thick undoped GaN buffer layer (BL) was grown under this growth condition. The polarity of the GaN layer is Ga, which is indicated by the (2x2) reconstruction observed in the RHEED pattern, observed at 500 °C under NH_3 flux. Following this step, a 700 nm Si-doped *n*-type GaN layer and five (In,Ga)N/GaN quantum wells (QWs) were grown. The barrier and well thicknesses are 10 and 1.6 nm, respectively. A 20-nm-thick $Al_{0.1}Ga_{0.9}N$:Mg electron-blocking layer was grown to block the electrons and avoid the *e*-*h* recombination in the *p*-GaN side.[32] Finally, 200 nm of *p*-type GaN was deposited to complete the whole light-emitting device. The Mg concentrations are in the range of $2x10^{19}$ to $8x10^{19}/cm^3$ according to the results measured by secondary ion mass spectrometry (SIMS). Two types of LED structures were fabricated, named LED-A and LED-B, with different growth temperatures for the (In,Ga)N layers, *i.e.*, 580 and 550°C for LED-A and LED-B, respectively.

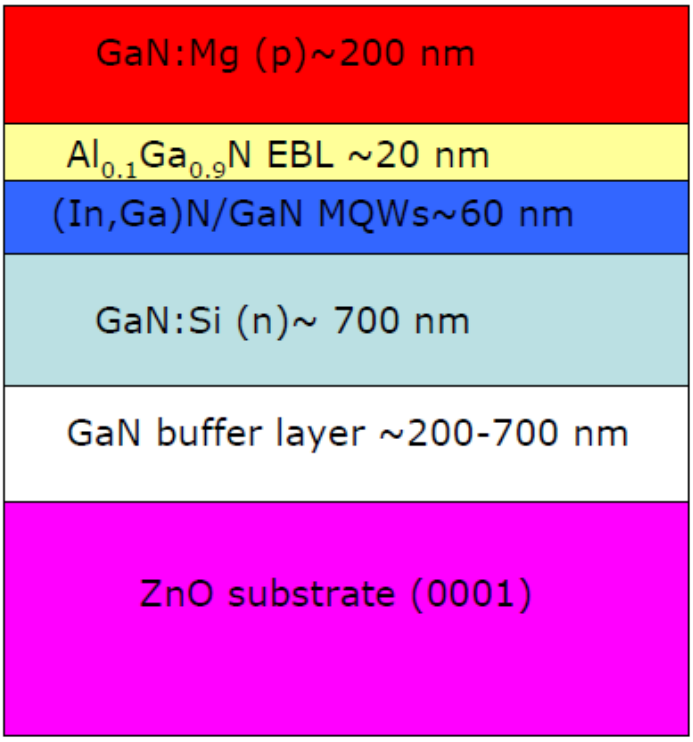

Figure IV. 19. Scheme of the LED structures.

The LED chips are fabricated on the epitaxial wafers. Figure IV. 20 shows a photograph of the LED chips on a ZnO substrate. All the mesas are etched in square shape. There are four groups of mesas with sizes ranging from 140x140 μm^2 to 460 x460 μm^2.

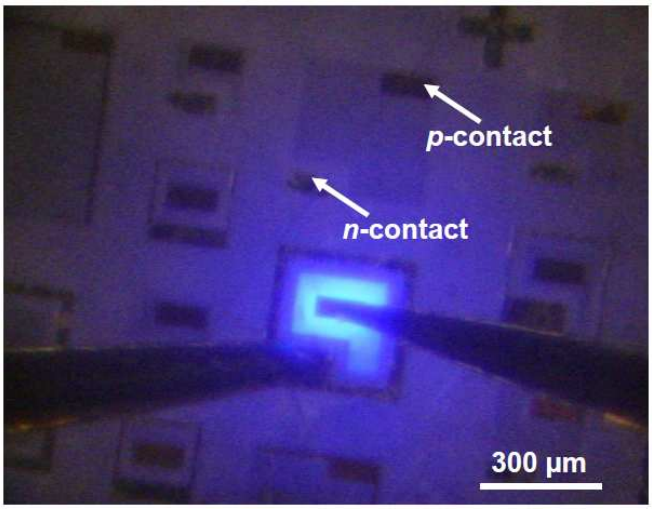

Figure IV. 20. Photograph of the LED chips (LED-A) on a ZnO substrate.

A planar configuration is adapted as shown in Figure IV. 21. At first, a metal semi-transparent layer (STL) (Ni: 50 Å/Au: 50Å) is deposited on the *p*-GaN layer, to improve the current spreading in the LED structure.[33] The *p*-contact (Ni: 200 Å/Au: 1000Å) is then deposited upon the STL. The wafer is etched by reactive ion etching (RIE) (*p*-GaN and the MQW layer) until the *n*-GaN is reached, to form squared shape mesas. The *n*-contact (Ti: 150 Å/Al: 750Å/Ni: 200 Å/Au: 1000Å) is deposited. Finally, the LED chip is annealed under O_2 for 5 minutes, at 350 °C.

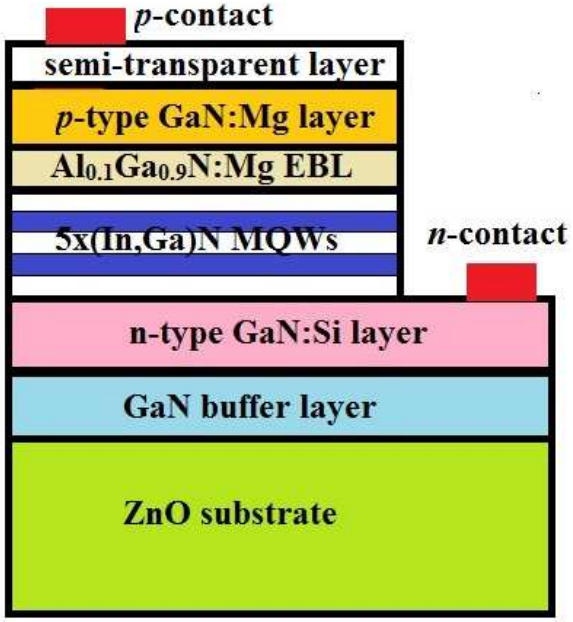

Figure IV. 21. Schematics of the LED chip with a planar structure.

IV.4.2. Optical properties

Photoluminescence (PL) experiments were performed with an excitation at 244 nm, using a frequency-doubled Ar^+ laser, operating at 20mW.

An (In,Ga)N/GaN MQW heterostructure is grown as a reference. This heterostructure is identical to the active region of LED-A. Figure IV. 22 shows the photoluminescence (PL) spectrum of this heterostructure recorded at room temperature. The MQW emission can be clearly observed at 415 nm, indicating the successful carrier confinement by the QWs grown on ZnO. The FWHM of this peak is 22 nm at room temperature. The broad peak at 490 nm originates from the deep-level emission (DLE) from the ZnO substrate,[34] which is excited by the emission from the (In,Ga)N QWs and the GaN layer. This assumption is confirmed by the broad emission band in the PL spectrum recorded from the back side (ZnO substrate side) of the sample. The modulated shape of this band is the consequence of the thin-film Fabry-Perot interferences.

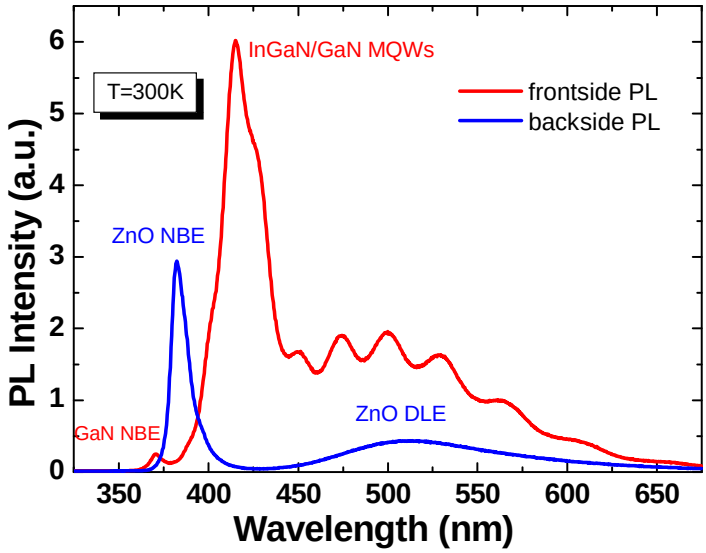

Figure IV. 22. Photoluminescence measurements under a 244 nm excitation using a frequency-doubled Ar^+ laser (20mW) of an (In,Ga)N/GaN multi-QW structure (at room temperature), from both front and back sides.

Low-temperature (13 K) PL measurements are also performed on the complete LED structures. PL spectrum of LED-B is shown in Figure IV. 23. The emission of the (In,Ga)N/GaN QWs is observed at 448 nm. The emission peak at 379 nm is related to the donor acceptor pairs (DAPs). The DAP emission is much stronger than the GaN band edge, whereas an opposite situation is found for a 600-nm-thick nonintentionally doped GaN

reference layer on ZnO (dotted line in Figure IV. 23). Noteworthy, these observations are similar to what has been observed for nondoped and Mg-doped GaN layers grown on sapphire substrates[35].

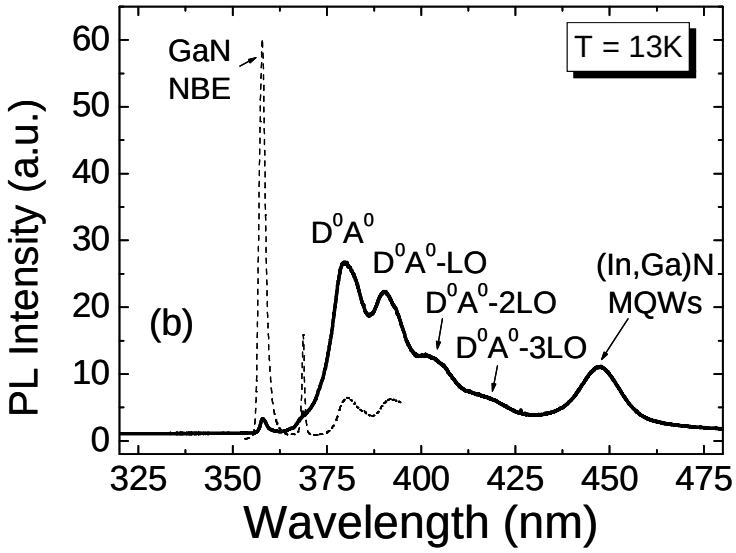

Figure IV. 23. PL spectra (13 K) of a GaN/(In,Ga)N LED structure (full line) and a GaN layer (dashed line) grown on c-ZnO substrates.

IV.4.3. Electrical properties

The transmission line method (TLM) is adapted for the determination of the *n*- (*p*-) contact resistance, as well as the *n*- (*p*-) GaN resistivity.[36] Three groups of contacts are deposited on the *n*-GaN (*n*), *p*-GaN (p_e), and STL (p_s) layer surfaces, respectively. The scheme of the contacts is shown in Figure IV. 24. Each group consists of eight contacts, and these contacts are in rectangular shape (*L* x *w*: 60 x130 µm^2). The distances between the contacts (*l*) are 5, 10, 20, 40, 80, 120 and 160 µm, respectively.

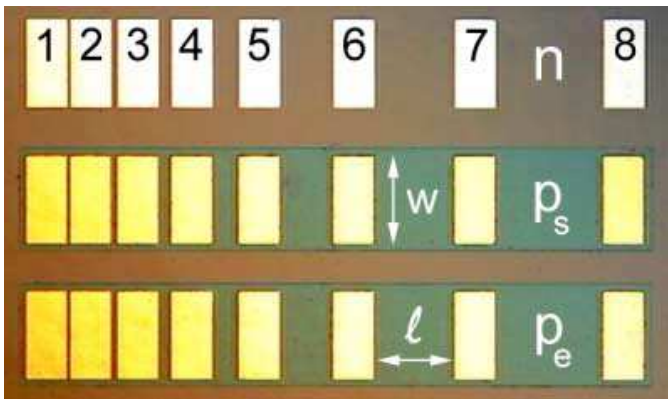

Figure IV. 24. Photograph of the metal contacts deposited on the *n*-GaN (*n*), *p*-GaN (p_e), and STL (p_s) layer surfaces, designed for TLM measurements.

The current-voltage (I-V) curves are recorded between two neighboring contacts. Figure IV. 25 shows I-V curves recorded between each pair of neighbouring contacts deposited on the n-GaN layer of a LED structure.When varying the applied voltage from -0.5 to 0.5 V, the measured current changes linearly with the voltage. The *I-V* curves are fitted by:

$$I = I_0 + \frac{1}{R}V \qquad \textbf{(IV. 2)}$$

The resistance between two contacts (R) can be deduced from the slope of the fitting curve.

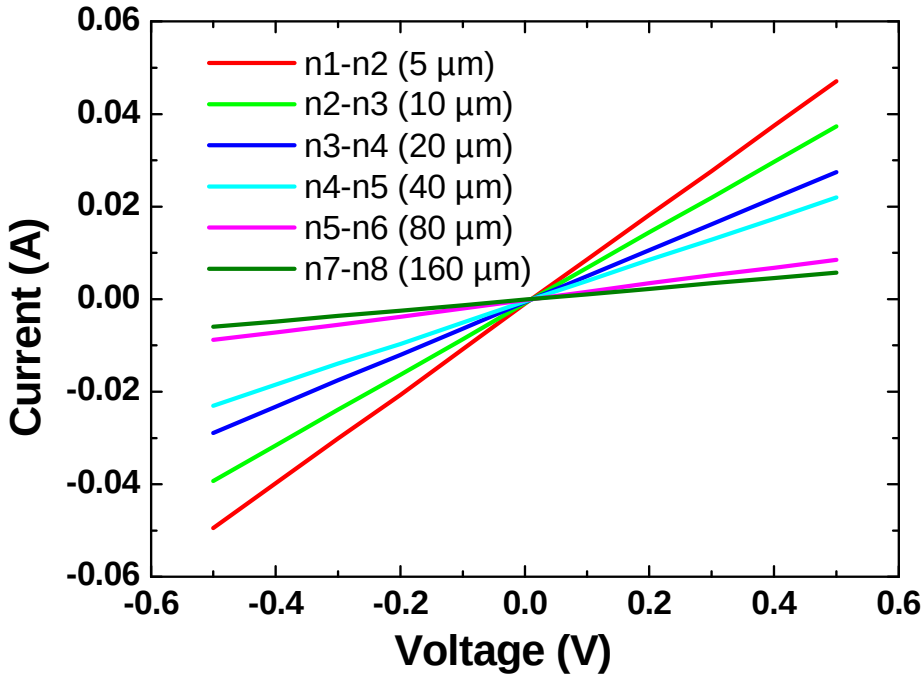

Figure IV. 25. I-V curves recorded between each pair of neighbouring contacts deposited on the *n*-GaN layer of a LED structure.

The total resistance between two contacts can be expressed by:

$$R = 2R_c + R(l), \qquad \textbf{(IV. 3)}$$

where R_c represents the contact resistance, and $R(l)$ represents the series resistance of the *n*- (or *p*-) GaN layer between two contacts separated by a distance *l*.

The series resistance of the *n*- (or *p*-) type GaN layer can then be calculated by:

$$R(l) = \rho \frac{l}{wd}, \qquad \textbf{(IV. 4)}$$

where ρ is the resistivity, w =130 µm is the contact length, and d is the n- (or p-) type GaN layer thickness. In our LED structures, the thicknesses of the n- and p-GaN layers are l_n=700 nm and l_p=200 nm, respectively. The n-GaN layer resistances are plotted as a function of the contact distance l in Figure IV. 26. The experimental data is fitted using Eq. IV.3 and IV.4. The contact resistance of the n-GaN (R_c^n) is deduced to be 3.93 Ω. The contact resistivity can be calculated by $\rho_c = R_c^n L w$, and a value of 3.1x10^{-5} Ω•cm^2 is obtained. For comparison, a contact resistivity of 6.0x10^{-7} Ω•cm^2 has been obtained for a Ti/Al/Ti/Au contact with a doping level of 1.4x10^{20} /cm^3.[37] The slope of the R-l curve is deduced to be k=0.5 Ω/µm. Then, the resistivity of the n-GaN can be determined by $\rho = kwd$ as 4.2 x10^{-3} ± 0.3 x 10^{-3} Ω•cm.

Similar measurements have been carried out on p-GaN layers. However, due to the high resistance and lack of valid experimental data, the precision of the obtained results is limited. A p-GaN resistivity of ~ 50 Ω•cm is found (in agreement with measurements performed by I. C. Robin in LETI, Grenoble). This value is higher than the current standard of 1 Ω•cm. The main reason is the low hole concentration, which is limited to ~ 10^{16} / cm^3.

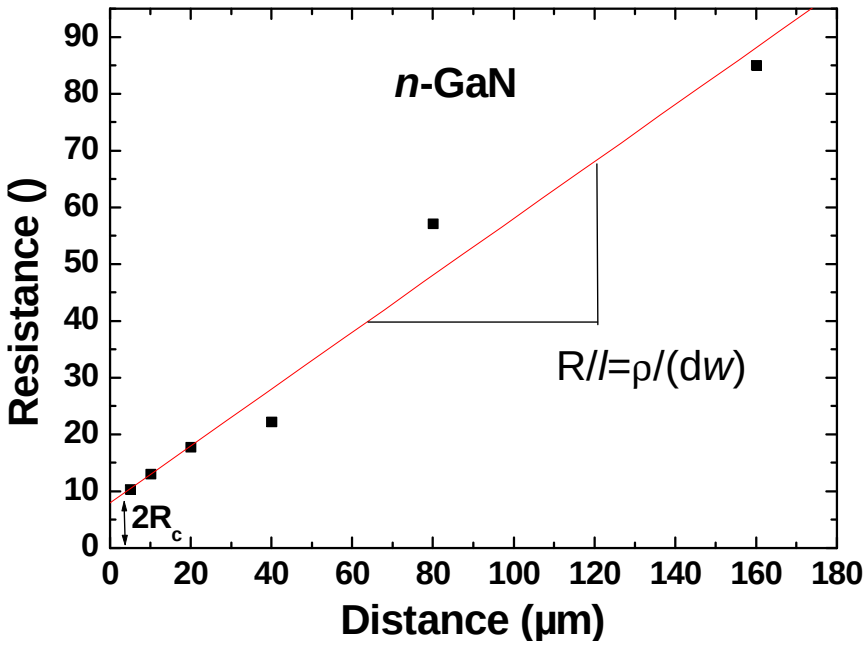

Figure IV. 26. Typical *n*-GaN layer resistance measured by TLM as a function of the contact distance *l*.

SIMS measurements have been carried out to investigate the atomic distribution in the LED structure (in collaboration with I. C. Robin, J. L. Santailler and G. Feuillet, LETI, Grenoble). The concentrations of O, H, Si, Al and Ga have been measured and shown in Figure IV. 27. The concentration of O decreases rapidly from ~10^{23}/cm^3 to 3x10^{17}/cm^3 in the first 200 nm GaN layer. During this stage, the incorporation of O in GaN mainly arises from the O out-diffusion from the substrate. The O concentrations remain at the level of 3x10^{17}/cm^3 in the GaN:Si layer, which indicates that the out-diffusion is no longer the source of O incorporation. The back etching of the substrate by H_2 has been proposed as another source of O impurities[38]. In our MBE reactor, where NH_3 is used as the N source, H_2 is produced after the decomposition of NH_3 at the surface of the substrate. O and Zn atoms are then produced in the reaction between H_2 and ZnO on the back side of the substrate. The O, Zn, as well as H, may be incorporated into the GaN layer during the growth. Indeed, the O concentration variation follows that of H after the initial stage, which is one proof of the O incorporation arising from the H_2 back etching. The O concentration increases to 8 - 9x10^{18}/cm^3 in the (In, Ga)N/GaN MQW layer, and slightly decreases to a level of 1 - 2 x10^{18}/cm^3 in the *p*-GaN layer. The fluctuation of the O concentration in the (In,Ga)N/GaN MQW structure could be explained by the use of different NH_3 fluxes during the growth of the barriers and the wells. A ten times higher NH_3 flux is used during the growth of the (In,Ga)N layers, compared with that of the GaN barriers, which leads to a stronger substrate etching. The concentration of Zn impurities in GaN is in the order of ~ 10^{16}/cm^3, which is one order of magnitude lower than that of O. Therefore, it is expected to have a much weaker influence on the electronic properties of the LEDs. The Mg concentration is measured to be ~ 5x10^{18}/cm^3.

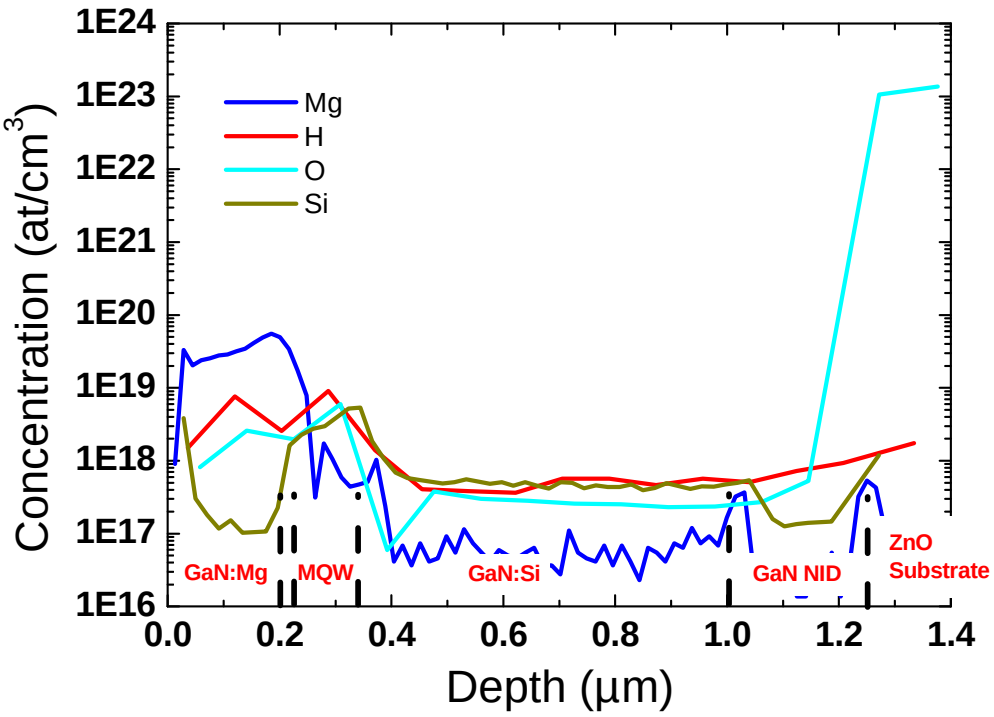

Figure IV. 27. H, O, Si, Al, and Ga concentrations in the LED structure measured using SIMS.

The Si doping level is measured to be 5-6 x 10^{17}/cm^3 in the *n*-type GaN layer, and the Mg doping level is 3-4 x 10^{19}/cm^3 in the *p*-GaN layer. The strong difference between the Mg doping level and the hole concentration (~10^{16} / cm^3) can be explained by the NID of O. Indeed, O acts as a donor in GaN and, hence, partly compensates the *p*-type doping. Therefore, the O NID needs to be further reduced to improve the *p*-GaN resistivity and enhance the hole concentration.

Since the O incorporation in *p*-GaN layers is mainly induced by the substrate back etching, several methods have been proposed to reduce the H_2 etching: i) the back side of the substrate could be protected by depositing one layer of molybdenum; ii) N_2 plasma could be used as the N source to avoid the utilization of NH_3; iii) the use of lower growth temperatures to reduce the substrate etching rate, as well as the atomic out-diffusion. Actually, an O doping level as high as 10^{21}/cm^3 has been detected in GaN layers grown on ZnO substrates using MOCVD, due to the high growth temperatures (~1000 °C).[38] In our study, the lower growth temperatures of MBE (~800 °C for the GaN growth) are an advantage in reducing the O incorporation.

Finally, the reduced [O] residual together with the high [Mg] allow us to observe a uniform blue electroluminescence even at current values as high as 80 mA, which indicates a good current spreading in the LEDs (Figure IV. 28). It deserves to be noticed that if the *p*-type GaN layer is too resistive, the current spreading would be limited and the electroluminescence

would mainly come from the region close to the *p*-contact. In our case, although the *p*-doping is partly compensated, the resistivity of the *p*-layer is sufficiently low to get a good current spreading.

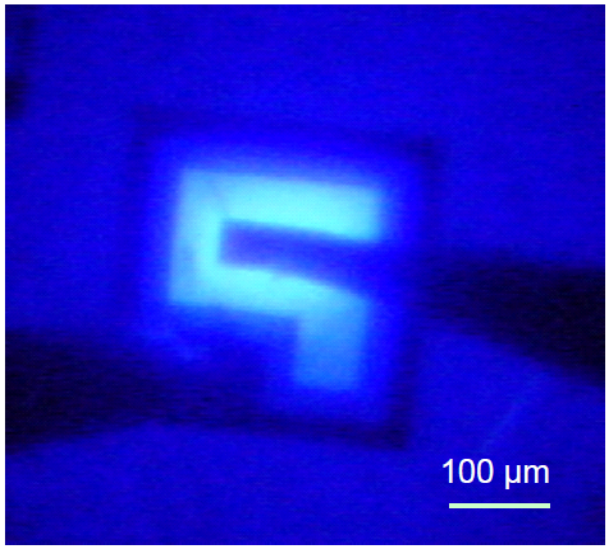

Figure IV. 28. Photograph of a (300 x 300 µm^2) LED-A device operating at a current of 80 mA.

After the fabrication of the devices, the performances of our LEDs have been evaluated at room temperature. The equivalent electrical circuit of the LED structure is illustrated in Figure IV. 29. V represents the applied voltage. R_{serie} and R_{shunt} represent the serie and shunt resistances, respectively. I_d represents the current passing through the diode and I_L is the leakage current, which can be calculated from $I_L = V / R_{shunt}$.

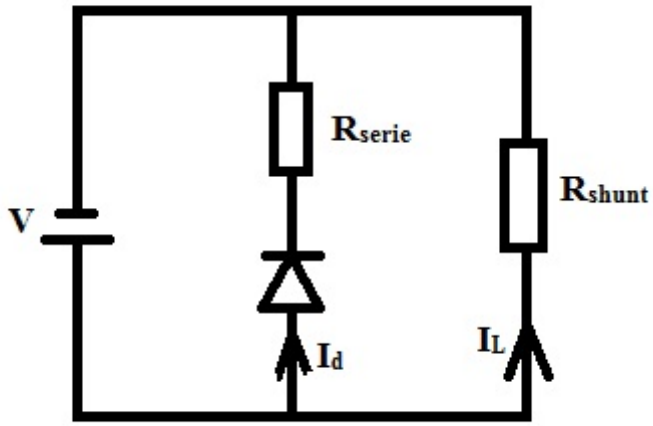

Figure IV. 29. Scheme of the equivalent electrical circuit of the LED structure.

Figure IV. 30 shows the current-voltage (I-V) curve of an LED-A device recorded under both forward and reverse currents. We can observe the typical rectification behaviour of a diode, which is described by:

$$I(V) = I_s\left[\exp\left(\frac{eV - R_s I_d}{nk_B T}\right) - 1\right] + I_L, \qquad \textbf{(IV. 5)}$$

where I_s is the saturation current, and n is the ideality factor ($1 \le n \le 2$). Leakage current values between 10 - 50 µA are measured on the LEDs under 2 V reverse voltage. This value is higher than the values reported for LEDs grown on GaN template using MBE, which in the range of nA under -2 V voltage[39]. The leakage paths are attributed to the threading defects. Forward voltages at 20 mA are found between 4 and 6 V. From the slope between 20 and 100 mA of the I-V characteristics, series resistances between 50 and 100 Ω are deduced. Compared with the results reported on similar LED structures grown on GaN / sapphire MOCVD templates,[35,39] the larger values of forward voltages and series resistances found here are due to the high resistivity values (~ 50 Ω.cm) of the *p*-GaN layers.

To conclude, the I-V characteristics indicate two directions for further improvements of the LEDs grown on ZnO substrates: one is the enhancement of the hole concentration in *p*-GaN layers by reducing the O NID; the other is the reduction of the threading defects in the GaN layers to reduce the leakage current.

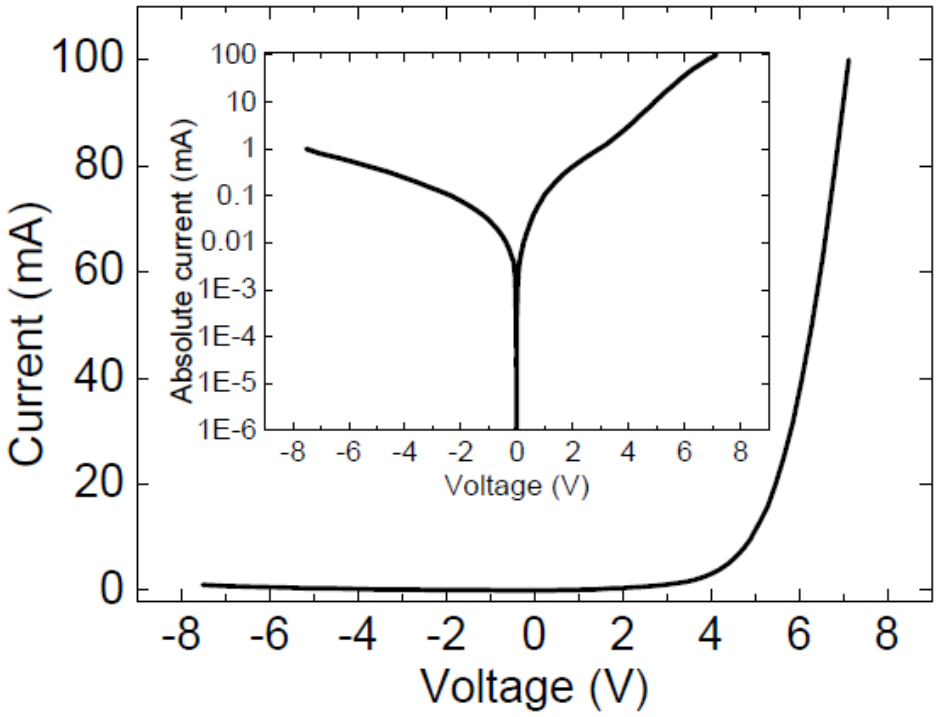

Figure IV. 30. I-V characteristics of a LED. The inset represents the curve in semilogarithmic scale. The forward voltage at 20 mA is ~ 5.5 V.

IV.4.4. Electroluminescence

Electroluminescence (EL) spectra have been collected using an optical fiber, which is connected to a CCD camera. The acquisition time is set to 10 ms. Figure IV. 31 shows the EL spectra of LED-A and LED-B at an injection current of 50 mA. The LED-A has an emission peak at 415 nm, while that of LED-B is 450 nm. The EL energy difference between the two types of LED is due to the different In contents in the (In,Ga)N QWs, which results from the different growth temperatures. A higher growth temperature leads to a lower In incorporation, as well as a higher photon energy. The In contents are 10% for LED-A and 15% for LED-B, as estimated from the transition energies. The peak positions of the LEDs coincide well with the PL spectra shown in Figure IV. 22 and Figure IV. 23. It confirms that the EL comes from recombinations in the (In,Ga)N / GaN MQWs. The FWHM of the EL peak is 21 nm, which is comparable to those of blue LEDs grown on sapphire substrates by MBE[39].

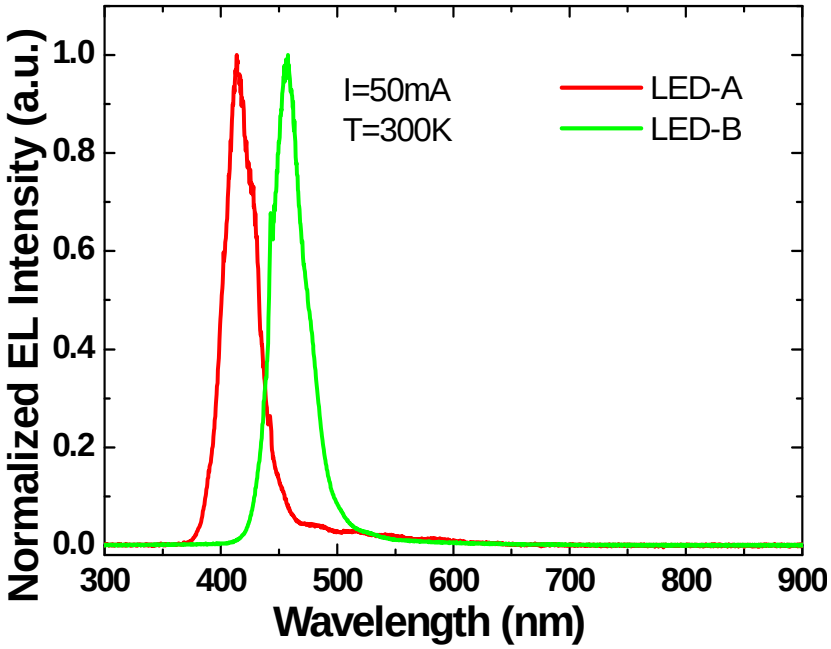

Figure IV. 31. EL spectra of LEDs emitting at a wavelength of 415 nm (LED-A) and 450 nm (LED-B) at a current of 20 mA.

Figure IV. 32 shows the EL spectra of an LED-A device under different injection currents. As expected, the intensity of the EL increases when the injection current increases. At low current injection (below 20 mA), the emission peak blue-shifts as the current increases. It is a typical phenomenon for LEDs grown along the polar [0001] direction, as the QCSE is partly compensated by carrier screening when the current increases.[40] At higher current injection (> 20 mA), the peak position is red-shifted due to the self-heating of the device and

the semiconductor band gap decrease with the increasing temperature. The DLE of ZnO at 490 nm is very weak in all the EL spectra and it does not have a significant influence on the EL color.

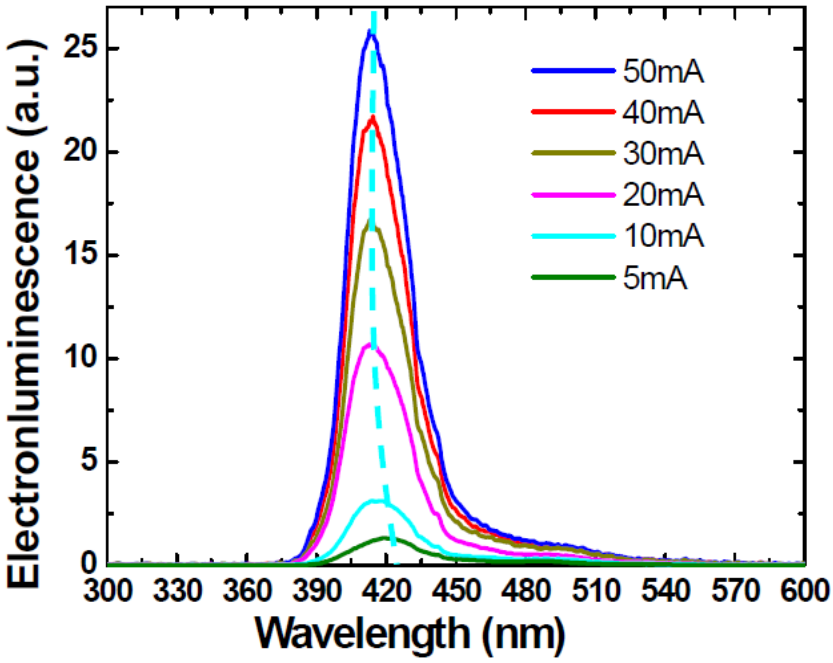

Figure IV. 32. Variation of a LED-A EL spectrum with increasing injection currents.

The output power of the LEDs is recorded using a calibrated Si photodiode from the back side of the LEDs. Figure IV. 33 shows the room-temperature output power under continuous injection conditions as a function of the input current of a LED-A device. The power at 20 mA is 40 µW. As the injection current increases, the output power increases and reaches a maximum of 0.1 mW.

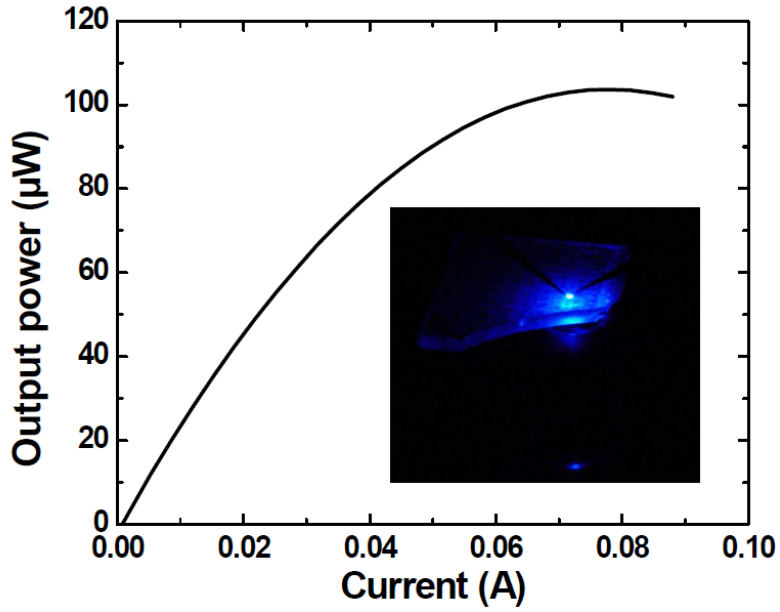

Figure IV. 33. Output power of a LED-A device versus injection current.

Figure IV. 34 compares the optical output power of LEDs grown on different substrates, using MOCVD and MBE. The output power of our LEDs grown on ZnO substrates is still low compared with the current standards of blue LEDs grown by MOCVD on sapphire substrates but importantly, it is already comparable to those of LEDs entirely grown by MBE on Si or sapphire substrates.[41,42] It indicates that ZnO substrates offer an alternative choice for the development of LED technologies using MBE.

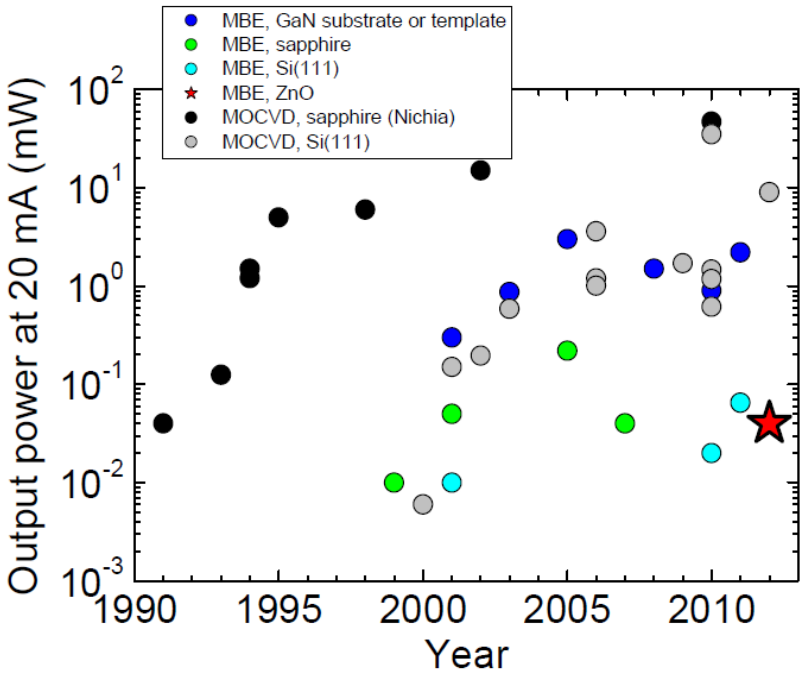

Figure IV. 34. Comparison of optical output powers at 20 mA of different types of LEDs.

IV.5. Conclusions

In this chapter, an annealing process has been developed to prepare the ZnO substrate for the epitaxial growth, and a smooth ZnO surface with atomic steps have been obtained after annealing.

GaN layers with both Ga- and N- polarities have been grown on O face ZnO substrates. The polarity determination mechanism has been analyzed and a $ZnGa_2O_4$ interfacial layer has been identified as the polarity inversion center. The formation of this cubic interfacial layer can be controlled by adjusting the nucleation layer growth temperature and III / V ratio in a NH_3 source MBE. An N-polar layer is obtained when growing GaN directly on O face ZnO (without the formation of an interfacial layer), and a Ga-polar layer is obtained in presence of a $ZnGa_2O_4$ interfacial layer. On the other hand, Ga-polar GaN layers are systematically grown on Zn face ZnO substrates.

Structural and optical properties of GaN layers have been characterized. Thick GaN layers (~ 600 nm) are found to be tensilely strained on ZnO. Donor bound excitons and free excitons related emissions are observed in low temperature (10 K) PL spectra, and thermal quenching behaviors of these emissions have been discussed.

An efficient approach for the fabrication of monolithic nitride light-emitting devices on ZnO by MBE has been demonstrated. A growth process for the fabrication of blue-emitting (In,Ga)N/GaN multi-QW-based LED structures on c-plane (0001) ZnO substrates has been developed. The LED structures show promising optical and electrical characteristics. These characteristics are a further step towards the fabrication of nitride-based optoelectronic devices on ZnO substrates and provide an alternative solution for the development of GaN thin-film engineering.

References

[1] D. Ehrentraut, H. Sato, Y. Kagamitani, H. Sato, A. Yoshikawa, and T. Fukuda., Prog. Cryst. Growth Charact. Mater. **52**, 280 (2006).

[2] S. Nakamura, M. Senoh, S.-I. Nagahama, N. Iwasa, T. Yamada, T. Matsushita, Y. Sugimoto, and H. Kiyoku, Jpn. J. Appl. Phys. **36**, L1059 (1997).

[3] S. Nakamura, M. Senoh, N. Iwasa, and S. Nagahama, Appl. Phys. Lett. **67**, 1868 (1995).

[4] X.-Q. Shen, T. Ide, S.-H. Cho, M. Shimizu, S. Hara, H. Okumura, S. Sonoda, and S. Shimizu, Jpn. J. Appl. Phys. **39**, L16 (2000).

[5] K. Dong, D. Chen, B. Liu, H. Lu, P. Chen, R. Zhang, and Y. Zheng, Appl. Phys. Lett. **100**, 073507 (2012).

[6] X. Gu, M. A. Reshchikov, A. Teke, D. Johnstone, H. Morkoc, B. Nemeth, and J. Nause, Appl. Phys. Lett. **84**, 2268 (2004).

[7] G. Namkoong, S. Burnham, K.-K. Lee, E. Trybus, W. Alan Doolittle, M. Losurdo, P. Capezzuto, G. Bruno, B. Nemeth, and J. Nause, Appl. Phys. Lett. **87**, 184104 (2005).

[8] A. Kobayashi, Y. Kawaguchi, J. Ohta, H. Fujioka, K. Fujiwara, and A. Ishii, Appl. Phys. Lett. **88**, 181907 (2006).

[9] A. Kobayashi, Y. Shirakura, K. Miyamura, J. Ohta, and H. Fujioka, J. Cryst. Growth **305**, 70 (2007).

[10] T. Ohgaki, J. Ceram. Soc. Jpn. **117**, 475 (2009).

[11] M. Mesrine, N. Grandjean, and J. Massies, Appl. Phys. Lett. **72**, 350 (1998).

[12] A. R. Smith, R. M. Feenstra, D. W. Greve, M.-S. Shin, M. Skowronski, J. Neugebauer, and J. E. Northrup, Appl. Phys. Lett. **72**, 2114 (1998).

[13] F. C. Frank, Acta Cryst. **4**, 497 (1951).

[14] B. Heying, E. J. Tarsa, C. R. Elsass, P. Fini, S. P. DenBaars, and J. S. Speck, J. Appl. Phys. **85**, 6470 (1999).

[15] M. Sumiya, K. Yoshimura, T. Ito, K. Ohtsuka, S. Fuke, K. Mizuno, M. Yoshimoto, H. Koinuma, A. Ohtomo, and M. Kawasaki, J. Appl. Phys. **88**, 1158 (2000).

[16] M. Seelmann-Eggebert, J. L. Weyher, H. Obloh, H. Zimmermann, A. Rar, and S. Porowski, Appl. Phys. Lett. **71**, 2635 (1997).

[17] D. A. Stocker, E. F. Schubert, and J. M. Redwing, Appl. Phys. Lett. **73**, 2654 (1998).

[18] J. W. Downs, F. K. Ross, and G. V. Gibbs, Acta Cryst. **B41**, 425 (1985).

[19] H. Yu, S. Wang, N. Li, W. Fenwick, A. Melton, B.Klein, and I. Ferguson, J. Crystal Growth **310**, 4904 (2008).

[20] J. Elsner, M. Haugk, G. Jungnickel, and Th. Frauenheim, Solid State Commun. **106**, 739 (1998).

[21] M. Leroux , B. Beaumont, N. Grandjean, P. Lorenzini, S. Haffouz, P. Vennégues, J. Massies, and P. Gibart, Mater. Sci. Eng. B **50**, 97 (1997).

[22] M. Sumiya, K. Yoshimura, K. Ohtsuka, and S. Fuke, Appl. Phys. Lett. **76**, 2098 (2000).

[23] R. Liu, A. Bell, F. A. Ponce, C. Q. Chen, J. W. Yang, and M. A. Khan, Appl. Phys. Lett. **86**, 021908 (2005).

[24] S. Ghosh, P. Misra, H. T. Grahnb, B. Imer, S. Nakamura, S. P. DenBaars, and J. S. Speck, J. Appl. Phys. **98**, 026105 (2005).

[25] T. Gühne, Z. Bougrioua, P. Vennégues, M. Leroux, and M. Albrecht, J. Appl. Phys. **101**, 113101 (2007).

[26] M. Leroux, N. Grandjean, B. Beaumont, G. Nataf, and F. Semond, J. Appl. Phys. **86**, 3721 (1999).

[27] S. Fischer, C. Wetzel, E. E. Haller, and B. K. Meyer, Appl. Phys. Lett. **67**, 1298 (1995).
[28] B. Monemar, J. Cryst. Growth **189–190**, 1 (1998).
[29] W. Gotz, N. M. Johnson, C. Chen, H. Liu, C. Kuo, and W. Imler, Appl. Phys. Lett. **68**, 3144 (1996).
[30] H. Xing, D. S. Green, H. Yu, T. Mates, P. Kozodoy, S. Keller, S. P. DenBaars, and U. K. Mishra, Jpn. J. Appl. Phys. **42**, 50 (2003).
[31] E. Zacks and A. Halperin, Phy.Rev. B **6**, 3072 (1972).
[32] Z. Liu, J. Ma, X. Yi, E. Guo, L. Wang, J. Wang, N. Lu, J. Li, I. Ferguson, and A. Melton, Appl. Phys. Lett. **101**, 261106 (2012).
[33] W. C. Chong and K. M. Lau, physica status solidi (c) **4**, 2646 (2007).
[34] J. Liu, Y. Zhao, Y. J. Jiang, C. M. Lee, Y. L. Liu, and G. G. Siu, Appl. Phys. Lett. **97**, 231907 (2010).
[35] A. Dussaigne, B. Damilano, J. Brault, J. Massies, E. Feltin, and N. Grandjean, J. Appl. Phys. **103**, 013110 (2008).
[36] A. Weimar, A. Lell, G. Brüderl, S. Bader, and V. Härle, physica status solidi (a) **183**, 169 (2001).
[37] D.-F. Wang, S. Feng, C. Lu, A. Motayed, M. Jah, S. N. Mohammad, K. A. Jones, and L. S.-Riba, J. Appl. Phys. **89** , 6214 (2001).
[38] S. Wang, N. Li, E. Park, Z. Feng, A. Valencia, J. Nause, M. Kane, C. Summers, and I. Ferguson, Phys. Status Solidi C **5**, 1736 (2008).
[39] S. Dalmasso, B. Damilano, N. Grandjean, J. Massies, M. Leroux, J.L. Reverchon, and J.Y. Duboz, Mat. Sci. Eng. B **82**, 256 (2001).
[40] T. Mukai, M. Yamada, and S. Nakamura, Jpn. J. Appl. Phys. **37**, L1358 (1998).
[41] N. Grandjean, B. Damilano, and J. Massies, J. Phys.: Condens. Matter **13**, 6945 (2001).
[42] H. Tang, S. Haffouz, A. Powell, J. A. Bardwell, and J. Webb, Appl. Phys. Lett. **86**, 121110 (2005).

Chapter V. Nonpolar (In,Ga)N heterostructures grown on ZnO (11-20) substrates

In this chapter, the growth of *a*-plane GaN layers on bulk ZnO substrates (*a*-plane) is presented. Two methods, based on the use of either a NH_3 or a plasma source to provide the nitrogen species, have been adapted for the growth of the GaN nucleation layers. The surface morphological, structural and optical properties of GaN layers grown using both methods are studied and compared. In addition, nonpolar and polar (In,Ga)N / GaN MQWs are grown on *a*- and *c*-plane GaN / ZnO templates, respectively. The optical properties of the MQWs are studied and compared.

V.1. Substrate preparation

Like the surface of c-plane ZnO substrate (Section IV.1), a high density of colloidal silica dots and scratches are present on the surface of as-received a-plane ZnO substrates (Figure V. 1 (a)). Therefore, an annealing process is implemented to improve the surface morphology before the growth.

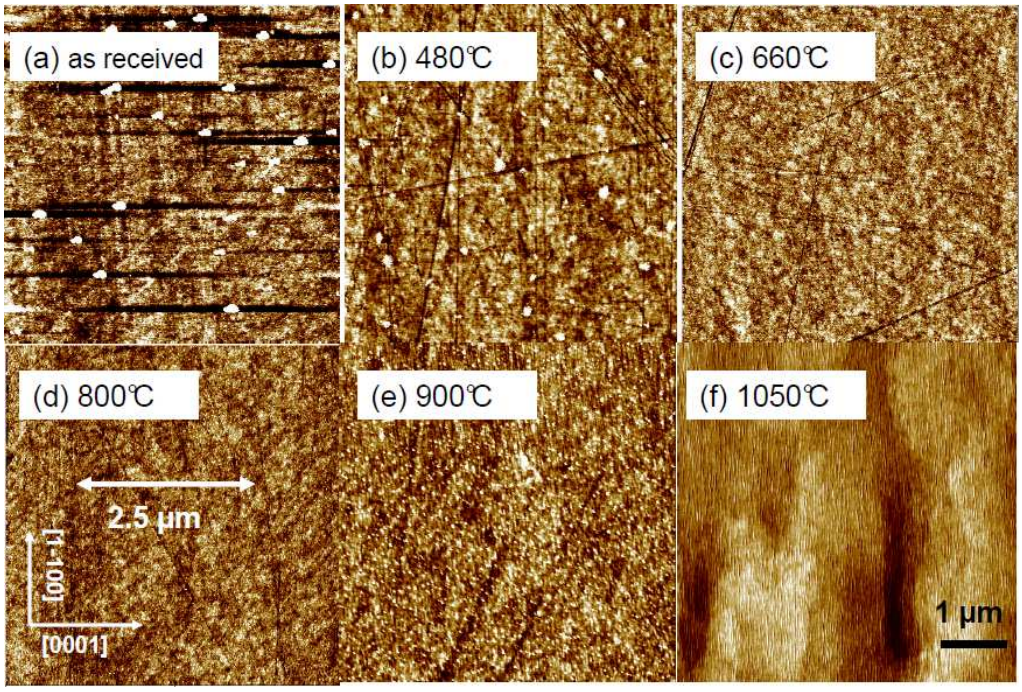

Figure V. 1. A-plane ZnO surface morphologies characterized by AFM. The six images represent the surface of a ZnO substrate (a) as-received, and after annealing at (b) 480 °C, (c) 660°C, (d) 800 °C, (e) 900 °C and (f) 1050 °C, respectively. The vertical scale is 1 nm for (a)-(e), and 5 nm for (f).

The annealing process is carried out under O_2 atmosphere following the method introduced in Section IV.1. Different temperatures have been used to search the most efficient annealing condition for the a-plane substrates. The duration of the annealing process is 2 min. Figure V. 1 shows the surface morphologies of ZnO after annealing at different temperatures, ranging from 480 to 1050 °C. First, the colloidal silica islands can be removed from the surface when the annealing temperature is above 650 °C. Second, the density of scratches is reduced when the annealing temperature is above 770 °C. However, when the temperature is above 900 °C, a high density of dots appears and the surface roughness increases. Finally, if the substrate is annealed at 1050 °C, ordered stripes are observed on the surface, elongated along the *m* $[1\bar{1}00]$ direction. The surface roughness increases significantly to 0.56 nm. Therefore, the typical annealing temperature for *c*-plane substrates (1000 °C) can not be applied to the annealing of *a*-plane substrates.

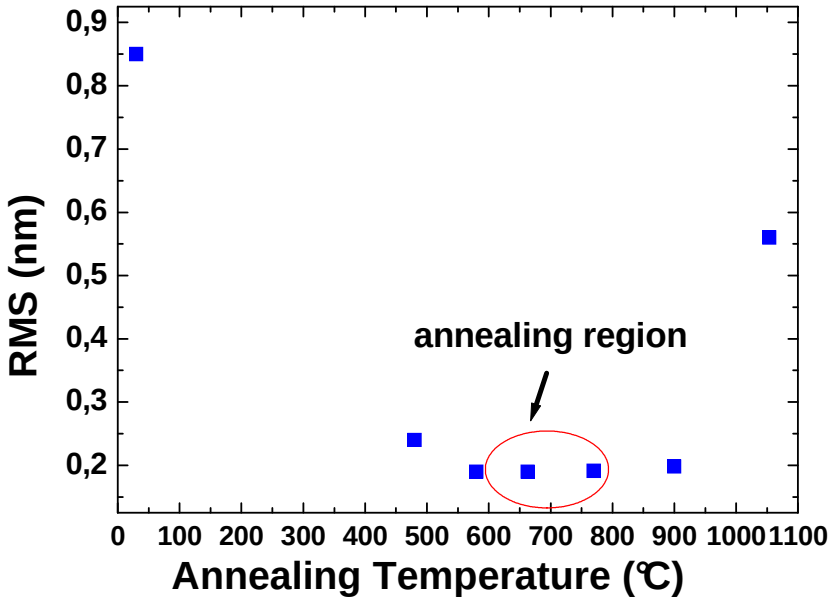

Figure V. 2. Surface roughness of a-ZnO substrates after annealing, as a function of the annealing temperature. The scanning area is 5 x 5 µm^2.

Figure V. 2 shows the surface roughness of *a*-ZnO substrates after annealing, as a function of the annealing temperature. When the temperature is below 600 °C, the rms roughness decreases with temperature due to the evaporation of the colloidal silica. The roughness increases rapidly when the temperature is above 900 °C, as stripes start to appear

on the surface. A stable annealing region, ranging from 600 to 800 °C, is found, where a minimum roughness as low as ~ 0.2 nm can be obtained. Considering that an annealing temperature above 650 °C can remove the scratches, a temperature range between 700 and 800 °C is proposed as the annealing window for a-plane ZnO substrates. However, surface stripes can still be observed from AFM images with larger scan size (30 x 30 μm^2). These stripes have an average width of 2.5 µm, and an average height of 1 nm, as shown in Figure V. 1. They are mainly oriented along the *m*-[1-100] direction. It can be explained by the lower thermal stability of the ZnO basal plane (0001) compared with the prismatic plane (1-100). From this difference, the evaporation rate of ZnO is faster during annealing along the c-<0001> axis, and then, stripes elongated along m-<1-100> are formed. These results indicate that it is difficult to obtain atomically flat surfaces on *a*-ZnO substrates, like the morphology obtained on *c*-ZnO substrates (Section IV.1).

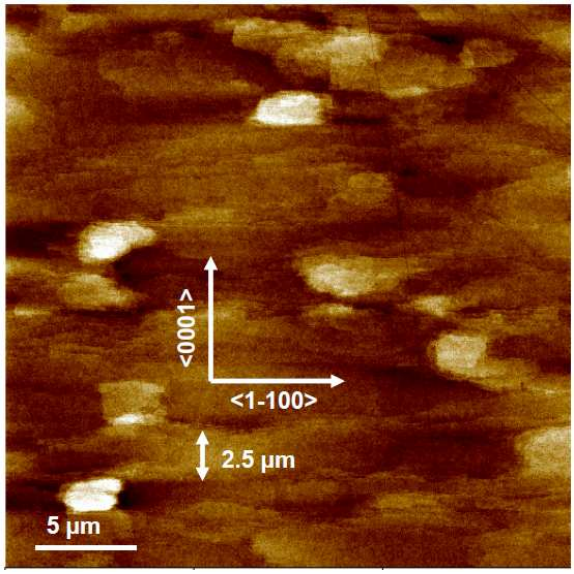

Figure V. 3. Surface morphology of an *a*-ZnO substrate after annealing at 770°C. The vertical scale is 5 nm.

After the annealing procedure, the substrate is introduced into the MBE chamber, and the surface is characterized *in situ* by RHEED. Figure V. 4 shows the diffraction patterns when the incident electron beam is along the <0001> and <1-100> directions. Streaky lines are observed when the incident beam is along the <0001> direction, whereas along the <1-100> direction, 3D spots with a slight V-shape pattern are observed. The spots are attributed to the surface roughness arising from the stripes, and the V-shape pattern results from the reflection of the incident beam on stripe facets.

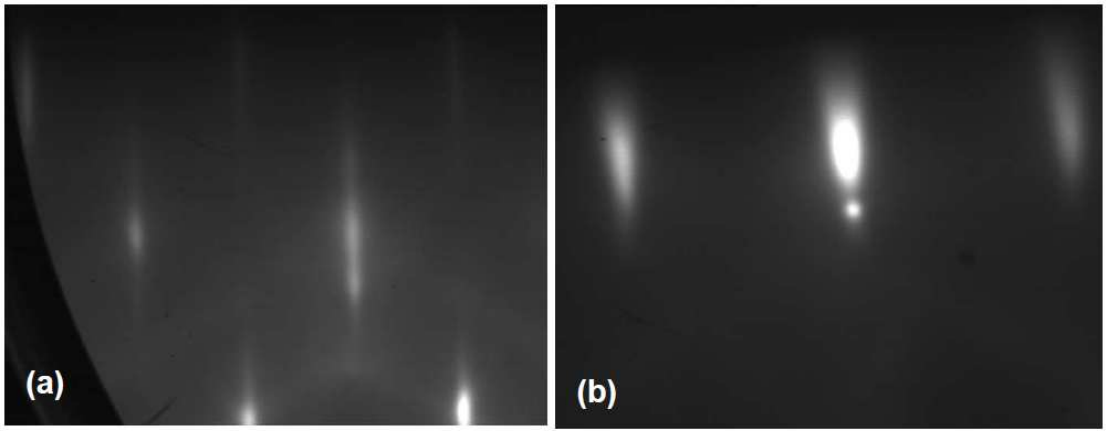

Figure V. 4. RHEED patterns of an a-ZnO substrate surface when the incident electron beam is along the (a) *c*-<0001> and (b) *m*-<1-100> directions, respectively.

V.2. GaN layer growth

V.2.1. GaN layers grown by NH_3 source MBE

The GaN layers are deposited on a-ZnO substrates by MBE. The nitrogen species are provided by the decomposition of NH_3.

The growth is initialized at low temperature to minimize the formation of DGs. A thin GaN layer of 2 nm is deposited at 500 °C. By adjusting the Ga cell temperature and the NH_3 flux, the III / V ratio is set close to unity. Actually, the low RHEED intensity indicates that the growth is slightly under Ga rich condition (Figure V. 5 (a) and (b)). It can be explained by the low cracking efficiency of NH_3 on the low temperature surface of the substrate.[1]

The substrate temperature is then raised to 620 °C and 30 nm GaN is deposited. As shown in Figure V. 5 (c) and (d), the intensity of the diffraction lines increases compared to the nucleation stage. The V / III ratio is slightly above unity in this case, owing to the increased NH_3 cracking efficiency with the substrate temperature. However, the RHEED pattern switches gradually from streaky lines to a spotty pattern along <0001>. It indicates a 3D growth mode of the epitaxial layer. At the same time, some additional points, on both sides of the main diffraction lines (Figure V. 5 (c)), appear. It is the typical feature observed during the 3D growth of *a*-GaN layers. The origin of this feature is attributed to the nucleation of disoriented grains growing on the *a*-GaN surface (Section III.2.2).

The growth temperature is then increased progressively to 760 °C and another 30 nm GaN layer is grown. When the incident beam is along the <0001> direction, the line intensity in the RHEED pattern becomes stronger as the layer thickness increases, indicating the

graduate coalescence of the islands (Figure V. 5 (e)). V-shape patterns are also observed, which locate at the position where the additional points were observed in the previous stage (Figure V. 5 (c)). It may correspond to the redistribution of the disoriented phases after the temperature is increased. These V-shape patterns are only observed along the <0001> direction, suggesting that stripes along this direction start to appear. At this stage, the RHEED pattern remains spotty when the incident beam is along the <1-100> direction (Figure V. 5 (f)).

Finally, a 640 nm thick GaN layer is grown at 800 °C, with a V / III ratio of ~ 2. The RHEED pattern turns to streaky lines when the incident beam is along both directions (Figure V. 5 (g) and (h)), which indicates that a 2D growth mode is achieved. The growth is terminated with the deposition of a 700 nm thick GaN layer in total.

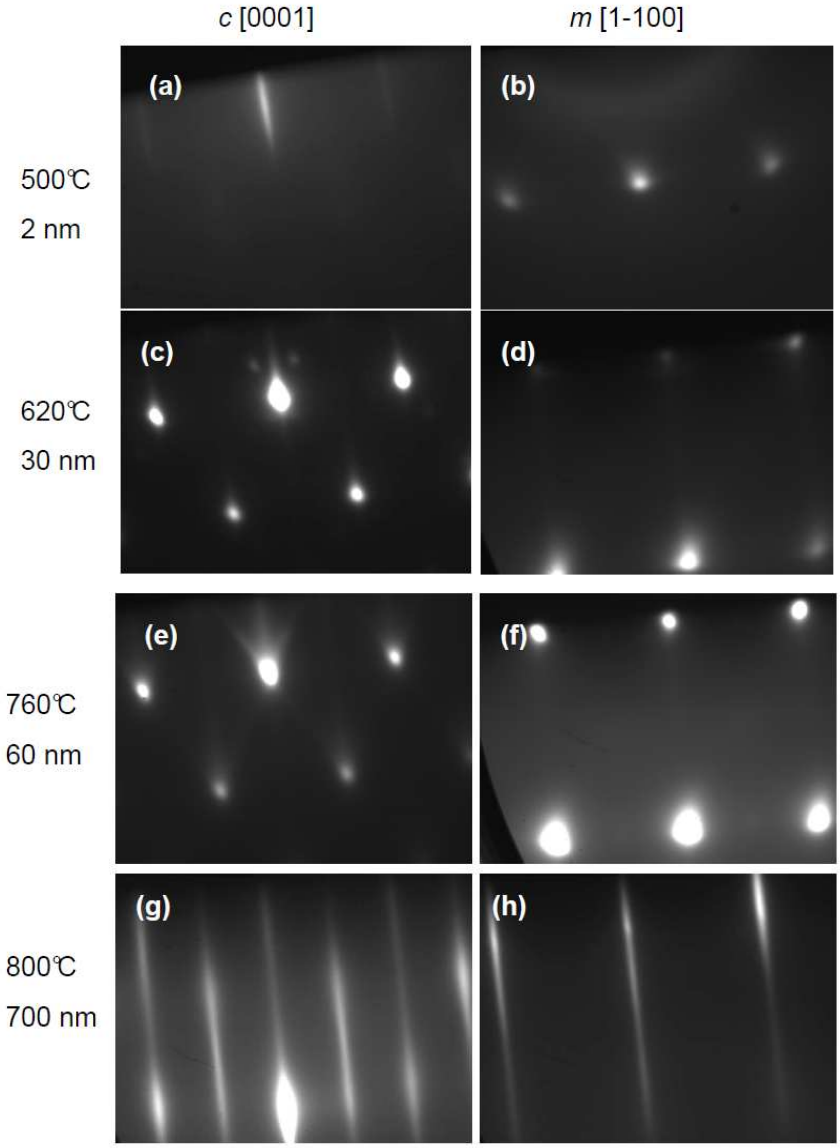

Figure V. 5. Evolution of the RHEED pattern at different stages of the growth, including the diffraction patterns obtained when the incident e-beam is along <0001> and <1-100> directions.

V.2.2. GaN layers with the nucleation layer grown by plasma assisted MBE

The suppression of interfacial reactions and atomic species diffusion requires a low temperature growth (< 600 °C) at the nucleation stage. However, the low cracking efficiency of NH_3 may limit the crystal quality of the nucleation layer. Therefore, a N_2 plasma RF cell is proposed as the nitrogen source for the nucleation layer growth.

In this study, a 100 nm GaN nucleation layer is grown using plasma assisted MBE (PAMBE). The growth is carried out at 400 °C. The N flux is set at a constant value of 0.5-sccm and the RF source at a power of 450 W. A Ga-rich growth mode (III / V > 1) is adopted. The growth rate is 0.2 µm / h, which is determined by the N flux. Figure V. 6 (a) shows the RHEED pattern captured at the end of the nucleation layer growth. The spotty pattern indicates a 3D growth mode of the nucleation layer. It is attributed to the low growth temperature, which limits the diffusion of the adatoms on the substrate surface. The surface morphology of the nucleation layer is characterized by AFM (Figure V. 6 (b)). The surface is covered by islands with an average diameter of ~ 30 nm. The surface rms roughness is 11 nm. No morphological anisotropy is observed at this stage.

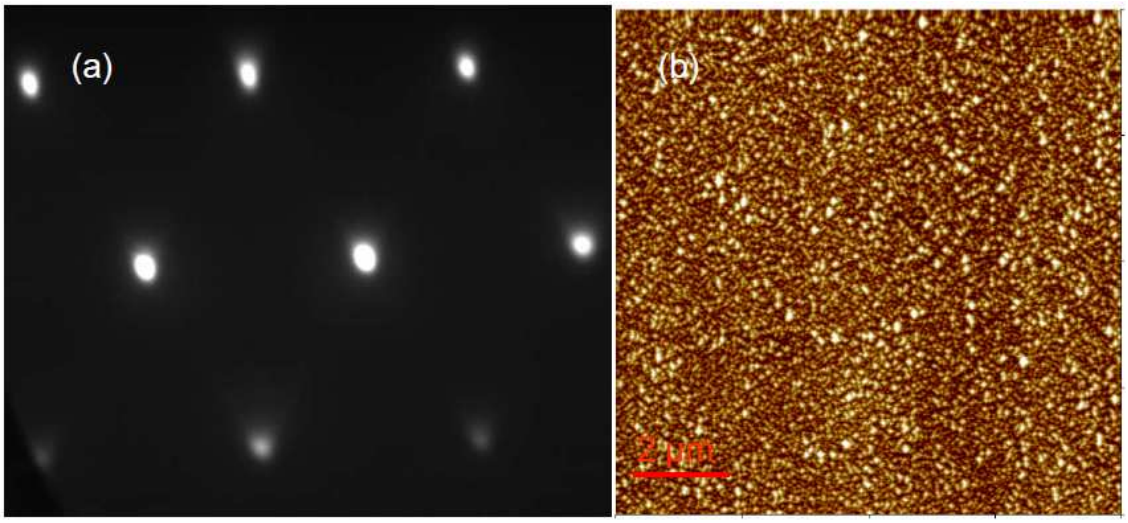

Figure V. 6. (a) RHEED pattern of a 100 nm nucleation layer grown by PAMBE, when the incident beam is along the <0001> direction. (b) Surface morphology of the nucleation layer measured by AFM. The vertical scale is 80 nm.

After the deposition of the nucleation layer, NH_3 is used as the nitrogen source to continue the growth. A 100 nm thick buffer layer is deposited on the nucleation layer, during which the substrate temperature is raised progressively from 550 to 750 °C. The growth is

carried out under strong N rich conditions (V / III > 10). In the last stage, a 500 nm thick GaN layer is grown at 800 °C with a similar III / V ratio. Figure V. 7 shows the RHEED pattern of the GaN surface at the end of the growth. Compared with the PAMBE grown nucleation layer, the lines suggest the coalescence of the islands. However, these lines are still diffuse and spotty, indicating a rough surface morphology.

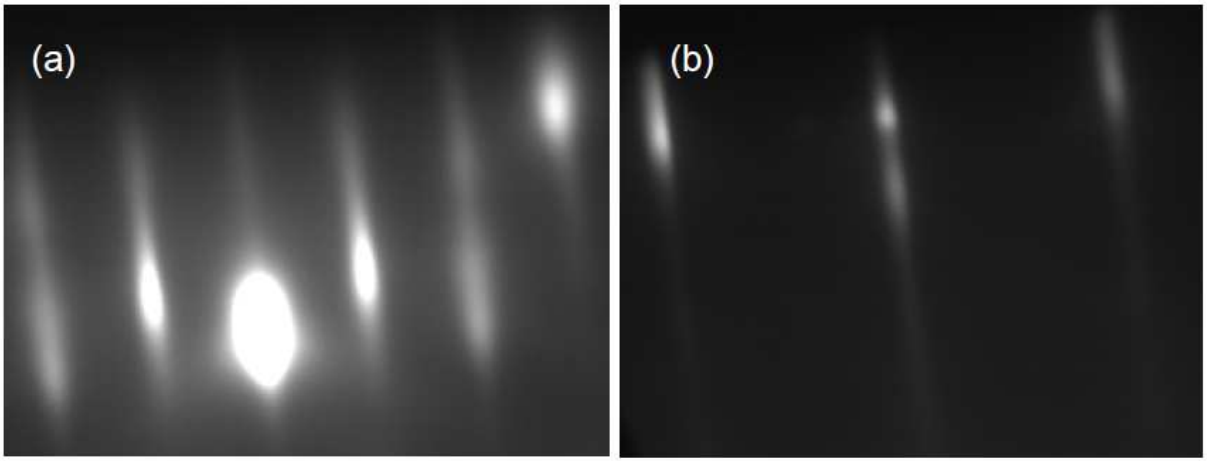

Figure V. 7. RHEED patterns of the GaN surface at the end of the growth, when the electron beam is along the (a) <0001> and (b) <1-100> directions, respectively.

V.3. Structural & optical properties of a-GaN layers

Figure V. 8 (a) shows the surface of the GaN layer completely grown using NH_3, characterized by AFM. Strong stripes along the <0001> direction are present on the surface. This morphology is attributed to the different growth rates of GaN along <0001> and <1-100> directions.[2] The rms roughness is 21 nm.

Figure V. 8 (b) shows the surface of a GaN layer with the nucleation layer grown by PAMBE. A similar morphology with strong stripes oriented along the <0001> direction is observed. The rms roughness is 27 nm. In addition, pits with a density of ~ 2 x 10^7 / cm^2 are present on the surface. Such pits have been observed on *a*-plane GaN grown on r-plane sapphire substrates by NH_3 source MBE.[2] They mainly have a triangular shape, which is very similar to the V-shape defects observed in *c*-GaN layers, but with the triangular cross section in the growth plane (Figure I. 21). Ni *et al.* have shown that the NH_3 flux is the critical factor which influences the formation of the triangular pits, and the density and size of the pits can be dramatically reduced by reducing the NH_3 flux.[2] As a comparison, no pit is formed on the surface of the sample fully grown using NH_3 (Fig. V. 8 (a)). It can be explained by the

reduced NH_3 flux used during the growth of the GaN layer of this sample during the last growth steps (*i.e.* at higher temperatures (750 – 800 °C)) compared with the NH_3 flux used for the same growth sequence in the sample with a buffer layer grown by a N plasma source (leading to a five times lower V / III ratio).

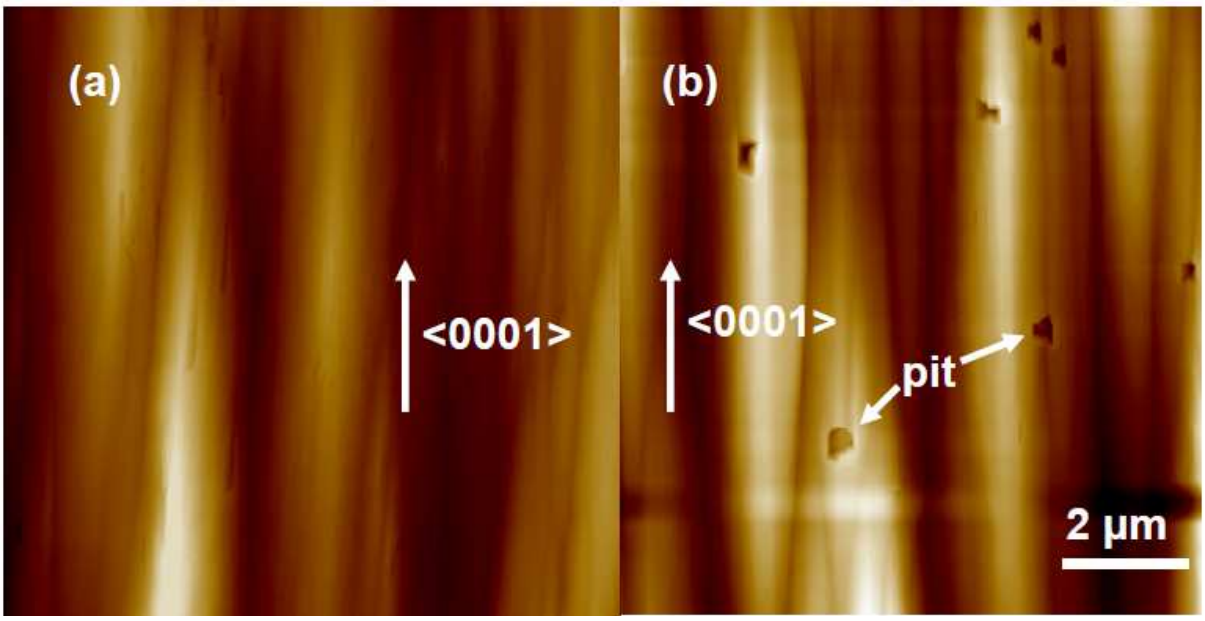

Figure V. 8. Surface morphology of GaN layers (a) grown completely by NH_3 source MBE and (b) with a PAMBE nucleation layer. The vertical scale is 150 nm.

The structural properties of the GaN layers have been characterized by XRD. Figure V. 9 shows the 2θ/ω diagram of the GaN layer grown completely using NH_3. The four main diffraction peaks are related to the ZnO (110), ZnO (220), GaN (110) and GaN (220) planes. It indicates that an *a*-plane GaN phase has been successfully grown on the a-plane ZnO substrate. However, two additional peaks, labelled as I_1 (30°) and I_2 (63°) are also observed. The origin of these peaks is not clear.

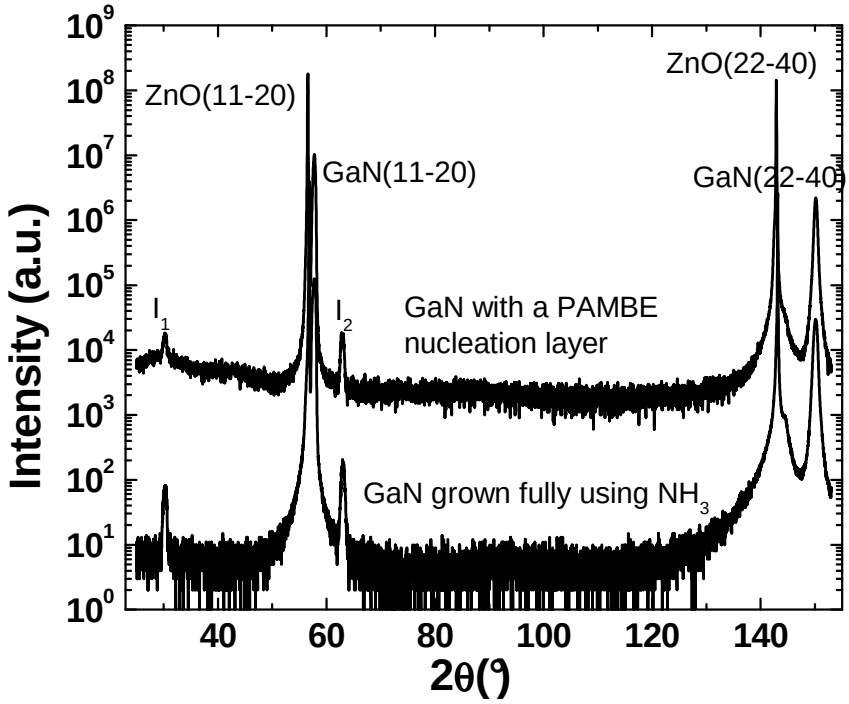

Figure V. 9. XRD 2θ/ω diagram of 0.7 µm-thick GaN layers on *a*-ZnO substrates grown using only NH_3 and using N from a plasma source for the nucleation layer.

Figure V. 10 shows the comparison of the FWHM of GaN (110) rocking curves, between a GaN layer grown on a ZnO / *r*-sapphire template and the GaN layers grown on ZnO bulk substrates (with and without the PAMBE nucleation layer). Similar to the GaN layer grown on the ZnO template, which has been discussed in detail in Section III.2.2, GaN layers grown on bulk a-ZnO substrates show clear anisotropic structural properties. When the incident beam is along the <0001> directions, the GaN (110) rocking curve has a minimum FWHM value of ~ 1500 arcsec, while it has a maximum value when the incident beam is along the <1-100> directions. Similar FWHM values indicate that the GaN layers completely grown by using NH_3 on the ZnO template and the bulk ZnO substrate have close crystal perfection. However, the x-ray rocking curve of the GaN layer grown with a PAMBE nucleation layer shows much lower FWHM values: 798 and 940 arcsec when the incident beam is along *c*- and *m*-axes of GaN, respectively. These values are comparable with the results obtained from growing *a*-GaN on *r*-plane patterned sapphire substrate (PSS) by MOCVD.[3] It means that growing GaN with a low temperature PAMBE nucleation layer can be an effective way to achieve high quality crystals.

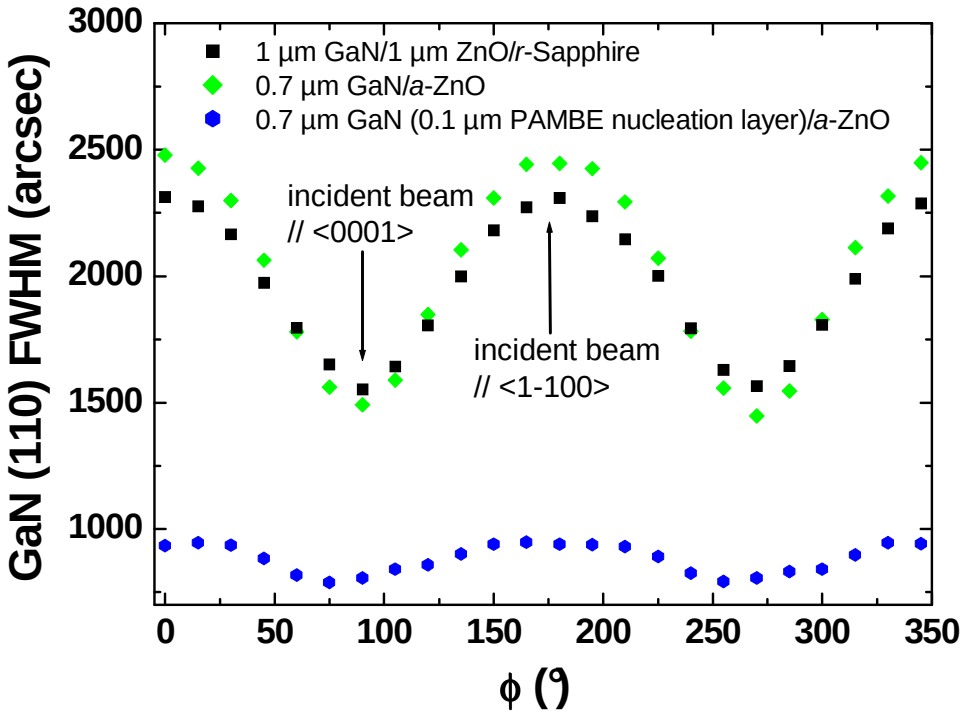

Figure V. 10. FWHM variation of the GaN (110) rocking curve as a function of the φ azimuth angle (the incident beam direction), for GaN layers grown on an *a*-ZnO / sapphire template and on *a*-ZnO bulk substrates (with and without a PAMBE nucleation layer).

Figure V. 11 shows the low temperature PL spectra of the two GaN layers grown on *a*-ZnO substrates. The spectra of both samples are dominated by the emission related to the GaN NBE at 3.472 eV. The NBE emission intensity of the GaN layer with a PAMBE nucleation layer is ~ 30 times stronger than that of the fully NH_3 grown GaN. The FWHM of this peak is 5.9 and 4.2 meV for the GaN layers with and without a PAMBE nucleation layer, respectively. These values are strongly reduced compared with those obtained from the GaN layers grown on ZnO templates (typically 15meV, cf. chap. II section ….). It is seen as the signature of a reduced impurity incorporation during the growth. The 3.36 eV emission peaks in both samples are related to the ZnO substrate, which is indirectly excited by the emission from the GaN epi-layers. The emission from DAPs and their longitudinal optical phonon replica (DAP-LO) can be observed at 3.27 eV and 3.18 eV, respectively. In addition, the origin of the peaks at 3.41 eV (I_1) and 3.39 eV (I_2) is not clear, and they might be ascribed to defect related levels.

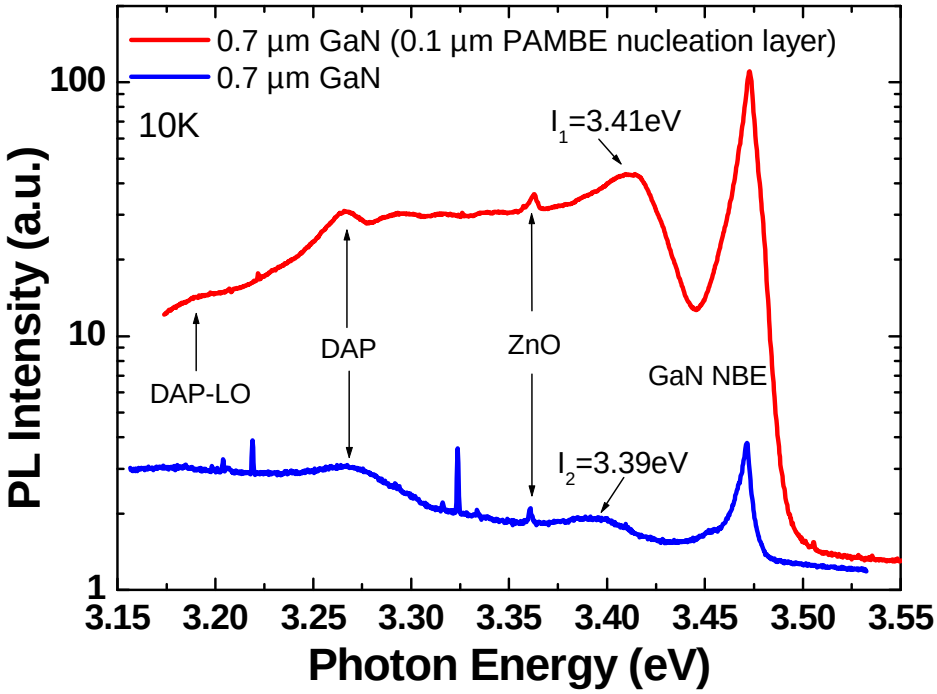

Figure V. 11. PL spectra of a-GaN layers grown on ZnO with and without a PAMBE nucleation layer, recorded at 10 K.

V.4. Comparison of polar and nonpolar (In, Ga)N / GaN MQWs

According to the study of the lattice parameters in Section IV.3.1, GaN layers are tensilely strained on ZnO substrates. Taking advantage of this tensile strain, GaN / ZnO templates should be more suitable for the growth of $In_{1-x}Ga_xN$ layers with high Indium content (x> 15%), due to the larger LPs of $In_xGa_{1-x}N$ alloys compared with GaN. This property is important for the fabrication of light emitting devices emitting at long wavelengths (> 500 nm). However, the In incorporation rate in the (In,Ga)N layers is influenced by many factors. Besides the lattice mismatch between the $In_{1-x}Ga_xN$ layer and the GaN template, as well as the growth conditions, the crystal orientation may also influence the In incorporation rate when growing $In_{1-x}Ga_xN$ layers. For instance, the In incorporation is very different between $In_{1-x}Ga_xN$ layers grown on different planes. Browne *et al.* have shown that growing on the semipolar (20-21) and the nonpolar *m*-(1-100) planes exhibit higher In incorporation efficiency than on the c-plane, while the In incorporation efficiency is lower on the semipolar (11-22) plane.[4] Therefore, it is important to compare the In incorporation efficiency between

c- and *a*-plane $In_{1-x}Ga_xN$ layers, as well as the optical properties of c- and a-plane $In_xGa_{1-x}N$ / GaN MQWs.

In this study, four (In,Ga)N / GaN MQW heterostructures were grown on both c- and a-plane GaN templates. The structures of the samples are listed in Table V. 1. The GaN templates, including a ~ 500 nm thick Si doped n-type GaN layer and a ~ 0.8 µm thick GaN buffer layer, were grown on *c*- (O face) and *a*-plane ZnO substrates. The MQW heterostructures consist of ten (In,Ga)N / GaN quantum wells (QWs). The GaN barrier thickness is 10 nm, and the (In, Ga)N well thickness is 1.5 nm. The growths were carried out under similar conditions, including the same NH_3 flux and the same Ga and In fluxes (with beam equivalent pressures of $1.1x10^{-7}$ and $8.0x10^{-8}$ Torr for Ga and In, respectively). To compare the In incorporation properties on c- and a-oriented layers, samples D469 and D472 were grown on c- and *a*-plane templates using the same temperature (560 °C), respectively. Samples D470 and D471 were grown at a higher temperature (580 °C) on c- and *a*-plane templates, respectively.

Sample name	Growth plane	GaN template	(In,Ga)N layer Growth temperature	GaN barrier thickness	(In,Ga)N well thickness	QW number
D469	c-plane	0.5 µm GaN:Si /0.8 µm GaN	560 °C	10 nm	1.5 nm	10
D470	c-plane	0.5 µm GaN:Si /0.8 µm GaN	580 °C	10 nm	1.5 nm	10
D471	a-plane	0.5 µm GaN:Si /0.8 µm GaN	580 °C	10 nm	1.5 nm	10
D472	a-plane	0.5 µm GaN:Si /0.8 µm GaN	560 °C	10 nm	1.5 nm	10

Table V. 1. Description of the structures and growth conditions of the (In,Ga)N/GaN MQWs studied in this section.

The optical properties of the MQWs were investigated by PL. The four samples were cooled down to 10 K and excited by a double-frequency Ar^+ laser (λ =244 nm). Figure V. 12 shows the low temperature PL spectra. The main emission peak of sample D469 locates at

401 nm (~ 3.09 eV), which is attributed to the emission from the MQWs. By assuming an internal electric field in the (In,Ga)N well as ~ 2.2 MV/cm when the In content is 20%,[5,6] the field can be estimated approximately by a linear interpolation method when the In content is low (< 15%). According to the emission energy, the Stokes shift in this QW is assumed to be in the range of 0 - 80 meV.[7] Therefore, the In content in (In,Ga)N layer of sample D469 is estimated to be 12 ± 1%, according to the envelop function calculation of the QW energy levels. The FWHM of this peak is 16 nm. The peaks related to the GaN layer and the ZnO substrate can be observed at 357 nm (3.47 eV) and 369 nm (3.36 eV), respectively. The MQW related emission peak in D472 locates at 372 nm (~ 3.33 eV), which is ~250 meV higher in energy than that of the *c*-plane MQWs. The FWHM of this peak is 9.6 nm, which is much lower than that of D469. By assuming the absence of the internal electric field and a Stokes shift range of 0 – 30 meV in the *a*-plane MQWs,[7] the In content is estimated to be 6 ± 1% in sample D472. The comparison of the In contents in sample D469 and D472, which are grown under the same conditions, indicates that it is more difficult to incorporate In in *a*-plane compared with the *c*-plane (In, Ga)N layers. When the (In,Ga)N layers are grown at 580 °C, the incorporated In contents are lower than those grown at 560 °C in both *a*- and *c*- plane cases, as indicated by the shorter MQW emission wavelengths. The emission intensity of *a*-plane MQWs is ~ 10 times lower than that of *c*-plane MQWs, due to the lower crystal quality. These results coincide with the conclusions obtained from the (In,Ga)N/GaN MQWs grown on sapphire substrates.[8] It suggests that specific growth conditions should be developed to optimize the fabrication of higher In content (In,Ga)N layers on *a*-plane surfaces.

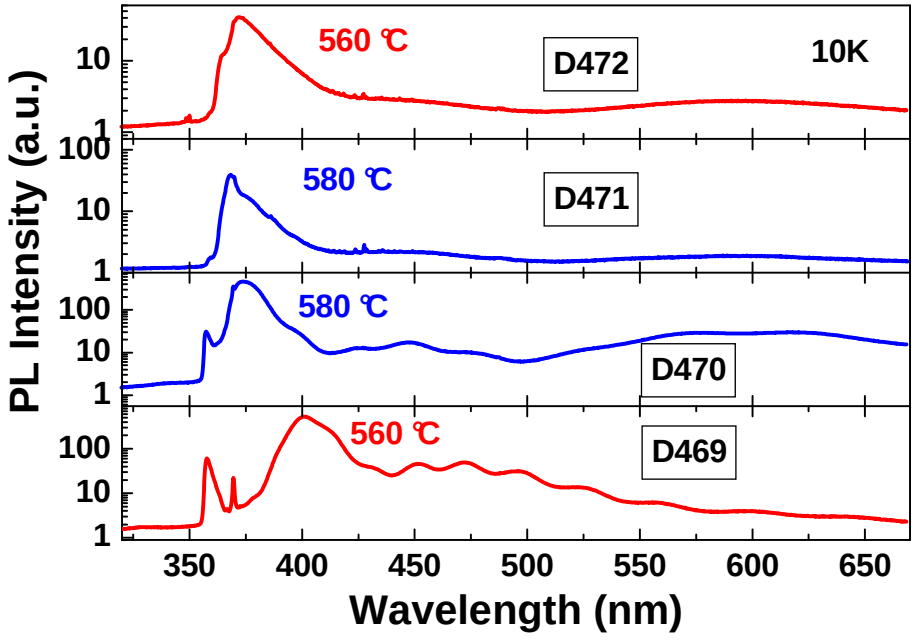

Figure V. 12. PL spectra of *c*- (D469 and D470) and *a*- (D471 and D472) plane (In,Ga)N / GaN MQWs recorded at 10 K (same intensity scale for each sample).

The emission peak of the MQWs in D470 locates at 373 nm (~ 3.32 eV), which is very close to that of the D472 (*a*-plane MQWs). Due to the similarity of the QW confinement energy in D470 and D472, temperature dependent PL measurements were performed on these samples to compare the QW confinement properties of the polar and nonpolar MQWs. Figure V. 13 shows the Arrhenius plot of the integrated QW emission intensity as a function of temperature, performed on samples D470 and D472, and the experimental curves are fitted using Eq IV.4. In the case of sample D470, a single quenching channel with an activation energy of 125 meV is deduced from the best fit. This activation energy is close to the QW confinement energy (~ 150 meV), which is calculated from the energy difference between the GaN barrier and the QW emission (Rydberg energies have been considered). Therefore, the quenching of D470 MQW emission is mainly attributed to the escape of the carriers from QWs to GaN barriers.

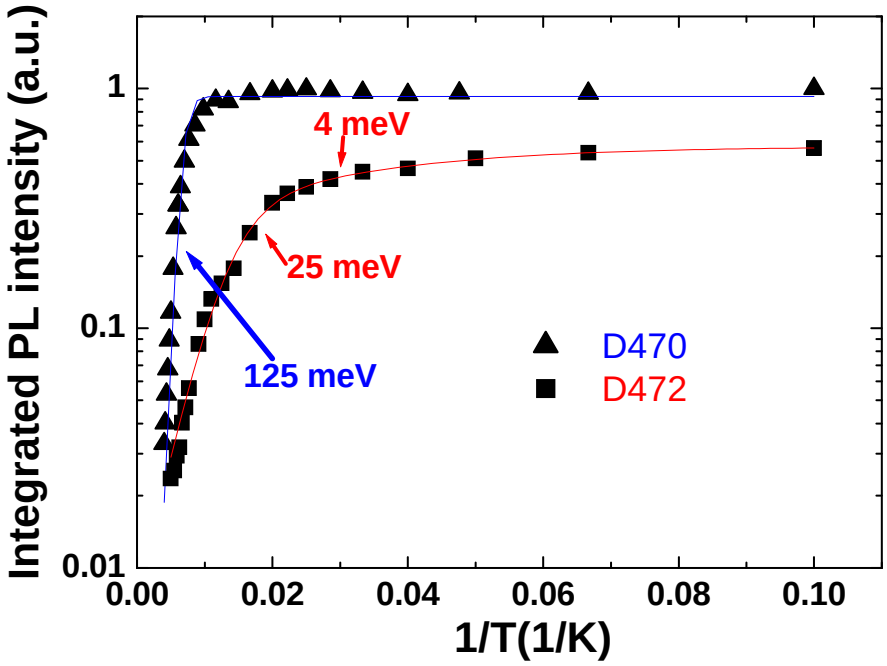

Figure V. 13. Arrhenius plot of the temperature dependence of the integrated PL intensity of c-plane (D470, triangular) and a-plane (D472, square) (In,Ga)N / GaN MQWs.

A similar fitting is performed on sample D472. As the temperature increases, the intensity of the a-plane MQW emission diminishes much faster than that of the c-plane MQW. Two quenching channels are deduced. Channel 1 has an activation energy of ~ 4 meV. It may correspond to the activation of excitons from localized states in the MQWs to free states,

which enables the excitons to be captured by non-radiative recombination centers. Channel 2, which has an activation energy of 25 meV, has a stronger impact on the quenching of the MQW emission. As the QW confinement energy is much higher (~ 150 meV), it means that the QW emission is quenched through this channel before the escape of carriers to the barrier. It may be attributed to some defect related non-radiative recombination centers in *a*-plane MQWs. These results suggest that our *c*-plane MQWs have high crystal quality, and *a*-plane MQWs are more defective than *c*-plane MQWs.

The QCSE can be an important factor influencing the transition energy of the MQWs, especially in the polar case. To investigate the internal electric field in the QW, excitation power dependent measurements are performed on both *c*- and *a*-plane MQWs. The samples are excited by a double-frequency Ar^+ laser (244 nm) at 10 K. An optical density is placed in front of the laser beam to adjust the intensity of the beam reaching the sample surface.

Figure V. 14 shows the low temperature PL spectra of the (In,Ga)N / GaN MQWs under different excitation powers. In both *c*- and *a*- plane cases, no clear shift of the peak positions of the MQW emission is observed (although a slight shift of ~ 10 meV can be estimated in the *c*-plane case), when the excitation power was increased over three orders of magnitude (from 20 μW to 20 mW). It means that the screening effect of interfacial charges normally observed in the polar MQWs is very weak,[7] probably due to the thin QW layer and the low In content. It also suggests that there is no internal electric field in the *a*-plane (In, Ga)N / GaN MQWs, which supports the previous assumption when estimating the In content.

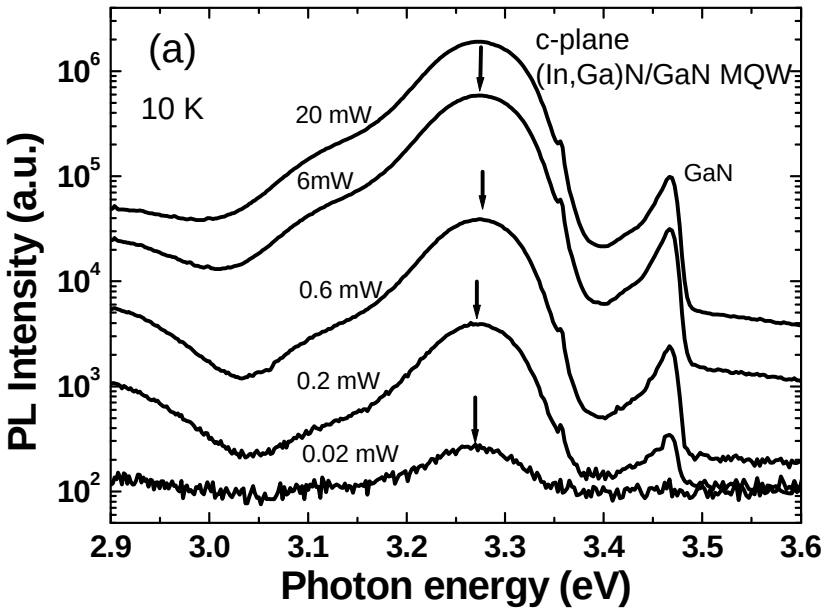

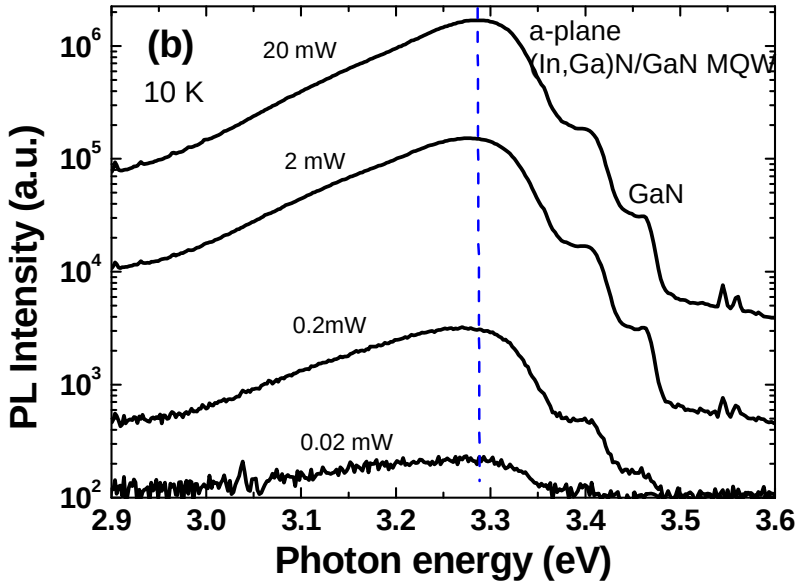

Figure V. 14. Low temperature (10 K) PL spectra of (a) c-plane and (b) a-plane (In,Ga)N / GaN MQWs as a function of the excitation power.

Finally, the optical polarization properties of the polar and nonpolar MQWs are compared. The polarization measurements are performed on samples D470 and D472, following the method introduced in Section III.2.5. Figure V. 15 presents the variation of the integrated PL intensity of the MQWs as a function of the electric field oscillation angle. It shows that the emission from the c-plane MQW is isotropic, and that of the a-plane MQWs is strongly polarized along the m-axis of the wurtzite crystal.

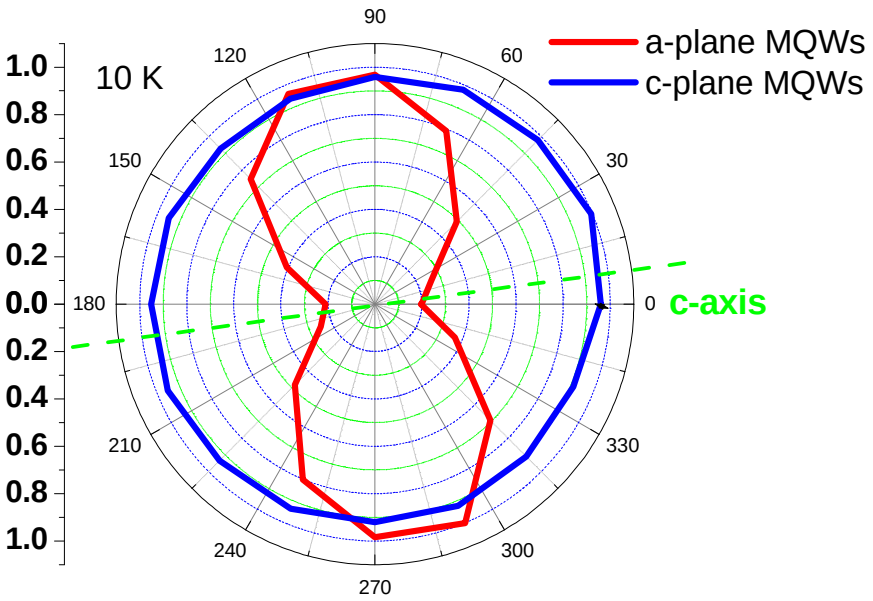

Figure V. 15. Integrated PL intensity of the (In,Ga)N / GaN MQW emission as a function of the oscillation angle of the electric field E, from *a*- and *c*-plane MQWs. The dotted line indicates the direction of the c-axis of the epi-layer.

To understand the polarization behaviour of the nonpolar MQWs, the oscillator strengths between the conduction band and the three sub-valence bands of the (In,Ga)N layers are simulated using the **k•p** method introduced in Section I.2.

In the first step, the lattice parameters of the GaN layer are determined following the XRD method introduced in Section III.2.4. The obtained results are listed in Table V. 2. The lattice constants represented by ***a***, ***b*** and ***c*** have been illustrated in Figure III.18. Considering the (In,Ga)N layers in the heterostructures are very thin (1.5 nm), it is reasonable to assume that they are coherently grown on the GaN layer and no strain relaxation process has occurred. Therefore, the in-plane lattice constants of the (In,Ga)N layers, ***a*** and ***c***, are equal to that of the GaN layer. As the In content in D472 has been estimated to be 6 %, the lattice constants of the relaxed $In_{0.06}Ga_{0.94}N$ layer can be deduced from the lattice constants of bulk GaN and InN materials following Vegard's law, and the results are listed in Table V. 2.

sample	b ($\AA$)	a ($\AA$)	c ($\AA$)
D472	3.1883	5.5223	5.1908
$In_{0.06}Ga_{0.94}N$	3.210	5.560	5.2163
Bulk InN[8]	3.5376	6.1273	5.7064
Bulk GaN	3.189	5.5235	5.185
Bulk ZnO	3.250	5.6292	5.207

Table V. 2. Measured lattice parameters of the GaN layer in sample D472, compared with lattice parameters of bulk GaN, InN, ZnO and fully relaxed $In_{0.06}Ga_{0.94}N$.

The residual strain in the (In,Ga)N layers along the two in-plane directions can be obtained following Eq. III.4: ε_{yy} = - 0.67% and ε_{zz} = - 0.49%. The strain along the growth direction ε_{xx} can be deduced from the in-plane strains following Eq. I.10, by assuming that the stress along the growth direction equals zero. A tensile strain of 0.39% is obtained.

Finally, the k•p method is applied to the (In,Ga)N alloy and the transition matrix elements between the conduction band and the sub-valence bands are simulated. In this simulation, the deformation potential parameters D_1-D_5, the crystal field spitting energy Δ_1 and the spin-orbit splitting energy $3\Delta_2$ of the (In,Ga)N alloy is assumed to obey Vegard's

law.[9] These parameters are calculated from the parameters of the two end point materials, GaN and InN, and listed out in Table V. 3.

Parameters	GaN[10]	InN[11]	$In_{0.06}Ga_{0.94}N$
D_1 (eV)	-41.4	-3.7	- 39.1
D_2 (eV)	-33.3	4.5	-31.0
D_3 (eV)	8.2	8.2	8.2
D_4 (eV)	-4.1	-4.1	-4.1
D_5 (eV)	-4.7	-4.0	-4.6
Δ_1 (meV)	9.2[12]	19.0	9.8
$3\Delta_2$ (meV)	18.9[12]	5.0	18.1

Table V. 3. Deformation potentials, crystal field spitting energies and spin-orbit splitting energies of GaN, InN and fully relaxed $In_{0.06}Ga_{0.94}N$ deduced from Vegard's law.

Table V. 3 shows the simulation results of the oscillator strengths between the conduction band and the sub-valence bands. The excitons are noted as X_1, X_2 and X_3 from the lowest to the highest transition energy (Section III.2.5). It indicates that the X_1 exciton, which contributes to the largest part of the emission, is polarized along the [1-100] direction. This result is in good agreement with experimental observations, which means that the polarization behaviour of the (In,Ga)N / GaN MQWs is mainly determined by the selection rules of the X_1 exciton.

Therefore, a laser diode based on (In,Ga)N / GaN MQWs may benefit from the polarization properties of the nonpolar MQWs. By designing the ridge direction of the waveguide along the [0001] direction, the optical gain of the transverse electric field (TE) mode, which has the electric field oscillating along the [1-100] direction, may be enhanced due to the strong coupling between the waveguide mode and the MQW emission.

Exciton	*x* [11-20]	*y* [1-100]	*z* [0001]
X_1	0.002	0.967	0.030
X_2	0.010	0.029	0.961
X_3	0.987	0.004	0.009

Table V. 4. Simulated oscillator strengths of the transitions between the conduction band and the three sub-valence bands, based on the (In,Ga)N strain states of sample D472. The oscillator strengths are normalized and listed along three orthogonal directions.

V.5. Conclusions and perspectives

The annealing process of *a*-plane ZnO substrates has been studied, and a temperature range of 700-800 °C under O_2 is proposed as the annealing condition. NH_3-MBE and PAMBE are used to grow the GaN nucleation layers on *a*-ZnO substrates. The **a**-plane GaN layers, with two types of nucleation layers, have been grown successfully on *a*-ZnO substrates and the structural and optical properties are compared. GaN layers with a layer grown using N plasma source show higher crystal perfection and stronger PL emission.

In the second part, polar and nonpolar (In,Ga)N / GaN MQWs have been fabricated on *c*- and *a*-plane GaN / ZnO templates, respectively. The PL emission from the MQWs is observed in both cases. The In incorporation efficiency of *a*-plane (In,Ga)N layers is found to be lower than that of *c*-plane layers, under the same growth conditions. When the temperature increases, the nonpolar MQW emission intensity decreases faster than the polar case, and possible quenching processes have been analyzed. Finally, the nonpolar MQW emission is polarized along the [1-100] direction due to the break of the in-plane symmetry, in agreement with the theoretical investigation of the transition matrix elements between the conduction band and the valence band based on the **k•p** theory.

In the future, a full PAMBE growth process should be developed and optimized, as the adaption of a PAMBE nucleation layer has improved the structural and optical properties of GaN. The growth process of (In,Ga)N layers should be optimized to enhance the In incorporation efficiency on the *a*-plane surface. The growth on *m*-plane ZnO substrates, along which orientation a higher In incorporation efficiency has been reported,[4] should be investigated. Finally, nonpolar nitrides based LEDs on ZnO substrates should be fabricated.

References

[1] M. Mesrine, N. Grandjean, and J. Massies, Appl. Phys. Lett. **72**, 350 (1998).

[2] X. Ni, Y. Fu, Y. T. Moon, N. Biyikli, and H. Morkoç, J. Crystal Growth **290**, 166 (2006).

[3] G. Yoo, H. Park, D. Lee, H. Lim, S. Lee, B. Kong, H. Cho, H. Park, H. Lee, and O. Nam, Curr Appl Phys. **11**, S90 (2011).

[4] D. A. Browne, E. C. Young, J. R. Lang, C. A. Hurni, and J. S. Speck, J. Vac. Sci. Technol. A **30**, 041513 (2012).

[5] F. Bernardini and V. Fiorentini, Phys. stat. sol. (b) **216**, 391 (1999).

[6] K.-M. Song, J.-M. Kim, B.-K. Kang, D.-H. Yoon, S. Kang, S.-W. Lee, and S.-N. Lee, Appl. Phys. Lett. **100**, 212103 (2012).

[7] R. W. Martin, P. G. Middleton, K. P. O'Donnell, and W. Van der Stricht, Appl. Phys. Lett. **74**, 263 (1999)

[8] M. F. Wu, S. Q. Zhou, A. Vantomme, Y. Huang, H. Wang, and H. Yang, J. Vac. Sci. Technol. A **24**, 275 (2006).

[9] J. Bhattacharyya, S. Ghosh, and H. T. Grahn, Appl. Phys. Lett. **93** (5), 051913 (2008).

[10] S. Ghosh, P. Waltereit, O. Brandt, H. T. Grahn, and K. H. Ploog, Phys. Rev. B **65**, 075202 (2002).

[11] I. Vurgaftman and J. R. Meyer, J. Appl. Phys. **94**, 3675 (2003).

[12] P. Misra, U. Behn, O. Brandt, H. T. Grahn, B. Imer, S. Nakamura, S. P. DenBaars, and J. S. Speck, Appl. Phys. Lett. **88**, 161920 (2006).

Conclusions and perspectives

This research was carried out at the Centre de Recherche sur l'Héthéro-Epitaxie et ses Applications of the Centre National de la Recherche Scientific (CRHEA-CNRS) in Sophia Antipolis, France.

This work was partly supported by the Agence National de Recherche (ANR) under the framework of the ‘‘HENOPOIN2’’ project.

The main aim of this work was to investigate the integration of nitrides based heterostructures on (Zn,Mg)O, on both polar and nonpolar planes. The growths were carried out by molecular beam epitaxy (MBE). The structural and optical properties of the heterostructures have been characterized and discussed. The conclusions of this study mainly consist of five parts:

1. **The preparation of *c*- and *a*- plane ZnO substrates.** High densities of colloidal silica dots and scratches are present on the surface of as-received ZnO substrates. An annealing process was carried out to obtain a smooth surface. Annealing at 1000 °C under O_2 atmosphere for two minutes has been found to be an optimal annealing condition for *c*-plane ZnO substrates. After this annealing process, a smooth surface (*rms* ~ 0.2 nm) with atomic steps was obtained. The annealing of *a*-plane ZnO surfaces is more difficult. A temperature range between 700 – 800 °C was found to be the most adapted, which is much lower than that of *c*-ZnO. After annealing, colloidal silica dots and scratches were efficiently removed. However, stripes along the [1-100] direction were still observed, owing to the different atomic evaporation rate between *c*- and *m*-planes.

2. **The growth of *a*-plane (Al,Ga)N heterostructures on (Zn,Mg)O / *r*-sapphire templates.** A-plane GaN layers have been grown on (Zn,Mg)O templates with different Mg contents. Stripes are observed along the <0001> direction due to a faster GaN growth rate along the *c*-axis. The Mg content in the (Zn,Mg)O templates was found to have a strong influence on the quality of GaN epi-layers. When the Mg content is in the range of 25 - 40%, GaN epilayers have the highest crystal perfection and lowest density of disoriented grains. It is attributed to the higher surface stability and smoother morphology of (Zn,Mg)O compared to ZnO. The near band edge emission of GaN dominates the low temperature PL spectrum, and the NBE emission was found to be polarized along the <0001> axis. By taking into account the anisotropic in-plane strain of the GaN layer, **k•p** calculation was performed to calculate the excitonic transition energy and oscillator strengths between the conduction band

and the valence band. The PL emission was found to be mainly contributed by X_2 exciton recombinations. A group of $Al_{0.2}Ga_{0.8}N$ / GaN MQWs, with well thicknesses ranging from 0.5 to 7 nm, were fabricated on the *a*-GaN layers. As the QW thickness increases, no energy drop due to the presence of an internal electric field was observed, which indicates the absence of quantum confined Stark effect in the nonpolar heterostructures.

3. **The study of the polarity determination mechanism of GaN layers grown on *c*-plane ZnO substrates.** Ga- and N polar GaN layers have been grown on O face ZnO substrates, and it was found that interfacial reactions play an important role in the polarity inversion. The formation of a $ZnGa_2O_4$ interfacial layer between the ZnO substrate and the GaN layer can be controlled by adjusting the growth temperature and the III / V ratio during the GaN nucleation layer growth. When the nucleation layer was grown in Ga rich conditions, a $ZnGa_2O_4$ interfacial layer was formed and a Ga-polar GaN was grown. On the other hand, when the nucleation layer was grown in N rich conditions, the GaN layer was grown directly on the surface of the ZnO substrate (O face), and a N polar GaN layer was obtained. The Ga- and N- polar GaN layers show specific structural and optical properties (surface morphology, chemical stability, and photoluminescence, *etc.*). Meanwhile, Ga polar GaN layers were always grown on Zn face ZnO substrates, independently of the nucleation layer growth temperature.

4. **The demonstration of blue light emitting diodes on ZnO substrates.** Light Emitting Diode (LED) structures, including GaN *p*-*n* junctions and (In,Ga)N MQWs, have been grown on *c*-plane ZnO substrates. The O non-intentional incorporation has been reduced by adapting a low temperature nucleation layer, which mainly arises from the substrate back etching by NH_3 and atomic out diffusion. *P*-type GaN layers were successfully grown on ZnO, overcoming the compensation effect of the O level. The diodes show clear rectification behaviour, with voltages of 4 -5 V at 20 mA. By adjusting the (In,Ga)N layer growth temperature, LEDs with EL emission ranging from 415 to 450 nm were fabricated. A homogeneous blue emission is observed. An optical output power of ~ 40 μW is obtained at 20 mA injection current and saturated at ~ 0.1 mW when the injection current reached 100 mA. These values are comparable with LEDs grown directly on sapphire substrates by MBE.

5. **A-plane (In,Ga)N heterostructures grown on bulk *a*-ZnO substrates.** In the first step, *a*-plane GaN layers have been grown on *a*-ZnO substrates. Two methods were used to grow the nucleation layers, using either NH_3 or N plasma as N sources. Structural and optical properties of *a*-GaN layers have been studied. The GaN layers grown with a N plasma

nucleation layer show higher crystal perfection and stronger PL emission intensities. C- and a-plane (In,Ga)N / GaN MQWs have been grown on bulk ZnO substrates. Using similar growth conditions, the In incorporation efficiency was found to be lower on *a*-plane surfaces than on *c*-plane surfaces, which is estimated from the QW transition energies. The emission from the *a*-plane MQWs was found to be strongly polarized along **E** // *m* direction, which agrees with the selection rules determined by the transition matrix elements between conduction and valence bands.

The above results indicate that ZnO is a promising material as a substrate for GaN. It opens the possibility of using ZnO substrates to fabricate nitride based optoelectronic devices, on both polar and nonpolar planes. A series of studies should be carried out for the further development of this technology. Substrate back etching during the growth should be avoided by protecting the back side of the substrate or using N plasma as nitrogen source, to reduce the O non-intentional doping. Vertical structure flip chip LEDs could be an approach to improve the current spreading, by removing the ZnO substrate using a chemical etching method. The adaption of an InN buffer layer, which has shown sharp interfaces on ZnO substrates,[1] could be an approach to further improve the GaN crystal quality. A full N plasma source MBE growth process should be developed, which has shown advantages in the growth of *a*-plane GaN layers. Furthermore, the growth of nonpolar GaN heterostructures should also be carried out on *m*-plane ZnO substrates, as higher In incorporation efficiencies can be expected when growing along this orientation.[2]

Conclusions et perspectives

Cette recherche a été menée au Centre de Recherche sur l'Héthéro-Epitaxie et ses Applications (CRHEA), un laboratoire du Centre National de la Recherche Scientifique (CNRS) à Sophia Antipolis (06). Ce travail a été financé en partie par l'Agence Nationale de Recherche (ANR) dans le cadre du projet Jeune Chercheur « HENOPOIN2 » (Hétérostructures Non Polaires Intégrées à base d'Oxydes (II-O) et de Nitrures (III-N) pour applications optoélectroniques, 2012 - 2015), coordonné par Jean-Michel CHAUVEAU.

L'objectif principal de ce travail était d'étudier l'intégration des nitrures sur des hétérostructures à base d'oxyde de zinc (ZnO), sur deux plans dits « polaire » (plan c (0001)) et « non polaire » (plan a (11-20)). Les croissances ont été réalisées par épitaxie par jets moléculaires (EJM). Les propriétés structurales et optiques des hétérostructures ont été caractérisées et discutées. Les principales conclusions de cette étude sont détaillées en cinq points:

1. La préparation des substrats ZnO plan a et c. De fortes densités de défauts (îlots nanométriques constitués de résidus de silice colloïdale) et de rayures sont présents sur la surface des substrats ZnO. Un procédé de recuit a été développé pour obtenir une surface lisse et éliminer les défauts colloïdaux. Les conditions optimales de recuit pour les substrats de plan c de ZnO ont été obtenues avec une température de 1000°C sous atmosphère d'oxygène pendant deux minutes. Après cette étape de recuit, on obtient une surface lisse (rugosité RMS ~ 0,2 nm) avec des marches atomiques. Les conditions de recuit et la préparation des surfaces de ZnO plan a sont plus difficiles à obtenir. Une température comprise entre 700 et 800°C a été jugée la plus adaptée (nettement inférieure aux conditions obtenues pour le plan c). Après recuit, les résidus de silice colloïdale et les rayures ont été efficacement éliminés. Cependant, une morphologie de surface anisotrope est observée, constituée d'une structure en « lattes » allongées suivant la direction <1-100>, en raison du taux d'évaporation atomique différent entre les plans c et m.

2. La croissance d'hétérostructures (Al, Ga)N sur tremplins (Zn, Mg)O/saphir plan r. Des couches de GaN plan a ont été épitaxiées sur des couches tremplins de (Zn, Mg)O

avec différentes concentrations en Mg. Une morphologie de surface anisotrope est observée, constituée de « lattes » allongées suivant la direction <0001>. Cette anisotropie de croissance est la conséquence d'une vitesse de croissance de GaN plus grande le long de l'axe c. La teneur en Mg dans les tremplins de (Zn, Mg)O a une forte influence sur la qualité des couches cristallines de GaN. Lorsque la teneur en Mg est comprise entre 25 et 40%, les couches épitaxiées de GaN ont une perfection cristalline la plus élevée et la plus basse densité de grains désorientés. Ceci est attribué à une plus grande stabilité thermique de la surface de (Zn, Mg)O ainsi qu'à une rugosité de surface plus faible que celles de ZnO. L'émission de bord de bande de GaN domine le spectre de photoluminescence (PL) à basse température, et l'émission est polarisée selon l'axe <0001>. En tenant compte de la contrainte anisotrope dans le plan de la couche de GaN, un calcul de type « k • p » permet d'accéder à l'énergie de transition excitonique et à la force d'oscillateur entre la bande de conduction et la bande de valence. L'origine de l'émission de PL s'est avérée être principalement due à la contribution liée aux recombinaisons excitoniques X_2. Une série d'échantillons constitués de multi-puits quantiques (MPQs) de GaN/$Al_{0.2}Ga_{0.8}N$, avec des épaisseurs de PQs variant de 0,5 à 7 nm, ont été fabriquées sur des couches de GaN plan a. Quand l'épaisseur du PQ augmente, aucune diminution de l'énergie de PL due à la présence d'un champ électrique interne n'a été observée, ce qui indique l'absence d'effet Stark confiné quantique dans les hétérostructures GaN/$Al_{0.2}Ga_{0.8}N$ non polaires plan a.

3. L'étude du mécanisme de détermination de la polarité des couches de GaN épitaxiées sur substrats ZnO plan c. Des couches de polarité Ga et N ont été épitaxiées sur des substrats ZnO face O. Il a été constaté que les réactions à l'interface GaN/ZnO jouent un rôle important dans l'inversion de polarité. La formation d'une couche d'interface de gallate de zinc ($ZnGa_2O_4$) entre le substrat ZnO et la couche de GaN peut être contrôlée en ajustant la température de croissance et le rapport III/V au cours de la croissance de la couche de nucléation de GaN. Lorsque la couche de nucléation est épitaxiée dans des conditions riches en Ga (c-à-d avec un rapport III/V>1), une couche interfaciale de $ZnGa_2O_4$ se forme et la couche de GaN adopte une polarité Ga. D'autre part, lorsque la couche de nucléation est épitaxiée dans des conditions riches en N (c-à-d avec un rapport III/V<1), la couche de GaN croît directement (sans formation d'une couche interfaciale de $ZnGa_2O_4$) sur la surface du substrat de ZnO (face O), et une couche de GaN de polarité N est obtenue. Les couches GaN de polarité Ga et N présentent des propriétés structurales et optiques spécifiques (morphologie de surface, stabilité chimique, photoluminescence, etc.) Par contre, dans le cas de la

croissance sur des substrats ZnO face Zn, les couches GaN sont toujours de polarité Ga, indépendamment de la température de croissance et du rapport III/V de la couche de nucléation.

4. La réalisation de diodes électroluminescentes émettant dans le bleu sur substrat de ZnO. Des structures permettant la réalisation de diodes électroluminescentes (DELs), incluant des jonctions p-n de GaN et des multi-puits quantiques (MPQs) (In, Ga)N comme zone active, ont été épitaxiées sur des substrats de ZnO plan c. L'incorporation non-intentionnelle d'oxygène (O) a été réduite en adaptant les conditons de croissance de la couche de nucléation (utilisation d'une température de 550°C). L'origine de la présence d'oxygène a ainsi été identifiée comme venant principalement de la gravure de la face arrière du substrat par l'ammoniac (utilisé comme source d'azote) et de mécanismes d'interdiffusion entre le substrat et la couche de nitrures. Des couches de GaN de type p ont été épitaxiées avec succès sur ZnO, surmontant l'effet de compensation lié au niveau O. Les caratéristiques courant-tension des DELs montrent un comportement redresseur, avec des tensions de 4 -5 V à 20 mA. En ajustant la température de croissance de la couche (In, Ga)N, des DELs présentant une émission d'électroluminescence allant de 415 à 450 nm ont été fabriquées. Une émission bleue homogène sur la totalité de la DEL est observée. Une puissance optique de sortie de ~ 40 µW est obtenue pour un courant d'injection de 20 mA avec une saturation à ~ 0,1 mW lorsque le courant d'injection atteint 100 mA. Ces valeurs sont comparables aux DELs épitaxiées directement sur des substrats de saphir par EJM.

5. Epitaxie d'hétérostructures (In, Ga)N sur substrats massifs de ZnO plan a. Dans une première étape, des couches de GaN plan a (11-20) ont été épitaxiées sur un substrat ZnO. Deux méthodes ont été utilisées pour épitaxier les couches de nucléation, en utilisant soit l'ammoniac (NH_3), soit un plasma d'azote comme source d'azote (N). Les propriétés structurales et optiques des couches de GaN plan a ont été étudiées. Les couches de GaN épitaxiées avec une couche de nucléation utilisant le plasma N présentent de meilleures propriétés structurales et une émission de photoluminescence de plus forte intensité. Des multi-puits quantiques (MPQs) (In, Ga)N/GaN ont ensuite été épitaxiés sur les plans a et c de substrats de ZnO. En utilisant des conditions de croissance similaires pour les deux plans de croissance, il a été montré que l'efficacité d'incorporation de l'In est inférieure sur plan a, ce qui a été estimé à partir des énergies de photoluminescence des puits quantiques. L'émission des MPQs plan a est fortement polarisée selon la direction E // <1-100>, ce qui est en accord

avec les règles de sélection déterminées par les éléments de la matrice de transition entre les bandes de conduction et de valence.

Les résultats ci-dessus indiquent que le ZnO est un matériau prometteur comme substrat pour GaN. Ils montrent la possibilité d'utiliser le ZnO pour fabriquer des dispositifs optoélectroniques à base de nitrures, sur les plans polaire (c) et non polaire (a). Quelques axes d'étude devraient être privilégiés pour la poursuite du développement de cette technologie. Ainsi, la gravure par la face arrière des substrats lors de la croissance doit être évitée en protégeant la face arrière du ZnO, ou bien en utilisant le plasma N comme source d'azote. Cela permettra de réduire le dopage non intentionnel en oxygène. Des DELs à structure verticale « flip-chip » pourrait être une approche pour réduire les courants de fuite, en retirant le substrat ZnO par un procédé de gravure chimique. L'utilisation d'une couche tampon d'InN, qui permet l'obtention d'interfaces abruptes sur des substrats ZnO,[1] pourrait être une approche pour améliorer la qualité cristalline du GaN. De plus, des procédés de croissance EJM par source plasma N devraient être développés, suite aux résultats obtenus lors de l'épitaxie de couches de GaN plan a. En outre, la croissance d'hétérostructures de GaN non polaires devrait également être effectuée sur des substrats ZnO plan m, au regard des résultats publiés montrant une meilleure efficacité d'incorporation de l'In selon cette orientation.[2]

References

[1] Y. Cho, O. Brandt, M. Korytov, M. Albrecht, V. M. Kaganer, M. Ramsteiner, and H. Riechert, Appl. Phys. Lett. **100**, 152105 (2012).

[2] D. A. Browne, E. C. Young, J. R. Lang, C. A. Hurni, and J. S. Speck, J. Vac. Sci. Technol. A **30**, 041513 (2012).

Appendix I. Calculation of (Al,Ga)N / GaN QW transition energies

The QW transition energies were calculated following a 1D finite barrier potential QW model (illustrated in Figure AI. 1). The barrier height is determined by the band gap energy difference between $Al_{0.2}Ga_{0.8}N$ and GaN.

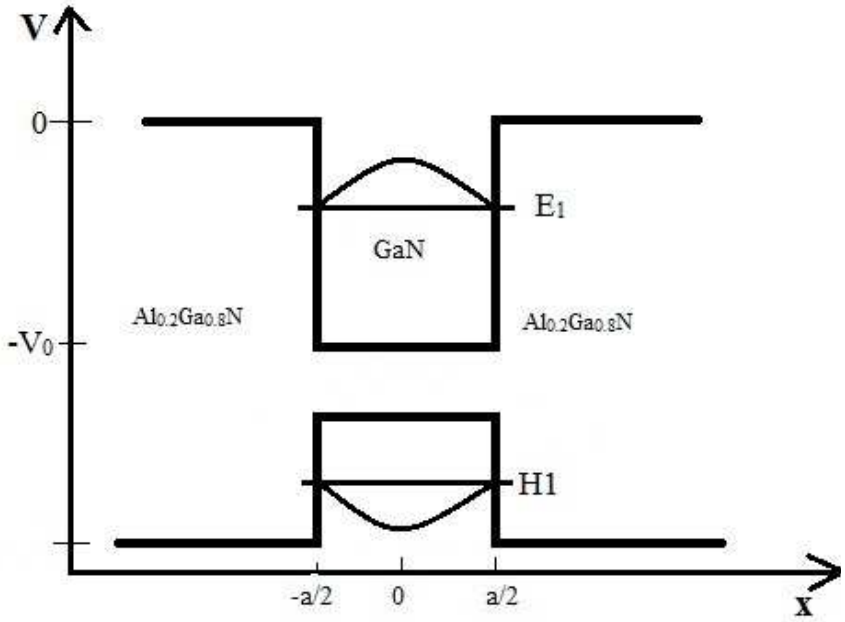

Figure AI. 1. 1D finite barrier potential model of the Al0.2Ga0.8N/GaN QW band structure.

The band gap energies of the strained GaN QW and the $Al_{0.2}Ga_{0.8}N$ barriers were deduced from the photoluminescence (PL) spectra of the GaN layer and the $Al_{0.2}Ga_{0.8}N$ barriers in Fig. III. 23 by:

$$E_g = E_{PL} + E_{bound} + E_{Loc} + E_{Ry}, \quad \textbf{(A. 1)}$$

E_{PL} is the band edge energy deduced from the PL spectrum. E_{bound} is the energy drop of the excitons bound to the donors or acceptors, and it has been determined to be 6 meV for GaN in Section III.2. E_{Loc} represents the localization energy of the excitons in the $Al_{0.2}Ga_{0.8}N$ alloy, due to the potential fluctuation, which may result from the inhomogeneities of the Al content, the surface roughness and the strain.[1] In (Al,Ga)N alloys, $E_{bound} + E_{Loc}$ can be

obtained from the deviation of the measured PL data and the Varshni fitting of the temperature evolution curve of the PL emission energy. For (Al,Ga)N alloy with 20% Al, a value of 25 meV has been measured.[1] E_{Ry} is the exciton binding energy, and this value has been found to be 26 meV for GaN.[2] The exciton binding energy of $Al_{0.2}Ga_{0.8}N$ is estimated as 30 meV according to the electron effective mass. All there values are listed in Table AI. 1.

layer	E_{PL}	E_{bound} ($E_{bound} + E_{Loc}$)	E_{Ry}	E_g
GaN QW	3.478	0.006	0.026	3.510
$Al_{0.2}Ga_{0.8}N$ barrier	3.800	0.025	0.030	3.855

Table AI.1. Energies related to the GaN QW and the Al0.2Ga0.8N barrier, in eV.

The band offset is determined roughly by assuming that the conduction band offset is two times larger than the valence band offset.[3] Therefore, we have:

$$V_{0CB} = \frac{2}{3}(E_{gAlGaN} - E_{gGaN}),$$
$$V_{0VB} = \frac{1}{3}(E_{gAlGaN} - E_{gGaN}). \qquad \textbf{(A. 2)}$$

In the conduction band, the potential is described by:

$$V(x) = \begin{matrix} 0, & |x| > a/2 \\ V_0, & |x| < a/2 \end{matrix}, \qquad \textbf{(A. 3)}$$

where x is the coordinate axis along the growth direction and the center of the QW is set at x=0. a is the thickness of the QW. The bottom of the barrier conduction band is set as $V = 0$, and the bottom of the well at $-V_0 = -V_{0CB} = -0.23eV$. Then, the Schrödinger equations in the well and barrier regions are:

$$-\frac{\hbar^2}{2m_e}\frac{d^2}{dx^2}\Psi(x) = E\Psi(x), \qquad \left(|x| > \frac{a}{2}\right)$$
$$-\frac{\hbar^2}{2m_e}\frac{d^2}{dx^2}\Psi(x) - V_0\Psi(x) = E\Psi(x), \qquad \left(|x| < \frac{a}{2}\right) \qquad \textbf{(A. 4)}$$

where m_e is the electron effective mass. We define $k_0 = \sqrt{\frac{2m_e V_0}{\hbar^2}}$, $\kappa = \sqrt{-\frac{2m_e E}{\hbar^2}}$, and $k = \sqrt{\frac{2m_e (V_0 + E)}{\hbar^2}}$, then Eq. A. 4 can be rewritten as:

$$\frac{d^2}{dx^2}\Psi(x) - \kappa^2 \Psi(x) = 0, \qquad \left(|x| > \frac{a}{2}\right)$$

$$\frac{d^2}{dx^2}\Psi(x) + k^2 \Psi(x) = 0. \qquad \left(|x| < \frac{a}{2}\right) \tag{A. 5}$$

Together with the boundary conditions,

$$\begin{aligned} &\Psi\big|_{x=\pm\infty} = 0, \\ &\Psi_w\Big|_{x=\pm\frac{a}{2}} = \Psi_b\Big|_{x=\pm\frac{a}{2}}, \\ &\frac{d\Psi_w}{dx}\Big|_{x=\pm\frac{a}{2}} = \frac{d\Psi_b}{dx}\Big|_{x=\pm\frac{a}{2}} \end{aligned} \tag{A. 6}$$

the wave function of the electron in the QW structure can be determined, and the fundamental state is an even function with a cosine shape, as shown in Eq. A. 7. The electron wave function for the fundamental state is:

$$\Psi_{1l} = B_1 e^{\kappa x}, \qquad \left(x < -\frac{a}{2}\right)$$

$$\Psi_{1w} = A_1 \cos(k_1 x), \quad \left(-\frac{a}{2} < x < \frac{a}{2}\right) \tag{A. 7}$$

$$\Psi_{1r} = B_1 e^{-\kappa x}, \qquad \left(x > \frac{a}{2}\right)$$

Ψ_{1l} and Ψ_{1r} represent the wave functions in the left and right side of the QW, respectively; Ψ_{1w} is the wave function in the QW. A_1 and B_1 are constants. The tunnel length of the wave function into the barrier is $\lambda = \frac{1}{\kappa} = \frac{\hbar}{\sqrt{2m_e(-E)}}$, which is inversely proportional to the square

root of the total energy -*E*. To satisfy the boundary conditions, the energy levels are discrete and should satisfy:

$$\left|\cos\frac{ka}{2}\right| = \frac{k}{k_0}, \qquad \tan\frac{ka}{2} > 0 \tag{A. 8}$$

Two sides of Eq. A. 8 are plotted as a function of $\frac{ka}{2}$ and shown in Figure AI. 2. It shows that when the QW thickness is 3 nm, *k* has only one solution. It means that there is only one confined energy level in the conduction band. Then, the electron confinement energy can be deduced from $E_e = V_0 + E = \frac{\hbar^2 k^2}{2m_e}$.

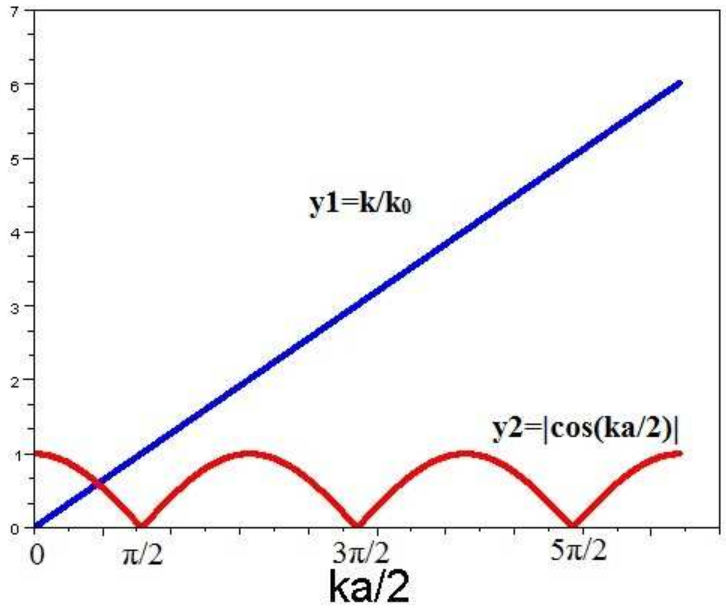

Figure AI. 2. Simulated solution of Eq. A. 8 as a function of $ka/2$, assuming the QW thickness a = 3 nm.

The hole QW confinement energy E_h can be calculated following the same model, by introducing the valance band offset (Eq. A.2) and the hole effective mass (Table I.4).

References

[1] N. Nepal, J. Li, M. L. Nakarmi, J. Y. Lin, and H. X. Jiang, Appl. Phys. Lett. **88**, 062103 (2006).

[2] A. Viswanath, J. I. Lee, Dongho D. Kim, C. R. Lee, and J. Y. Leem, Phy.Rev. B **58**, 16333 (1998).

[3] Wan X.-J., Wang X.-L., Xiao H.-L., Wang C.-M., Feng Ch., Deng Q.-W., Qu S.-Q., Zhang J.-W., Hou X., Cai S.-J., and Feng Z.-H., Chin. Phys. Lett. **30**, 057101 (2013).

Appendix II. Polarization properties of *a*-plane (Al,Ga)N / GaN MQW emission

The polarization behaviours of the PL emission from the MQWs (Fig. III. 23) are more complicated than that of thick a-GaN layers grown on (Zn,Mg)O / r-sapphire templates (chap. III, section III.2.5). In particular, the MQW emission peak is broadened by defect related levels. The trapping of free excitons in the defect related states may influence the polarization behaviours of the emission, and it is difficult to be resolved from the CW PL spectra due to the large line width (50-90 meV) of the peaks (Fig. III. 23).

As shown in Fig. III. 26, the peak position of the MQW emission blue-shifts by ~ 30 meV when the temperature is increased from 11 to 100 K. As discussed in details by P. Corfdir et al.,[1] this behaviour can be attributed to the thermal activation of excitons trapped in quantum well wire (QWW) states, which are formed by the intersection of the QW layers with basal stacking faults (BSFs) present in the structure. The excitons are activated to free QW states when the temperature increases. To study the influence of trapping states on the polarization property of the QW emission, the polarization of the QW emission was measured at both 11 and 100 K. Figure AII. 1 shows the integrated PL intensity of the MQW emission from N1660, which has a well thickness of 2 nm. The MQW PL emission is polarized in parallel to the [0001] direction, identical to the polarization of the GaN layers studied in Section III. 2. 5. Also, there is almost no change of polarization degree when the temperature is increased from 11 to 100 K.

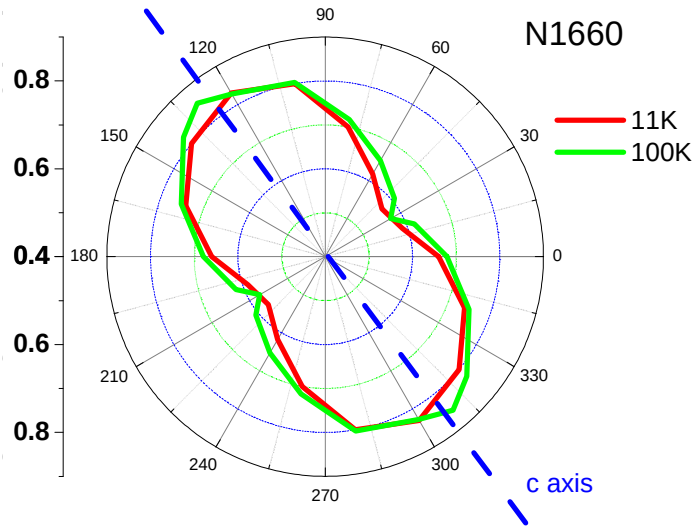

Figure AII. 1. Integration of a 2-nm thick GaN / $Al_{0.2}Ga_{0.8}N$ MQW (N1660) PL intensity (3.45eV - 3.54eV) as a function of the polarization angle at 11 and 100 K.

However, the PL emission of other GaN / $Al_{0.2}Ga_{0.8}N$ MQW heterostructures from the same series of samples was found to show different polarization behaviours. Figure AII. 2 shows the PL spectrum of sample N1692 (cf. chap. 3, section III. 3. 1, table III. 5) when polarized along *m*-[1-100] and *c*-[0001] directions. The spectra were recorded at 11 and 100 K. At low temperature (11K), the emission peak is mainly polarized perpendicularly to the *c* axis (along [1-100] axis), with a polarization degree of 0.49. After the temperature was raised to 100 K, the polarization degree along *m* direction was reduced to 0.18. It indicates that the polarization along the *m* direction is enhanced when the excitons are trapped in the defect related states.

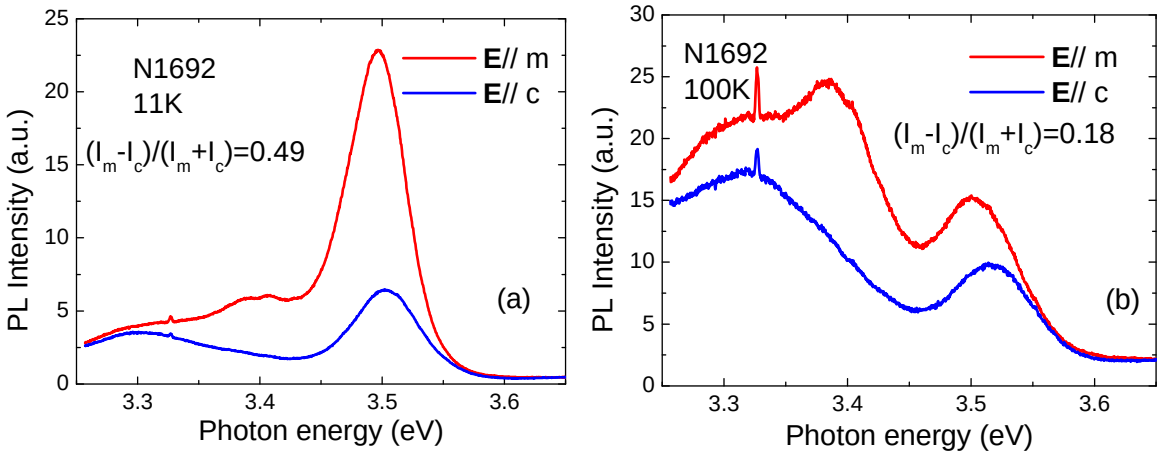

Figure AII. 2. PL spectrum of a 5-nm thick GaN / $Al_{0.2}Ga_{0.8}N$ MQW (N1692) when polarized along *m* and *c* directions, at (a) 11 K and (b) 100 K, respectively.

Figure AII. 3. presents the polarization properties of a third GaN / $Al_{0.2}Ga_{0.8}N$ MQW heterostructure (sample N1662) at 11 and 100 K. It indicates that the polarization degree of the MQW emission along *m*-axis has been reduced when the temperature is increased from 11 to 100K, which is very similar to the behaviour observed in Figure AII. 2 for sample N1692.

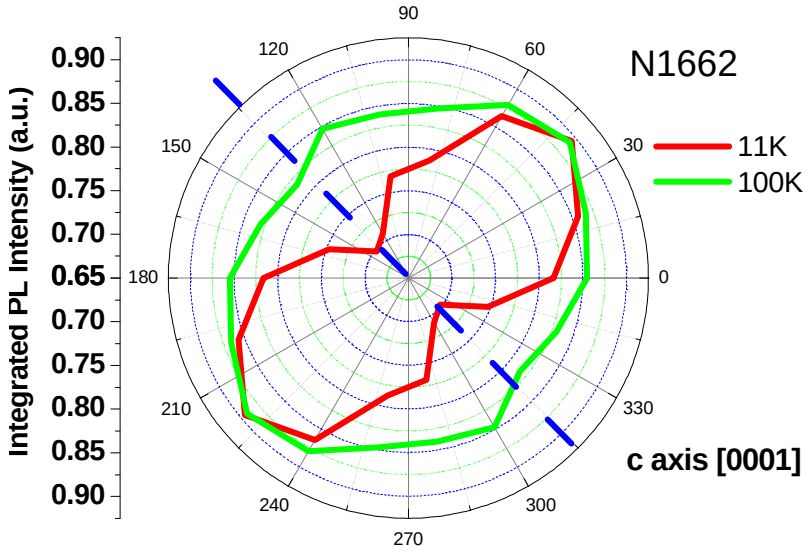

Figure AII. 3. Integrated PL intensity of a 3-nm thick GaN / $Al_{0.2}Ga_{0.8}N$ MQW (N1662) emission as a function of the electric field oscillation angle, at 11 and 100 K.

Figure AII. 4 shows the PL spectra of a fourth GaN / $Al_{0.2}Ga_{0.8}N$ MQW heterostructure (sample N1690) when polarized along [1-100] and [0001] directions, at 11 and 100 K, respectively. Contrary to sample N1692 (Figure AII. 2), the maximum polarization direction is found to switch from the [1-100] direction at 11 K to the *c* direction at 100 K. At the same time, the transition energy of the main emission peak is blue-shifted by ~ 20 meV, which is attributed to the detrapping of excitons from defect related states. This result implies that the defect related states modifies the polarization behaviour of the excitons.

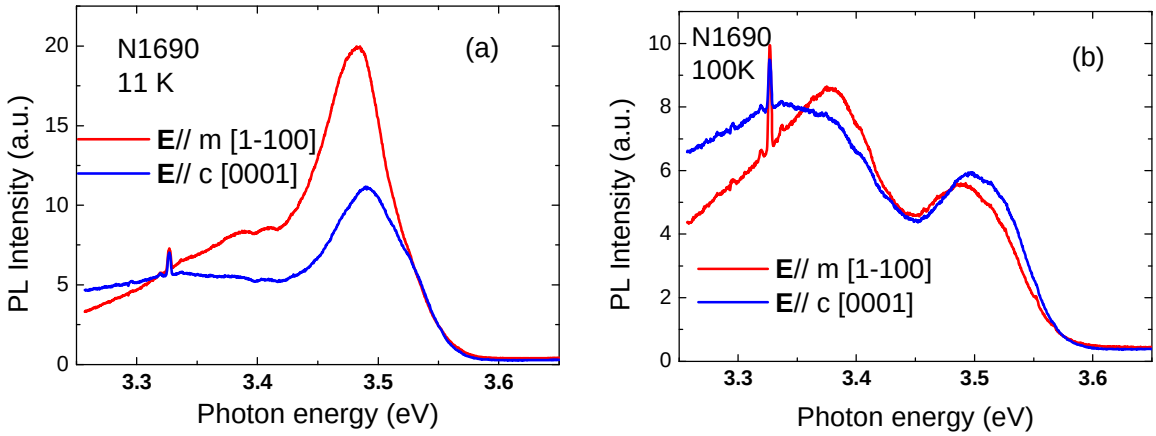

Figure AII. 4. PL spectra of a 7-nm thick GaN / $Al_{0.2}Ga_{0.8}N$ MQW (N1690) when polarized along *m* and *c* directions, at (a) 11 K and (b) 100 K, respectively.

k•p calculations have been performed to understand the intrinsic polarization behaviours of the MQW emission. In the first step, the strain states of the GaN layers in the MQWs were determined. The lattice parameters of the GaN layers have been calculated and compared with those of bulk GaN. Table AII.1 summarizes the strain values of GaN reference layers (cf. chap. 3, section III. 3. 1, table III. 3) and that of the MQW heterostructures, along the two in-plane directions.

sample	Layer	ε_{yy} [1-100]	ε_{zz} [0001]
N1704	GaN 1µm	0.27%	-0.06%
N1653	GaN 1µm	0.17%	-0.07%
N1662	GaN 1µm +MQWs	-0.18%	-0.22%
N1690	GaN 1µm +MQWs	0.03%	0.09%
N1692	GaN 1µm +MQWs	0.02%	-0.03%
N1693	GaN 1µm +MQWs	-0.15%	-0.08%
MQW average		-0.06%	-0.07%

Table AII. 1. In-plane strain values of GaN reference layers and GaN / $Al_{0.2}Ga_{0.8}N$ MQW heterostructures grown on (Zn,Mg)O / r-sapphire templates.

At first, there is a large variation of the lattice parameters (LPs) between the samples which can be attributed to the different (Zn,Mg)O template layers used in this study (cf. chap. 3, section III. 3. 1, table III. 5). However, a general trend can be found, which is that the strain along the *c* direction is compressive for all the GaN layers and heterostructures (except for sample N1690, which is characterized by the thicker GaN QW layers). The main differences arise from the in plane ***a*** parameter, which has a tensile strain for the GaN reference layers, while of the strain is compressive in average for the MQW heterostructures. The main difference is attributed to the role played by the $Al_{0.2}Ga_{0.8}N$ layers in the strain relaxation mechanism of the structures, owing to the large compressive lattice mismatch with GaN (-0.48% along [11-20] and -0.78% along [0001]). Indeed, the total thickness of the $Al_{0.2}Ga_{0.8}N$ layers is 120 nm, and a strain relaxation on the GaN template is expected. Therefore, the thin GaN layers inserted in the MQWs are assumed to be grown coherently with the $Al_{0.2}Ga_{0.8}N$ barriers.

The simulated oscillator strengths of the different MQW structures are listed in Table AII. 2. The results indicate that the MQW emission should be polarized along the *m* [1-100] direction. These results are different from those found for the GaN reference layers, because the strain along the *m* direction is switched from tensile to compressive in the MQW case.

Exciton	N1690 MQW (7 nm)			N1662 MQW (3 nm)		
	x [11-20]	*y* [1-100]	*y* [0001]	*x* [11-20]	*y* [1-100]	*y* [0001]
X_1	0.652	0.345	0.003	0.064	0.885	0.050
X_2	0.250	0.535	0.216	0.534	0.001	0.465
X_3	0.098	0.121	0.781	0.401	0.114	0.485

Exciton	N1692 MQW (5 nm)			N1693 MQW (0.5 nm)		
	x [11-20]	*y* [1-100]	*y* [0001]	*x* [11-20]	*y* [1-100]	*y* [0001]
X_1	0.643	0.352	0.005	0.182	0.805	0.013
X_2	0.200	0.456	0.344	0.668	0.107	0.225
X_3	0.157	0.192	0.651	0.151	0.088	0.761

Table AII. 2. Simulated oscillator strengths of X_1, X_2, and X_3 excitons, along three orthogonal directions, respectively, for the different GaN / $Al_{0.2}Ga_{0.8}N$ MQW structures grown on (Zn,Mg)O / r-sapphire templates.

TEM results have shown that a high density of BSFs ($4 \times 10^5 - 1 \times 10^6$ / cm) are present in the GaN layers (cf. chap. 3, section III. 2. 2). These BSFs are oriented perpendicularly to the *c* axis of the GaN layer. Furthermore, in a quantum wire structure, it has been shown that the strongest emission is polarized along the quantum wire direction.[2] According to this theory, the emission from the excitons confined in QWW states [ref. 1] should be polarized perpendicularly to the *c* axis.

Together with the experimental observations, we believe that the excitons in the MQWs were trapped in the QWRs at low temperature (~10 K). Under this confinement, the polarization degree along the *m* direction is enhanced. When the temperature increases, the excitons are activated from the QWR states, and the MQW emission shows the polarization behaviours of free excitons.

Moreover, the surface morphology may also influence the emission polarization. Keller *et al* have studied the polarization spectroscopy of the (Al,Ga)N / GaN MQWs grown along the *c* [0001] direction, where surface steps parallel to the GaN [11-20] direction were observed, with a step height of 1-2 nm.[3] The emission from the MQW was found polarized along the direction of the surface steps. The polarization behaviour was attributed to the confinement effect of the step, which behaves like a QWR. In our MQW layers, a high

density of surface stripes is present on the surface (Fig. AII. 5). The stripes are along the *c* direction, which may enhance the polarization of the emission along this direction.

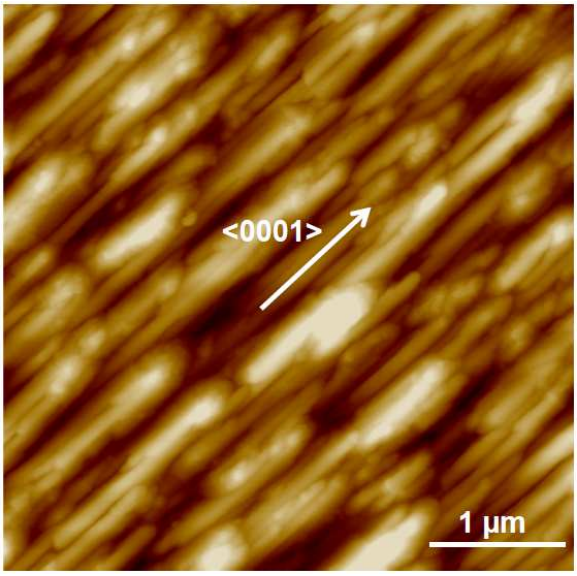

Figure AII. 5. Typical surface morphology of the surface of a GaN / $Al_{0.2}Ga_{0.8}N$ MQW structure (sample N1692) measured by the AFM. The vertical scale is 50 nm.

To conclude, the polarization behaviours of the MQWs were investigated, using both experimental and theoretical methods. Several factors may influence the polarization properties: the surface morphology, the QWWs formed by the intersection of BSFs and the MQW structure, and the intrinsic properties determined by the crystal orientation and the residual strains. The influence from a QWW confinement [ref. 1] is high at low temperature, since in our series of MQW structures, the MQW emission is found to be polarized perpendicularly to [0001] at low temperature (~ 10K).[1] This behaviour may be modified when the temperature is increased to above 100 K, mainly due to the thermal activation of the excitons from QWW states to free states.

[1] However, at low temperature (10 K), in the case of sample N1660, the PL emission is polarized in parallel to the [0001] direction (Figure AII .5). The reason for this specific behaviour is still unclear.

References

[1] P. Corfdir, P. Lefebvre, L. Balet, S. Sonderegger, A. Dussaigne, T. Zhu, D. Martin, J.-D. Ganiere, N. Grandjean, and B. Deveaud-Pledran, J. Appl.Phys **107**, 043524 (2010).

[2] C. R. McIntyre and L. J. Sham, Phy.Rev. B **45**, 9443 (1992).

[3] S. Keller, N. Pfaff, S. P. DenBaars, and U. K. Mishra, Appl. Phys. Lett. **101**, 182103 (2012).

Acknowledgements

This work has been carried out at the Center de Recherche sur l'Hetero Epitaxie et ses Applications (CRHEA-CNRS). During this process, I have received assistance from many people, and I would like to thank all of them here.

At the beginning, I would like to thank Jean Yves Duboz for giving me this chance to work in CRHEA as a PHD student, where I have spent three important years in my life.

I want to thank the supervisors of my thesis: Julien Brault and Jean Michel Chauveau. They brought me into the field of compound semiconductors, and they have spent a lot of time to help me finish this thesis. I want to thank them for encouraging me to make progress in research and forgiving my mistakes. I thank Jean Massies, as the director of my thesis, for his help and discussions during my study.

I would like to thank Mathieu Leroux for helping me improve my knowledge in solid state physics, and his critical discussions on my photoluminescence results. The discussions with Borge Vinter deepen my understanding on semiconductor theories，and I want to thank him for his kindness to me. I want to express my respect to M. Leroux and B. Vinter for their academic attainments.

I want to thank Philippe Vennéguès for performing TEM studies on my samples. Oliver Tottereau, Maud Nemoz and Monique Teisseire are also acknowledged for their collaborations and technical support in various fields including AFM, SEM, XRD, PL and CL. I thank Sébastien Chenot for all his help in clean room. I also want to thank Michèle Pefferkorn, Isabelle Cerutti and Anne Marie Galiana for their help in administrative affaires.

I would like to thank Andreas Wieck from Ruhr Bochum University for giving me a chance to visit his lab and perform electrical measurements in Bochum. I want to thank Bruno Daudin from CEA-INAC for his assistance in the plasma assistant MBE growth. I would thank Guy Feuillet, Jean-Louis Santailler and Ivan-Christophe Robin from CEA-LETI for providing us ZnO substrates and performing the SIMS measurements. I want to thank Pierre

Lefebvre, Pierre Valvin, and Bernard Gil from Université Montpellier II for the time resolved PL studies.

I thank my parents for their encouragement during my thesis. I also want to thank my landlady, Regina Neustch. She has provided me such a nice place to live and taken care of me a lot during the last three years, which allows me to concentrate on my thesis. I want to thank all the players of CRHEA football team, for the pleasant leisure time we have spent together.

I want to thank the Université Nice Sophia Antipolis for the financial support during all my study, which allows me to have three year enjoyable life in Cote d'Azur. Finally, I want to thank the great country of France. I have spent five years here, where I acquire knowledge, learn about a totally different culture, and grow up. I enjoy the beautiful nature scene, the friendly people, and the delicious food. I wish peace and prosperity for this great land.